SEISMIC BEHAVIOR OF COMPOSITE STEEL FRAME-REINFORCED CONCRETE INFILL WALL STRUCTURAL SYSTEM

Xiangdong Tong
Walter P. Moore & Associates, Inc.
Houston, Texas

Arturo E. Schultz
Department of Civil Engineering
University of Minnesota
Minneapolis, Minnesota

Jerome F. Hajjar
Department of Civil Engineering
University of Minnesota
Minneapolis, Minnesota

Carol K. Shield
Department of Civil Engineering
University of Minnesota
Minneapolis, Minnesota

A Report from the National Science Foundation
U.S.-Japan Cooperative Research Program
Phase 5, Composite and Hybrid Structures
National Science Foundation Grant No. CMS-9632506

Report No. ST-01-2
Department of Civil Engineering
Institute of Technology
University of Minnesota
Minneapolis, Minnesota 55455-0116

April 2001

Abstract

A composite steel frame-reinforced concrete infill wall, in which the steel and concrete components work integrally through mechanical connectors, offers significant advantages as an earthquake-resistant structural system for buildings located within regions subjected to earthquakes. This project was aimed at the investigation of the seismic behavior of the composite steel frame-reinforced concrete infill wall structural system through a combined experimental and analytical research program.

The primary part of this research was conducting a cyclic loading test on one two-story, one-bay specimen, which represented the bottom two stories of a six-story prototype structure at approximately one-third scale. Partially-restrained (PR) connections were used to join the wide flange steel columns and beams. The infill was cast using regular concrete. Confined headed studs were used as the interface connectors.

The test showed that this system provided sufficient strength to resist the design lateral loads and ample stiffness to control system drift. Adequate redundancy was provided to the system by alternate load paths, such as shear stud-infill interaction and truss action due to steel frame-infill interaction. At the design lateral load level, 80-90% of the lateral shear force was transferred from the steel frame to the infill through the headed studs, and approximately 80% of the overturning moment was carried by the steel columns. The ultimate strength of the specimen was induced by crushing of the concrete in the corners, yielding and fracture of the studs, and formation of plastic hinges in the PR connections. Adequate confining reinforcement was critical to enhance the strength and ductility of the studs in the infill panels. The failure of the studs was controlled by low cycle fatigue.

The second part of this thesis includes a description of linear elastic finite element analysis for use in design and a plastic mechanism analysis procedure to verify lateral

Acknowledgements

Funding for this research was provided by the National Science Foundation (Grant No. CMS-9632506) under Dr. Shih-Chi Liu as part of the U.S.-Japan Cooperative Research Program, Phase 5, Composite and Hybrid Structures, and by the University of Minnesota. This support is gratefully acknowledged. The assistance in this research of Paul M. Bergson, William K. Saari, Jian Zhao, Sara D. Prochnow, Nels Ojard, Dmitri Jajich, Justin Ocel, Meredith Mormann, and Alex Lindblad is greatly appreciated. The authors would also like to thank Lawrence A. Kloiber of LeJeune Steel Co., Minneapolis, Minnesota, for assisting with the fabrication of the test specimen, and Grace Products and Mineral Solutions for donating materials for the experiment. Any opinions, findings, or conclusions and recommendations expressed in this material are those of the authors and do not necessarily reflect the views of the National Science Foundation.

Table of Contents

List of Figures

List of Tables

Chapter 1

Introduction

1.1 Background

Steel-concrete composite structures comprising the lateral load resisting systems in buildings in seismic areas have been widely explored and developed, with increasing recognition of the benefits obtained from several different types of the composite structures. In a composite steel-concrete lateral load resisting structural system, the steel and concrete components work integrally, such as the encased composite truss members in the Bank of China Tower in Hong Kong, composite shear walls in the First City Tower in Houston, and high-strength concrete infilled steel pipes in the Two Union Square in Seattle (Taranath, 1997). Among the different types of composite lateral-resistance systems, the steel frame-reinforced concrete (RC) infill wall system has been the subject of research within the National Science Foundation (NSF) U.S./Japan Cooperative Research Program on Composite and Hybrid Structures following the 1994 Northridge earthquake in California.

The 1994 Northridge earthquake revealed some unexpected problems regarding the seismic response of the steel moment-resisting frames, especially their connection regions (FEMA, 2000). Cracks were found to occur in the fully-restrained girder-flange-to-column-flange weld and even to propagate into the column flange and web, leading to

expensive structural repairs. A series of solutions have been proposed to eliminate or reduce these connection problems directly, such as the removal of backing bars and the use of high quality welding materials (FEMA, 2000). However, a final consensus has not been reached in the earthquake engineering community regarding modifications to the design and construction procedure for moment-resisting frames. An alternative method is to reduce the seismic demands on steel frames by avoiding the use of fully-restrained connections. This philosophy has led to the development of the composite steel frame-RC wall system, utilizing the high shear stiffness of the RC infill wall to attract most of the lateral shear forces from earthquake motions.

Although initial design provisions for the composite steel frame-RC infill wall systems have been proposed in NEHRP (1997), this system is rarely used in practice in the United States due to lack of sufficient research. In Japan, design recommendations for earthquake-resistant design of this type of composite system has been implemented (AIJ, 1985). It is also well known that two buildings of this type behaved satisfactorily during the Great Kanto Earthquake of 1923 in Japan, while other buildings were badly damaged (Makino et al., 1980; Makino, 1984).

1.2 Advantages of the Composite Steel Frame-Reinforced Concrete Infill System

In the composite steel frame-RC infill system (Figure 1.2.1), the steel columns and girders serve as boundary members to resist gravity loads and most of the overturning moment, while the RC infill walls carry most of the shear forces. The RC infill walls have the benefiit of increasing the lateral stiffness dramatically, thus avoiding excessive drift and reducing the seismic demands on the steel frames. This provides the opportunity to use partially-restrained (PR) connections in conjunction with lighter steel framing instead of more expensive fully-restrained connections, which are required in the more common steel moment frames (without infill walls). Adequate interface connections, such as headed stud shear connectors, can be used to transfer shear forces uniformly between the

1.3.1 Experimental Research on the Seismic Behavior of Infilled Frames

Research on infilled frames started with the investigation of their static behavior under monotonic lateral loading (e.g., Benjamin and Williams, 1957; Holmes, 1961) with the intention of developing an effective method to predict their ultimate lateral strength. With the recognition that the lateral loading imposed on infilled frames is induced by dynamic phenomena producing reversing load histories, such as earthquakes, wind, or explosions, researchers began to focus their efforts on the cyclic load behavior of infilled frames. During the last three decades, experiments with three different types of loading have been carried out to simulate dynamic phenomena, especially seismic forces: cyclic static and dynamic load tests, pseudo-dynamic tests, and shake-table tests.

Mallick and Severn (1968) performed half-cyclic dynamic load tests on small scale, two-story infilled steel frames, where the cyclic load was applied to the infilled frame in one direction only. The steel frames comprised 0.75 inch $\times$ 0.75 inch square steel bars and the story dimension was 24 inch $\times$ 24 inch. The dynamic characteristics, such as the damping ratio and the energy dissipation capacity, were compared between infilled steel frames with and without interface shear connectors. It was found that using a small number of shear connectors in loaded corners could prevent the rotation of the infill walls inside the steel frames and increase the stiffness of the system. However, they failed to see any strength increase with the use of shear connectors. The frequencies and mode shapes of multi-story infilled steel frames were obtained analytically using two models: a shear model in which the axial deformation of the steel components was ignored, and a cantilever model in which the bending deformation of the steel frame members was ignored. Test results showed that the cantilever model was better than the shear model for analysis of multi-story infilled steel frames, particularly for those with a height/span ratio greater than 2.

Liauw (1979) conducted both static and dynamic cyclic load tests on both integral and non-integral steel frames with RC infill walls. The four-story steel frame models comprised 22 mm $\times$ 22 mm square steel bars, with the size of infill being either 305 mm

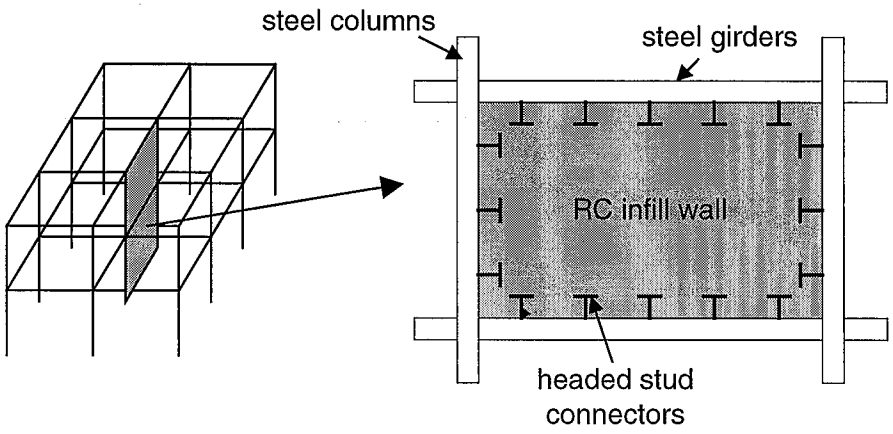

Fig. 1.2.1 The Composite Steel Frame-RC Infill Wall System

steel frames and infill walls to ensure effective composite action. This reduces the probability of unfavorable failure mechanisms such as the premature formation and crushing of the compression struts in the RC walls. Experiments conducted by Makino et al. (1980) and Makino (1984) indicated that this system develops a pattern of closely-spaced cracks with small widths. Such cracks may be repaired at a reasonable cost after a moderate earthquake. Another advantage of this composite system is its convenience for construction, since the columns and girders can be used as forms and form supports for efficient casting of the concrete.

1.3 Literature Review

Historically, five different types of infill have been considered in the study of the behavior of infilled frames: brick, clay tile, concrete block, plain concrete, and reinforced concrete. The surrounding framing in these studies comprised either reinforced concrete or steel members. The following literature review focuses on the steel frame-RC infill wall system due to its distinctive behavior, with a brief summary of other infilled frames. According to Liauw et al. (1983a, 1983b), infilled frames may be divided into two categories: (1) those with connectors along the interfaces between the frames and the infill walls are called integral infilled frames; and (2) those without are called non-integral infilled frames. These definitions are used in the following literature review.

× 610 mm × 22 mm or 305 mm × 610 mm × 22 mm (height × width × thickness). The reinforcement ratio for the infill wall was 0.56%. In contrast to the conclusion drawn by Mallick and Severn (1968), the presence of the interface connectors was shown to increase both frame stiffness and strength significantly. Furthermore, failure of the integral infilled steel frames was induced largely by shear between the steel frames and the infill walls, instead of by the diagonal compression failure of the infill walls in the non-integral infilled steel frames. The dynamic characteristics of these systems were studied further in another series of cyclic tests (Liauw and Kwan, 1985) on similar infilled steel frames having three different interface configurations: (1) no connectors; (2) connectors welded only along the infill wall/steel girder interface; and (3) connectors welded along the entire infill wall/steel frame interface. The tests showed that the infilled steel frames with the Type 3 interface configurations were the most reliable type of construction because they possessed the highest energy dissipation capacity, the greatest damping ratio in the nonlinear range of deformation and the slowest stiffness degradation.

In Japan, two sets of tests were conducted to investigate the behavior of portal steel frames infilled with reinforced concrete, subjected to combined action of constant gravity loading and static cyclic lateral loading (Makino et al., 1980). The portal steel frames were approximately one-third scale and comprised wide-flange sections. There were two specimens in each set, one of which had the strong axis of the steel columns oriented perpendicular to the plane of the infill wall, and the other having the weak axis of the steel columns oriented perpendicular to the plane of the infill wall. The portal steel frames in the first set of tests were cyclically loaded well into the inelastic range of behavior before casting of the infill walls. The two virgin portal steel frames used in the second set of tests had the same sizes as those in the first set, respectively. A few headed studs were employed with the objective of preventing out-of-plane failure of the infill walls. The composite action of system resulted in a uniformly distributed crack pattern in the RC infill walls. The infilled frames having columns bent about their strong axis were shown to have ductile behavior as good as those of typical bare steel frames. It was also concluded that an infilled steel frame having the steel frame pre-loaded into the inelastic

range of behavior can have almost the same strength as a virgin steel frame with RC infill walls. A tentative design recommendation was proposed by Makino (1984) with the backing of more experimental research, in which the primary variable was the cross section area ratio between the concrete and the steel column. Also in Japan, another research group (Hayashi and Yoshinaga, 1985, 1986, 1987, 1994) performed a series of similar tests on portal infilled steel frames, in which the width-to-height ratio was chosen as the main variable, and interface connectors were either headed studs or deformed bars.

Shake-table tests are believed to be the best approach for simulating the behavior of a structure during an earthquake. However, shake-table tests are expensive, especially for large scale models. Kwan and Xia (1995) reported a shake-table test on steel frames infilled with light reinforced concrete walls (non-integral). In their tests, the specimen comprised a pair of one-third scale infilled steel frames, connected through reinforced concrete floor slabs at each story, representing a one-bay, four-story structure. The steel frame comprised 40 mm × 40 mm × 2.5 mm high-yield tubes and story dimension is 1125 mm × 1500 mm (height × width). Accelerograms from the EI Centro earthquake were used to excite the shake-table, with progressively increasing magnitudes of acceleration being applied until failure of the specimen occurred. It was observed that the infill walls separated from the steel frames during early loading stages and acted as a diagonal compressive strut. The specimen reached its maximum strength when the corners of the infill walls in the first story were crushed. The specimen did not fail even when the applied peak acceleration was increased to 1.50g, although the frames were badly damaged. However, it was concluded that the RC infill walls would have collapsed out-of-plane, had there not been steel plates attached to the outside of the RC walls to keep them in place. It was also found that the natural frequency of the specimen decreased rapidly as the applied peak acceleration of the simulated earthquake was increased, while the damping increased from 1.7% to 11.0%.

Masonry is a traditional infill material for both steel and RC frame structures. A number of experimental studies have been carried out to evaluate the effect of masonry infill on the seismic behavior of the surrounding frames. Although it was found that

masonry infill can also significantly increase the stiffness and strength of frame structures (Klinger and Bertero, 1978; Mehrabi et al., 1996; Negro and Verzelett, 1996), designers in the United States are reluctant to treat unreinforced masonry infill as a structural element in seismic regions due to several unfavorable characteristics of the masonry infill. For example, Mander and Nair (1994) found that the shear strength of brick infill walls was greatly affected by cyclic loading; Mosalam et al. (1997) reported that there were significant pinching zones in the hysteretic load-displacement curves from his cyclic load tests on two-bay masonry infilled steel frames. Furthermore, shake-table tests indicated that it is often unavoidable for the masonry infill to collapse out-of-plane as a result of increased acceleration of ground motion (Dawe et al., 1989; Kwan and Xia, 1995).

1.3.2 Analysis of Infilled Frames

During the last three decades, different approaches have been proposed for the prediction of the ultimate strength of infilled steel frames subjected to monotonic lateral load. Holmes (1961) proposed that the infill wall be replaced by an equivalent diagonal strut having a width equal to one-third of the diagonal length of the infill wall. In his elastic model, no axial deformation was included in the steel members and the infilled steel frame achieved its maximum lateral strength when the equivalent strut reached a limiting value of compressive strain. The corresponding deflection was calculated based on the shortening of the equivalent strut. Stafford Smith (1966) proposed an expression relating the width of the equivalent strut to the properties of the frame and infill wall. The width of the equivalent strut varied with value of the following non-dimensional factor:

$$\lambda h = \left(\frac{E_c t h^3 \sin 2\theta}{4 E_s I} \right)^{1/4} \tag{1.3.1}$$

where

E_c = elastic modulus of the infill material, ksi

E_s = elastic modulus of the frame material, ksi

t = thickness of the infill wall, inches

h = height of a single story, inches

I = moment of inertia of the frame columns, inch^4

θ = slope of the infill diagonal relative to horizontal

Stafford Smith and Carter (1969) further related the width of the equivalent strut not only to factor λh, but also to the variation of the elastic modulus of the infill material at different stress levels. Makino (1984) proposed a simplified formula to calculate the width of the equivalent strut based on Stafford Smith and Carter's work. In his formula, the width of the equivalent strut was only related to the diagonal length of the infill wall or the thickness of the infill wall. Liauw and Kwan (1983a) expressed the equivalent strut width as a fraction of $h\cos\theta$:

$$b = \frac{0.86}{\sqrt{\lambda h}}(h\cos\theta) \leq 0.45(h\cos\theta) \tag{1.3.2}$$

where, the non-dimensional factor parameter λh is defined in Eq. (1.3.1). This relation was obtained by parametric study using the finite element method. Despite the controversy on the determination of a reasonable width of the equivalent strut, the equivalent strut concept was applied in the elastic design of multi-story infilled frames by different researchers (Stafford Smith and Carter, 1969; Makino, 1984; Saneinejad and Hobbs, 1995). It should be noted that all the previous equivalent strut methods were established for the analysis of non-integral infilled frames.

A number of researchers have proposed analytical methods based on plastic analysis theory, because the equivalent strut method neglects the contribution of the steel frame and cannot fully represent the behavior of composite infilled steel frames up to their ultimate strength levels. Wood (1978) applied plastic analysis to non-integral steel frames, in which the collapse modes and loads depended on the bending strength of the steel frames and the crushing stress of the infill wall. However, an unrealistic assumption was made in his models that the whole infill wall would behave in a perfectly plastic

manner. Therefore, an empirical penalty factor, γ_p, was needed to reduce the effective crushing stress of the infill wall and to account for the discrepancy between the theoretical predictions and experimental results. Four different failure modes were identified in Wood's work: a composite shear mode, a shear rotation mode, a diagonal compression mode, and a corner crushing mode. Nadjai and Kirby (1998) extended the shear mode to non-integral infilled steel frames having different types of partially-restrained connections. The experimental and analytical results showed that the shear mode overestimated the shear capacity of the infill wall. Therefore, another panel reduction factor, α, was used to further reduce the value of the penalty factor, γ_p. Based on the results of a nonlinear finite element analysis and experimental observations, Liauw and Kwan (1983a and 1983b) proposed plastic analysis models for both integral and non-integral infilled steel frames, in which the infill wall always failed through crushing in the corner regions. Furthermore, the formation of plastic hinges in the steel frames was determined based on the distribution of the compressive crushing stress in the corner regions of the infill walls. The contribution of interface friction was neglected in these models. Based on nonlinear finite element analysis and model tests, Saneinejad and Hobbs (1995) developed an inelastic method to calculate the ultimate lateral load and cracking load of non-integral infilled steel frames. This method is similar to that proposed by Liauw and Kwan (1983a, 1983b), except that the effect of the interface friction force was included and plastic hinges were assumed to form only in the loaded corners.

1.4 Research Objectives

Although the advantages of using interface connectors in the composite steel frame-RC infill wall system was recognized by Liauw (1979), Liauw and Kwan (1983a, 1983b, 1985), the interface connectors in their test were bent from wires and the shapes are very uncommon in today's practice. Makino et al. (1980) and Makino (1984) did use the widely accepted headed studs, but only placed a few studs along the interfaces with the primary purpose of preventing out-of-plane collapse of the RC infill. Furthermore,

little effort has been devoted to the improvement of the strength and ductility of the interface connectors used in this structural system. In addition, little work has been done on using partially-restrained connections to minimize the cost of structural system. All of the previous tests of integral RC-infilled steel frames were conducted on either very small-scale models with uncommon steel shapes or on single-story frames. Therefore, testing on a larger scale, including at least two-story specimens, is needed to obtain a better understanding of the cyclic behavior of this composite structural system. The objectives of the proposed research are:

1) To investigate the cyclic behavior of composite steel frame-RC infill wall structural systems by performing cyclic static loading tests on a one-third scale, two-story, one-bay specimen. Strength and stiffness deterioration, energy dissipation capability, deformation capacity of the structural components, and proportions of the forces resisted by different members are the major concerns in the investigation.
2) To determine the effect of the strength and ductility of the headed stud connectors on the seismic behavior of this composite system, and to explore a feasible construction method of using headed stud connectors in this composite system.
3) To establish simple but rational design guidelines and suggestions for analysis modeling for this composite system based on the experimental results, as well as research results from other sources.
4) To provide data for the validation and calibration of computational models of this structural system, such as nonlinear, cyclic finite element analysis, which are being developed in separate research effort at the University of Minnesota.

The scope of this research is limited to hot-rolled steel wide-flange sections bent about their strong axis, and use of headed shear studs to achieve composite action. Normal strength steel and concrete are used in this work for all components.

interface connectors used in this structural system. In addition, little work has been done on using partially-restrained connections to minimize the cost of structural system. All of the previous tests of integral RC-infilled steel frames were conducted on either very small-scale models with uncommon steel shapes or on single-story frames. Therefore, testing on a larger scale, including at least two-story specimens, is needed to obtain a better understanding of the cyclic behavior of this composite structural system. The objectives of the proposed research are:

1) To investigate the cyclic behavior of composite steel frame-RC infill wall structural systems by performing cyclic static loading tests on a one-third scale, two-story, one-bay specimen. Strength and stiffness deterioration, energy dissipation capability, deformation capacity of the structural components, and proportions of the forces resisted by different members are the major concerns in the investigation.
2) To determine the effect of the strength and ductility of the headed stud connectors on the seismic behavior of this composite system, and to explore a feasible construction method of using headed stud connectors in this composite system.
3) To establish simple but rational design guidelines and suggestions for analysis modeling for this composite system based on the experimental results, as well as research results from other sources.
4) To provide data for the validation and calibration of computational models of this structural system, such as nonlinear, cyclic finite element analysis, which are being developed in separate research effort at the University of Minnesota.

The scope of this research is limited to hot-rolled steel wide-flange sections bent about their strong axis, and use of headed shear studs to achieve composite action. Normal strength steel and concrete are used in this work for all components.

1.5 Organization of Report

Chapter 1 of this report proposes the objectives of this research based on the discussion of research background and review of the work done by previous researchers in related topics. Chapter 2 presents the analysis and design of prototype structures, so as to determine typical member sizes for this system as per the limited current design provisions. Chapter 3 discusses the experimental program, including the specimen design, the test setup, the instrumentation plan, and the loading history.

Chapter 4 to Chapter 7 present the experimental results and synthesis of the test data: Chapter 4 presents the general behavior of the specimen, such as the strength and stiffness of the specimen, the energy dissipation capacity of the specimen, and the observed phenomena of each component; Chapter 5 evaluates the performance of the steel frame and reinforced concrete infill wall in detail; Chapter 6 analyses the performance of the interface headed stud connectors based on measured axial and bending strains and slip and separation demands; Chapter 7 illustrates the force transfer mechanism of the specimen and estimates the percentage of the force resisted by each component.

Chapter 8 compares results from the finite element analysis with test data, so as to establish an appropriate finite element analysis method for design. Chapter 9 verifies the plastic mechanism analysis methods proposed by other researchers and establishes the plastic mechanism for the two-story specimen in the present research. Chapter 10 proposes the recommendations for future experimental study based on the performance of this specimen. Chapter 11 outlines the conclusions drawn from both experimental results and analytical results.

Appendix A illustrates the design of the PR connections in the specimen. Appendix B documents the readings of the strain gages and LVDTs during the entire loading history. Appendix C documents the procedure for calculating the internal forces in the steel columns based on the test data of the column strain gages.

Chapter 2

Analysis and Design of Prototype Structure

To initiate this research, a series of prototype structures were analyzed and designed according to currently available U.S. seismic design provisions so as to identify appropriate member sizes. This chapter summarizes this study. Further details may be found in Tong et al. (1999).

2.1 Description of the Prototype Structure

The floor plan of the prototype structure, modified from Shahrooz et al. (1996), is shown in Figure 2.1.1. Four steel frames with RC infill walls are arranged in the North-South direction (each having a large doorway opening), while three are oriented in the East-West direction. These infilled steel frames form cores that can be used as elevator shafts and stairwells. The steel frames with RC infill walls serve as the primary lateral load resisting system, and most or all of the other steel framing carries gravity loads only. Prototype structures having 3, 6, and 15 stories were investigated. Each story was 13 feet high. The building was assumed to be located in NEHRP seismic area 7 or UBC seismic zone 4. Frame W1 (Figure 2.1.1) was taken as a representative frame of this composite system for two-dimensional analysis and design studies. For expediency, frame W1 was assumed to carry one-third of the lateral seismic loads in the N-S direction.

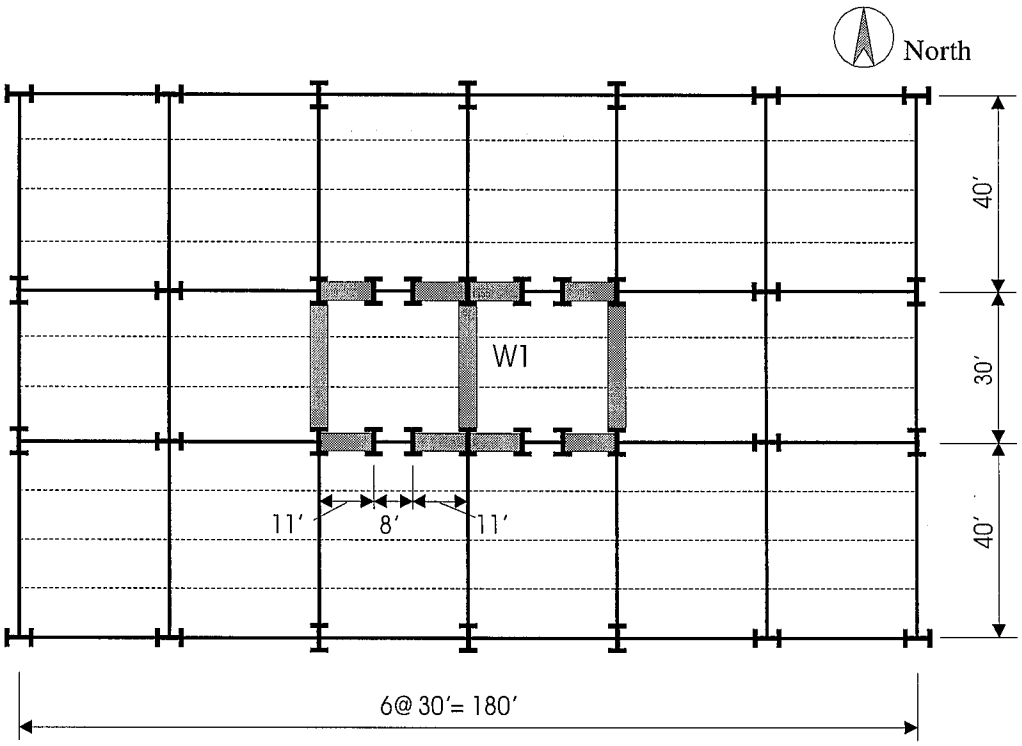

Fig.2.2.1 Floor Plan of the Prototype Structure
[after Shahrooz et al. (1996)]

2.2 Design Guidelines for the Prototype Structure

The behavior of the composite steel frame-infill wall structural system depends on many factors, such as the relative stiffness between the steel frames and the infill walls, the beam-column connection types, the strength and deformation capacity of the headed stud connectors along the interface, the reinforcement ratio in the infill wall, etc. A desirable progressive failure mode for this structural system, when it is subjected to increasing lateral load, is as follows: under service load, this composite structural system reacts elastically and no failure of studs occurs; with increase in lateral load, a significant amount of cracking develops uniformly across the RC infill wall and steel reinforcing bars in the infill wall yield gradually, and at the same time, the interface headed studs start to yield; with continued increase in lateral load, moderate yielding in the steel members occurs and a small number of corner studs start to fracture; the structure reaches its maximum strength after the concrete in the corner regions of each story crushes and a

sufficient number of plastic hinges form in the beam-to-column connections and at the column bases. The structure then maintains a large percentage of its maximum lateral strength to a 2-3% interstory drift through gradual crushing of the concrete and gradual failure of the headed studs along the interface. This progressive failure mode insures that the energy dissipation capacity of the structural system is utilized to a maximum. Energy can be dissipated through cracking of the concrete and yielding of the reinforcing bars in the infill walls, yielding of the headed stud connectors along the interface, crushing of the concrete in the corner regions, and yielding of the steel members and beam-to-column connections. Consequently, this composite system can be stiffer and stronger than comparable bare frames, potentially more ductile than the reinforced concrete infill walls, and can potentially dissipate a comparable amounts of energy as both.

To achieve the idealized behavior described above, the concept of a prescribed design lateral force is adopted from the NEHRP (1997). The onset of significant yielding of the structural system as a whole, which is primarily induced by cracking and yielding of reinforcing bars in the infill wall, as well as yielding of the studs, is expected at the design force level. The strength of the structural system over its design force level is mainly provided by crushing of concrete and yielding in the beam-to-column connections. The ability of the structural system to maintain its strength under larger deformations is insured by proper design and construction detailing.

The "Equivalent Lateral Force Procedure" in Section 5.3 of NEHRP (1997) was used to determine the design lateral forces of the prototype and their distribution over the height of the frame. Prototype structures having 3, 6, and 15 stories were investigated using linear elastic finite element analysis (Tong et al., 1999) and these analytical results will be summarized in the next section. Based in part on these results, the following tentative guidelines are proposed for designing the composite steel frame-RC infill wall structural system:

1) The bare steel frame shall have the capacity to resist the design gravity load.
2) The reinforced concrete infill wall shall have the ability to resist 100 percent of the design lateral force. The percentage of the design lateral force carried by

each of the boundary steel columns should be decided by an appropriate method.

3) The overturning moment due to the design lateral load shall be carried by the steel frame and the concrete infill walls together in proportion to their flexural stiffness.
4) Besides resisting axial and shear forces, the steel column also needs to resist a certain amount of bending moment.
5) The headed studs along the beam-infill wall interface should have the ability to resist 100 percent of the design lateral force, and the headed studs along the column-infill wall interface should have the same linear strength (i.e., shear strength per unit length of the interface) as those along the beam-infill wall interface.
6) Partially-restrained (PR) connections are recommended for the beam-to-column connections.

Guideline (1) is based on long-term deformation due to the fact that concrete creep and shrinkage will relax the gravity stresses from the infill walls. Therefore, the steel frames should be designed conservatively to carry all gravity loads.

2.3 Elastic Finite Element Analysis of the Prototype Structure

2.3.1 Model Description

Two load combinations, $1.2D+1.6L+0.5L_r$ and $1.2D+0.5L+0.5L_r+1.0E$, were adopted in the analysis and design of the prototype structure, where D represents the dead load due to self-weight of the structure and permanent elements of the structure, L represents the live load due to occupancy and moveable equipment, L_r represents roof live load, and E represents earthquake load (ASCE 7-95). The response modification coefficient $R = 6$ and the deflection amplification factor $C_d = 5.5$. The gravity load combination $1.2D+1.6L+0.5L_r$ was used to size the bare steel frame since it was required to have the capacity to carry design gravity load. The lateral load combination

1.2D+0.5L+0.5L_r+1.0E was used to check the strength and stiffness of the composite system.

The finite element software SAP2000 (CSI, 1996) was employed in the analysis. The composite steel frame-RC infill wall W1 (Figure 2.2.1) was discretized using two types of elements: beam elements and membrane elements. Beam elements were used to construct the steel frame model, while the infill wall was modeled using membrane elements. For these preliminary design studies, linear elastic analysis was used and second-order effects were determined to be negligible. The modulus of elasticity of the wall element material, concrete, was 3600 ksi, and the modulus of elasticity of the frame material, steel, was 29000 ksi. Two methods were used to simulate the interface conditions. In the first method, membrane and beam elements shared nodes along their interfaces such that no relative displacement (i.e. separation and slip) occurs along the interface. This assumption implies that the headed studs have infinite shear and axial stiffness, and was used in the analysis of all 3, 6, and 15 story infilled steel frame W1. The corresponding analytical results are discussed in Section 2.3.2. In the second method, the headed stud connectors were modeled explicitly by using beam elements and it is discussed in Section 2.3.3.

2.3.2 Analytical Results for the Fully-Composite Model

This section summarizes the design and analysis results of the 3, 6, and 15 story fully-composite infilled steel frames W1 (Tong et al.,1999). Three parameters were included in the finite element analysis of the 3, 6, and 15 story structures: fully-restrained (FR) connections versus pin connections; beam sizes; and systems with and without steel outrigger frames. Following the design guidelines outlined in the last section, the steel and concrete components of each model were chosen to meet both the strength and drift requirements. As an example, Figure 2.3.1 shows the dimensions and component sizes of the 6 story infilled steel frame with FR connections. The load shown in the figure is corresponding to the lateral load combination 1.2D+0.5L+0.5L_r+1.0E.

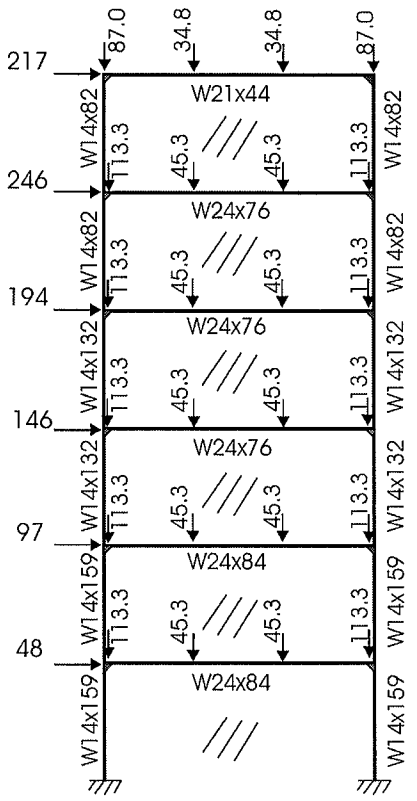

* 10 inch thick walls, load in kips

Figure. 2.3.1 The Six Story Prototype Structure

The following conclusions were drawn from the finite element analysis of the 3, 6 and 15 story fully composite RC infilled steel frames without the outriggers.

1) The RC infill walls carried majority of the lateral force.

As an example, Figure 2.3.2 shows the lateral force distribution of the six-story fully composite RC infilled steel frame. It shows the shear force resisted by the infill walls is approximately 100% in the middle portion of each story, but exhibits a sharp change near the interface between the concrete panels and the girders. It exceeds the total lateral force by approximately 10 percent near the locations of the girders. However, at the actual location of the interface with the girders, the shear force carried by the infill walls decreases about 10-15 percent as the shear force shifts into the connections. The lateral force carried by the RC infill wall was always greater than 90% of the total lateral load.

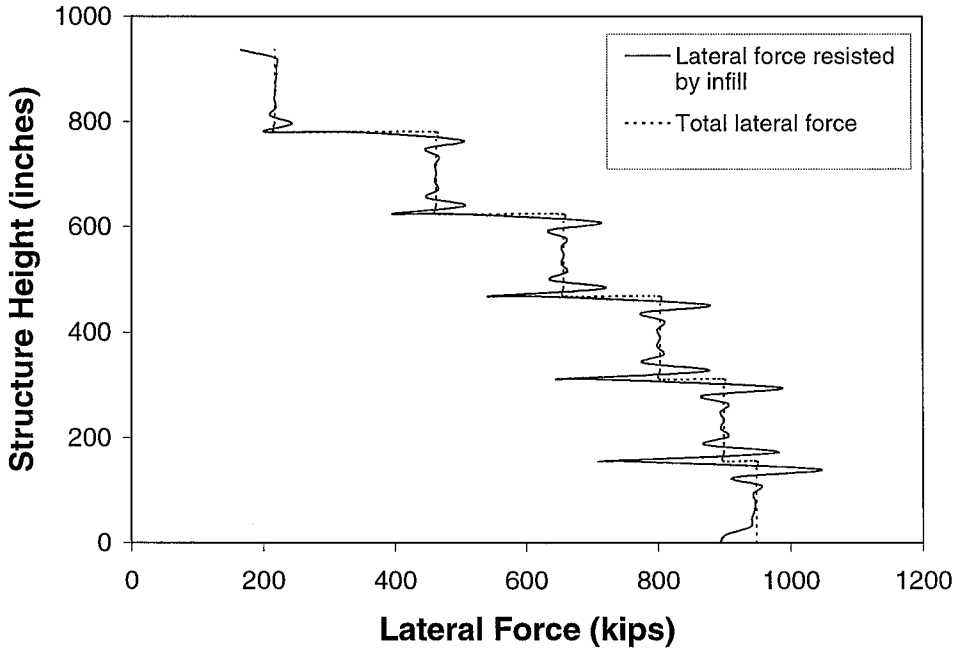

Fig. 2.3.2 Lateral Force Distribution along the Height of the Six Story Prototype Structure

1) The overturning moment was shared by the steel columns and the infill walls. The finite element analysis shows that at the ground level, the proportion of the overturning moment resisted by steel columns was nearly 30% for the 3 story frame, 40% for the 4 story frame, and 60% for the 15 story frame. As an example, Figure 2.3.3 shows the overturning moment distribution of the six-story fully composite RC infilled steel frame.

2) The differences between the response, such as drift and internal forces of the composite structure with fully-restrained beam-to-column connections and that of the composite structure with pin beam-to-column connections, are negligible. This observation indicates the potential to use partially-restrained (PR) connections in the composite steel frame-RC infill wall structural system. Of course, a certain stiffness of connection is needed to maintain the strength and integrity of the structural system after substantial damage accumulates in the infill wall during a severe earthquake.

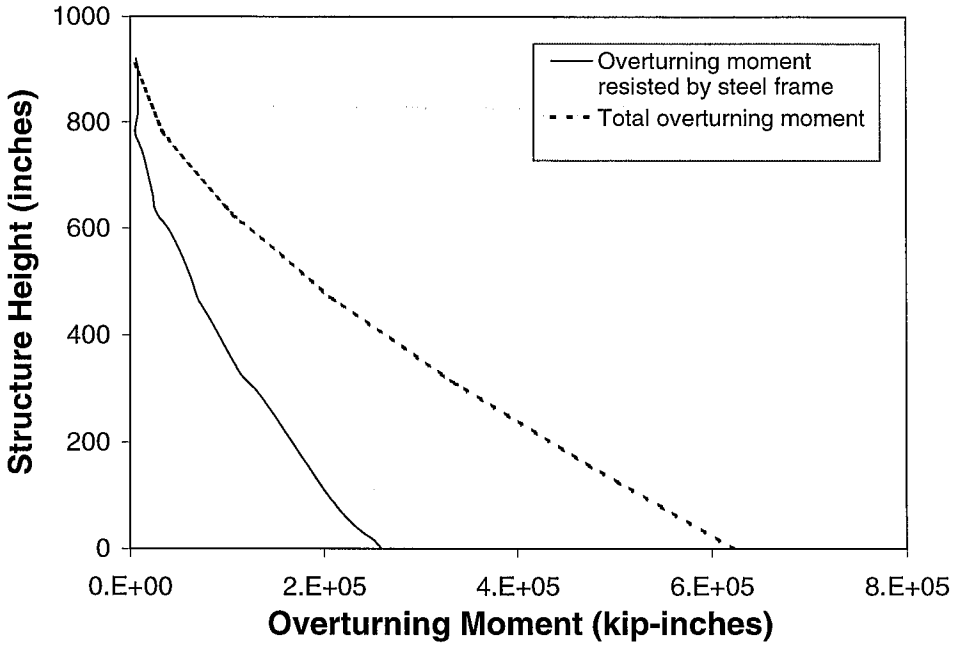

Fig. 2.3.3 Overturning Moment Distribution along the Height of the Six Story Prototype Structure

3) The size of the beam has little effect on the behavior of this composite structural system.

This behavior is understandable since the beam is stiffened by the RC infill walls on both sides so that the main function of the beam is to transfer the lateral load between two adjacent stories.

For the mid-rise composite system such as the 15 story frame, large columns and 21 inch thick RC walls had to be used to meet the story drift limits (Tong et al., 1999). Such large tensile and compressive forces at the base of the columns (3896 kips and -6152 kips, respectively) may be difficult for a foundation to carry, and any special treatment of the foundations will increase construction costs. Consequently, a steel frame or an outrigger could be added to the 15 story composite system to help share the overturning moments and reduce the story drifts. As an alternative, the floor plan could

be altered to decrease the requirement on any single bay of the composite system. Details are not discussed here since it is not the principal focus of this research.

2.3.3 Effect of Headed Stud Connector Stiffness

To investigate the effect of the stiffness of interface headed stud connectors on the behavior of the structural system, for the 6 story RC infilled steel frames with pin connections, the stud was modeled explicitly by using a beam element to connect the steel member and the RC infill wall. The analysis remained linear elastic and second-order effects were neglected. The stud beam element was defined so that it had the same axial stiffness and shear stiffness of a common headed stud with 3/4 inch diameter.

2.3.3.1 Determination of Shear Strength of Headed Studs

The headed studs connecting the infill wall and the steel frame in this prototype analysis were five inches in length and 3/4 inches in diameter. This type of stud is used extensively in composite construction. The number of headed stud connectors was determined simply based on their shear strength in the prototype structure design. At the time of designing the prototype structure, the design shear strength was calculated according to the AISC (1993) equation as follows:

$$Q_u = Q_{sn} = 0.5 A_{sc} \sqrt{f_c' E_c} \tag{2.3.1}$$

where,

Q_{sn} = nominal shear strength of the stud, kips

A_{sc} = cross section area of the stud shaft, inch^2

f_c' = compressive strength of the concrete of the infill wall, ksi

E_c = modulus of elasticity of the concrete of the infill wall, ksi

According to Eq. (2.3.1), the shear capacity of a headed stud with 3/4 inches in diameter used in the prototype structure was 26 kips. As a result, 41 studs were used along each beam-infill interface to transfer the lateral loads effectively, and 21 studs were used along

each column-infill interface so that the stud spacing along each column was the same as that along each beam.

Saari (1998) provided a more accurate assessment of the cyclic strength of the shear studs in infill walls, which is included in the specimen design in the next chapter.

2.3.3.2 Determination of the Stiffness of Headed Studs

The shear load-slip relation of headed studs proposed by Ollgaard et al. (1971) was used to determine the shear stiffness of the headed stud with 3/4 inches in diameter. The empirical formula describing the relationship is:

$$Q = Q_{sn}(1 - e^{-18\Delta})^{2/5} \tag{2.3.2}$$

where,

Q_{sn} = nominal shear strength of the stud, kips

Δ = slip of the stud along the steel-concrete interface, inches

Q = shear load, kips

Figure 2.3.4 shows the relationship of the normalized shear force (Q/Q_{sn}) versus the slip of a headed stud connector. The secant shear stiffness $K_{ss} = Q/\Delta$ can be obtained with respect to different load or slip levels. It is infinite at zero load, but decreases quickly as the slip increases. It was decided that the secant shear stiffness to be used in the finite element analysis should be K_{ss} = 422 kips/inch, which was defined at slip Δ = 0.05 inches.

It was assumed that, under shear force, the stud element deforms as if both ends of the stud element are fixed. As a result, the shear stiffness of the stud element was

$$K = \frac{12E_eI_e}{L_e^3} \tag{2.3.4}$$

This stiffness should equal the secant shear stiffness K_{ss} determined above. The input value of the moment of inertia of the stud element, I_e, was then determined based on this requirement, since the length of each stud element, L_e, was specified as 5 inches and the modulus of elasticity of stud element, E_e, was specified as 29,000 ksi.

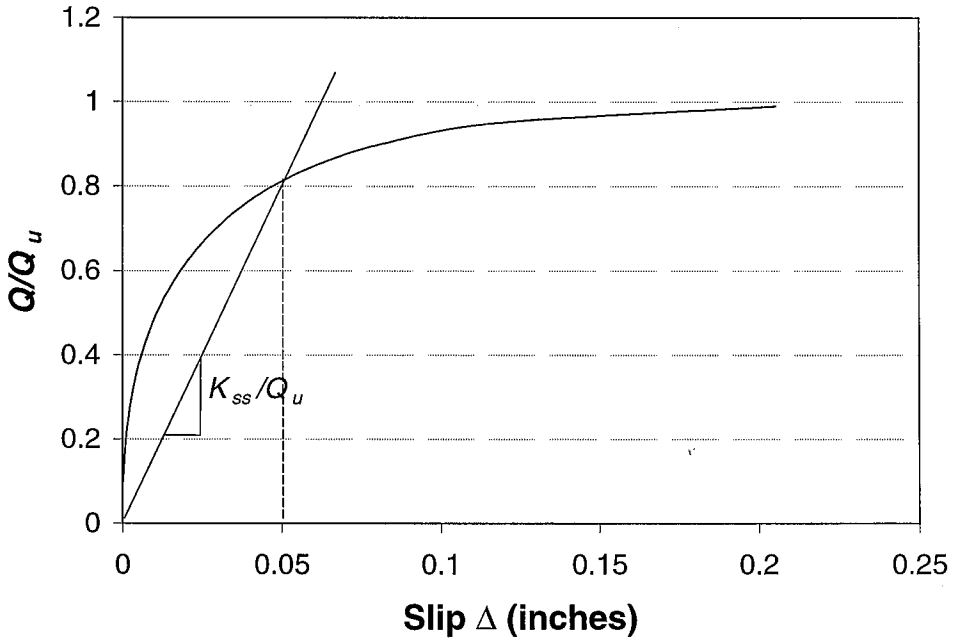

Fig. 2.3.4 Shear Load-Slip Relationship of the ϕ3/4 Inch Stud

Cook et al. (1992) observed in his experiments that the failure mode of a headed stud (with sufficient confinement) under tensile force was a shank fracture with little slip, and the load was transferred to the concrete through direct bearing on the stud head. Consequently, if any crushing of the concrete is neglected, the axial stiffness of one stud can be simply taken as: $K_{ts} = EA/L$, where L is the length of the stud shaft; A is the area of the cross section of the stud shaft; and E is the elastic modulus of the steel. Given the dimension of the headed stud described in the last paragraph, the tensile stiffness was thus taken as K_{ts} = (29,000*0.442)/(5-0.375) = 2772 kips/inch, based on the assumptions that sufficient confinement was provided and any axial slip due to crushing of concrete was neglected.

2.3.3.3 Analytical Results

The analysis indicated that the maximum story drift increases substantially after considering the shear stiffness of the interface headed stud connector. Figure 2.3.5 shows

the lateral displacement of the two 6 story RC infilled steel frames, one without stud elements (fully composite) and the other with stud elements. The maximum story drift increased by approximately 40% over that for the fully-composite model. However, the maximum story drift of the model with stud elements was $0.25C_d = (0.25)5 = 1.25$ inches, still well below the drift limitation required by NEHRP (1997), which was 3.12 inches.

Table 2.3.1 shows the internal forces at the base of the first story column. It indicates the tensile force in the windward column increased approximately 22% when the stud stiffness was considered, but there was almost no change in the compressive force in the leeward column. The shear force in the windward column increased approximately 6.45 times in the windward column and approximately 8 times in the leeward column when the stud stiffness was considered. The windward column carried approximately 15% of the total lateral force and the leeward column carried approximately 30% of the total lateral force in the model with stud element. However, the column still satisfied the strength requirements per AISC (1997).

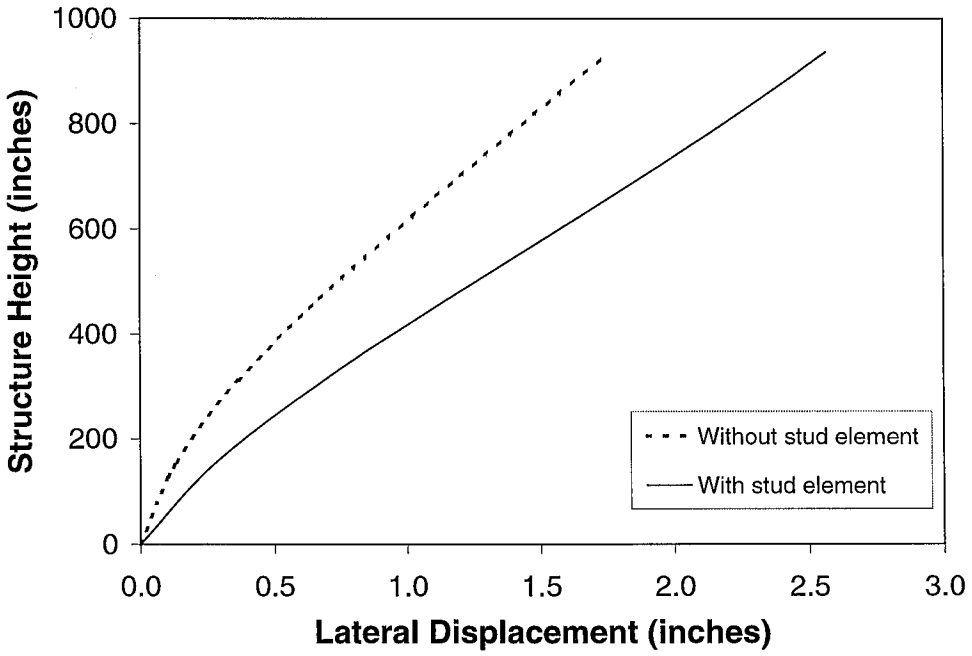

Fig. 2.3.5 Comparison of the Lateral Displacements of Two Finite Element Models

Table 2.3.1 Maximum Internal Forces in the Steel Columns of Six Story Frames

Frame*[1]	A		B	
Column*[2]	C1	C2	C1	C2
Axial Force (kips)	506.61	-923.46	590.94	-926.43
Shear Force (kips)	19.34	31.31	144.13	283.46
Bending Moment (kip-inches)	690.31	966.10	2448.05	3268.72

1: A–the RC infill steel frame without stud element
B– the RC infill steel frame with stud element
2: C1–the windward column; C2–the leeward column

The internal forces of the stud along first story interfaces are listed in Table 2.3.2. The element numbers for studs along the top and bottom interfaces increase from windward column C1 to leeward column C2. The element numbers for studs along the column-infill wall interfaces increase from the bottom to the top. The table shows that shear force for each stud was below its design shear strength. Along the bottom interface, the maximum shear force for the studs was less than 60% of its design shear strength; along the top interface, the maximum shear force for the studs was less than 80% of its design shear strength. The shear force for the studs along the interface between the column and infill were even smaller. However, along the bottom and top interfaces of the first story, the studs close to the windward column had to endure high tensile force due to the effect of overturning moment. Along the bottom portion of the left interface (the windward column-infill wall interface) and along the top portion of the right interface (the leeward column-infill wall interface), the studs also needed to endure high tensile force due to deformation incompatibility between the steel column and the infill wall. The maximum tensile strength of a headed stud connector is the tensile strength of the stud shaft. It is 23.9 kips for the headed stud used in design if the yield strength is defined as 54 ksi, as recommended by PCI (1992). It can be seen from the table that internal forces of a number of studs exceeded this limit. If the interaction of tension and shear is

Table 2.3.2 Forces in the Studs along the First Story Interfaces (kips)*[1]

Num	Bottom Interface		Top Interface		Num	Right Interface		Left Interface	
	Axial	Shear	Axial	Shear		Axial	Shear	Axial	Shear
1	67.37	9.15	-1.22	3.52	1	43.98	9.85	-142.07	1.23
2	66.31	9.93	20.59	7.58	2	33.18	10.10	-78.22	3.01
3	60.26	10.25	27.23	9.96	3	23.67	9.77	-31.98	3.36
4	54.49	10.65	29.37	11.47	4	16.74	9.41	-16.94	3.54
5	48.85	10.98	29.32	12.72	5	11.62	8.82	-9.32	3.41
6	43.42	11.30	28.04	13.66	6	7.91	8.32	-5.14	3.35
7	38.26	11.61	26.06	14.50	7	5.35	7.72	-3.19	3.19
8	33.35	11.89	23.62	15.19	8	3.60	7.20	-2.04	3.08
9	28.69	12.18	20.88	15.83	9	2.48	6.65	-1.67	2.94
10	24.29	12.44	17.87	16.36	10	1.80	6.18	-1.54	2.82
11	20.15	12.71	14.57	16.86	11	1.40	5.68	-1.65	2.72
12	16.26	12.95	10.87	17.30	12	1.19	5.28	-1.55	2.64
13	12.62	13.19	6.56	17.71	13	1.03	4.85	-0.51	2.59
14	9.24	13.42	1.18	18.10	14	0.87	4.54	0.50	2.54
15	6.16	13.64	0.81	18.46	15	0.58	4.19	1.76	2.53
16	3.41	13.86	0.51	18.70	16	0.21	4.03	4.05	2.52
17	1.12	14.10	-1.20	18.84	17	-2.66	3.77	7.73	2.57
18	-4.85	14.34	-7.39	18.92	18	-9.05	3.82	13.41	2.59
19	-14.79	14.51	-15.09	19.01	19	-23.79	3.66	21.55	2.69
20	-22.57	14.60	-22.24	19.08	20	-64.57	4.01	33.37	2.66
21	-29.54	14.67	-28.98	19.12	21	-99.75	3.80	44.02	3.07
22	-36.16	14.70	-35.57	19.13					
23	-42.66	14.70	-42.10	19.09					
24	-49.14	14.69	-48.69	19.03					
25	-55.69	14.65	-55.41	18.91					
26	-62.36	14.59	-62.72	18.77					
27	-69.23	14.51	-72.69	18.56					
28	-76.31	14.41	-87.36	18.46					
29	-83.69	14.28	-84.15	18.28					
30	-91.39	14.14	-89.10	17.91					
31	-99.52	13.96	-95.39	17.51					
32	-108.07	13.76	-102.02	17.06					
33	-117.23	13.51	-108.66	16.54					
34	-126.94	13.25	-115.31	15.99					
35	-137.58	12.89	-121.78	15.33					
36	-148.98	12.53	-128.18	14.67					
37	-162.19	11.94	-134.27	13.83					
38	-177.19	11.39	-140.33	13.02					
39	-196.67	10.24	-145.67	11.87					
40	-230.80	9.22	-150.38	10.76					
41	-214.83	5.01	-68.40	8.37					

1: The shear strength of the ϕ3/4 inch headed stud is 26 kips, and the tensile strength of the ϕ3/4 inch headed stud is 24 kips.

considered, even more studs were unable to resist the required forces from the elastic finite element analysis. This result implies that the studs close to the corner regions will yield at the design load level. Therefore, the windward column needs to resist more tensile force due to the decrease of the tensile stiffness of the headed studs, and the remaining studs need to resist more shear force. The headed studs in the prototype structure were simply designed to resist shear force. This is not necessarily a sound approach since the corner studs have to endure high tensile force at the same time. In the next chapter, an attempt is made to account for the interaction of tension and shear on the headed stud connectors in the design of the specimen. However, the stress demand and deformation demand of the headed stud connectors is not truly known either in the prototype structure design nor in the specimen design, and this remains one of the primary objectives in this research.

Chapter 3

Experimental Program

This chapter discusses several key issues of the specimen design: choice of dimensions, detailing of the PR connections, design of the interface headed studs, and design of wall reinforcement. The test setup is illustrated and material properties of the specimen are reported. The instrumentation plan is then specified to capture both the global and local behavior of the specimen.

3.1 Specimen design

3.1.1 Specimen dimensions

The two-story, one bay specimen, designed according to the similitude requirements (Sabnis et al., 1983) that relate the model to the prototype, was meant to represent the bottom two levels of the six story prototype infilled steel frame at approximate one-third scale. Figure 2.3.1 shows the dimension and member size for the six-story prototype structure. To scale down the prototype structure to the specimen, two independent scale factors, S_σ and S_l,, were chosen for stress σ and length l, respectively; all remaining scale factors were either equal to unity or were functions of S_σ and S_l. For example, the scale factor of moment of inertia was S_l^4 and that of the section area was S_l^2. The resulting specimen size after scaling is shown in Figure 3.1.1. The steel columns

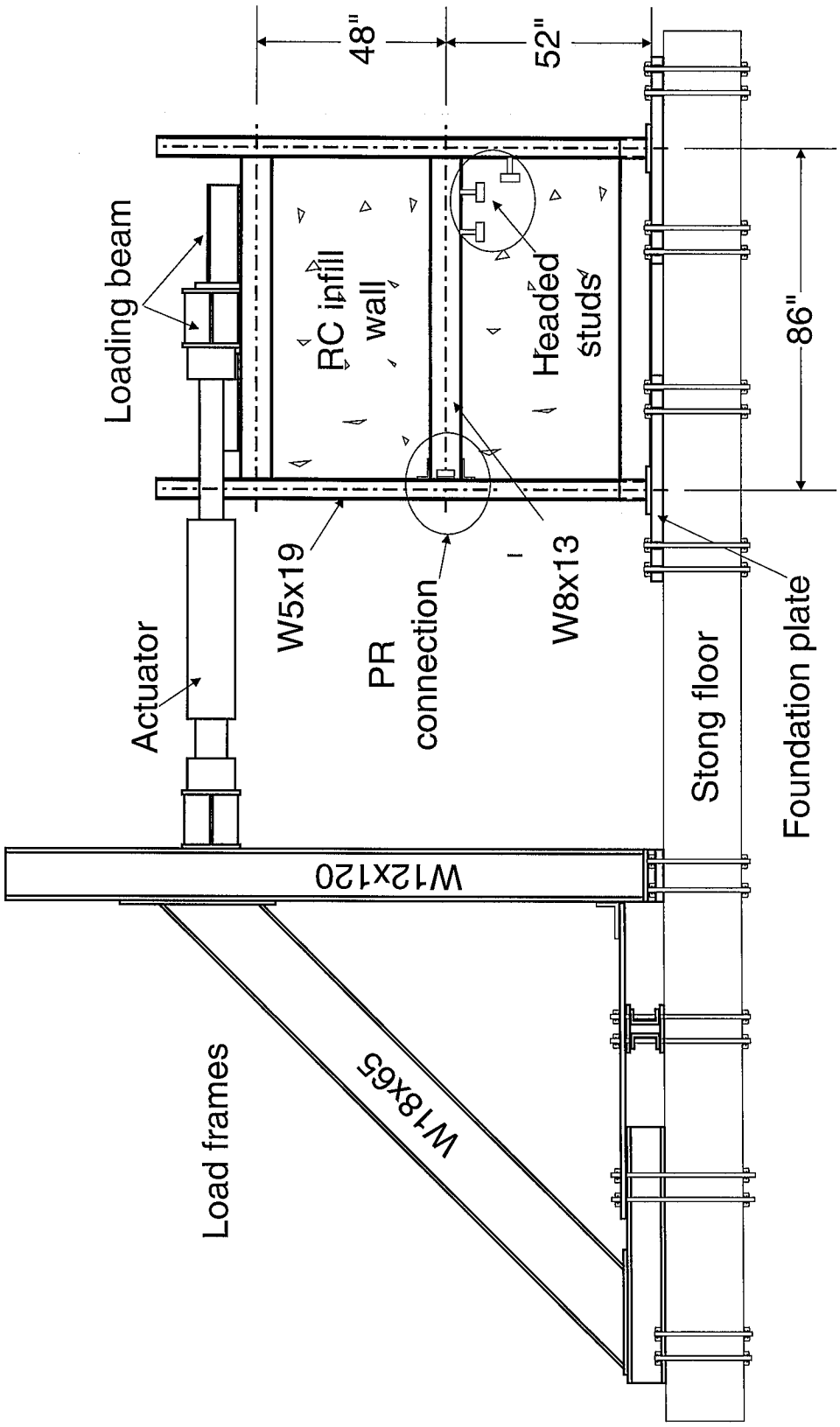

Fig. 3.1.1 Specimen Dimensions and Test Setup

comprised W5x19 wide-flange shapes, while the steel beams comprised W8x13 wide-flange shapes. The column material was A572 Grade 50 steel and the beam material was A36 steel, the same as those of the prototype structure. The RC infill wall was 3.5 inch thick, with the 28 day compressive strength of the concrete targeted at 3.5 ksi. Number 2 deformed reinforcing steel bars were used as the infill wall reinforcement. These bars were purchased from CTL Inc. (skokie, IL) and originated from a mill in Sweden. They have similar material properties to domestic reinforcing bars in regular sizes. Partially-restrained connections were used to connect the middle beam and the top beam to the columns. Table 3.1.1 compares the geometry and material-related properties of the prototype structure and the specimen. For a practical true model involving reinforced concrete (Sabnis et al., 1983), S_σ shall be 1 and S_l shall be 3 in one-third scaling in order

Table 3.1.1 Geometry and Material Properties
of the Prototype Structure and the Specimen

Item ID	Item	Prototype structure	Specimen	Scale factor	Ideal Scale factor
Geometry	Story height (inches)	156	48	3.25	3
	Frame spacing (inches)	360	86	4.18	3
	Wall thickness (inches)	10	3.5	2.86	3
	Section area of the column (inch^2)	46.7	5.54	8.42	9
	Web area of the column (inch^2)	9.39	1.16	8.09	9
	Moment of inertia of the column (inch^4)	1900	26.2	72.5	81
	Plastic modulus of the column (inch^3)	287	11.6	24.7	27
	Section area of the beam (inch^2)	24.7	3.84	6.43	9
	Web area of the beam (inch^2)	11.4	1.84	6.20	9
	Moment of inertia of the beam (inch^4)	2370	39.6	59.8	81
	Plastic modulus of the beam (inch^3)	224	11.4	19.6	27
Material	Nominal yield strength of frame steel (ksi)	50/36	50/36	1	1
	Elastic modulus frame steel (ksi)	29000	29000	1	1
	Nominal compressive strength of wall concrete (ksi)	4	3.5	1.14	1
	Yield strength of reinforcing bar (ksi)	60	60	1	1
	Elastic modulus of concrete (ksi)	3640	3400	1.07	1

to meet the similitude requirement. As a result, the ideal scale factors for geometry and material properties were determined in accordance to their dimensions and are listed in Table 3.1.1. Due to the limited sizes of commercially available wide-flange shapes, the W5×19 column is the section that is both compact and has the closest scale factors to the ideal scale factors for its geometrical properties. The scale factors for the geometrical properties of the W8×13 beam are approximately 70%-75% of the ideal scale factors. However, the numerical analysis of the prototype structure indicated the beam size had little effect on the structural behavior of this composite system during the elastic range. Furthermore, according to Liauw and Kwan (1983a, 1983b), it was the moment capacity of the connection that played an important role in determining the failure modes and maximum lateral strength of this type of composite system. Therefore, it was believed that a little oversize of the beam would not affect the structural behavior of the specimen as long as the partially restrained connection was properly detailed. The item that has the maximum discrepancy between the scale factor and the ideal factor is the frame spacing, which was scaled down 4.18 times from the prototype structure to the specimen. The major reason for adopting this value was to insure that the maximum capacity of the loading system, which was provided by two 110 kips actuators, was sufficient.

According to the equivalent lateral force procedure in NEHRP (1997), the design base shear force for the six-story prototype structure was 948 kips. This lateral force was then distributed vertically along the structure to compute the structural response and select the appropriate members. It is of great interest to know the specimen responses under the corresponding scaled design lateral force. Because the majority of the design lateral force is to be carried by the RC infill wall, the approximate scale factor of the design lateral force could be estimated in accordance with the cross-section dimensions of the infill wall and concrete properties. Dimensional analysis of reinforced concrete shows that the scale factor of a concentrated load is $S_\sigma(S_l)^2$. Comparison of the prototype structure and the specimen resulted in:

$$S_\sigma = \frac{f_c'(prototype)}{f_c'(specimen)} = \frac{4}{3.5} = 1.14$$

$$S_l^2 \approx \frac{t \times L_w(prototype)}{t \times L_w(specimen)} = \frac{10 \times 330}{3.5 \times 81} = 11.64$$

Therefore, the approximate scale factor for the design lateral force was 13.3, which yielded a design base shear force of the specimen as approximately 71 kips. This design lateral force was used in detailing the headed stud connectors along the interfaces and the reinforcement in the infill wall, as shown in the following sections.

3.1.2 Beam-to-Column Connection Design

In almost all of the previous static or cyclic tests on infilled steel frames, the beams were welded to the columns across the full cross section so as to act as a fully-restrained (FR) connection (Mallick and Severn, 1968; Liauw and Kwan, 1983a, 1983b; Makino, 1984; Kwan and Xia, 1995). Recently, Nadjai and Kirby (1998) analyzed the behavior of non-composite infilled steel frames with semi-rigid connections using the finite element method. In the specimen tested in this work, PR connections comprising a top-and-seat-angle and a double-web angle were used for the following reasons. First, in the steel frame with composite reinforced concrete infill wall system, the girders are mainly used to transfer the lateral shear forces and carry gravity loads. The moment-rotation response of the girders has little effect on the system behavior in the elastic stages of lateral loading (Nadjai and Kirby, 1998). Finite element analysis of the composite reinforced concrete infilled frames indicated that there was no major difference between the elastic behavior of the system with FR connections and that using PR or pin connections (Tong et al., 1998). Therefore, expensive FR connections are not warranted at low load levels. Second, with an increase of lateral load and crushing of the concrete panel corners, the girders will be required to resist a certain amount of moment, which is induced by the spread of the corner interface normal forces caused by the concrete crushing. Also, with the degradation of the concrete panel stiffness, the steel frame must contribute its lateral stiffness to ensure the integrity of the system later in an earthquake. Thus, some amount of connection rotational stiffness, strength, and ductility

are required. Third, the failure mechanism and a corresponding design procedure of the PR connection comprising a top-and-seat-angle and a double-web angle have been provided by Kim and Chen (1998). Although their design formulas are based on the study of static behavior of bare steel frames, this type of PR connection has proven to have stable hysteretic behavior when subjected to cyclic load (Leon and Shin, 1995).

Figure 3.1.2 provides the detailing of the PR connection in this specimen. The deflection pattern of this PR connection subjected to bending is shown in Figure 3.1.3 (Kim and Chen, 1998). It can be seen that the collapse mechanism of the top angle may be modeled by the development of two plastic hinges, one at the edge of the bolt head and the other along the k-line of the vertical leg. The deformation pattern also shows that the web angles can contribute to the moment resisting capacity. Design of this PR connection is documented in Appendix A, which is adapted in part from the procedures proposed by Kim and Chen (1998). All the shear force was assumed to be carried by a L2×2×5/16×5 double-web angle. Because the PR connection may endure a high concentrated shear force caused by the compressive strut action of the concrete infill wall, the double-web angle and the corresponding high strength bolts were sized to have at least the same shear resistant capacity ϕV_n as that of the W8×13 beam, thus reducing the possibility of a shear failure of the PR connection. This decision was made based on the fact that a moment-resistant failure mode of the connection usually has a better energy dissipation capacity than the shear failure mode. In the specimen, the double-web angle was connected to the column flange by using A325 bolts with 1/2 inches in diameter, but had to be welded to the beam web because there was not enough clearance for bolting. Typically, the angles would be bolted to the beam web in a full-scale structure. However, this detailing will not change the failure mechanism of the web angles appreciably because the plastic hinges were expected to form in the angle legs that were bolted to the column flanges (Figure 3.1.3).

A L5×3×5/16×5 angle was chosen for the top and seat angles. The angle was selected so that the stiffness of the top or seat angle was less than that of the column flange, which is 0.43 inch thick. Each top and seat angle was connected to the beam

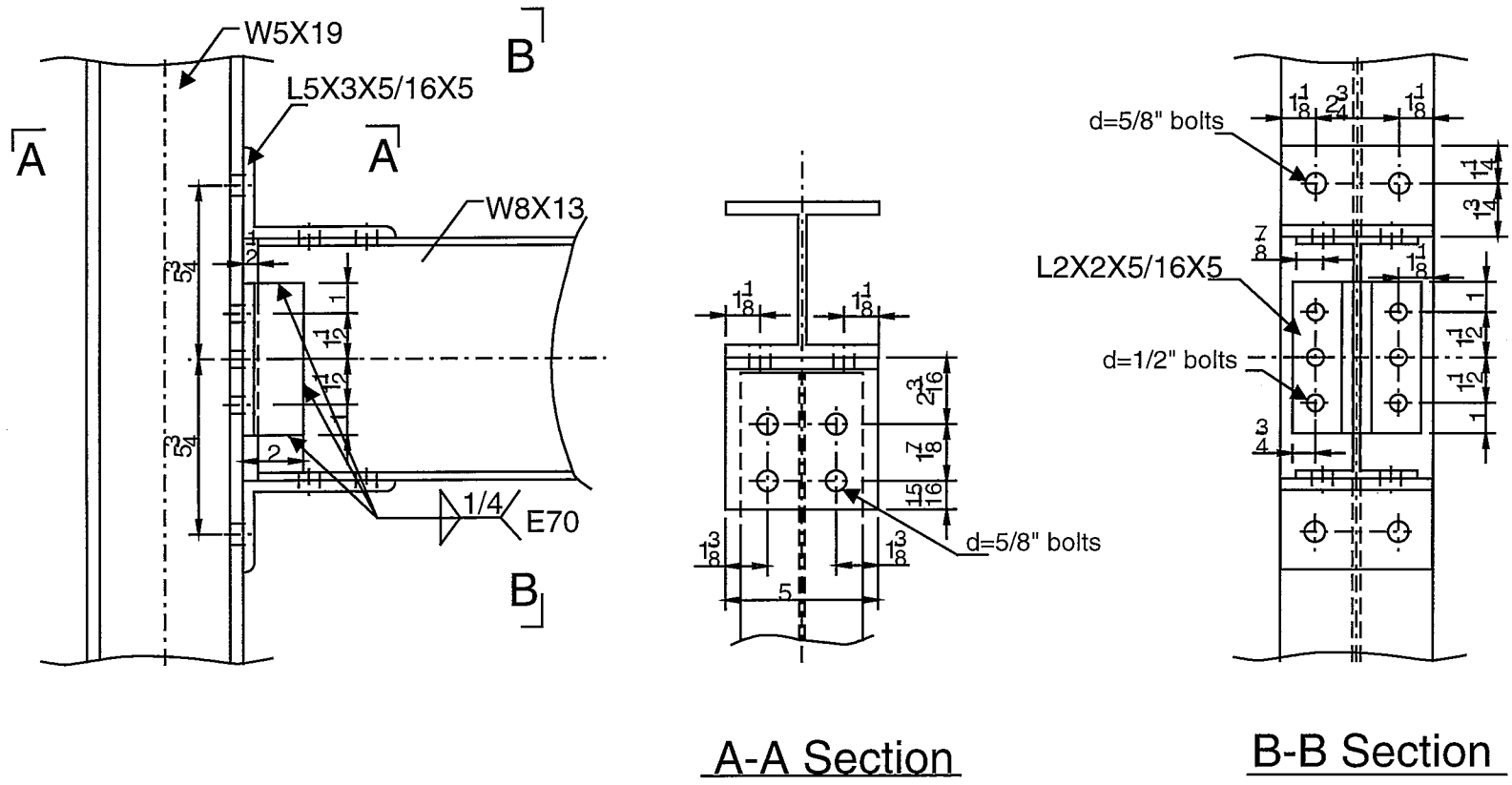

Fig. 3.1.2 Partially-Restrained Connection Detailing

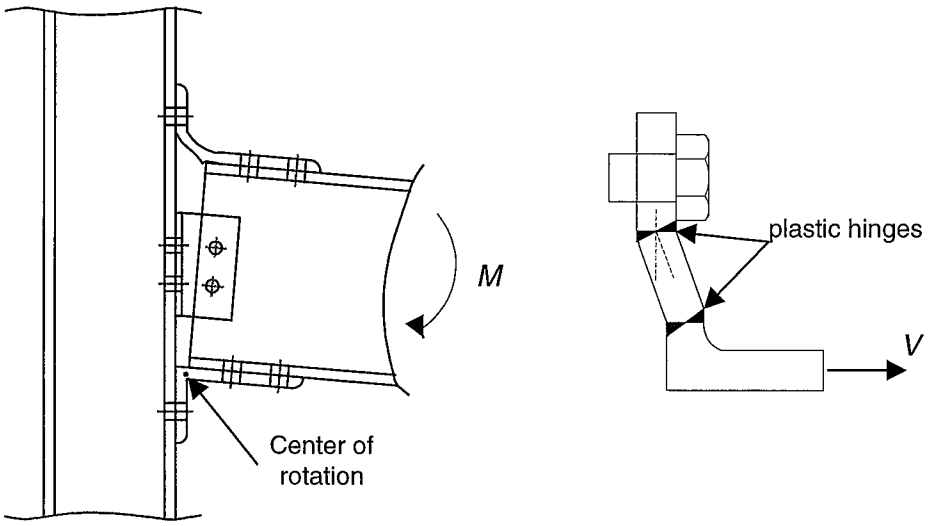

Fig. 3.1.3 Deformation of the PR Connection Subjected to Bending
[after Kim and Chen (1998)]

flange by using four A490 bolts with 5/8 inches in diameter and was connected to the column flange by using two A490 bolts with 5/8 inches in diameter. All bolts were detailed as slip critical. The ultimate moment capacity contributed by all parts of the connection was approximately 460 kip-inches, 88% of nominal plastic moment strength of the beam (Appendix A). However, corner crushing of the infill wall will induce a non-uniform bearing force on the top portion of the windward column or the bottom portion of the leeward column, especially on the portion near the beam-to-column joint. This bearing force may then induce a certain amount of tensile force in the PR connection. As a result, the PR connection is actually subjected to the interaction of moment and tension and the actual moment capacity of the PR connection will be reduced by the effect of the axial tensile force. The model of Kim and Chen (1998) only predicts the pure moment capacity of the PR connection and gives no consideration on the effect of an axial tensile force. In designing the PR connection of this specimen, the axial tensile force was assumed to equal the nominal shear resistance capacity of the column. Conservatively, a linear moment-axial force interaction equation was used to include the effect of the axial tensile force on the moment capacity of the PR connection. As calculated in Appendix A,

the moment capacity of the PR connection was estimated to be approximately 55% of the nominal plastic moment strength of the beam due to the inclusion of the axial force.

3.1.3 Design of the Headed Stud Connectors along the Interfaces

Headed stud connectors were installed along the interfaces of the RC infill wall and the steel members to ensure the composite action of the specimen. The interface connectors should be designed in accordance with their two primary properties: strength and ductility. According to the possible plastic failure mechanisms of infilled steel frames (Liauw and Kwan, 1983a, 1983b), the strength of interface connectors has significant effect on the maximum strength of the entire composite system. This is discussed further in Chapter 9. Ductility of the interface connectors plays a major role in retaining system integrity and increasing energy dissipation capacity.

For a single headed stud connector loaded in shear in the concrete, there are four primary failure modes, as shown in Figure 3.1.4. Breaking-out of the concrete (Figure 3.1.4.(c)) usually occurs at connectors located near the free edges of the concrete. Prying-out of the concrete (Figure 3.1.4.(d)) only occurs to connectors with a small ratio of embedment depth to shank diameter. Using sufficient embedment depth usually can eliminate this type of failure. For the majority of the headed stud connectors loaded in shear, shearing of the connector shank or the crushing of the concrete in the bearing zone are the two significant failure modes, which were observed at the same time in the same specimen in many tests (Ollgaard et al., 1971). The shear strength of a single headed stud in AISC (1993) and PCI (1992) is determined in accordance with these two failure modes. However, as shown in Figure 3.1.5, due to the limited thickness of the infill wall, the dispersal of the concentrated shear load into the concrete may induce cracks in three different orientations in the concrete: ripping, shear, and splitting (Oehlers, 1989). The cracking tends to propagate into the bearing zone and relieve the tri-axial stress-field on this part of concrete, so that the concrete in the bearing zone will crush prematurely. As a result, the specified shear strength in standard codes can not be achieved and the ductility of the connectors is also reduced. For a group of headed stud connectors loaded in shear in the infill wall, Figure 3.1.5 shows that another possible failure mode is caused by

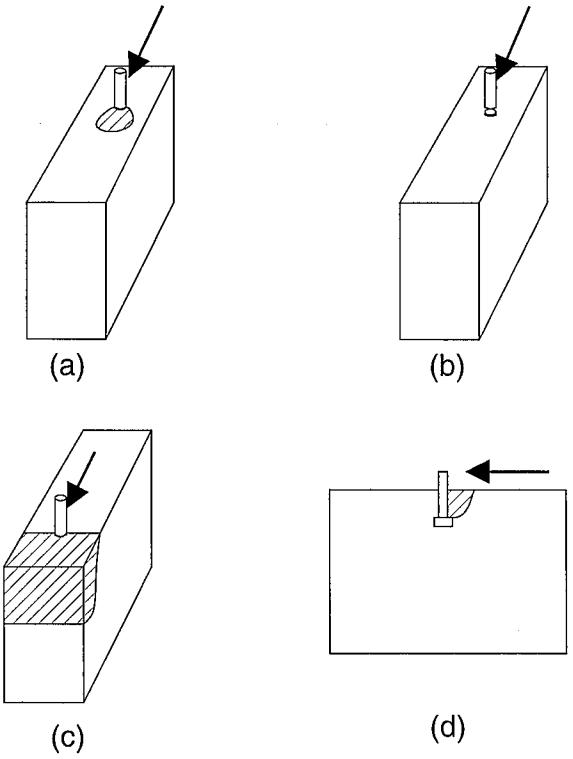

Fig. 3.1.4 Failure Modes of a Headed Stud Connector Loaded in Shear

(a) crushing of the concrete (b) shearing off of the connector shank
(c) breaking out of the concrete (d) prying out of the concrete

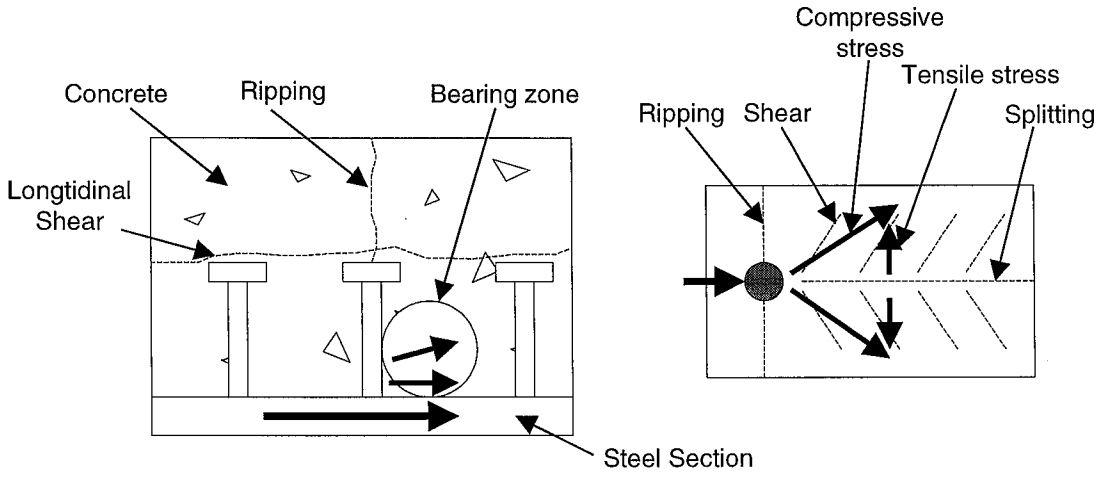

Fig. 3.1.5 Shear Force Transfer Mechanism of a Headed Stud Connector
[after Oehlers (1989) with minor changes]

cracking just above the head of the headed studs and through the entire section of the concrete.

Additionally, linear elastic finite element analysis of the prototype structure (Tong et al., 1999) indicated that the headed studs in this composite structural system, particularly in the corners of the panels, are under the interaction of tension and shear. This phenomenon was also observed in Liauw's tests (Liauw and Kwan, 1983b, 1985). Therefore, the connectors placed at the corners are required to provide enough tensile strength and ductility to delay the separation between the RC infills and the steel frame members. In Liauw's tests (Liauw and Kwan, 1983b, 1985), because of the weak confinement provided by the limited wall thickness, the maximum tensile strength of the headed stud connectors in the infill wall was controlled by concrete failure, involving the pull-out of a concrete cone. This type of connector failure generally gives relatively lower tensile strength and ductility, and thus the composite action may be deteriorated by the premature separation between the RC infills and the steel frame members.

In order to characterize these complex shear and failure modes, in an earlier portion of this research, a series of twelve experiments were conducted to investigate the strength and ductility of shear studs in RC wall panel (Saari, 1998). The parameters included: 1) monotonic or cyclic shear loading; 2) zero tensile loading or monotonic tensile loading with the force equal to approximately 50% of the nominal tensile strength of the headed stud; 3) confining with either perimeter bars placed along the base of the studs or with steel reinforcing cages (see Figure 3.1.6) and; 4) use of a ductility enhancing polymer cone. The tests showed that the reinforcing cage mitigated the primary types of cracking so that the fracture of the stud base in the base metal became the controlling failure mode. The impact of using the reinforcing cage resulted in the increase of stud strength and ductility. When axial tension, approximately 50% of the nominal tensile strength of the stud, was applied, the monotonic shear strength was 27% larger when the confining cage was used instead of the perimeter bar scheme, and the maximum slip achieved was three times larger. The impact of applying the axial tension on the stud resulted in the decrease of the shear strength. In the monotonic tests on the

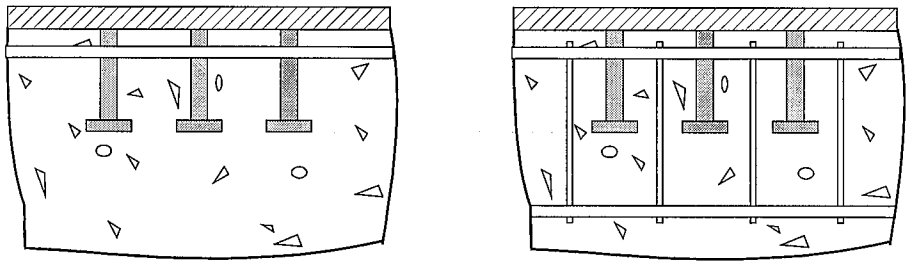

(a) Perimeter bar (b) Reinforcing cage

Fig. 3.1.6 Confinement of Headed Stud Connectors

specimens with confining cages, the shear strength of the stud reduced by nearly 40% when the axial tension was applied. The introduction of cyclic loading translated to a loss of approximately 17% in the stud shear strength, and resulted in a reduction of 70% to 80% in the deformation capacity displayed by the specimen with confining cages. A ductility enhancing device, comprising a plastic cone placed around the shank at the base of the stud, increased deformation capacity by approximately 60% for cyclic loading.

Because adequate confining reinforcement is critical to achieve strength and ductility for studs in an infill wall, steel confining cages were adopted in this specimen. The headed stud was 3/8 inches in diameter and 2.5 inches in total length, so that the ratio of stud length to diameter (2.5 to 3/8) was the same as that of a typical full scale stud (5 to 3/4). The thickness of the head itself was 5/16 inches and the diameter of the head was 3/4 inches.

The design shear strength of the stud was determined based on the following equation:

$$\begin{aligned} \phi Q_{sn} &= \phi\psi_1 0.5 A_{sc}\sqrt{f_c' E_c} \le \phi\psi_1 A_{sc} F_u \\ &= (1.0)(0.85)(0.5)(0.1104)\sqrt{3.5\times 3372} = 5.09\,\text{kips} \\ &\le (1.0)(0.85)(0.1104)(60) = 5.63\,\text{kips} \end{aligned} \tag{3.1.1}$$

where

f_c' = compressive strength of the concrete of the infill wall, ksi

E_c = young's modulus of the concrete of the infill wall, ksi

F_u = minimum specified tensile strength of the stud material, ksi

A_{sc} = cross section area of the shear stud shaft, inch^2

Equation (3.1.1) was modified from AISC (1993) with one additional factor ψ_1 to represent the detrimental effect of low cycle fatigue on the shear stud connectors during an earthquake. The 15% strength reduction resulting from using ψ_1 was based on the cyclic stud tests conducted as part of this research project (Saari, 1998).

Due to the presence of confining cages, the design tensile strength of the 3/8 inch stud was governed by the stud shank failure and determined in accordance to the following formula provided by PCI (PCI, 1992):

$$\begin{aligned}\phi P_{sn} &= \phi A_{sc} F_y = \phi A_{sc}(0.9F_u) \\ &= 1.0\times 0.1104\times(0.9\times 60) = 5.96\,\text{kips}\end{aligned} \tag{3.1.2}$$

where

F_y = nominal yield strength of a stud connector, ksi

The effect of the cyclic loading on the tensile strength of the stud was not considered due to the lack of sufficient experimental results.

For headed studs subjected to combined cyclic shear and tension in an infill wall, the strength capacity was governed by the following equation from PCI (PCI, 1992):

$$\left[\left(\frac{Q_s}{\phi Q_{sn}}\right)^2 + \left(\frac{P_n}{\phi P_{sn}}\right)^2\right] \le 1.0 \tag{3.1.3}$$

where

$\phi = 1.0$

As seen from Eq. (3.1.3), the presence of the tensile force in the stud can result in a significant reduction of shear strength of the headed stud. If the tensile force is 50% of the tensile strength of the stud, the maximum allowable shear strength will be reduced by 14%. In order to include the effect of axial force in design, it was assumed conservatively that the shear strength of a stud should be neglected as long as Eq. (3.1.3) was breached based on the elastic analysis of the structure at the design force level.

The finite element analysis results of the prototype structure were used to estimate the percentage of the studs that breached the interaction Eq. (3.1.3). For a headed stud used in the prototype structure with sufficient confinement (the stud was 3/4 inches in diameter and 5 inches in length), Eq. (3.1.1) gives a design shear strength of approximately 22 kips and Eq. (3.1.2) gives a design tensile strength of approximately 24 kips. The internal forces of the studs along the most critical interface, the bottom interface of the first story, are listed in Table 2.3.2 due to the lateral load combination discussed in Chapter 2. It can found that approximately 25% of the studs (11 studs from the total of 41 studs) along the bottom interface breach the interaction Eq. (3.1.3).

It was assumed that, as in the prototype structure, 25% of the studs along the beam-infill interface in the specimen would breach the interaction equation at the design force level, and the remaining 75% of the studs needed to resist 100% of the design lateral load. As discussed in Section 3.1.1, the design lateral load for the specimen was determined to be approximately 71 kips. As a result, 18 headed studs were placed along the beam-infill wall interface at 4 inch spacing to transfer the 71 kips design lateral load (75% of the total shear capacity of 18 studs is 69 kips, which is smaller than the 71 kips design lateral load by 2.8%). It was also assumed that the shear force per unit length along the column–infill interface was the same as that along the beam–infill interface. Therefore, the headed studs along the column–infill interface were also placed at 4 inch spacing.

The confining reinforcement cages, comprising rectangular hoops and four horizontal bars, were placed all around the infill wall perimeter in the specimen. The detailing of confining cages is shown in Figures 3.1.6 and 3.1.7. The rectangular hoop was 5 inch high and 2.5 inches wide, arranged at 2 inch spacing. Four horizontal bars were tied to the corners of the rectangular hoop to form the confining cage. Cold-drawn No.3 gage steel was used to construct the rectangular hoops and No. 2 reinforcing bar was used as the horizontal bars. These sizes hold to the one-third scale requirements relative to the dimensions of confining cages that would be used in a full-scale infill wall (Saari, 1998).

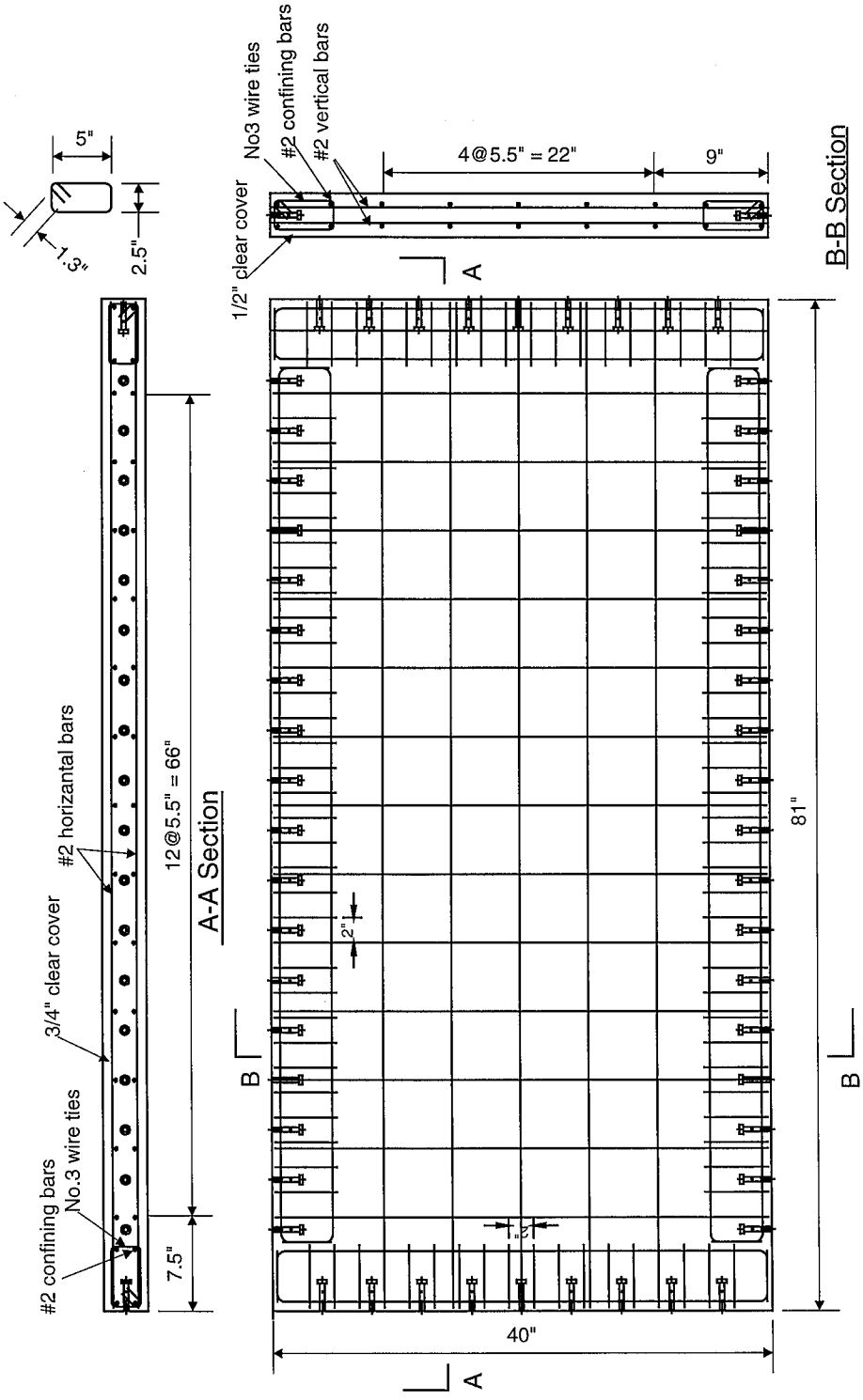

Fig. 3.1.7 Detailing of Confining Cages and Wall Reinforcement

3.1.4 Design of the Wall Reinforcement

The infill wall of the specimen was assumed to carry 100% of the lateral design shear force and 40% of the corresponding overturning moment. According to Section 9.3.4.1 in the ACI building code (ACI, 1995), a reduction factor of 0.6 was used to calculate the shear strength of the RC infill walls. Both the horizontal and the vertical reinforcement ratios were 0.51%, achieved by two curtains of No. 2 bars spaced at 5.5 inches. The estimated shear strength of the RC infill wall was 78.5 kips. Detailing of the wall reinforcement is shown in Figure 3.1.7.

A key problem of this detail is the development of the reinforcing bars. The development length of a No. 2 bar is approximately 6 inches without a hook at the end or 5.1 inches with a hook in accordance with ACI (1995). Therefore, the height of the reinforcement cage theoretically should be at least greater than 5.1 inches to ensure that the reinforcement can approach its yield strength within the confining reinforcement cage. In actual construction, No. 6 or No. 7 bars are usually used as the wall reinforcement. If the concrete compressive strength of the prototype structure is 4000 psi and a hook is used at the bar end, the development length will be approximately 14.2 inches for No. 6 bars and 16.6 inches for No. 7 bars. That means the reinforcement cage in the prototype structure should be at least 14-15 inches high. Such a reinforcement cage is feasible but may be not economical in practice. However, if the wall reinforcement has the same enlarged end as the stud head, a portion of the tensile force in the connectors may be transferred through direct strut action between the reinforcement head and the surrounding concrete so that the development length can be reduced. Such reinforcement is called T-headed reinforcement and is manufactured by friction welding a steel plate head to the end of a standard reinforcing bar. In this project, it was achieved by threading a nut to the end of a bar. An increasing amount of research work on T-headed reinforcement has been done in recent years because of its advantages in detailing, construction, and fabrication (DeVries, 1996; Wallace et al., 1998). It has been shown that a development length of 8 to 10 bar diameters is sufficient to develop the yield stress of a bar having a T-head (Bode and Roik, 1987; Balogh et al., 1991). For the above

reasons, T-headed reinforcing bars were used in the present project, which was fabricated by electric arc welding a 3/8 inch nut to the end of the No.2 bar.

3.2 Material Properties

The steel frames were fabricated by LeJeune Steel Company in Minnesota, and the concrete for constructing the infill wall was mixed in the Structural Engineering Laboratory at the University of Minnesota. A series of tests were conducted to measure the material properties of both the steel and concrete material. Tension testing of steel coupons was conducted in accordance with SSRC Technical Memorandum No. 7 (SSRC, 1998). Two sets of cylinders were used to obtain the compressive strength (ASTM C39), elastic modulus (ASTM C469), and splitting tensile strength (ASTM C496) of the concrete, respectively. Material properties of the reinforcing bars were provided by CTL Inc. in Skokie, Illinois. Material properties of the headed studs were provided by Stud Welding Associates in Elyria, Ohio.

3.2.1 Steel Material Properties

The material properties of the steel components are reported in Table 3.2.1 and include: static yield stress F_{ys}, dynamic yield stress F_{yd}, ultimate tensile stress F_u, modulus of elasticity E_s, strain hardening modulus E_{sh}, and strain at initiation of strain hardening ε_{sh}. The material properties were obtained by performing tension tests on coupons taken from the steel members. Similar components were made from the same heat of steel for both specimens. Coupons WA-1 and WA-2 were removed from different legs of the web angle L2×2×5/16. Coupons TSA-1 and TSA-2 were removed from different legs of the top-and-seat angle L5×3×5/16. Coupons CW-1 and CW-2 were removed from the web of column member W5×19, and coupons CF-1 and CF-2 were removed from the flange of the W5×19. Coupons BW-1 and BW-2 were removed from the web of beam member W8×13, and coupons BF-1 and BF-2 were removed from the flange of the W8×13.

The coupons were fabricated by cutting a 2 inch ×18 inch block from additional steel pieces provided from the heat, and then milled to the required dimensions as shown in Figure 3.2.1. Tension testing of coupons was performed in an MTS hydraulic testing machine in the Structural Engineering Laboratory at the University of Minnesota. It is noted that, although the columns were A572 Grade 50, the static yield strength was approximately 45 ksi.

Table 3.2.1 Material Properties of Steel Members

Location	Coupon	F_{ys} (ksi)	F_{yd} (ksi)	F_u (ksi)	E_s (ksi)	E_{sh} (ksi)	ε_{sh} (με)
Web Angle	WA-1	41.0	45.6	66.9	28,500	500	19,500
	WA-2	38.2	42.7	67.7	28,000	450	20,000
Top and Seat Angle	TSA-1	52.4	57.0	74.1	29,200	480	21,200
	TSA-2	52.9	57.2	77.3	28,300	520	18,600
Column	CW-1	46.3	50.7	75.5	32,000	680	18,100
	CW-2	44.9	49.1	73.2	29,700	620	21,700
	CF-1	45.0	48.7	69.6	30,500	570	12,700
	CF-2	45.3	49.5	72.4	29,300	470	15,100
Beam	BW-1	53.7	59.6	80.3	32,000	550	26,800
	BW-2	53.1	59.1	78.2	30,800	480	27,700
	BF-1	49.0	54.0	76.5	29,700	690	18,200
	BF-2	49.7	55.0	74.4	28,100	610	22,500

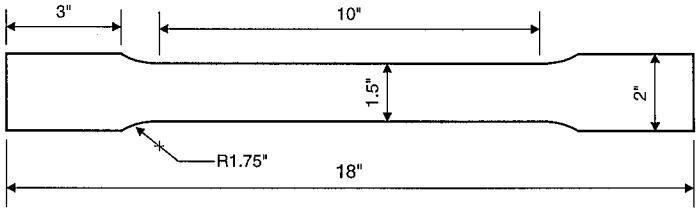

Fig. 3.2.1 Coupon Dimensions

3.2.2 Concrete Material Properties

The infill walls were cast in place with two batches of concrete, with the first story being cast two days before the second story. Casting was initiated by pouring the

concrete through three portal openings cut into the form on the east side of the wall, spaced uniformly across the mid-height of the panel. When the vibrated concrete reached the bottom of the portals, these portals were sealed with wood blocks, and the concrete pour continued through three chutes at the top of the infill panel, also spaced uniformly along the width of the panel. The concrete was allowed to harden 72 hours before removal of the forms. After removal of the forms, the concrete was covered with burlap and kept continuously moist for four days. The concrete that formed in the chutes was then chipped off and sanded smooth. Thirty-six 4 inch×8 inch cylinders were cast for each batch of concrete mix. Half of the cylinders were moist-cured (ASTM C192), and the others were cured under the same conditions as the infill panels.

Content of the concrete mix included: cement, pea gravel, sand, fly ash, water, and retarder. The properties of each material include:

Coarse aggregate: 3/8 inch maximum-size pea gravel (ASTM C33) with an oven-dry specific gravity of 2.63, absorption of 1.33%, and oven-dry rodded unit weight of 104 lb per cu ft.

Fine aggregate: Natural sand (ASTM C33) with an ovendry specific gravity of 2.61 and an absorption of 1.07%. The fineness modulus was 2.70.

Cement: Type III (ASTM C150)

Fly ash: Class F (ASTM C618)

Retarder: WR Grace Daratard-17 (ASTM C494)

For the concrete mix, the water to cementitious material ratio was 0.71, the coarse aggregate to cementitious material ratio was 2.64, and the fine aggregate to cementitious material ratio was 3.38. The fly ash constituted 20% of the cementitious material by weight. The retarding admixture was 7 fl oz/100 lb cement in each batch of mix, which had approximately 0.35 cu yd of concrete. Table 3.2.2 shows the material properties of Mix 1 used for casting the first story wall of the specimen, and Table 3.2.3 shows the material properties of Mix 2 used for casting the second story wall of the specimen.

Table 3.2.2 Concrete Material Properties for the First Story of the Specimen

Curing	Properties	Testing date	Cylinder 1	Cylinder 2	Cylinder 3	Average
Moist-cured	Compressive strength (psi)	4 days	1887	1875	1675	1812
		7 days	2254	2161	2281	2232
		28 days	3598	3745	3587	3643
	Splitting strength (psi)	28 days	406	472	374	417
	Modulus of elasticity (ksi)	28 days	3485	3643	3753	3667
Same as the specimen	Compressive strength (psi)	28 days	4117	4062	4200	4126
		Test day	3607	3636	3836	3693
	Splitting strength (psi)	28 days	526	418	458	467
		Test day	448	413	382	414
	Modulus of elasticity (ksi)	Test day	3200	3558	3140	3259

Table 3.2.3 Concrete Material Properties for the Second Story of the Specimen

Curing	Properties	Testing date	Cylinder 1	Cylinder 2	Cylinder 3	Average
Moist-cured	Compressive strength (psi)	4 days	1634	1628	1687	1650
		7 days	2168	2006	2080	2084
		28 days	3430	3423	3520	3457
	Splitting strength (psi)	28 days	409	425	394	409
	Modulus of elasticity (ksi)	28 days	3219	2929	2983	2998
Same as the specimen	Compressive strength (psi)	28 days	3947	3584	3700	3743
		Test day	3631	3801	3992	3808
	Splitting strength (psi)	28 days	409	508	433	450
		Test day	397	454	385	412
	Modulus of elasticity (ksi)	Test day	3068	3292	2814	3052

3.2.3 Material Properties of Reinforcing Bars

The No. 2 model reinforcement was a hot-rolled deformed reinforcing bar with properties similar to Grade 60 reinforcement. The diameter was 0.25 inches and the

effective area was 0.05 square inches. According to the tension testing results provided by CTL, the yield strength of this No. 2 reinforcement was 62.5 ksi, the ultimate strength was 88.8 ksi, the yield strain was approximately 2000 με, and the maximum elongation was 17.8%.

3.2.4 Material Properties of Headed Studs

The material properties of the headed studs, as provided by Stud Welding Associates, included the yield strength of the stud steel at 62.3 ksi, the tensile strength of the stud steel at 80.2 ksi and the maximum elongation at 21.0% for a two inch gage length.

3.3 Test Setup

Figure 3.1.1 shows the test setup viewed from the west side of the Laboratory. The specimen is oriented parallel to the strong wall, along the north - south direction, in order to utilize the strong wall as part of the out-of-plane bracing system. Each of two "A" shaped loading frames comprised a W12×120 column and a W18×65 diagonal beam with a 45° angle. A W14×132 transverse beam was bolted at the top of these two "A" frame columns to act as a reaction support for the actuators. For the specimen, two W8x40 beams were placed at the top of the top beam and continuously welded along both edges of the flange of the top beam. A 1.25 inch thick end plate was welded to each W8×40 beam. Another W14×132 transverse beam was then fit into the gap between two W8×40 beams and bolted to the end plate of each beam. At each side of the specimen, one MTS hydraulic actuator was placed between the two W14×132 beams and bolted to the flange of each beam. The loading capacity of each actuator was 110 kips and the maximum stroke of each actuator was ±10 inches. The size of the loading frame was chosen so that its displacement at the reaction point was only 0.088 inches under 220 kips load (Nozaka et al.,1998).

Two 52 inch × 46 inch steel plates served as foundations for the specimen. Each foundation plate was 3 inch thick and was connected to the strong floor using eight B7

steel rods. The plates rested on a bed of hydrocal to insure level and uniform contact with the strong floor. Each column was then bolted to the foundation plate through its pre-welded base plate. Although the steel foundation plate had sufficient strength to resist the tensile force caused by the overturning moment, the weak transverse stiffness of the plates may result in undesirable vertical deformation under each column. Therefore, three W8×13 stiffening beams were welded along the top of each foundation plate to enhance its out-of-plane stiffness (Figure 3.3.1). Assuming 220 kips of lateral load was applied to the specimen and 100% of the overturning moment was carried by the steel columns, the tensile force of the windward column would be 245 kips (Figure 3.3.2). According to linear elastic finite element analysis, this tensile force yielded a vertical deformation of the steel foundation plate of approximately 0.08 inches, labeled as L_1 in Figure 3.3.2. Based on the assumption of rigid body rotation, the lateral displacement L_2 due to L_1 was $L_1(2h/L_w)$, equaling 0.089 inches for the specimen. Given an estimated deflection at the peak lateral load of 0.5 to 1.0 inch and a maximum stable deflection of 2 to 3 inches, the effect of deformation from both the load frame and the foundation plate on the system behavior were deemed to be negligible.

The W8×13 bottom beam of the specimen was welded to the foundation plate with continuous fillet welds. Therefore, part of the shear force carried by the RC infill wall in the first story could be first transferred to the bottom beam through the shear studs, and then transferred from the bottom beam to the two foundation plates through the fillet welds. The bottom beam was attached to the bottom of the column with a L2×2×1/4 double- web angle. Two 5/16 inch thick × 8 inch high plates were welded outside the column flanges across the flange tips to strengthen the bottom portion of the column by forming a box section, thus mitigating the possibility of premature failure of the column base (Figure 3.3.1).

Four sets of braces were installed to prevent the possibility of out-of-plane deformation of the specimen. As seen in Figure 3.3.3, this bracing system comprised four linear bearings. The shaft of the linear bearing block was fixed to a steel column through angles. Threaded rods were used to connect the bearing block and the specimen. Each

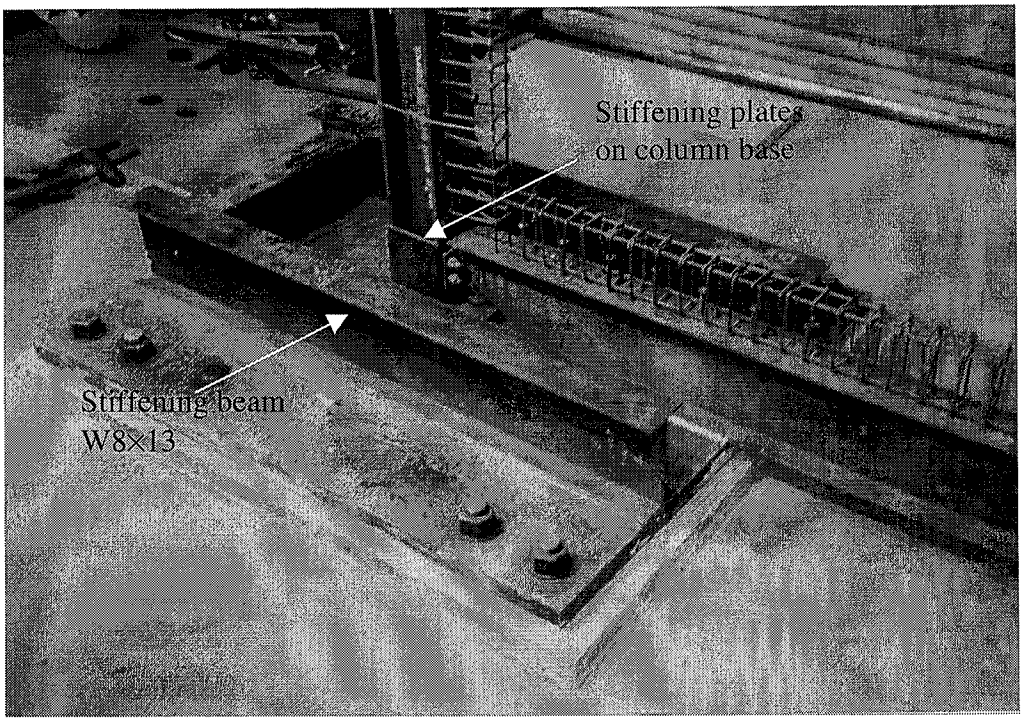

Fig. 3.3.1 View of the Foundation Plate and Column Base

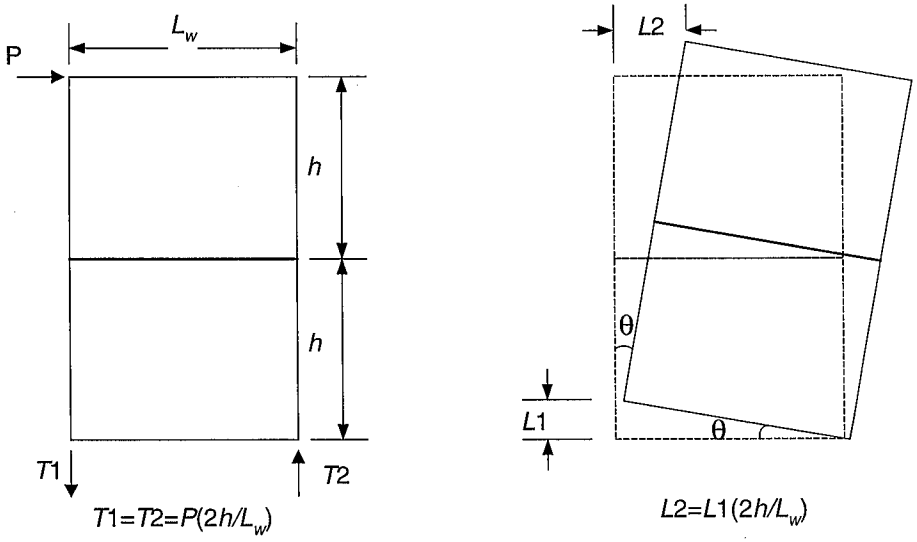

Fig. 3.3.2 Effect of the Out-of-Plate Deforamation of Foundation Plates

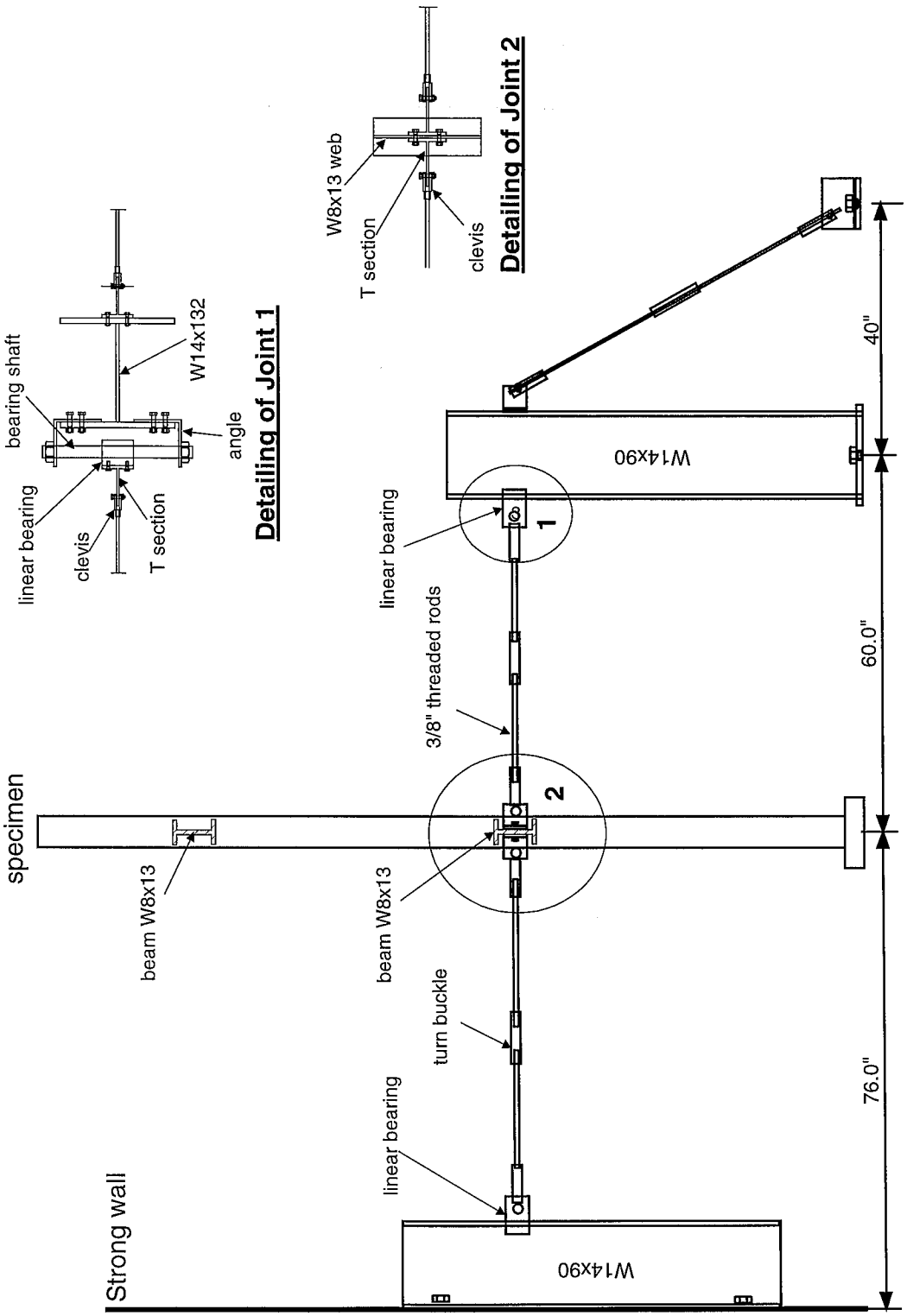

Fig. 3.3.3 Lateral Bracing Sytem

end of the threaded rod was connected to a WT steel section through a clevis. The WT section was then bolted to the bearing block at one end and bolted to the web of beam W8×13 at the another end. One turnbuckle was placed in the middle of each threaded rod to allow it to be tightened initially. The bracing systems were placed on both sides of the specimen because they act primarily in tension. Just prior to the test, each bracing rod was tightened with turnbuckles to achieve approximately 200 lbs of pretension, a small initial pretension force. In addition to the specimen bracing, a lateral bracing system was attached to the bracket of the east actuator and was supported against the strong wall.

3.4 Instrumentation

The specimen was heavily instrumented in order to obtain comprehensive information. Three types of instruments, including strain gages, linear variable differential transformers (LVDTs), and linear position transducers (LPTs) were employed to measure strains and displacements. The instrumentation details are described in the following sections according to the instrumentation objectives or to the instrumented locations. Figure 3.4.1 shows the instrumented specimen.

3.4.1 Global Response

To describe the global response of this system, three LVDTs were attached to the south column to measure the lateral story displacement of the system, with reference to the south foundation plate. As shown in Figure 3.4.2, a small frame bolted to the foundation plate was used to hold these three LVDTs. The nomenclature used to identify the LVDTs was based on their functions and locations. As shown in Figure 3.4.2, the first letter of the name was always L, representing LVDTs. The second and third letters described the function of the LVDT, the fourth and fifth letters described the location of the LVDT, and the sixth was the LVDT number to distinguish LVDTs having the same functions. This nomenclature method was used for all the LVDTs, as described in their corresponding figures.

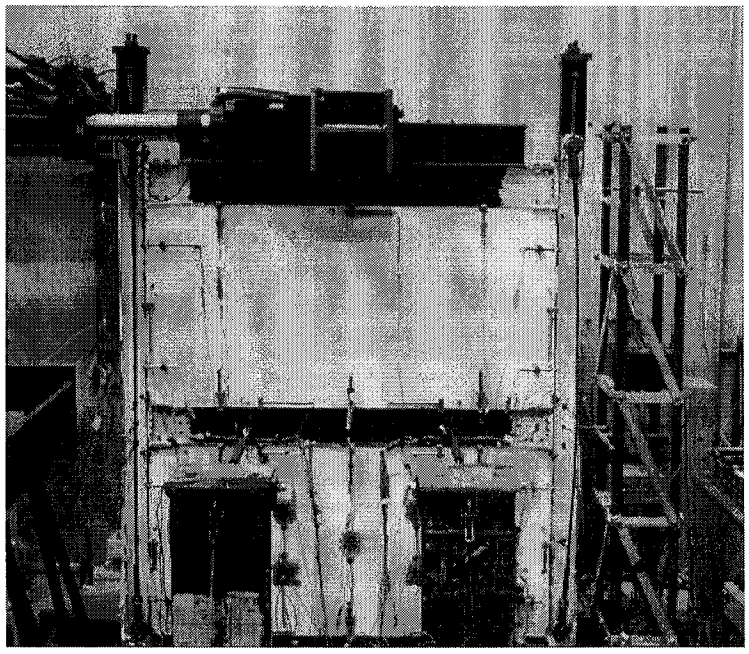

Figure 3.4.1 Instrumentation of the Entire Specimen

3.4.2 Steel Columns

Strain gages and strain rosettes were used to measure the deformation of the steel columns at critical locations in order to obtain strains and an estimate of the internal forces in the steel columns. As shown in Figure 3.4.3, strain gages and strain rosettes were placed at the bottom, the middle, and the top region of both steel columns in the first story, as well as at the bottom region of both steel columns in the second story. The strain gages were placed on the column flange, oriented in the longitudinal direction and 1.0 inch away from the edge of the flange. The strain rosettes were placed at the center of the web. The strain rosette of the north column had its legs oriented in the horizontal direction (0°), the vertical direction (90°) and the 45° direction, and the strain rosette of the south column had its legs oriented in the horizontal direction (0°), vertical direction (90°) and 135° direction. All the strain gages and strain rosettes were placed on the west sides of the steel columns. These strain gages and rosettes were TML Post-Yield Gages, capable of measuring strain up to ±15-20%. Figure 3.4.3 only shows strain gages on the north column. The strain gages on the south column were at symmetric locations to those

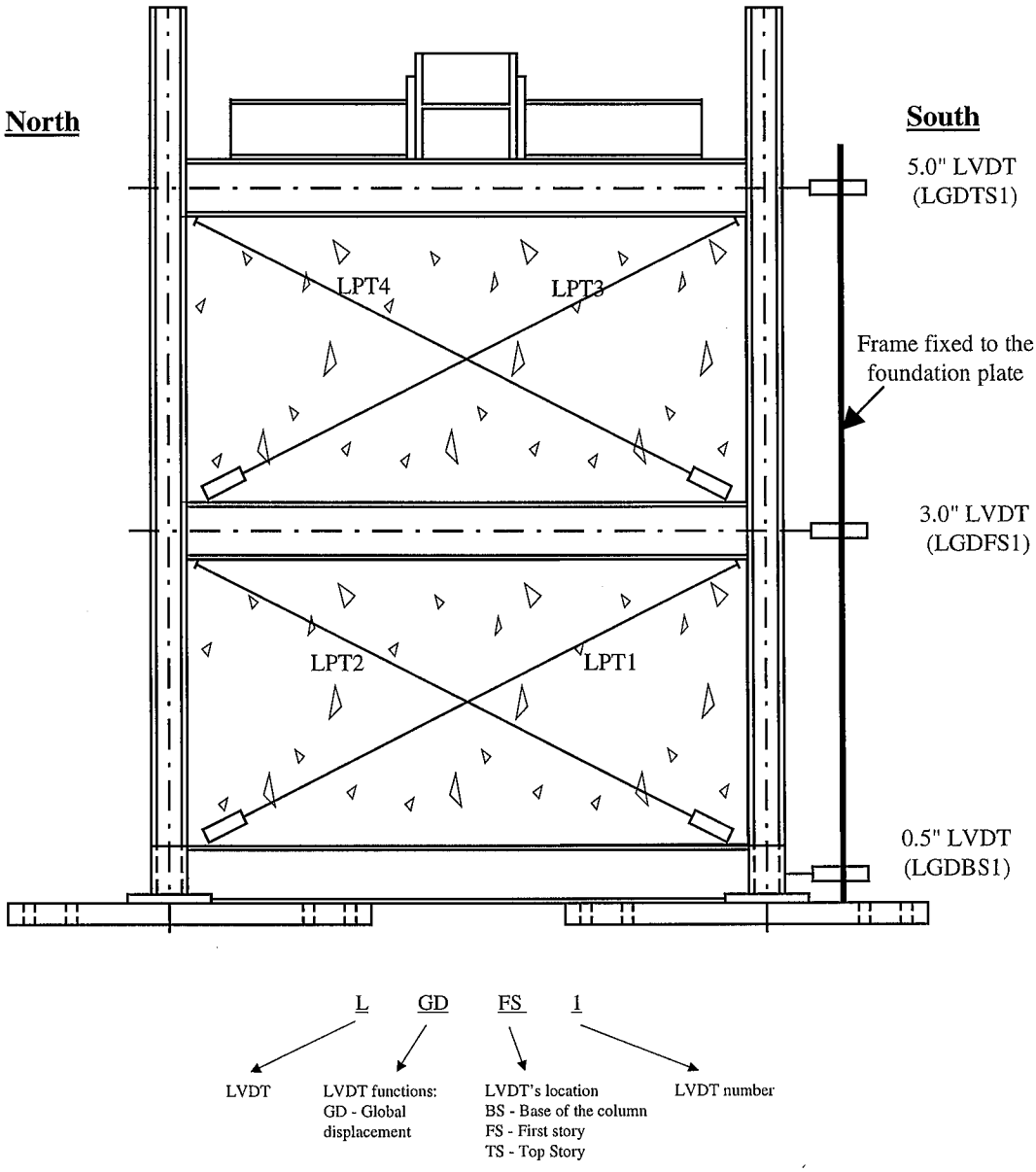

LPT- Linear position transducers

Fig. 3.4.2 Instrumetaion Plan: Global LVDTs

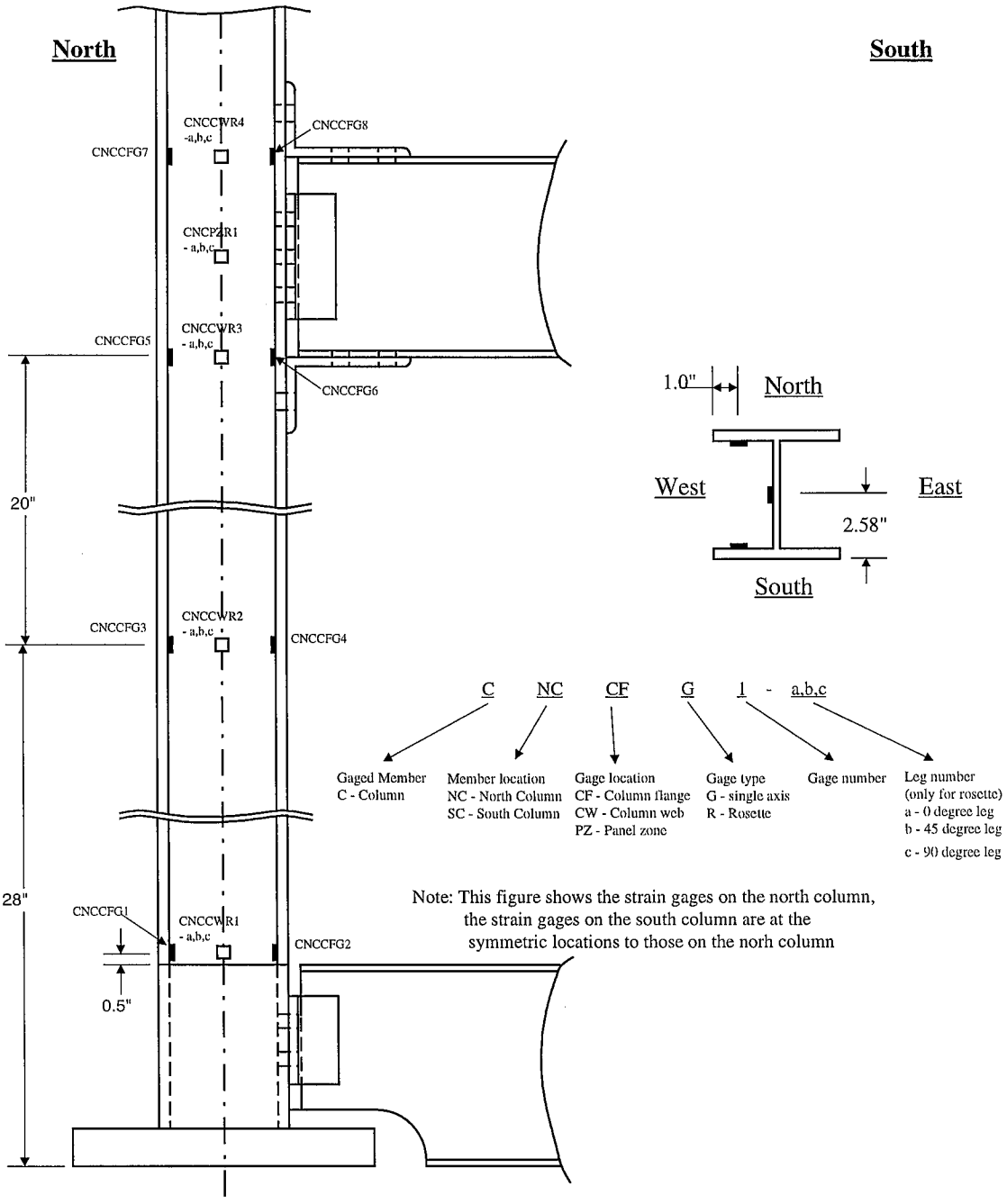

Fig. 3.4.3 Instrumentation Plan: Strain Gages on the Columns

on the north column. The nomenclature used to identify the strain gages was based on their functions and locations. As shown in Figure 3.4.3, the first letter described the name of the gaged member, the second and third letters described the member location relative to the laboratory, the fourth and fifth letters described the gage location relative to the member, the sixth described the gage type (with G representing a single gage or R representing a strain rosette), and the seventh was the gage number. If it was a strain rosette, there were three additional letters at the end of the name to represent the leg orientation of the strain rosette.

3.4.3 Reinforced Concrete Infill Walls

The behavior of the RC infill wall was quantified using the stress field of the infill panel and the deformation of the infill panel. In order to obtain the stress distribution pattern in the RC panel, nine strain rosettes were placed diagonally on the west side surface of the concrete panel of the first story (Figure 3.4.4). These strain rosettes were TML Polyster Wire Rossettes, capable of measuring strain up to ±2%. Each leg of this strain rosette was 60 mm long, suitable for measuring the strain of concrete with 3/8 inch maximum aggregate size. The behavior of the infill wall can also be represented by its diagonal deformation, which was measured by a pair of LPTs installed diagonally along the RC panel of each story (Figure 3.4.2).

3.4.4 Interfaces between Steel Members and Reinforced Concrete Infill Walls

It is important to gain an understanding of the coupling between global responses of the structure and the local demands placed upon the composite interface. In order to obtain the slip and separation demands of the interface studs, LVDTs were arranged along all of the interfaces between the steel frames and the RC infill walls. Figure 3.4.5 shows the positions of these 30 LVDTs, with those for measuring slip referred to as "slip" LVDTs and those for measuring separation referred to as "separation" LVDTs. As seen in Figure 3.4.6, the "separation" LVDTs were attached to the infill wall, and a spring system set the LVDT extension rod against an aluminum plate fixed to the flange

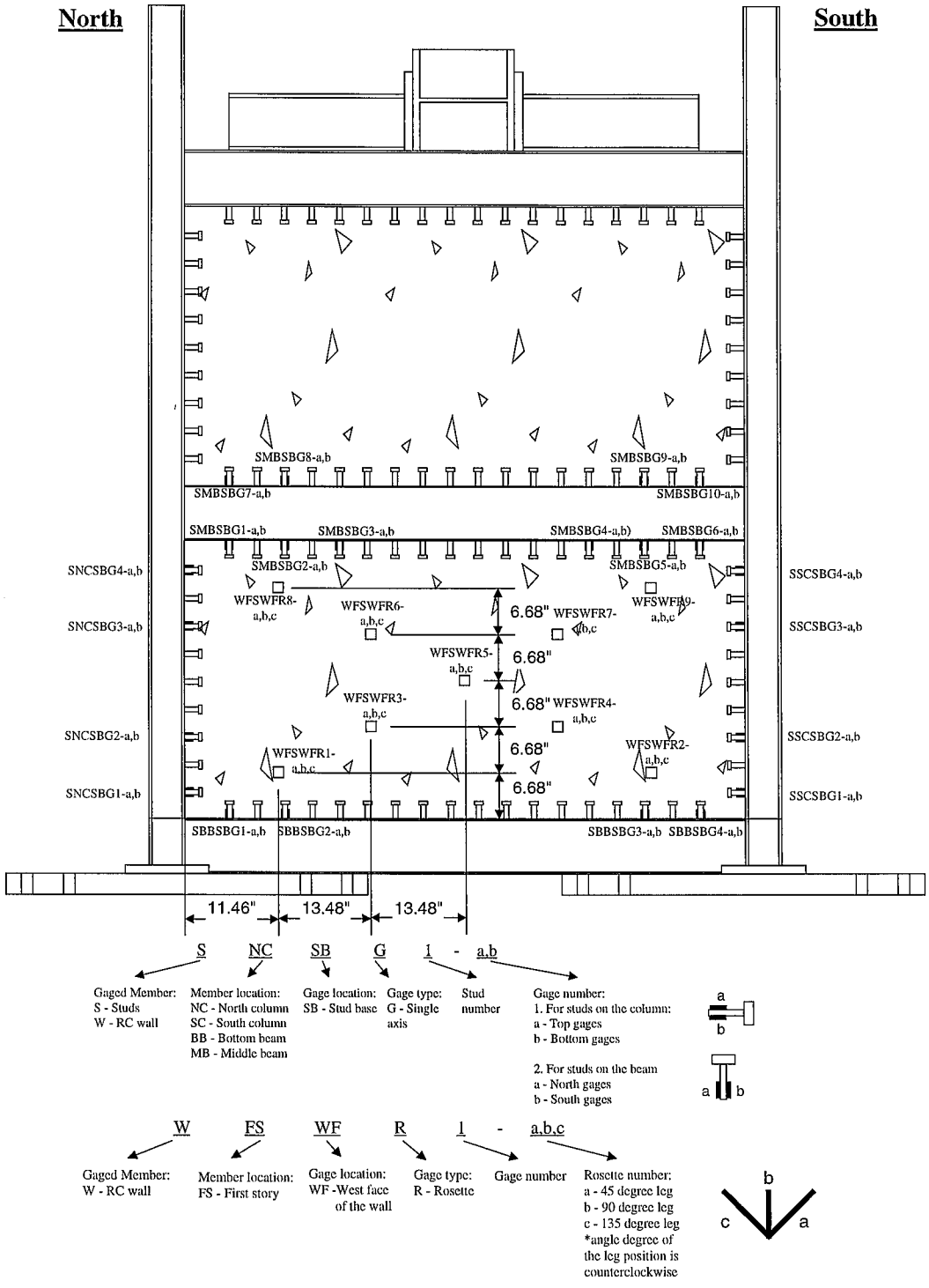

Fig. 3.4.4 Instrumentation Plan: Strain Gages on the Studs and Infill Walls

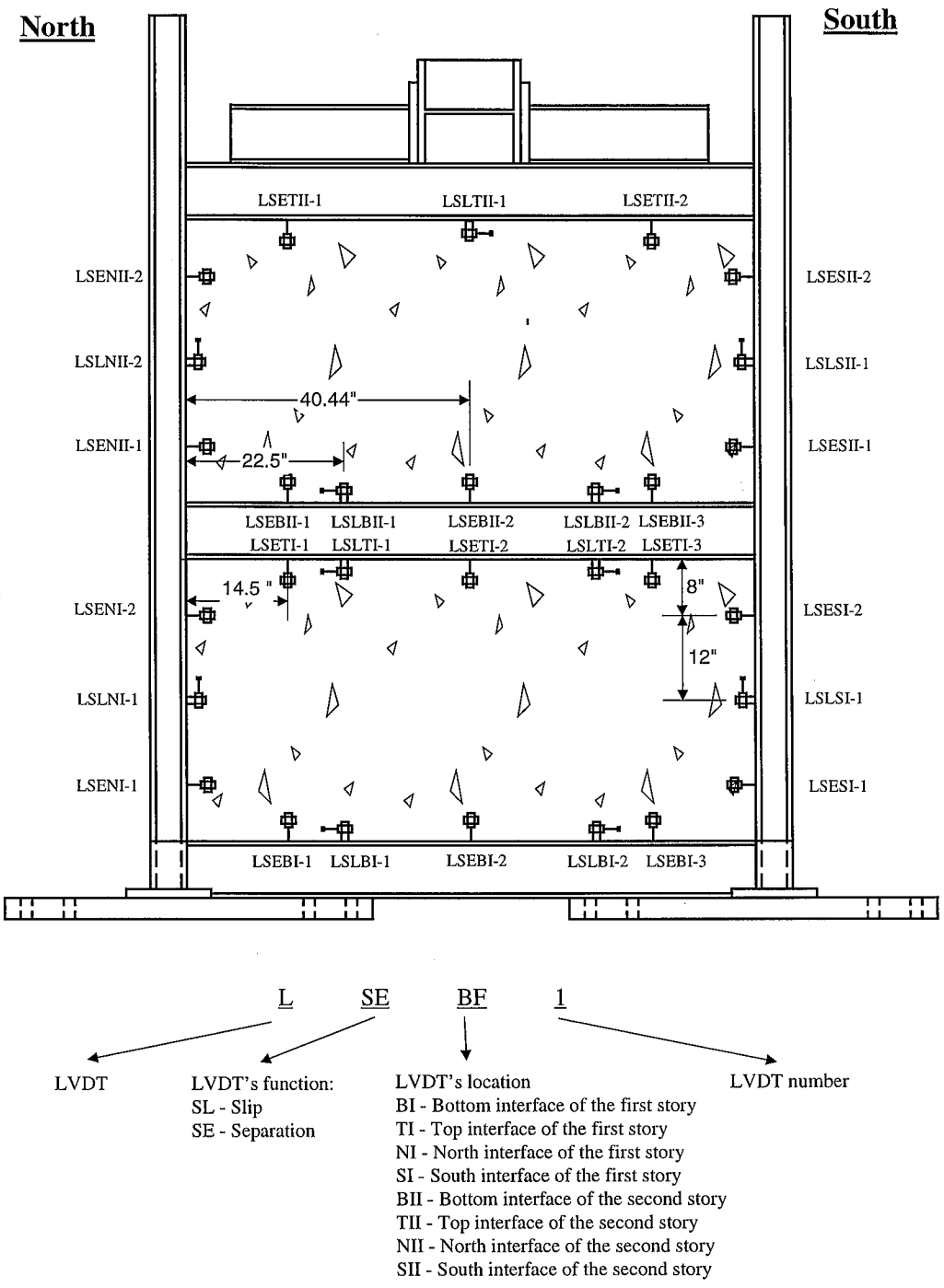

Fig. 3.4.5 Instrumentation Plan: LVDTs along the Interfaces between the Steel Members and RC Walls

of the steel member. The rod was prevented from moving parallel to the steel member by epoxying posts at either side of the rod.

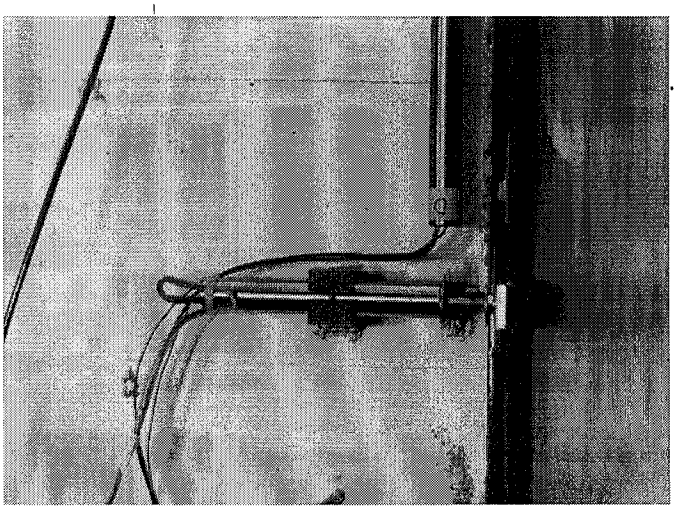

Figure 3.4.6 Installation of the Separation LVDTs

3.4.5 Headed Studs

To estimate the axial force and bending moment in the interface studs, a total of 22 studs were monitored with strain gages. Figure 3.4.4 shows the locations of these gaged studs, which were mainly located in the first story. Two strain gages were placed on the opposite sides of the stud shaft and were placed as close to the stud base as possible. The strain gages of each stud were covered by SB-tape (from TML), a water-proof coating, and then a layer of epoxy was applied to the top of the SB-tape for mechanical protection. Each lead wire of the strain gage was protected by a plastic sleeve. The nomenclature of the stud gages is slightly different from the other gages. The seventh number in the name represented the gaged stud number along a certain interface, and the letter "a" or "b" following represented the relative location of the strain gage to its corresponding stud shaft. Table 3.4.1 shows the distance from the center of each strain gage to the stud base. These stud gages were also TML Post-Yield Gages, the same as those used on the steel columns.

Table 3.4.1 Distance from the Strain Gage Center to the Stud Base*[1]

Gage Name	Distance to base	Gage Name	Distance to base
S_NC_SB_G_1a	1/4"	S_BB_SB_G_4a	5/16"
S_NC_SB_G_1b	1/4"	S_BB_SB_G_4b	5/16"
S_NC_SB_G_2a	1/4"	S_MB_SB_G_1a	9/32"
S_NC_SB_G_2b	1/4"	S_MB_SB_G_1b	9/32"
S_NC_SB_G_3a	1/4"	S_MB_SB_G_2a	9/32"
S_NC_SB_G_3b	1/4"	S_MB_SB_G_2b	9/32"
S_NC_SB_G_4a	1/4"	S_MB_SB_G_3a	9/32"
S_NC_SB_G_4b	1/4"	S_MB_SB_G_3b	9/32"
S_SC_SB_G_1a	1/4"	S_MB_SB_G_4a	9/32"
S_SC_SB_G_1b	1/4"	S_MB_SB_G_4b	9/32"
S_SC_SB_G_2a	1/4"	S_MB_SB_G_5a	9/32"
S_SC_SB_G_2b	1/4"	S_MB_SB_G_5b	9/32"
S_SC_SB_G_3a	1/4"	S_MB_SB_G_6a	9/32"
S_SC_SB_G_3b	1/4"	S_MB_SB_G_6b	9/32"
S_SC_SB_G_4a	1/4"	S_MB_SB_G_7a	5/16"
S_SC_SB_G_4b	1/4"	S_MB_SB_G_7b	5/16"
S_BB_SB_G_1a	1/4"	S_MB_SB_G_8a	5/16"
S_BB_SB_G_1b	1/4"	S_MB_SB_G_8b	5/16"
S_BB_SB_G_2a	1/4"	S_MB_SB_G_9a	5/16"
S_BB_SB_G_2b	1/4"	S_MB_SB_G_9b	5/16"
S_BB_SB_G_3a	5/16"	S_MB_SB_G_10a	5/16"
S_BB_SB_G_3b	5/16"	S_MB_SB_G_10b	5/16"

1: This table provides the measured distance from the center of each stud strain gage to the base of the stud, as shown below

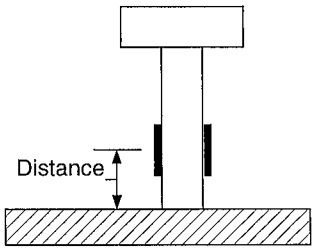

3.4.6 Partially-Restrained Connection Regions

The nomenclature of the LVDTs and strain gages in the connection regions are described in Figures 3.4.7 and 3.4.8, respectively. They were consistent with the nomenclature described in Sections 3.4.1 and 3.4.2. All the LVDTs in the connection regions were placed on the east side of the specimen and all the strain gages and rosettes were placed on the west side of the specimen.

At each connection region of the middle beam, two 0.5" LVDTs were attached to the top and bottom beam flanges to measure the rotation of the PR connection (LRONJ1 and LRONJ2 in Figure 3.4.7). One 0.1 inch LVDT (LSLNJ1 in Figure 3.4.7) was installed between the web angle and the column flange to measure the possible bolt slip in the web angles. One 0.1 inch LVDT (LSLNJ2 in Figure 3.4.7) was also installed between the column flange and the beam flange to measure the shear deformation of the PR connections.

In order to obtain the strain and an estimate of forces resisted by the PR connection, strain gages and strain rosettes were placed at both ends of the middle beam. At each end, five strain gages were placed along the longitudinal direction of the beam, at a position 6" away from the surface of the column flange. Two of these five gages were placed on the inside surface of the beam flange and were 0.75 inches away from the edge of the flange. Three of these five gages were placed on the west side of the beam web at a 2 inch spacing. One strain rosette was installed at the center of the beam web and near the web angle to measure the shear force resisted by the PR connection. To monitor the progression of the inelasticity in the top or seat angles, three gages were placed along the k-lines of each angle. One gage (ANJTAG1 of the top angle in Figure 3.4.8) was in the middle of the k-line of the vertical leg and the other two (ANJTAG2 and ANJTAG3 of the top angle in Figure 3.4.8) were near the edge of the horizontal leg.

Two 1/10 inch LVDTs were used to measure the column panel zone deformation, as seen in Figure 3.4.7. Four machine screws were welded to the four corners of each panel zone. The plastic holder of each LVDT was then mounted to the screw at the bottom corner and fixed along the diagonal angle. One end of the extension rod of the LVDT assembly was connected to a short piece of round aluminum rod, which could rotate freely around the screw at the top corner. In addition to the LVDT assembly, one strain rosette was placed at the center of each panel (Figure 3.4.3), with the purpose of directly measuring the shear strain and providing more detailed information beyond the average shear deformation taken from the diagonal displacement transducers.

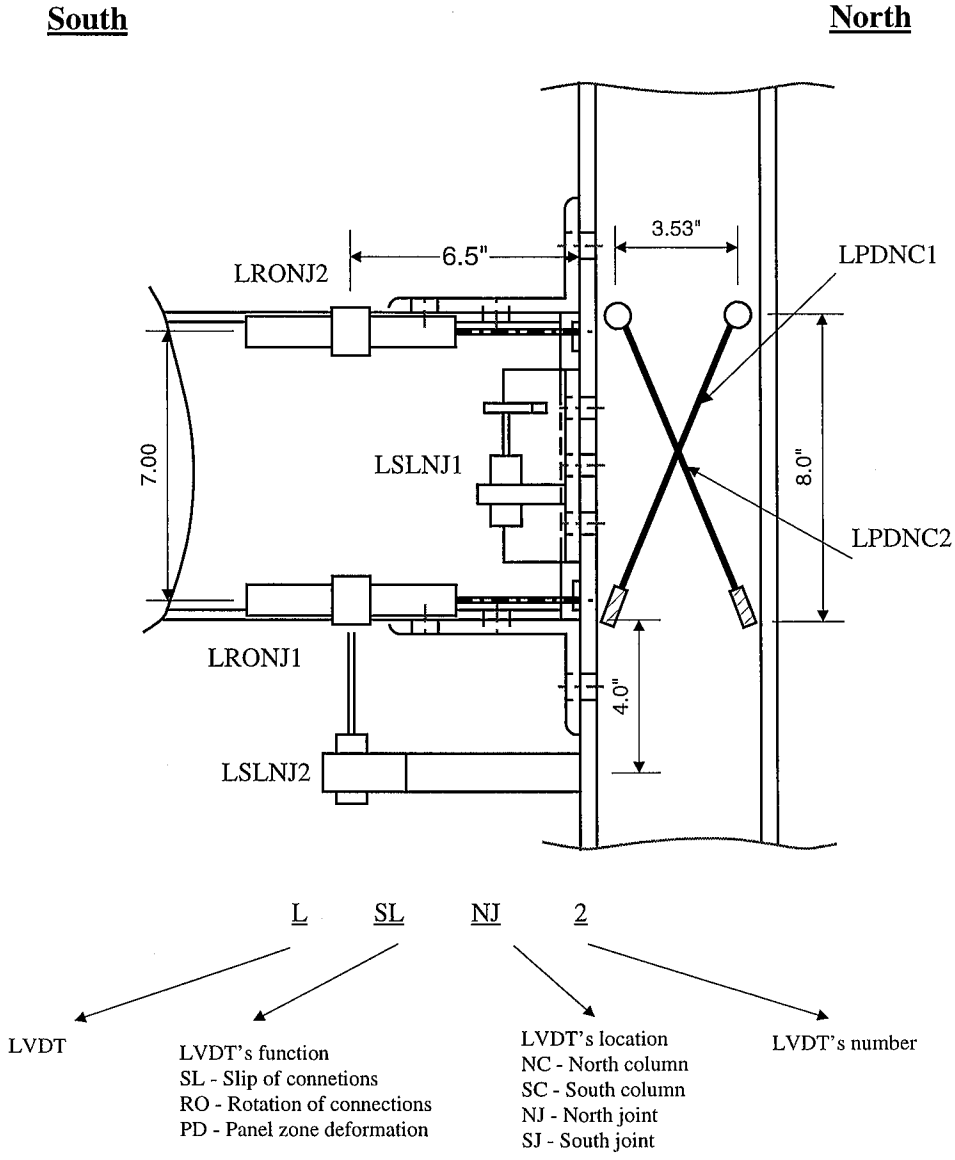

* LVDTs on the north connection region
of the middle beam-view from east side

Fig. 3.4.7 Instrumentation Plan: LVDTs in the Connection Region

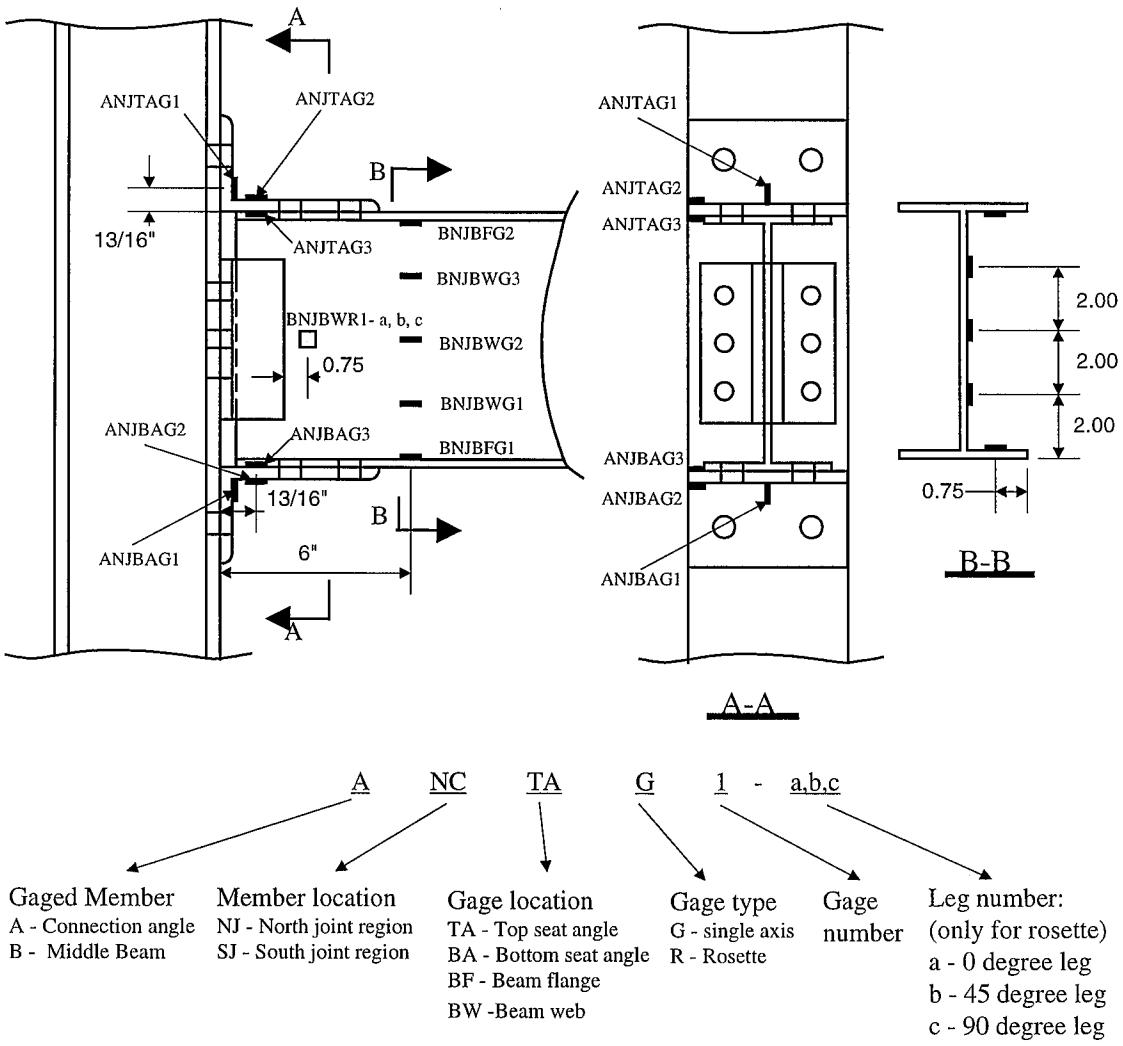

* Strain gages in the north connection region of the middle beam–view from west side

Fig. 3.4.8 Instrumentation Plan: Strain Gages in the Connection Region

3.5 Loading History

The cyclic loading history is shown in Figure 3.5.1. A total of 25 loading cycles were divided into 9 loading groups. Each group had 3 loading cycles except for the last two groups, which had 2 loading cycles each. The cyclic loading history was modified from SAC protocol for testing of steel beam-column connections and other steel specimens (SAC, 1997). In order to capture the characteristics of crack formation and

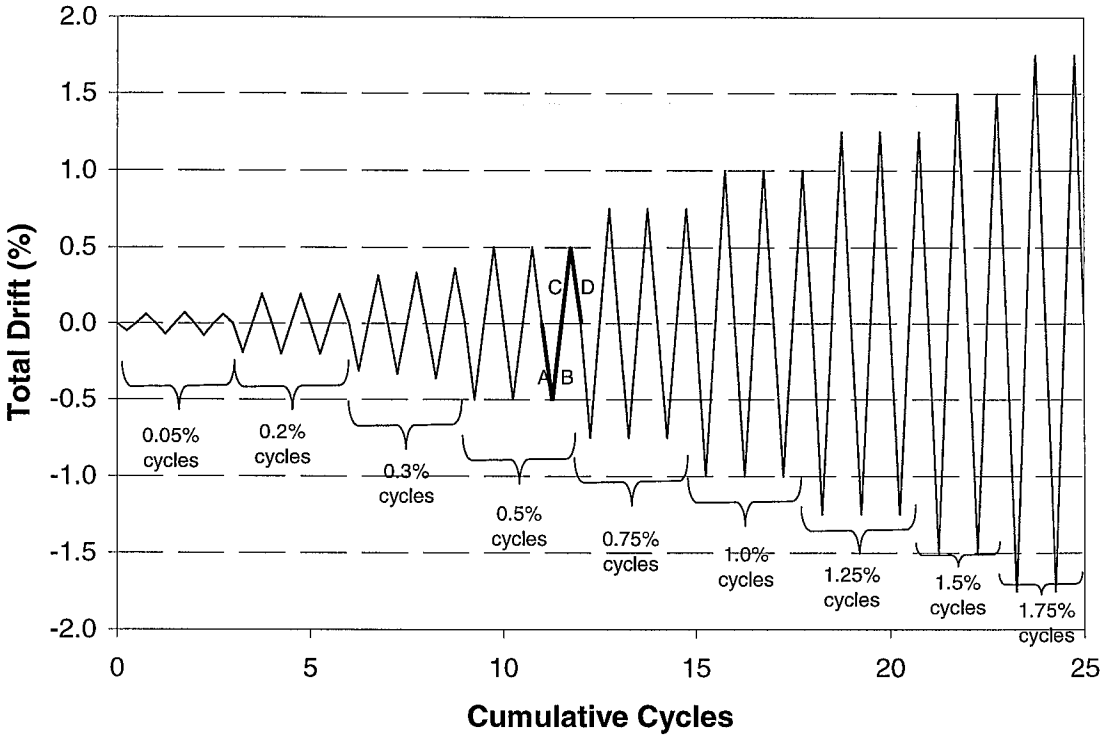

Fig. 3.5.1 Loading History

progression in the RC infill wall, 3 loading group were applied before the total drift reached 0.5%, and these first 3 loading groups was controlled by the peak lateral load, with 40 kips for Group1, 80 kips for Group 2 and 120 kips for Group 3. The loading history of the remaining 6 loading groups was controlled by the total drift of the specimen, with 0.5% for Group 4, 0.75% for Group 5, 1.0% for Group 6, 1.25% for Group 7, 1.5% for Group 8 and 1.75% for Group 9. During these 6 loading groups, the increment of the total drift was set at 0.25% instead of the 0.5% or 1% in SAC protocol (SAC, 1997) because the specimen exhibited quick change in lateral stiffness and strength in such an increment of total drift. During each loading cycle, the specimen was first loaded in the south direction, then unloaded, and then loaded in the north direction, then unloaded. The reading of the applied lateral load and lateral displacement at each story level were set to be negative when the specimen was loaded in the south direction, and positive when the specimen was loaded in the north direction.

In the following chapters, each loading group is sometimes referred to by using its the peak total lateral drift of the specimen during the first cycle of that loading group. Therefore, "0.05% cycles" represents loading group 1; "0.2% cycles" represents loading group 2; "0.3% cycles" represents loading group 3; "0.5% cycles" represents loading group 4; "0.75% cycle" represents loading group 5; "1.0% cycle" represents loading group 6; "1.25% cycle represents loading group 7; "1.5% cycles" represents loading group 8; and "1.75% cycles" represents loading group 9. Each loading cycle is named according to its corresponding loading group and the cycle number in that loading group. If necessary, one letter (A, B, C, or D) is attached to the end of the cycle name to refer a specified quarter cycle of that loading cycle. As shown in Figure 3.5.1, these four letters (A, B, C, D) represent the four quarters of each loading cycle in sequence. For example, cycle G5-3-A represents the first quarter cycle of the third cycle of loading group 5 ("0.75% cycles").

Chapter 4

General Behavior of the Specimen

This chapter reports the strength and stiffness of the specimen; describes the observed behavior of each of the component, such as the cracking and crushing of the RC infill wall, yielding of the steel frame, and fracture of the interface headed stud connectors; and evaluates the ductility and energy dissipation capacity of the specimen.

4.1 Summary of Specimen Performance

This section summarizes the performance of the specimen according to the loading history. During the 0.05% cycles, the specimen behaved approximately elastically and only a few diagonal cracks formed in the RC infill walls. During the 0.2% cycles, many more cracks formed in the infills of both stories, although no other phenomena were observed. During the 0.3% cycles, cracking of infill continued in both stories, and minor yielding occurred at the bases of both columns, in the web angles of the PR connections, and at both ends of the beams. During the 0.5% cycles, a few more cracks formed and others progressed in the infills of both stories, spalling of concrete occurred at the bottom corner of the second story, and yielding continued in the same regions of the steel members as during the 0.3% cycles. During the 0.75% cycles, the specimen reached its maximum lateral strength, no more new diagonal cracks formed, spalling of concrete at the bottom corner of the second story was more evident, moderate

yielding occurred at the bottom portions of the second story columns, and minor yielding occurred in the panel zones of the middle beam-to-column connection regions. During the 1.0% cycles, the peak strength of the specimen dropped by approximately 35% of the maximum strength of the specimen, crushing and spalling of concrete continued at the bottom corners of the second story and initiated in the top corners of the second story, yielding continued at the bottom portions of the columns in both stories, and evident deformation of the vertical legs of the PR connections was observed. During the 1.25% cycles, the peak strength of the specimen dropped to approximately 50% of the maximum strength of the specimen, more and more concrete spalled in the four corners of the second story, substantial yielding was observed in the bottom portions of the two columns in the second story, and permanent deformation occurred at the PR connections. During the remaining 1.5% and 1.75% cycles, the peak strength of the specimen stabilized at 70-80 kips, the crushing of concrete initiated in the top corners of the first story, and the existing plastic deformation of the steel members at these locations was further intensified.

4.2 Assessment of System Strength and Stiffness

The relationships of lateral load–total drift and lateral load–interstory drift are shown in Figure 4.2.1 to Figure 4.2.3. Figure 4.2.1 shows the total drift of the specimen versus the total lateral load. Figures 4.2.2 and 4.2.3 show the interstory drift of the second story versus the total lateral load, as well as that of the first story, respectively. The story height used to calculate the story drift was 48 inches for both stories.

The peak load of the first group of cycles was 40 kips. The specimen surpassed its design lateral load, which was approximately 70 kips, and reached 80 kips during the second group of cycles. The maximum lateral strength of the specimen was achieved during the first cycle of the 0.75% cycles (cycle G5-1). It was 164 kips when the specimen was loaded in the south direction and 159.5 kips when the specimen was loaded in the north direction. By this loading cycle, the drift of the second story started to dominate the overall structural response. It was nearly 1.0% at the peak of loading cycle

G5-1-C, compared to 0.4% for the first story. During the first cycle of the 1.0% cycles (cycle G6-1), the peak strength of the specimen degraded 10% when loaded in the north direction and 20% when loaded in the south direction, while the second story drift increased to 1.2% when loaded in the south direction and 1.6% when loaded in the north direction. The peak strength continued dropping during the next two loading cycles, reaching 100.9 kips in cycle G6-3-A and 90.6 kips in cycle G6-3-C. The peak strength dropped slightly during the next set of 1.25% cycles, when the maximum interstory drift of the second story surpassed 2%. Peak strength then stabilized at 70 kips in the south loading direction and 80 kips in the north loading direction during the remaining 1.5% and 1.75% cycles. Thus, at the end of the test, the strength of the specimen was close to the 70 kip design lateral load. The interstory drift of the second story surpassed 3% in the final cycle. The peak load and corresponding drift in each direction for each cycle of loading are tabulated in Table 4.2.1.

Two types of lateral stiffnesses from the load-interstory drift curve are defined herein to characterize structural behavior. The first definition, called the "equivalent

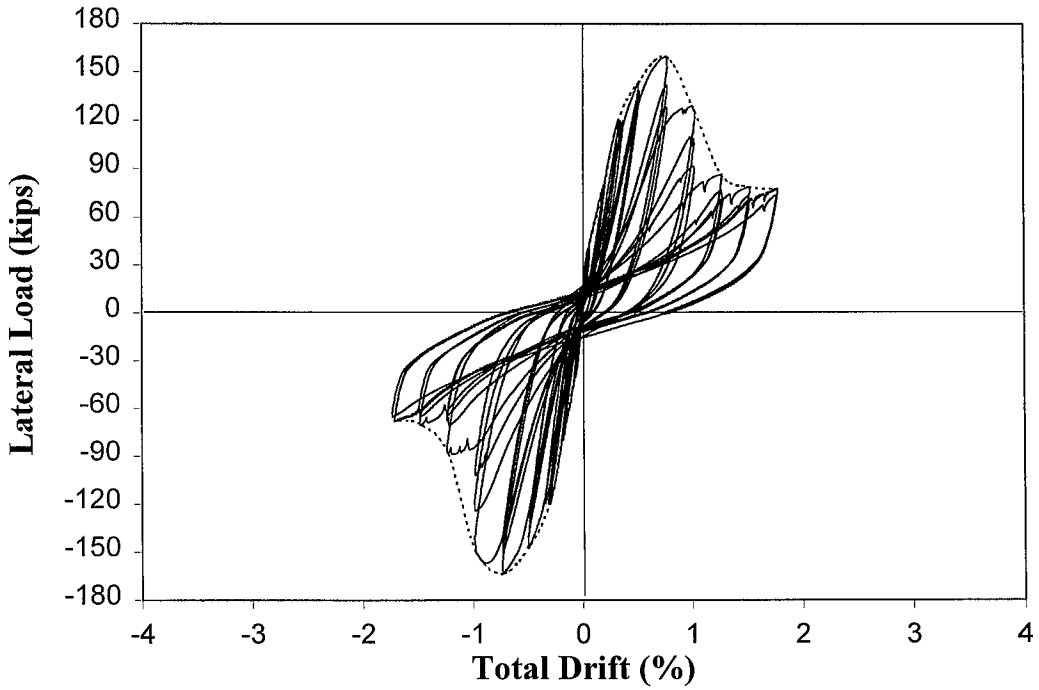

Fig. 4.2.1 Total Drift versus Lateral Load of the Specimen

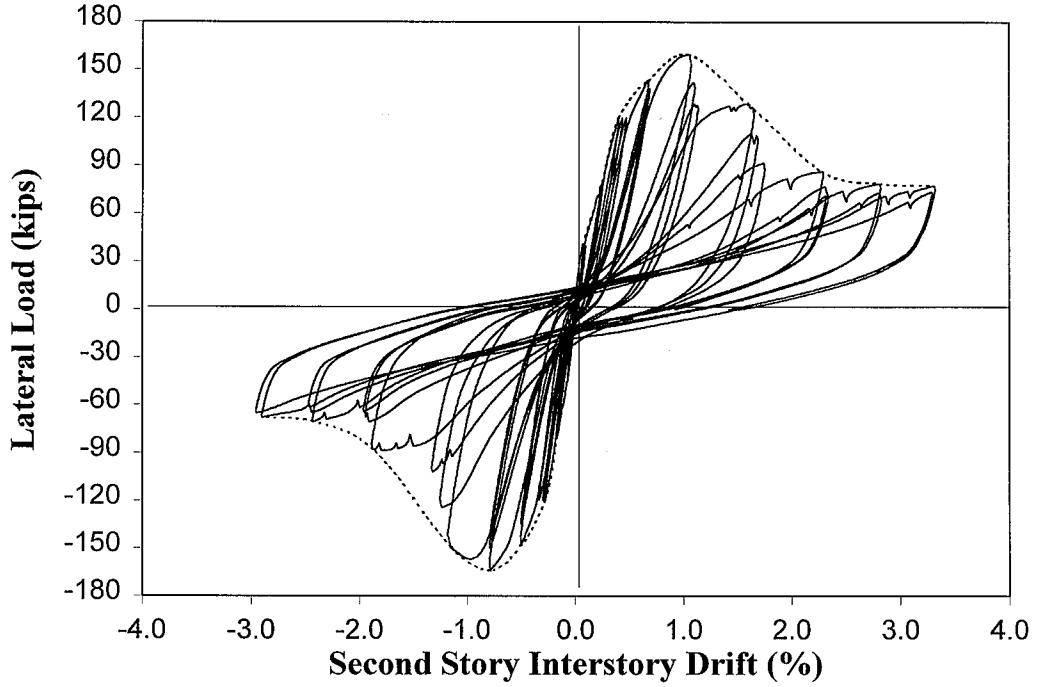

Fig. 4.2.2 Second Story Interstory Drift versus Lateral Load of the Specimen

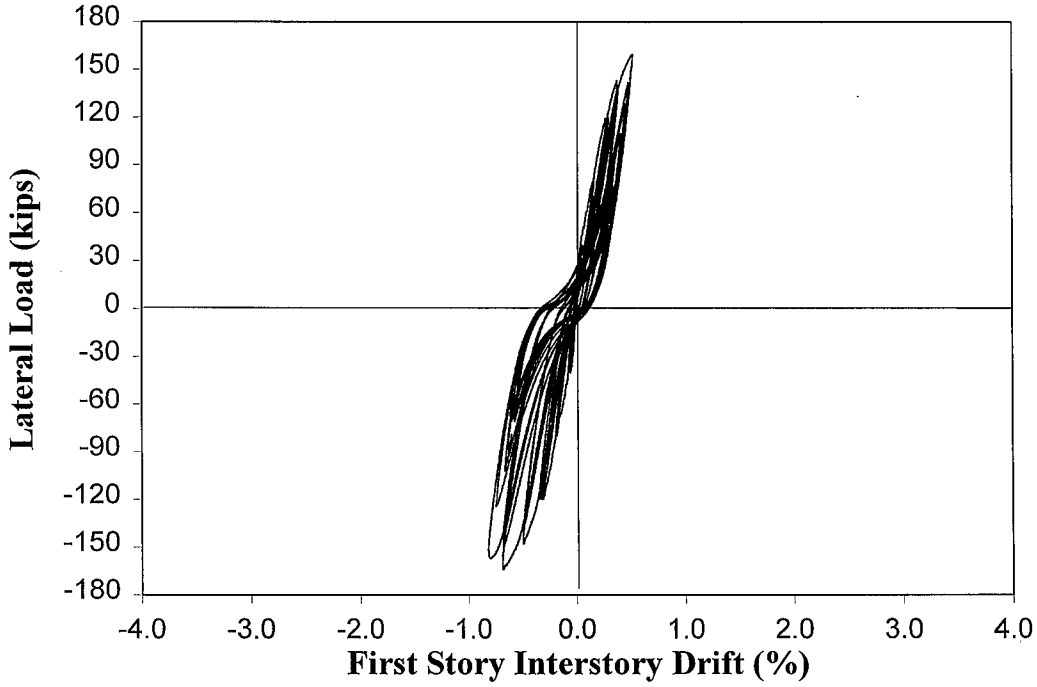

Fig. 4.2.3 First Story Interstory Drift versus Lateral Load of the Specimen

Table 4.2.1 Peak Load and Drifts for Each Cycle

Loading Group	Cycle No	South				North			
		Peak Load (kips)	Total Drift (%)	First Story Inter-story Drift (%)	Second Story Inter-story Drift (%)	Peak Load (kips)	Total Drift (%)	First Story Inter-story Drift (%)	Second Story Inter-story Drift (%)
0.05% cycles (40 kips)	G1-1	-39.2	-0.05	-0.042	-0.063	39.5	0.07	0.049	0.082
	G1-2	-39.6	-0.04	-0.066	-0.018	39.5	0.04	0.055	0.017
	G1-3	-39.0	-0.08	-0.073	-0.081	38.9	0.06	0.05	0.069
0.2% cycles (80 kips)	G2-1	-78.6	-0.18	-0.179	-0.186	78.7	0.19	0.166	0.219
	G2-2	-78.5	-0.20	-0.171	-0.229	78.9	0.19	0.168	0.206
	G2-3	-78.5	-0.21	-0.182	-0.228	79.1	0.19	0.174	0.206
0.3% cycles (120 kips)	G3-1	-118.0	-0.31	-0.297	-0.332	118.7	0.31	0.279	0.347
	G3-2	-118.4	-0.33	-0.314	-0.342	118.5	0.34	0.296	0.377
	G3-3	-118.3	-0.36	-0.332	-0.387	118.8	0.37	0.308	0.423
0.5% cycles	G4-1	-145.9	-0.50	-0.481	-0.527	141.7	0.51	0.389	0.627
	G4-2	-133.3	-0.50	-0.465	-0.534	137.2	0.52	0.396	0.646
	G4-3	-128.6	-0.49	-0.466	-0.523	128.7	0.51	0.384	0.632
0.75% cycles	G5-1	-164.0	-0.76	-0.673	-0.841	159.5	0.77	0.52	1.024
	G5-2	-147.7	-0.74	-0.666	-0.82	140.2	0.77	0.487	1.051
	G5-3	-142.0	-0.75	-0.667	-0.826	126.7	0.77	0.459	1.084
1.0% cycles	G6-1	-156.9	-1.02	-0.804	-1.234	128.8	1.03	0.469	1.585
	G6-2	-122.6	-1.01	-0.729	-1.298	110	1.02	0.417	1.622
	G6-3	-99.1	-1.02	-0.653	-1.379	90.3	1.03	0.364	1.701
1.25% cycles	G7-1	-88.5	-1.28	-0.618	-1.938	85.5	1.29	0.353	2.227
	G7-2	-70.6	-1.27	-0.561	-1.988	70.6	1.30	0.324	2.281
	G7-3	-63.2	-1.27	-0.542	-2.003	70.6	1.29	0.316	2.258

stiffness", is the slope of the line joining the peak strength and the point where the curve crosses the X-axis, as shown in Figure 4.2.4 (i.e., zero load, but, in general, nonzero displacement). The second definition, called the "peak-to-peak stiffness", is the slope of the line connecting the positive peak and the negative peak of the same loading cycle. These values are shown in Table 4.2.2. Since the drift of the second story assumed an increasingly dominant role in the overall structural response by the 0.75% loading cycles

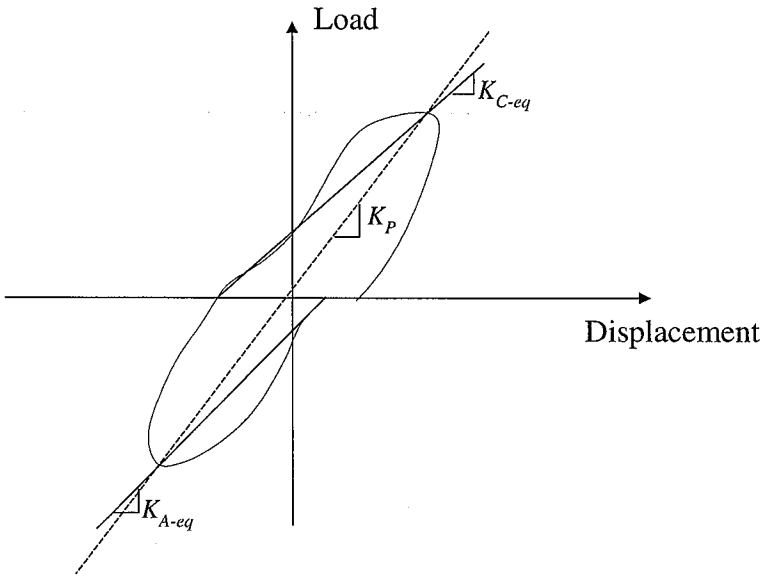

Fig. 4.2.4 Definition of Stiffnesses

Table 4.2.2 Lateral Stiffness of the Second Story

Loading Group	Cycle No.	Equivalent Stiffness $K_{A\text{-}eq}$ (kips/inch)	Equivalent Stiffness $K_{C\text{-}eq}$ (kips/inch)	Peak-to-Peak Stiffness K_P (kips/inch)
0.05% cycles (40 kips)	G1-1	1276	1069	1233
	G1-2	1130	935	1070
	G1-3	1003	953	1027
0.2% cycles (80 kips)	G2-1	900	610	786
	G2-2	708	637	756
	G2-3	720	636	751
0.3% cycles (120 kips)	G3-1	771	579	726
	G3-2	676	538	676
	G3-3	601	482	611
0.5% cycles	G4-1	531	371	511
	G4-2	440	370	476
	G4-3	436	364	463
0.75% cycles	G5-1	388	261	358
	G5-2	283	234	317
	G5-3	270	210	291
1.0% cycles	G6-1	254	134	232
	G6-2	131	117	169
	G6-3	102	87	128
1.25% cycles	G7-1	72	58	89
	G7-2	52	50	70
	G7-3	47	51	65

(see Figures 4.2.2 and 4.2.3), the stiffness was largely that of the second story thereafter. Thus, Table 4.2.2 only shows the stiffness of the second story at each loading cycle, where $K_{A\text{-}eq}$ is the equivalent stiffness of loading quarter cycle A of each cycle and $K_{C\text{-}eq}$ is the equivalent stiffness of loading quarter cycle C of each cycle. As seen from the table, $K_{A\text{-}eq}$ and $K_{C\text{-}eq}$ are not symmetric, with stiffness in the first loading direction, $K_{A\text{-}eq}$, almost always larger than that of the second loading direction, $K_{C\text{-}eq}$. This indicates that the damage from the loading process in one direction always degraded the stiffness in the other direction. Until the 1.25% drift cycles, the equivalent stiffness decreased faster in the north loading direction than in the south loading direction. This explains why the equivalent stiffness $K_{A\text{-}eq}$ had a closer value to the peak-to-peak stiffness K_p than did the equivalent stiffness $K_{C\text{-}eq}$. Figure 4.2.5 shows the relationship between the average second story drift and the peak-to-peak stiffness. In Figure 4.2.5, the average second story drift is the average value of the drifts in the two directions for each loading cycle. The peak-to-peak stiffness is normalized by the peak-to-peak stiffness of the first loading cycle G1-1.

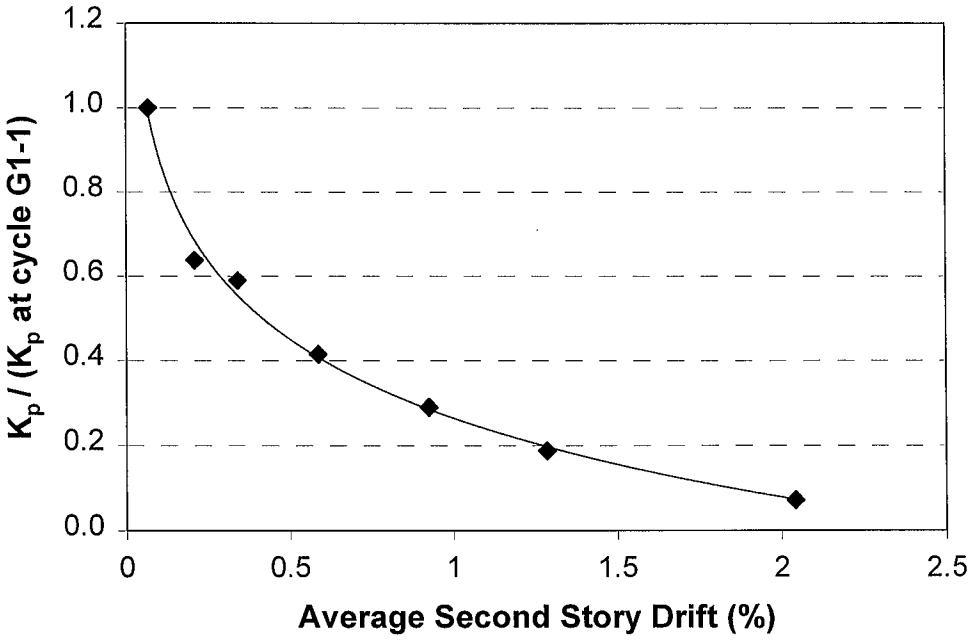

Fig. 4.2.5 Relationship Between Second Story Drift and Lateral Stiffness

Only results of the first cycle of each loading level are plotted in the figures to capture the variation of the peak-to-peak stiffness along the envelope of the hysteretic load-drift curve. It can be seen that the rate of decrease of the peak-to-peak stiffness diminished with the increase of average story drift. The stiffness K_p quickly dropped almost 60% from loading cycle G1-1 (0.07% average interstory drift) to G4-1 (0.59% average interstory drift), but only deceased another 20% from loading cycle G4-1 to G6-1 (1.29% average interstory drift).

4.3 Cracking and Crushing of Reinforced Concrete Infill Walls

This section summarizes the progression of the cracking and crushing in the RC infill walls. Figure 4.3.1 shows the crack patterns of the RC infill wall after each group of cycles. The shadowed areas in the figures are the locations where the concrete spalled and fell off during the test.

Only a few cracks formed in both stories during the first cycle of the 0.05% cycles, The majority of the cracking occurred during the 0.2% cycles, 0.3% cycles and 0.5% cycles, particularly during the first cycle of each group of cycles. As seen from Figure 4.3.1.(b) to (c), some of the cracks were the extensions of the tips of those cracks formed in previous loading cycles, and some were new occurrences during these three groups of cycles. Most of the cracks were through-cracks and were oriented at approximately ± 45° to a horizontal line, indicating that the cracking was primarily induced by shear force in the infill wall. The cracks that were oriented at approximately – 45° to a horizontal line formed and opened when the specimen was loaded in the south direction, and the cracks that were oriented at approximately + 45° to a horizontal line formed and opened when the specimen was loaded in the north direction. The widths of crack openings were small but were not recorded.

The spalling of the concrete at the bottom corner regions in the second story was first observed during loading cycle G4-2 (the second cycle of the 0.5% cycles). It was more evident when the specimen reached its maximum strength during loading cycle G5-1. This damage was the combined result of tensile ripping in one loading direction,

followed by the compressive crushing in the reverse direction. As seen in Figure 4.3.2, the tensile ripping was caused by the combined shear force from beam studs and tensile force from the column studs. The shear force from the beam studs, which transferred the lateral load from the infill wall to the middle beam, tended to break the corner concrete out (Figure 3.1.4.(c)). The tensile force from the column studs was associated with the deformation incompatibility between the steel column and the infill panel. Because there was a discontinuity of the reinforcing cages in the corners (i.e., no ties between the vertical reinforcing cages and the horizontal reinforcing cages in the corner region, and the longitudinal reinforcement of the top and bottom horizontal cages terminated at this location), cracking was initiated there and extended upwards into the infill wall due to the increasing shear force of the corner beam studs and the increasing tensile force developing between the column studs and the infill wall. Figure 4.3.3 shows the crack opening at the north-bottom corner of second story infill, when the specimen was loaded in the south direction during loading cycle G5-1.

During the 1.0% cycles, several short splitting cracks formed and expanded in one bottom corner region of the second story (i.e., the south corner region when the specimen was loaded in the south direction and north corner region when the specimen was loaded in the north direction), resulting in continued crushing and spalling of concrete in that region. Simultaneously, the vertical crack in the other bottom corner region of the second story opened to a width of 0.5 inches due to the tensile ripping force and did not fully close upon load reversal. At the same time, concrete spalling in the top corners of the second story was initiated. The severe disruption in the bottom corner regions might be responsible for the quick drop of lateral strength during the 1.0% cycles,

During the next 1.25% cycles, as seen in Figure 4.3.1.(g), the vertical cracks extended from the bottom corner region further up into the middle of the column-infill wall interfaces of the second story. More of the concrete crushed and spalled in the four corners of the second story. Figures 4.3.4 and 4.3.5 show the pictures of the north-bottom corner region and the south-bottom corner region in the second story after the 1.25% cycles, respectively. It can be observed that the hoops of the vertical reinforcement cages

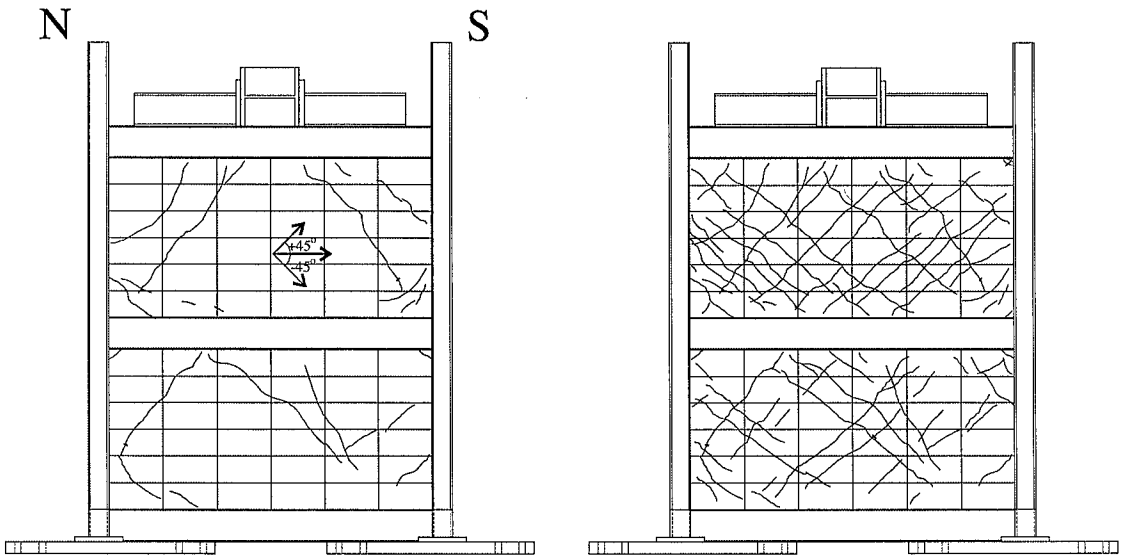

a) 0.05% Cycles

b) 0.2% Cycles

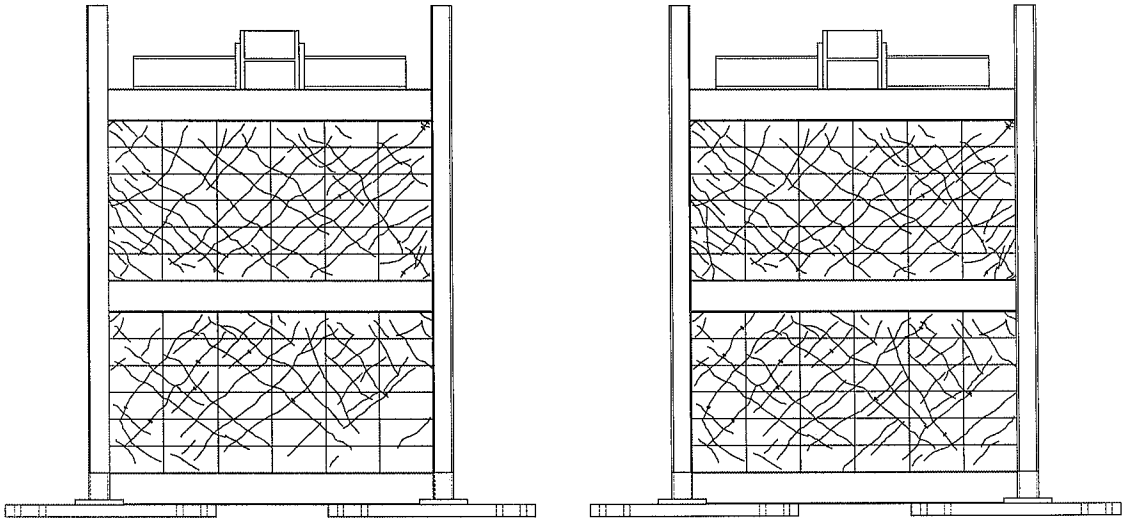

c) 0.3% Cycles

d) 0.5% Cycles

Fig. 4.3.1 Cracking Patterns of RC Infill Wall in Specimen

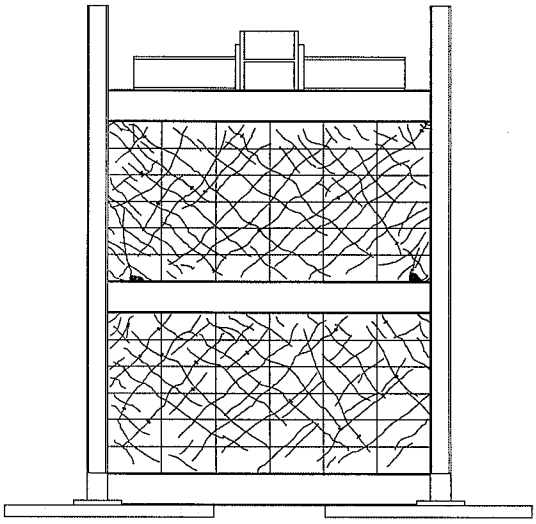

e) 0.75% Cycles

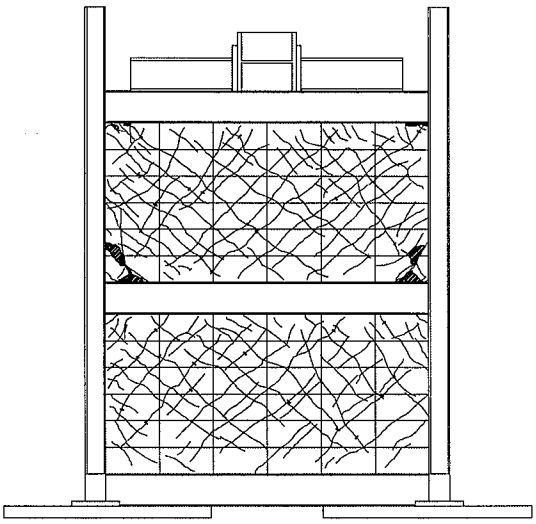

f) 1.0% Cycles

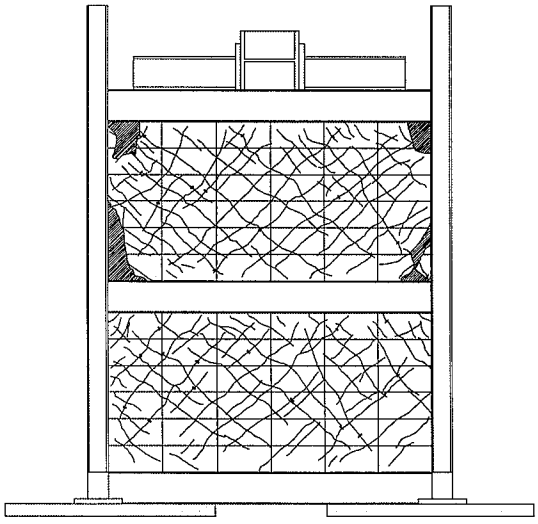

g) 1.25% Cycles

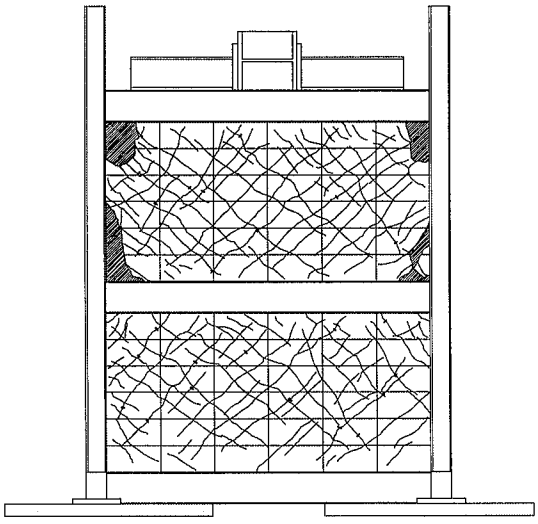

h) 1.5% Cycles

Fig. 4.3.1 (continued) Cracking Patterns of RC Infill Wall in Specimen

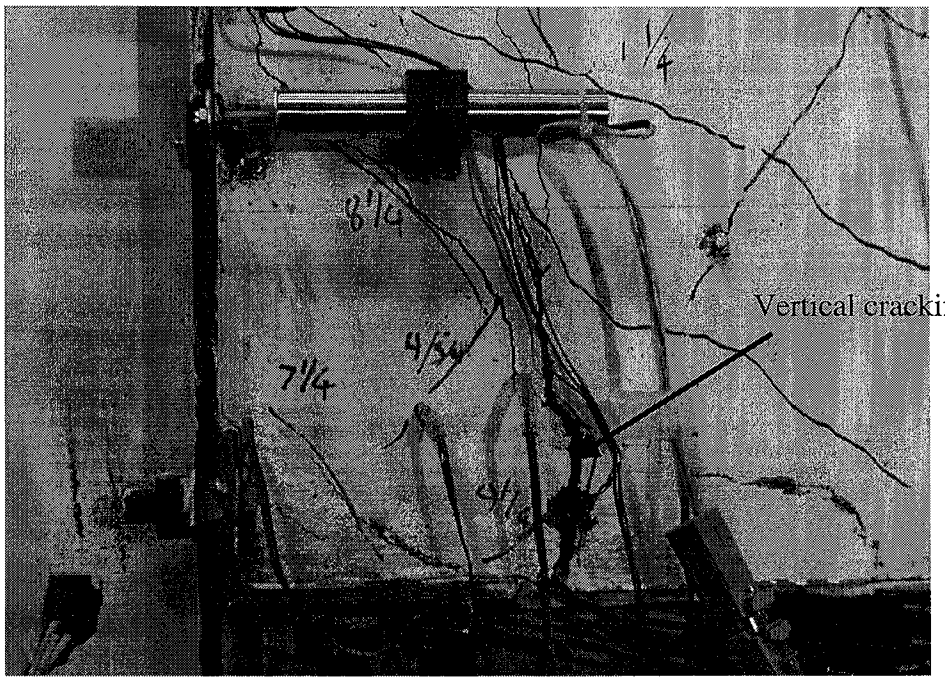

Fig. 4.3.3 Cracking in the North-Bottom Corner of the Second Story
at Peak Load of Cycle G5-1-A

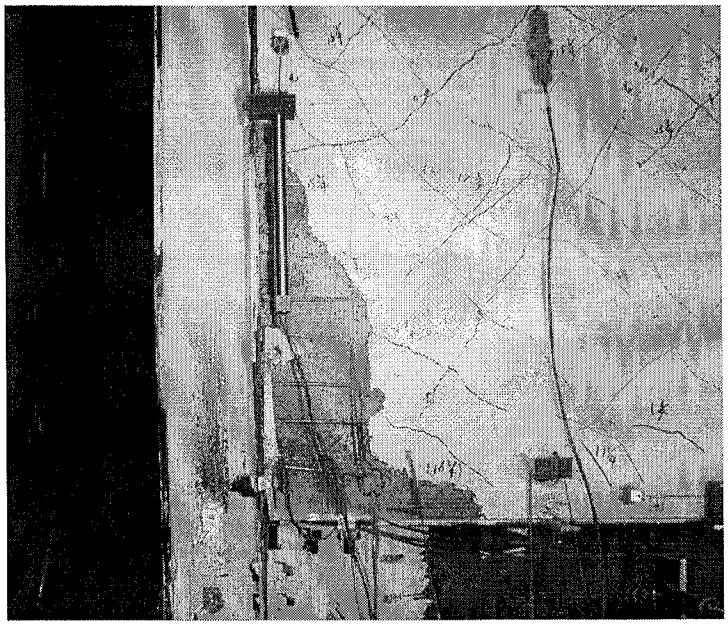

Fig. 4.3.4 North-Bottom Corner Region of Second Story after 1.25% Cycles

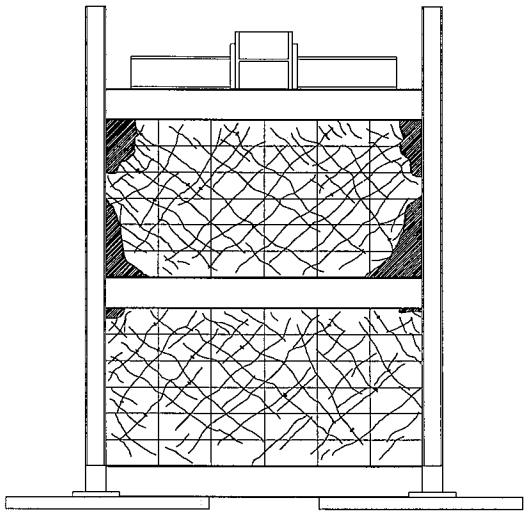

i) 1.75% Cycles

Fig. 4.3.1 (continued) Cracking Patterns of RC Infill Wall in Specimen

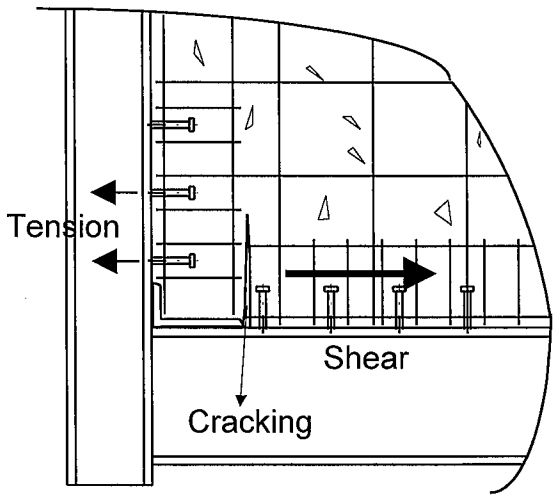

Fig. 4.3.2 Mechanism for Tensile Ripping

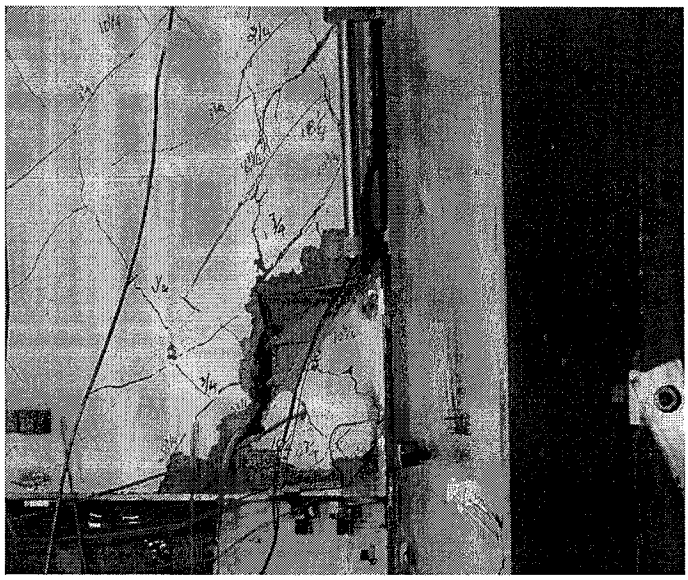

Fig. 4.3.5 South-Bottom Corner Region of Second Story after 1.25% Cycles

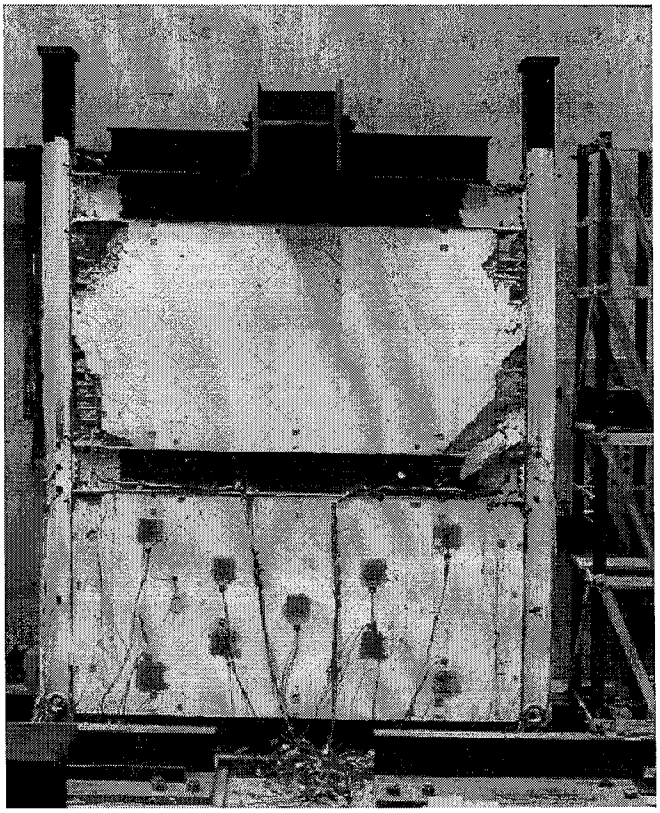

Fig. 4.3.6 View of the Specimen after Testing

bent out and yielded due to high compressive force in the concrete. In the bottom portion of the north interface of the second story, some concrete inside the reinforcement cage had fallen off.

The spalling and crushing concrete in the second story continued during the remaining 1.5% and 1.75% cycles. Minor crushing of the concrete was also observed in the top corner regions in the first story by the 1.5% cycles. Figure 4.3.6 shows the entire specimen after testing. It can be seen that, along the column-infill wall interfaces of the second story, the majority of concrete in the reinforcement cages had been crushed and fell out, except for a small portion of concrete in the middle that remained intact. This indicated that the composite structural system was close to a bare steel frame in the second story towards the end of the test.

4.4 Yielding of Steel Frame

This section summarizes the progression of the yielding in the steel members based on the location and appearance of the yield lines and the deformation of the steel frames. A few yield lines were first observed to appear on the stiffened bottom portion of the steel column after the first cycle of the 0.3% cycles (cycle G3-1). As shown in Figure 4.4.1, the yield lines on the outside surface of the column flange intersected each other at 45°, and apparently were caused by either tensile or compressive axial force along the flange. The yield lines on the web were approximately vertical and horizontal, largely due to the shear force in the column web. After the 0.3% cycles, several thin yield lines were found on all eight of the web angles of the PR connections, as well as at both ends of the middle and top beams. Although the number of the yield lines in the column base regions and at the ends of middle and top beams increased slightly during the 0.5% cycles, the amount and the appearance of these yield lines indicated that the yielding in steel frame was minor, and thus essentially negligible before the specimen reached its peak strength.

During the 0.75% cycles, new yield lines started to appear on the column flanges in the connection regions of the middle beam, and those yield lines intersected each other

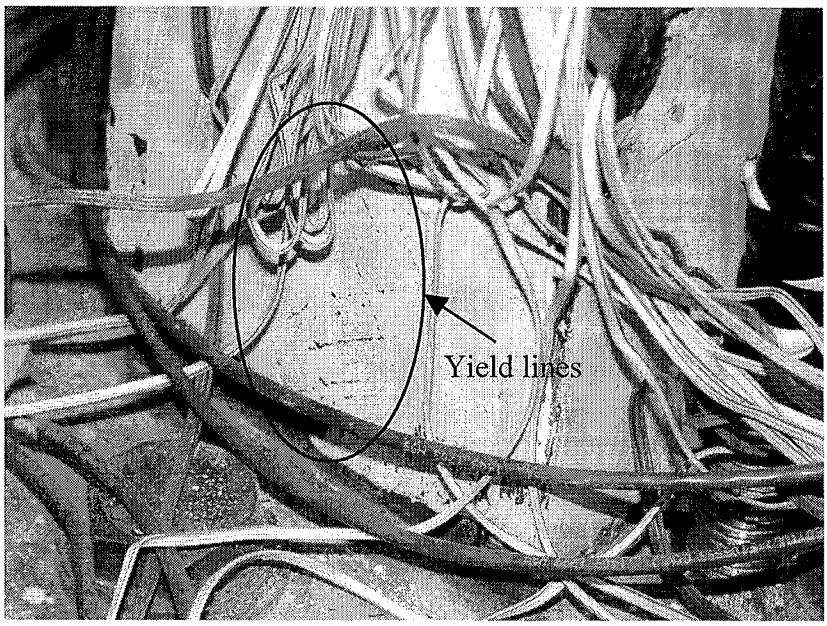

Fig. 4.4.1 Yield Lines on the Bottom Portion of the North Column Flange after Cycle G3-1

at 45°. At the same time, both horizontal and vertical yield lines appeared on the steel webs at the bottom portions of the second story columns. Figure 4.4.2 shows the yield lines in the north connection region of the middle beam after the 0.75% cycles. Moderate yielding thus had occurred at the center of the column web in this region, and minor yielding had occurred at the center of the panel zone.

During the 1.0% cycles, more yield lines appeared on the bottom portions of the second story columns, on both the flanges and the webs. After the first cycle of the 1.0% cycles, the bottom portion of the south column bent out slightly with permanent plastic deformation, but the bottom portion of the north column had much less permanent deformation. The vertical leg of the top and seat angles of the south connection deformed when the specimen was loaded in the south direction, and the vertical leg of the top and seat angles of the north connection deformed when the specimen was loaded in the north direction. Yield lines were observed along the k-lines of the web angles after these cycles, as well as along the locations of the high strength bolts that connected the web angles to the column flanges.

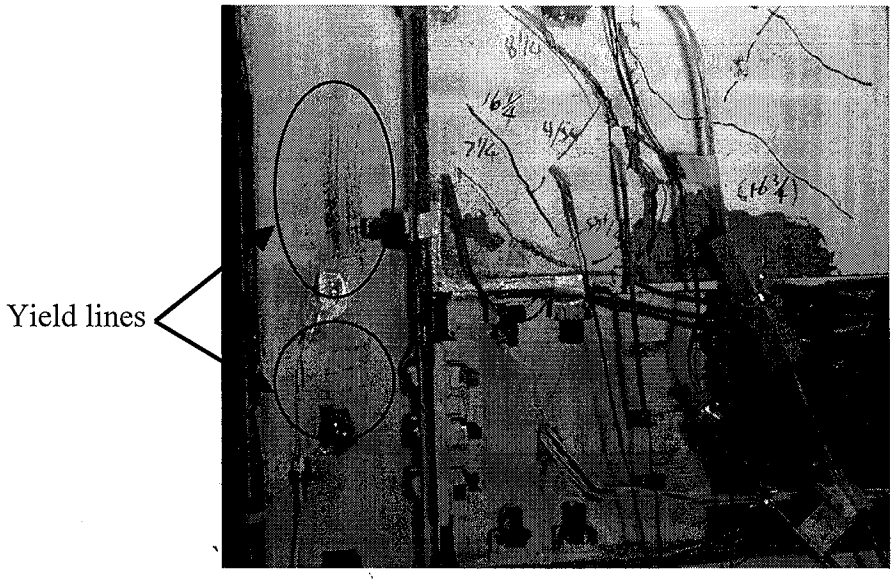

Fig. 4.4.2 Yield Lines in the North Connection Region of the Middle Beam after the 0.75% Cycles

During the 1.25% cycles, the steel frame started to show substantial yielding in the bottom portions of both steel columns in the second story. Permanent deformation occurred to the angles of the PR connections of both the middle and the top beams. The plastic deformation at these locations of the steel members were intensified during the remaining 1.5% and 1.75% cycles. Figure 4.4.3 shows the north bottom portion of the steel frame in the second story after the concrete infill wall was removed after the test. It can be seen that the bottom portion of the north columns in the second story was significantly bent out and that the vertical leg of the top and seat angles was pulled away from the column flanges.

4.5 Failure of Headed Stud Connectors

4.5.1 Post-Test Inspection of the Headed Studs

After testing, the concrete around each headed stud was carefully removed to inspect the status of each stud. It was found that a number of the headed studs failed by fracture at the stud base during the test. The locations of all fractured studs are shown in

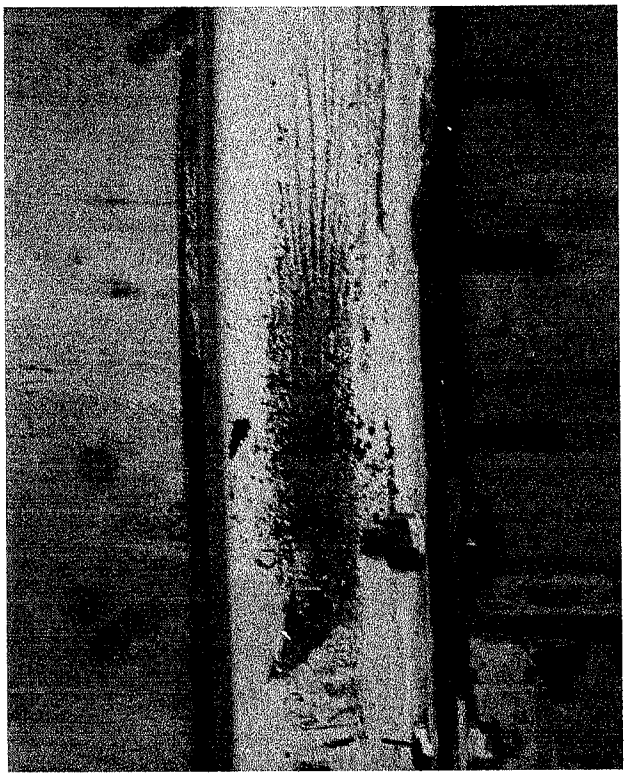

Fig. 4.4.3 Bottom Portion of the North Column in the Second Story after Testing

Figure 4.5.1. All studs along the top interface of the second story failed by fracture except that the first stud at the south end of the beam remained intact after the test. All studs along bottom interface of the second story failed by fracture. All studs along the top interface of the first story failed by fracture except that the one located at each end of the beam remained intact after the test. Along the bottom interface of the first story, ten studs located in the north portion failed by fracture. Although the concrete in the corner regions of the second story was severely crushed and the concrete in the corner regions of the first story was lightly crushed, the concrete along the beam-infill wall interfaces only had a few cracks and was still well confined by the reinforcement cages after the test. In contrast to the studs along the beam–infill wall interfaces, all studs along the column–infill wall interfaces remained intact during the test. However, for the studs along the column–infill wall interfaces in the second story, the surrounding concrete severely cracked and spalled.

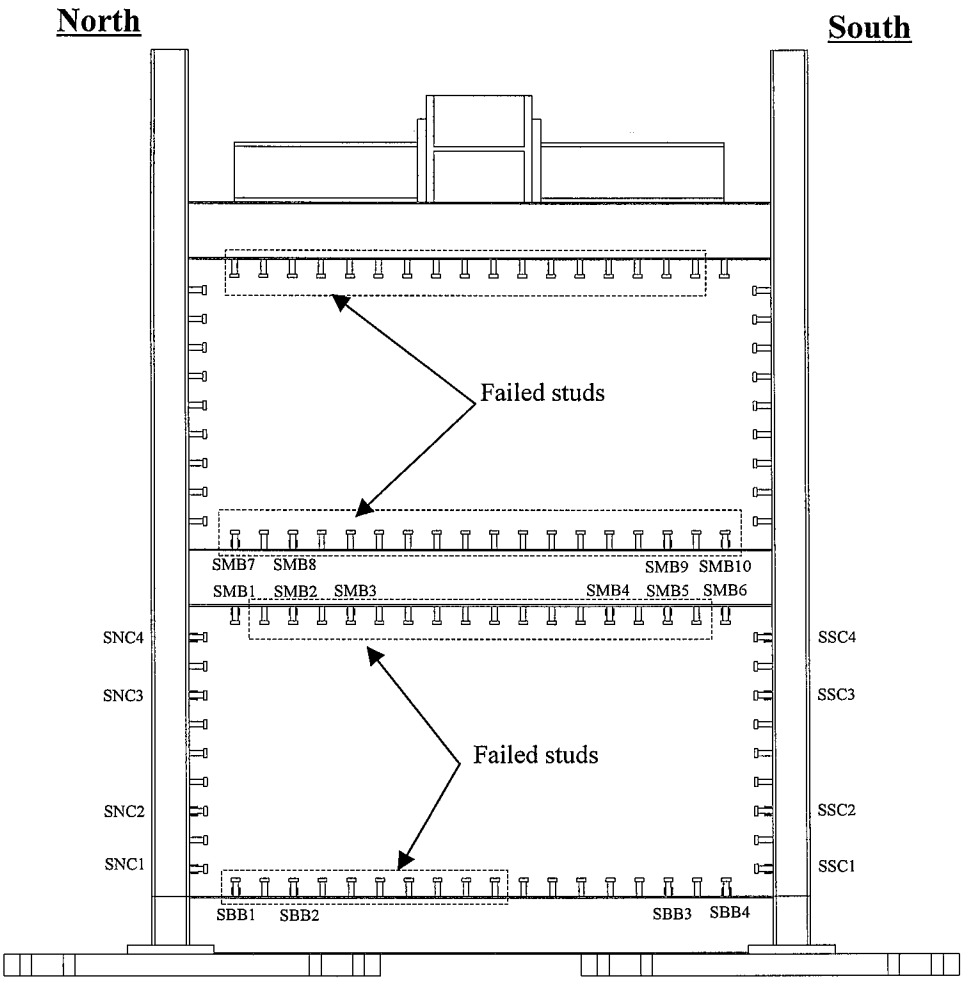

Fig. 4.5.1 Location of Fractured Studs

The failed studs had two different fracture shapes at their bases. Almost all the failed studs along the bottom interfaces of both stories had a flat fracture surface right at their bases, as shown in Figure 4.5.2. Although part of the surface was found to be shiny due to continued rubbing along the fractured surface after the stud failed, dimples existed in the remaining part of the surface. This indicated that the fracture of the studs along the bottom interfaces of both story was ductile. Almost all the failed studs along the top interfaces of both stories fractured just above the weld collar, and had either a concave surface or a convex surface, as shown in Figure 4.5.3. This fractured surface shape indicated that the studs along the top interface underwent larger deformation than the

studs along the bottom interface and appeared to be more ductile. The two different fracture types of the failed studs may be related to the interface conditions of either story. First, a thin layer of the concrete along the top surface of the infill wall tended to be weaker due to the casting procedure so that the concrete surrounding the base of the studs along the top interface could be crushed earlier than the concrete along the bottom interface. Furthermore, a small gap might have existed along the top interface due to concrete shrinkage. As a result, the section just above the weld collar would become the critical section. In contrast, the studs along the bottom interface were well confined by the concrete, so that the critical section was at the very base of the weld bead of the studs.

4.5.2 Audible Events

A series of loudly audible events (i.e., bangs) were recorded during most of the loading cycles. It was reasoned that these bangs were the result of a sudden low-cycle fatigue fracture of the headed studs, since all the bolted connections in the specimen and in the reaction frame were designed and installed as slip-critical connections and no slip was observed during the test at critical locations. Furthermore, other reasons for the bangs, while possible, were unlikely.

The recorded number of bangs was 46, fewer than the total number of fractured studs, which was 61. Thus it is clear that some of the stud failures did not make a loudly audible noise, or that more than one stud failed simultaneously, or nearly so, such that only one bang was identified. The load levels and story drifts of seven bangs were not recorded. Figure 4.5.4 shows the mapping of the 39 other bangs onto the lateral load–second story interstory drift curve and Figure 4.5.5 shows the mapping of these bangs onto the lateral load–first story interstory drift curve. Several tentative conclusions can be drawn from the two figures:

1) Approximately 26 studs failed before the specimen reached its maximum strength in cycle G5-1, if 6 of 15 inaudible fractures (having the same ratio as 20 out of 46 loudly audible fractures) were assumed to occur before the specimen reached its maximum strength. In reaching this conclusion, the ratio of inaudible stud failures before

peak load to the total (15) was assumed to be equal to the ratio of audible stud failures before peak load to the total (46).

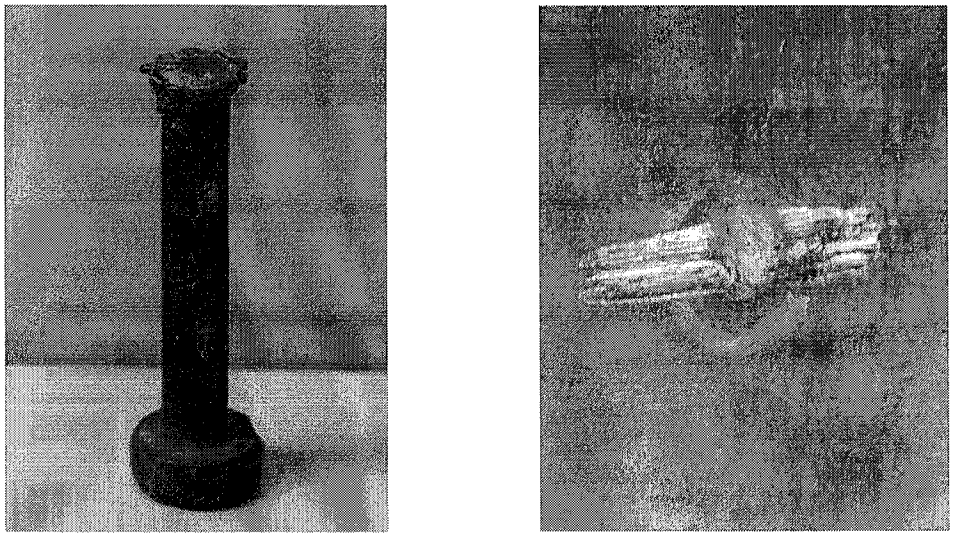

Fig. 4.5.2 Fracture Shape of the Studs along the Bottom Interfaces

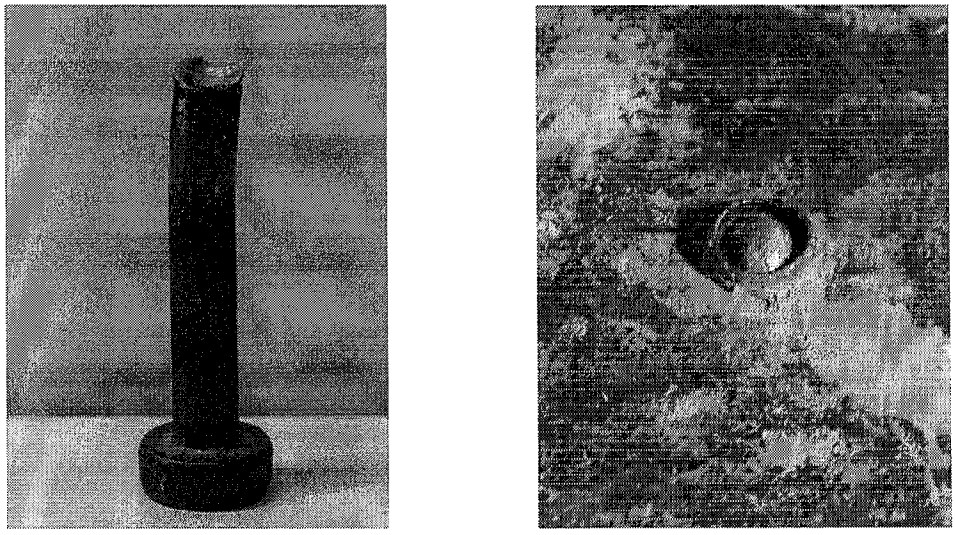

Fig. 4.5.3 Fracture Shape of the Studs along the Top Interfaces

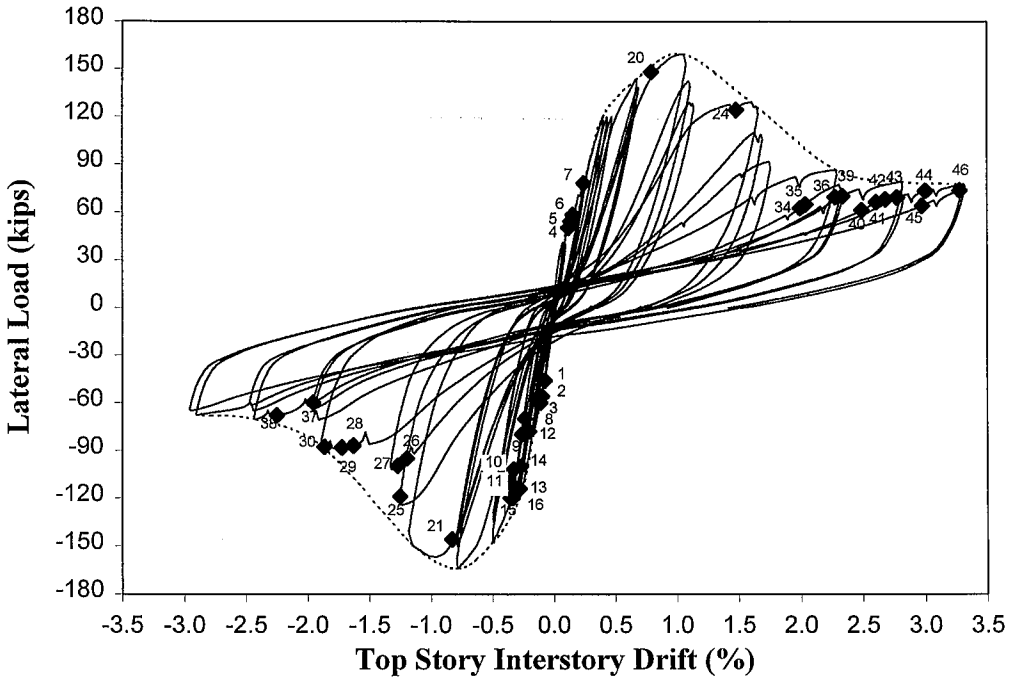

Fig. 4.5.4 Mapping of Audible Events onto the Load-Second Story Interstory Drift Curve

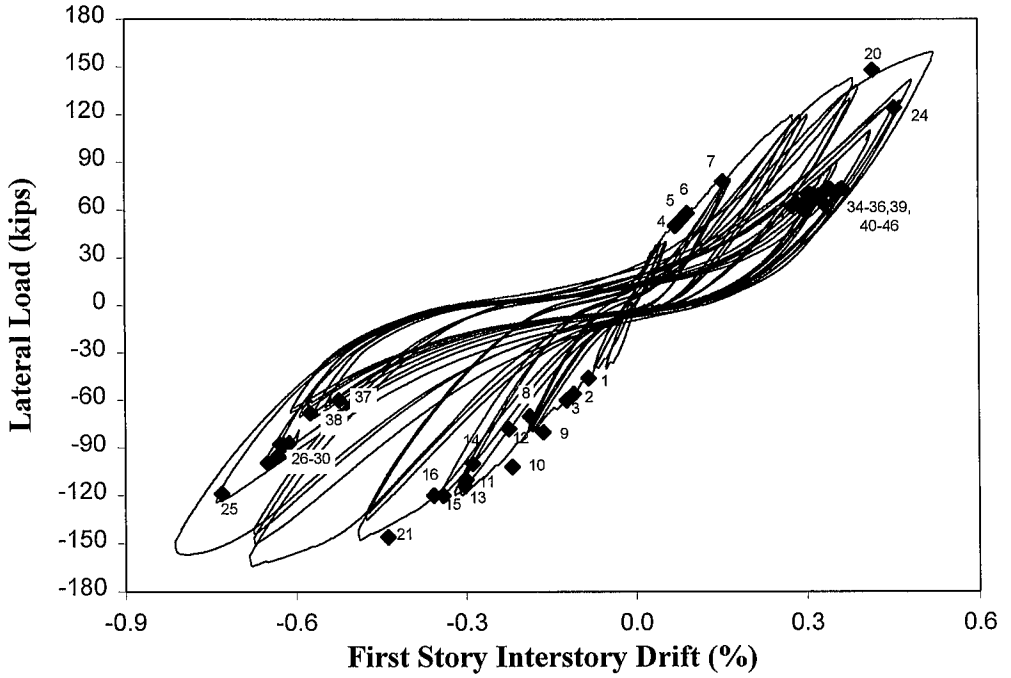

Fig. 4.5.5 Mapping of Audible Events onto the Load-First Story Interstory Drift Curve

2) Approximately 60% of the failures of studs (36 of 61) occurred by the end of the 1.0% cycles, which is partially responsible for the quick decrease in the specimen lateral strength after maximum value was reached during the first cycle of the 0.75% cycles.

3) The remaining studs failed by the 1.25% cycles and had little effect on the lateral strength of the specimen. The majority of these studs were likely along the beam-infill wall interface of the first story since the lateral strength of the specimen was largely controlled by the deterioration of the second story.

4.6 Evaluation of Ductility

There are a variety of ways to assess system and component ductility of structural systems. One typical index to measure the ductility of a structure is defined as follows:

$$\mu = \frac{\Delta_u}{\Delta_y} \tag{4.6.1}$$

where Δ_u is the displacement corresponding to a specified value of post-peak strength degradation. For example, the displacement at which the degraded strength reaches 85% of the maximum strength of the structure is often defined as the drift or deformation capacity, Δ_u. The displacement Δ_y corresponds to the limit where yielding of structures occurs. It should be noted that displacement is a general term in context. It can refer to drift, rotation, strain, etc. In addition, for a concrete structure or a structure with major concrete components, the relationship between the increasing applied force and the induced displacement is typically nonlinear from the initiation of loading. Therefore, a method of linear approximation has to be used to define reasonable values of the yield displacement, Δ_y.

Figure 4.6.1 shows the envelope of the lateral load–total drift relationship of the specimen, together with an idealized elastic–plastic approximation of this relationship. The breakpoint (pseudo-yield point) in the idealized bilinear approximation was established in accordance with two criteria. First, the envelopes for the drift versus lateral load curves (see Figures 4.2.1 and 4.2.2) show that a large decrease in tangent stiffness

occurred at the peak of the 0.3% cycles, indicating that this point can be regarded as the beginning of full yielding of the specimen. Therefore, it is assumed that the idealized yield strength F_y is approximately the average of the peak values for the 0.3% cycles and the maximum strength of the specimen, F_{max}. As a result, F_y is taken as 85% of the maximum strength of the specimen F_{max}. Second, the effective lateral stiffness corresponding to the elastic range is taken as a secant to the capacity curve at a lateral force equal to $0.6F_y$, the same as that defined in FEMA 273 (FEMA, 1997).

It is reasonable to define the point where the effective stiffness line intersects with the actual response curve of the specimen as the limit state of "elastic" response of the specimen. Therefore, the lateral force at the limit state of the "elastic" response of the specimen, where significant yielding of the structure occurs (NEHRP, 1997), is taken as $0.6F_y$. Figure 4.6.1 shows that the lateral force at the "elastic" limit state was accordingly specified as 83.5 kips in the south loading direction and 81.3 kips in the north loading direction. The total drift at yielding, Δ_y, was 0.32% in the south direction and 0.35% in the north direction. The drift capacity, Δ_u, was 1.02% in the south direction and 0.96% in the north direction. The corresponding ductility index, μ, was 3.19 in the south direction and 2.77 in the north direction.

It is also useful to examine the ductility capacity of a structure at the story level. Figure 4.6.2 shows the linear approximations of the second story interstory drift by utilizing the same approach proposed above. The resulting drift at yield of the second story, Δ_y, was 0.29% in the south direction and 0.42% in the north direction. The drift capacity, Δ_u, was 1.28% in the south direction and 1.48% in the north direction. The corresponding ductility index μ was 4.41 in the south direction and 3.52 in the north direction, which is approximately 30% higher than that based on the total deformation of the structure.

The specimen as a whole was unable to exhibit the same level of ductility as did the second story due to the fact that the distribution of the interstory drift changes. Figures 4.6.3 and 4.6.4 shows the ratio of the second story interstory drift to the first story interstory drift when the specimen reached its peak load in the first loading cycle of each

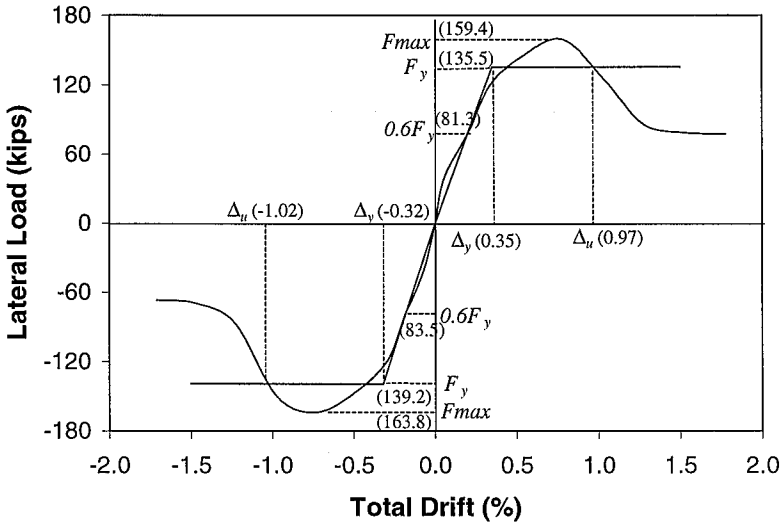

Fig. 4.6.1 Idealization of the Lateral Load-Total Drift Relationship

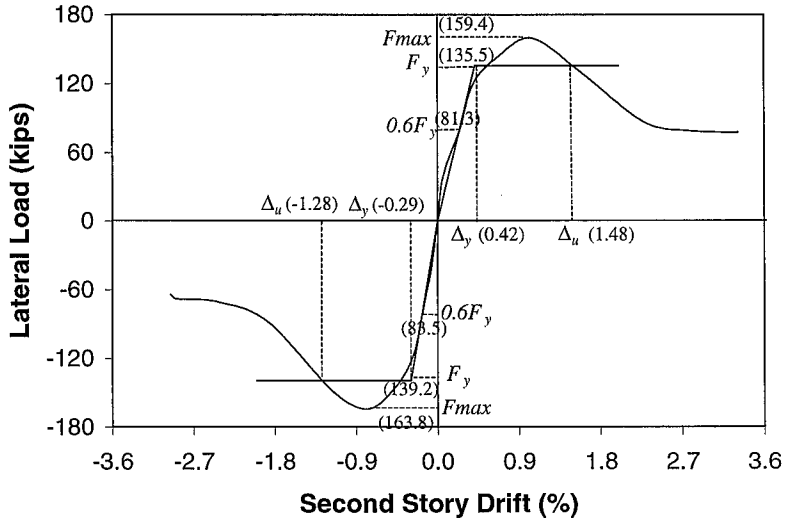

Fig. 4.6.2 Idealization of the Lateral Load-Second Story Drift Relationship

group of cycles. In the north loading direction, it can be seen that the second story interstory drift, Δ_2, and the first story interstory drift, Δ_1, increased in an approximately proportional manner in the first six groups of cycle. However, by loading cycle G7-1-A, Δ_2 was more than three times Δ_1, and the ratio of Δ_2 to Δ_1 kept increasing in later cycles.

The change in the distribution of interstory drift was even larger in the south loading direction. The ratio of Δ_2 to Δ_1 reached approximately 3.5 in loading cycle G5-1-C and reached almost 9.5 in loading cycle G9-1-C.

This change in the distribution of interstory drift of the specimen is related to the specific boundary conditions in this test. As shown in Figure 3.3.1, the bottom portion of each column was stiffened by welding two 8 inch high steel plates onto both sides of the steel column, and the bottom beam was welded to the 3 inch thick steel foundation plates to transfer part of the lateral load to the foundations. As a result, the deformation of the steel frame was highly restrained at the bottom of the first story. The effect of the boundary condition extended to the entire first story and crushing of the concrete was prevented in the four corner regions in the first story. In a real frame structure with a fixed base, although the stiffening effect on the first story columns always exists, a lesser extent of this effect is most likely expected because of three reasons: 1) a basement is usually constructed; 2) many buildings have a taller first story; and 3) column footings usually allow some rotation.

4.7 Energy Dissipation by Hysteretic Behavior

The energy dissipated through hysteretic behavior can be measured as the area enclosed in the load-deformation curve when the structure undergoes repeated cycles of loading. Figure 4.7.1 shows the energy absorbed in each loading cycle, which is normalized by the energy to yield the structural system, $W_y=F_y\Delta_y h$, where F_y (137.4 kips) is the average of the yield strengths at the two loading directions (Figure 4.6.1), Δ_y (0.335%) is the average of the corresponding total drifts (Figure 4.6.1), and h (96 inches) is the height of two stories. It can be seen that there was almost no energy absorbed in the first loading level, indicating that the structure basically responded elastically up to 40 kips of load (0.05% cycles, which are cycles 1-3 in Figure 4.7.1). The limited absorbed energy, 36.1% of W_y, during the 0.2% cycles (cycles 4-6) and 82.2% of W_y, during the 0.3% cycles (cycles 7-9) was likely due to the occurrence and growth of extensive cracking in the infill walls of both stories, as well as the minor yielding in the steel

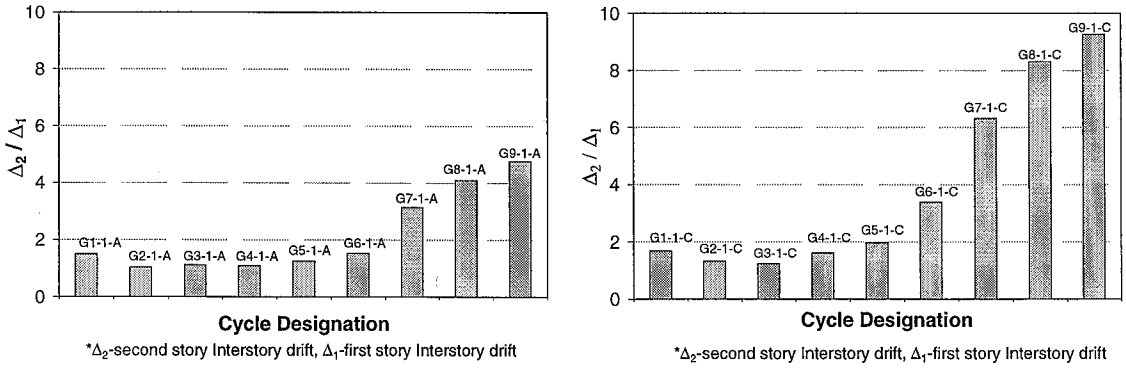

a) South Direction b) North Direction

Fig. 4.6.3 Ratio of the Second Story Interstory Drift to the First Story Interstory Drift at Peak Load

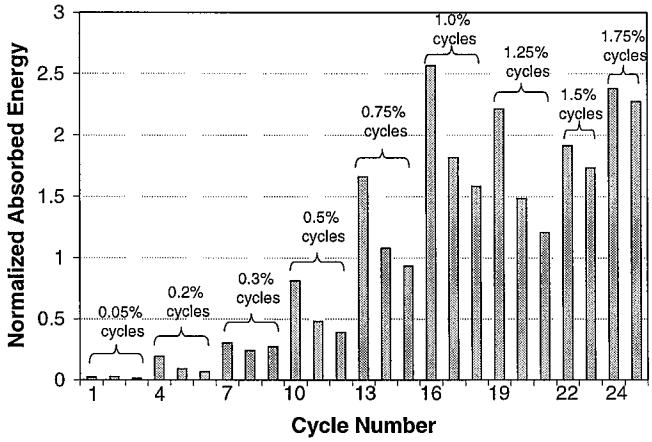

*Absorbed energy of each cycle is normalized by ($F_y \Delta_y h$)

Fig. 4.7.1 Hysteretic Energy Absorbed in Each Loading Cycle

members (at the base portion of the steel columns and in the beam webs and web angles in the connection regions). Although only a few new cracks appeared during the 0.5% cycles (cycles 10-12), the increasing amount of yielding in steel members, together with the yielding of the studs, are considered to have contributed to the continuous increase of energy dissipation. The absorbed energy further increased to 3.7 times W_y during the 0.75% cycles (cycles 13-15) due to several possible additional contributions from both the steel and RC members, such as the yielding in the bottom portion of both columns in the second story, the plastic deformation of the top-and-seat angles of the PR

connections, and the yielding in the infill reinforcing bars and in the confining cages of the headed studs. The energy dissipated in a single cycle reached its maximum value in the first cycle of the 1.0% cycles (cycle 16). In addition to the increasing yielding in the steel frames and in the steel bars of the RC infill and confining cages, the crushing of the corner concrete in the second story also played a major role in absorbing the energy during this cycle. The absorbed energy started to drop during the next 1.25% cycles (cycles 19-21) because the corner concrete in the second story had been crushed and fallen off the structure. However, extensive yielding of the steel components in the second story maintained the energy dissipation capability in the last two loading levels and even increased the energy dissipation capacity at the 1.75% drift level (cycles 24-25).

Figure 4.7.2 shows the percentage of the hysteretic energy absorbed by each story in each loading cycle. It can be seen that the amount of hysteretic energy absorbed by the two stories was approximately the same during the first four groups of cycles (cycles 1 to 12), indicating the two stories had approximately the same degree of damage. However, the percentage of the energy absorbed by the second story increased up to 60% during the 0.75% drift level (cycles 13-15) and was more than 75% during the 1.0% drift level (cycles 16-18). This increase continued in the last three loading levels, and the second story absorbed more than 90% of the energy during the last two loading cycles

Figure 4.7.1 indicates that the majority of the energy was dissipated during the 0.75% drift level to the the 1.75% drift level. Figure 4.7.2 then indicates that the majority

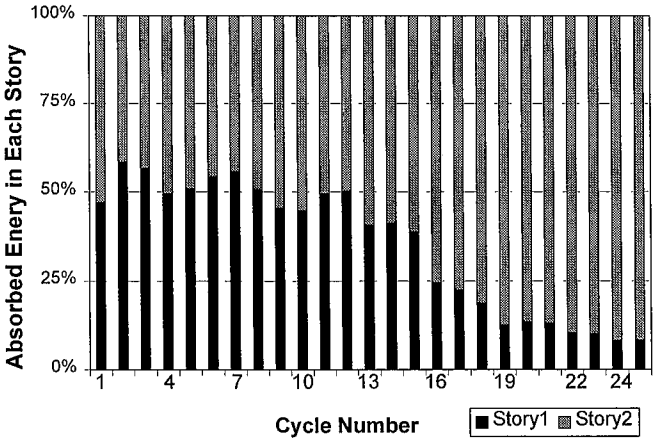

Fig. 4.7.2 Percentage of the Hysteretic Energy Absorbed by Each Story

of the energy was dissipated by the second story after the 0.75% drift level. Therefore, the plastic deformation of the second story constituted the primary contribution to the energy dissipation capacity of the strucural system. As discussed in the last section, the major factor reponsible for this behavior is the stiffening effect and strengthening from the fixty of the first story columns. This feature made the first story stronger than the second level though the beam, column and wall sections and the PR connections were nominally the same, thus preventing yielding of the first story. Consequently, the first story was unable to contribute measurably to energy dissipation.

4.8 Evaluation of the *R* factor

According to NEHRP (1997), the design of the prototype structure was based on internal forces resulting from a linear elastic analysis using the prescribed lateral design force. This prescribed lateral force was calculated by dividing the force that would be associated with elastic response by a response modification factor, symbolized as R. The value of the response modification factor R for special composite reinforced concrete shear walls with steel elements is proposed to be equal to 6 in NEHRP (1997). Since the specimen was a scaled model for the prototype structure, it is reasonable to evaluate the R factor based on the performance on the specimen.

The R factor can be derived as follows (NEHRP, 1997; Uang, 1991):

$$R = R_{\mu}\Omega \tag{4.8.1}$$

where the ductility reduction factor, R_{μ}, takes into account the reduction of the elastic design force due to plastic deformation. Newmark and Hall (1982) proposed relationships that can be used to estimate the ductility factor, R_{μ}, for an elasto-plastic SDOF system as follows:

$$\begin{aligned} R_{\mu} &= 1.0 && \text{for } T \le 0.03 \text{ second} \\ R_{\mu} &= \sqrt{2\mu - 1} && \text{for } 0.12 \text{ second} \le T \le 0.5 \text{ second} \\ R_{\mu} &= \mu && \text{for } T \ge 1.0 \text{ second} \end{aligned} \tag{4.8.2}$$

where μ is the ductility index and T is the period of the structure. It is unrealistic, if not

impossible, to assume that any SRCW frame will have T ≤ 0.03 second since T is approximately equal to N/10, where N = number of stories. For example, the period of the prototype structure was approximately 0.53 seconds. Thus only the last two categories of Eq. (4.8.2) are realistic. Wheret a great way SRCW structures will have T > 1 second, only the second branch of Eq. (4.8.2) is considered here. In Eq. (4.8.1), the overstrength factor, Ω, is defined as the ratio of the yield strength of the system, F_y, to the prescribed design lateral force, F_d, and can be written as

$$\Omega = \frac{F_y}{F_d} \tag{4.8.3}$$

The values of factors μ, F_y, and F_d for the entire specimen and for the second story were reported in Section 4.6. Table 4.8.1 lists the R factors based on both the system performance and the story performance of the second story. It can be observed that response modification factor, R, has higher value at the story level than at the system level. The average value of factor R is approximately equal to 4.8. Structural overstrength results from higher material strength than those specified in design, structural redundancy, strengthening from nonstructural members, strain hardening, and so on. In the actual construction, the material overstrength typically will be higher than that in this test specimen since the material strength of components was carefully controlled for this test specimen. Furthermore, typically, there will be several infilled frames in one lateral resisting direction, which gives more overstrength from structural redundancy. Considering all the possible resources for providing overstrength, it can be concluded that the recommended value of R = 6 in NEHRP (1997) is a reasonable and probably conservative value.

Table 4.8.1 Evaluation of the Response Modification Factor R

Level	Direction	μ	F_y (kips)	F_d (kips)	R_μ	Ω	R
System	South	3.19	139.2	70	2.32	1.99	4.62
	North	2.77	135.5		2.13	1.94	4.13
Story	South	4.41	139.2		2.80	1.99	5.56
	North	3.52	135.5		2.46	1.94	4.77

Chapter 5

Local Response of the Steel Frame and the Reinforced Concrete Infill Wall

This chapter highlights the characteristics of the strain and internal forces at the critical sections of the steel columns, the strain profiles and internal forces at both ends of the middle beam, and the behavior of the PR connection. It also discusses the patterns and magnitude of deformations in the RC infill wall.

5.1 Behavior of the Steel Columns

5.1.1 Characteristics of Strain Variation in the Steel Columns

Each steel column was instrumented with strain gages and rosettes at four cross sections to monitor its behavior, as shown in Figure 3.4.3. As representative examples of the data, Figures 5.1.1 and 5.1.2 show the strain versus total lateral load from strain gages C_NC_CF_G1 and C_NC_CF_G2, which were two gages placed on the flanges at the bottom of the north column in the first story. Figure 5.1.3 shows the shear strain γ_{xz} in the web center, also at the bottom of the north column in the first story. The coordinates for defining the strain profile are shown in Figure 5.1.4. The x-axis is in the horizontal direction, starting from the surface of the outside flange of the column. The z-axis is oriented along the direction of the column axis, starting from the center of the gages. The shear strain γ_{xz} was calculated using the recorded strains from the three legs of the strain

rosette as follows: $\gamma_{xz} = 2\varepsilon_{45} - \varepsilon_0 - \varepsilon_{90}$. The hysteretic strain-load relations of all the column strain gages are shown in Appendix B.1. The characteristics of each strain gage reading are listed in Table 5.1.1 and are discussed in this section. For a better understanding of the column behavior, the strain distributions in the *z* direction are plotted across the four gaged column cross sections in Figures 5.1.5 and 5.1.6. These strains are normal to the column cross sections and thus are induced by combined axial and bending forces. Figure 5.1.5 shows the strain distributions of both columns at the first cycle of each loading level, when the specimen reached the peak load in the south direction. Figure 5.1.6 shows the strain distributions of both columns when the specimen reached the peak load in the north direction.

At the bottom of the north column in the first story, Figure 5.1.1 shows the reading of strain gage C_NC_CF_G1 (on the outside flange) surpassed the yielding limit in tension at cycle G5-1-A, while Figure 5.1.2 shows the reading of gage C_NC_CF_G2 (on the inside flange) surpassed the yielding limit in tension at the same cycle during the load reversal. The yielding limit is defined as $\varepsilon_y = F_{ys} / E$, where F_{ys} is 45 ksi and E is 29,890 ksi as reported in Chapter 3. Therefore, the yielding limit for the column flange is approximately 1500 με. Table 5.1.1 lists that the maximum strains are 5270 με for gage C_NC_CF_G1 and 3490 με for gage C_NC_CF_G2, indicating none of the strains in either flange entered into the hardening range. The strain at initiation of strain hardening ε_{sh} is approximately 13,900 με as reported in Chapter 3. Figure 5.1.1 shows that the outside flange was in tension when the specimen was being loaded in the south direction and in compression when the specimen was being loaded in the north direction. This is expected because both the axial force and the bending moment at the bottom of the north column induced tensile stress in the outside flange when the specimen was loaded in the south direction, and they induced compressive stress when the specimen was loaded in the north direction. Also as seen in Figure 5.1.1, the strain of the outside flange reached its maximum value at cycle G6-1-A, and decreased gradually with each later cycle. Figure 5.1.2 shows that the inside flange was always in tension after the 0.05% cycles. This indicated that, after the 0.05% cycles, the tensile stress from the axial force

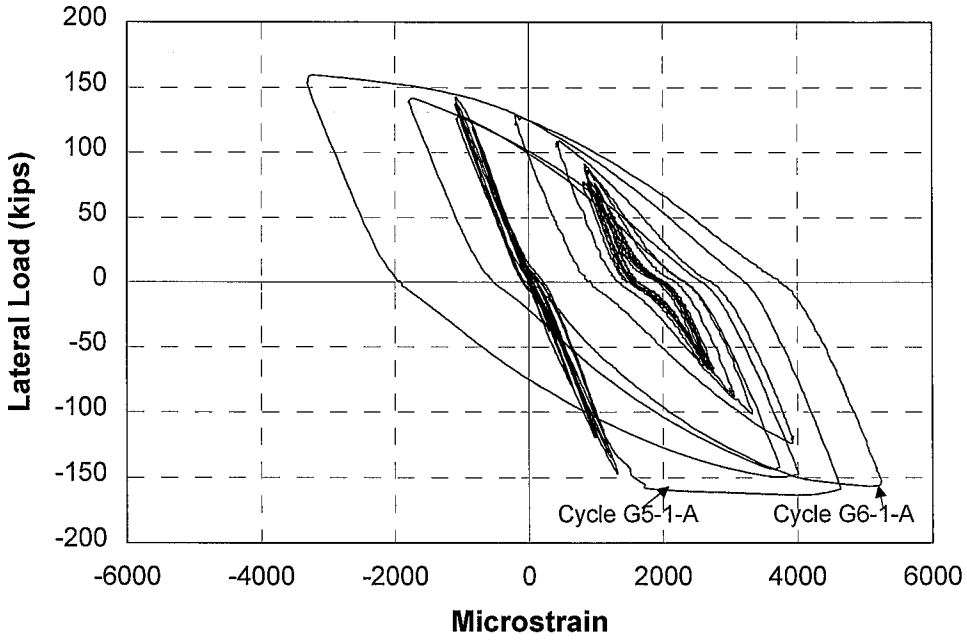

Fig. 5.1.1 Longitudinal Strain from Strain Gage C_NC_CF_G1

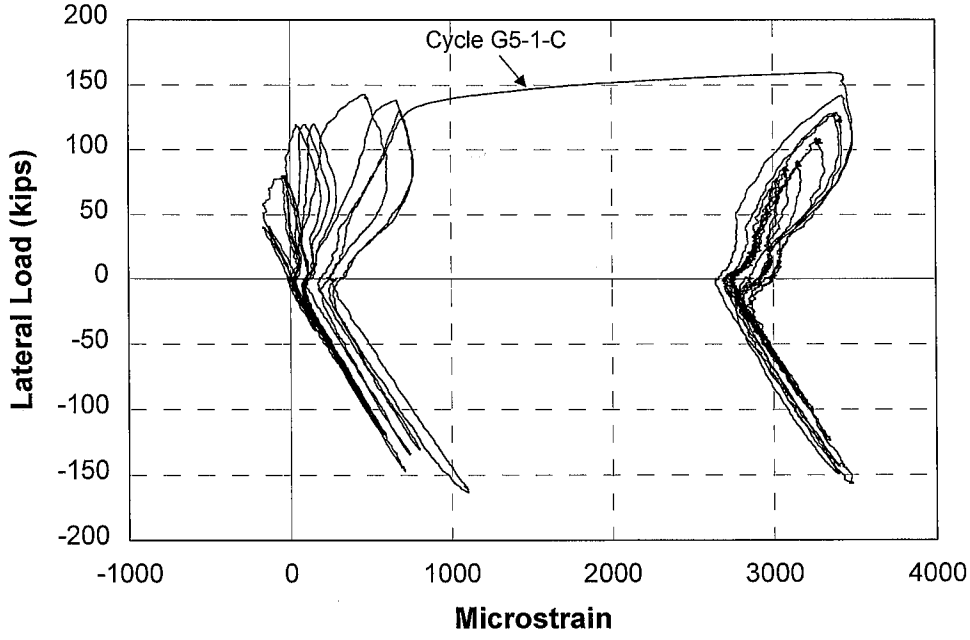

Fig. 5.1.2 Longitudinal Strain from Strain Gage C_NC_CF_G2

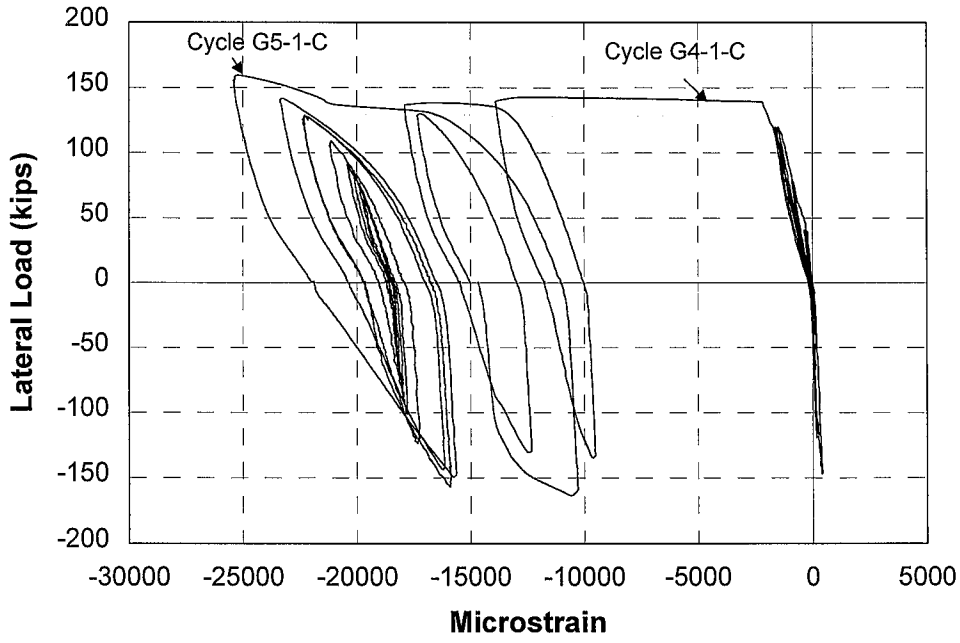

Fig. 5.1.3 Shear Strain from Strain Rosette C_NC_CW_R1

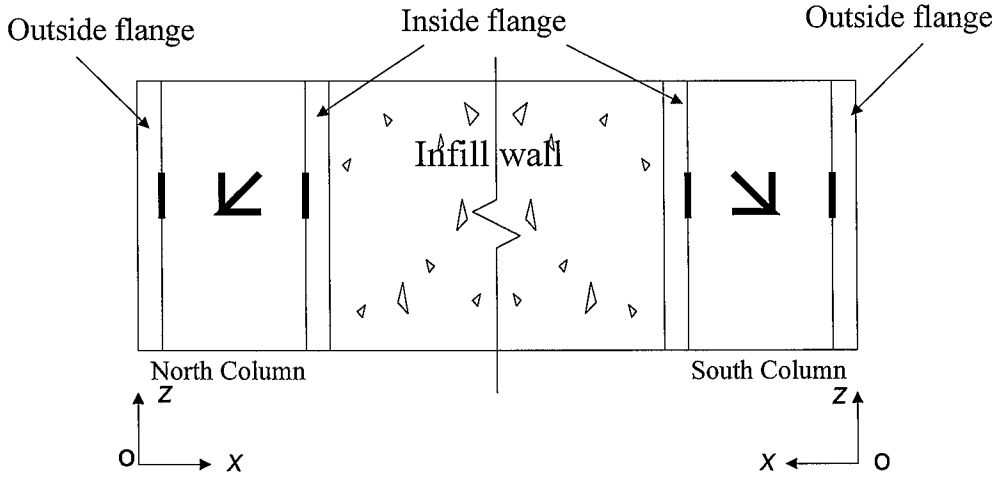

Fig. 5.1.4 Coordinates for Defining Strain Profiles across the Column Sections

Table 5.1.1 Strain Characteristics of Steel Columns

Location of each gage group	Individual location	Gage name	Maximum value	Cycle No. at Max. value	Minimum value	Cycle No. at Min. value	Yielding	Cycle No. if yielded	Harden-ing
Bottom of the north column in story 1	Outside flange	C_NC_CF_G1	5270	G6-1-A	-3340	G5-1-C	Yes, in tension	G5-1-A	No
	Inside flange	C_NC_CF_G2	3490	G5-1-D	-160	G1-1-C	Yes, in tension	G5-1-C	No
	Web center	C_NC_CW_R1a	72	G1-1-C	-605	G5-2-A	Yes, in combined compression and shear	G4-1-C	Yes
		C_NC_CW_R1b	611	G4-1-A	-13890	G5-1-C			
		C_NC_CW_R1c	1100	G4-1-A	-2000	G5-1-C			
		Shear strain	430	G4-1-A	-25400	G6-1-C			
Bottom of the south column in story 1	Outside flange	C_SC_CF_G1	1790	G5-1-C	-1357	G6-1-A	Yes, in tension	G5-1-C	No
	Inside flange	C_SC_CF_G2	900	C5-1-C	-168	G1-1-A	No		No
	Web center	C_SC_CW_R1a	262	G6-1, at 0 load	-389	G5-1-A	Yes, in combined compression and shear	G4-1-A	Yes
		C_SC_CW_R1b	504	G4-1-C	-6370	G6-1-A			
		C_SC_CW_R1c	1331	G5-1-C	-398	G3-1-A			
		Shear strain	315	C3-1-C	-12423	C6-1-A			
Middle of the north column in story 1	Outside flange	C_NC_CF_G3	1180	G5-1-A	-860	G9-1-C	No		No
	Inside flange	C_NC_CF_G4	970	G5-1-A	-390	G3-1-C	No		No
	Web center	C_NC_CW_R2a	200	G5-1-C	-335	G5-1-A	No		No
		C_NC_CW_R2b	407	G5-1-A	-253	G3-1-C			
		C_NC_CW_R2c	1166	G5-1-A	-560	G5-1-C			
		Shear strain	910	G9-1-C	-360	G9-2-A			
Middle of the south column in story 1	Outside flange	C_SC_CF_G3	1370	G5-1-C	-890	G6-1-A	No		No
	Inside flange	C_SC_CF_G4	870	G5-1-C	-460	G5-1-A	No		No
	Web center	C_SC_CW_R2a	160	C6-1-A	-270	G5-1-C	No		No
		C_SC_CW_R2b	580	G5-1-C	-327	G4-1-A			
		C_SC_CW_R2c	1090	G5-1-C	-620	G5-1-A			
		Shear strain	870	G9-1-A	-370	G9-1-C			

Table 5.1.1 (continued) Strain Characteristics of Steel Columns

Location of each gage group	Individual location	Gage name	Maximum value	Cycle No. at Max. value	Minimum value	Cycle No. at Min. value	Yielding	Cycle No. if yielded	Harden-ing
Top of the north column in story 1	Outside flange	C_NC_CF_G5	1270	G6-1-A	-1410	G9-1-C	No		No
	Inside flange	C_NC_CF_G6	1300	G9-2-C	-610	G9-2-A	No		No
	Web center	C_NC_CW_R3a	240	G5-1-C	-163	G8-1-C	No		No
		C_NC_CW_R3b	660	G9-1-C	-170	G9-1-A			
		C_NC_CW_R3c	930	G5-1-A	-340	G4-1-C			
		Shear strain	1280	G9-1-C	-920	G8-1-A			
Top of the south column in story 1	Outside flange	C_SC_CF_G5	1530	G9-2-C	-1540	G9-2-A	No		No
	Inside flange	C_SC_CF_G6	1140	G9-2-A	-600	G9-1-D	No		No
	Web center	C_SC_CW_R3a	270	G9-1-A	-30	G1-1-A	No		No
		C_SC_CW_R3b	860	G9-2-A	-260	G9-1-C			
		C_SC_CW_R3c	880	G5-1-C	-420	G5-1-A			
		Shear strain	1360	G9-2-A	-1230	G8-1-C			
Bottom of the north column in story 2	Outside flange	C_NC_CF_G7	7560	G9-1-A	-230	G5-1-C	Yes, in tension	G6-1-A	No
	Inside flange	C_NC_CF_G8	1440	C9-2-C	-1670	G9-2-A	Yes, in compression	G9-1-A	No
	Web center	C_NC_CW_R4a	2970	G5-1-C	-730	G5-1-A	Yes, in combined compression and shear	G5-1-C	Yes
		C_NC_CW_R4b	186	G5-2-A	-14480	G6-1-C			
		C_NC_CW_R4c	2140	G9-2-A	-1320	G6-1-C			
		Shear strain	0	G1-1	-29960	G6-1-C			
Bottom of the south column in story 2	Outside flange	C_SC_CF_G7	9910	G9-1-C	-1820	G9-1-A	Yes, in tension	G6-1-C	No
	Inside flange	C_SC_CF_G8	1520	G9-2-A	-1150	G9-1-D	No		No
	Web center	C_SC_CW_R4a	2220	G6-1-A	-1210	G9-1-C	Yes, in combined compression and shear	G5-1-A	Yes
		C_SC_CW_R4b	80	G3-1-C	-10840	G6-1-A			
		C_SC_CW_R4c	3110	G9-1-C	-1410	G6-1-A			
		Shear strain	0	G1-1	-22700	G6-2-A			

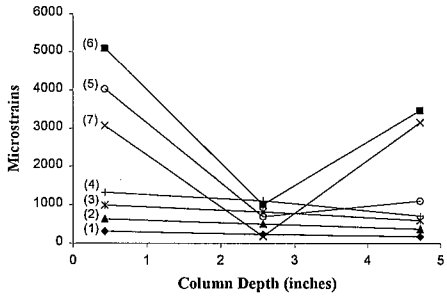

a1) Bottom Section of the North Column of Story 1

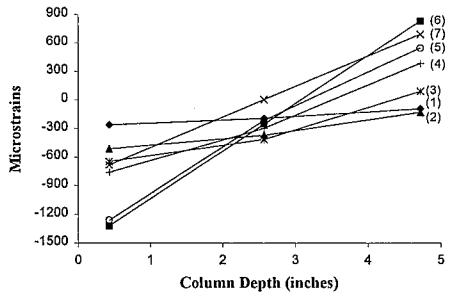

a2) Bottom Section of the South Column of Story 1

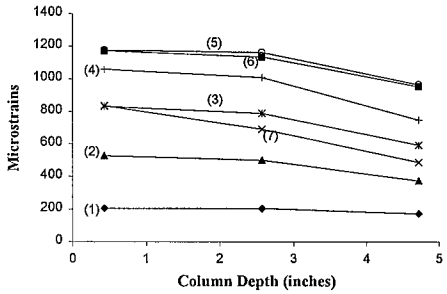

b1) Middle Section of the North Column of Story 1

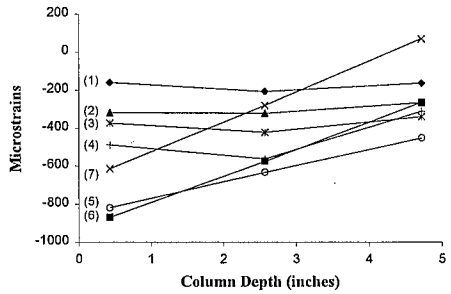

b2) Middle Section of the South Column of Story 1

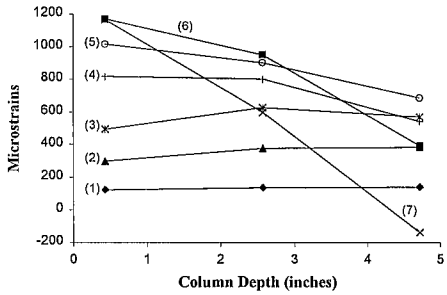

c1) Top Section of the North Column of Story 1

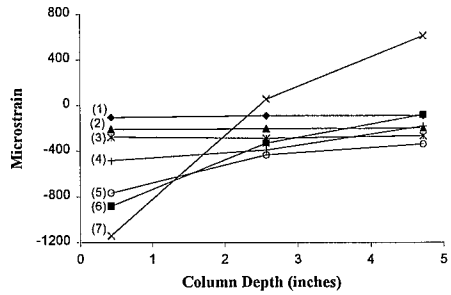

c2) Top Section of the South Column of Story 1

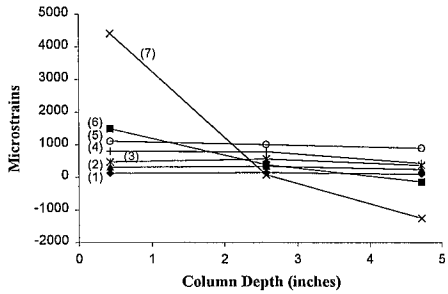

d1) Bottom Section of the North Column of Story 2

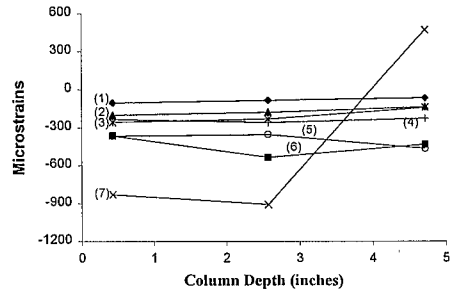

d2) Bottom Section of the South Column of Story 2

* (1) – G1-1; (2) – G2-1; (3) – G3-1; (4) – G4-1; (5) – G5-1; (6) – G6-1; (7) – G7-1

Fig. 5.1.5 Steel Column Longitudinal Strain Profiles at Peak Load of First Cycle of Each Loading Group in the South Direction

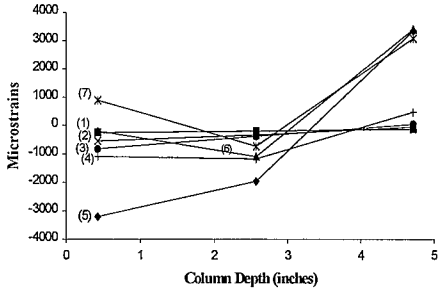

a1) Bottom Section of the North Column of Story 1

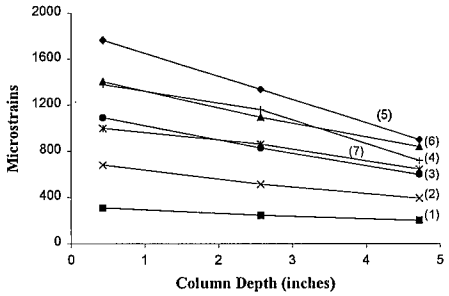

a2) Bottom Section of the South Column of Story 1

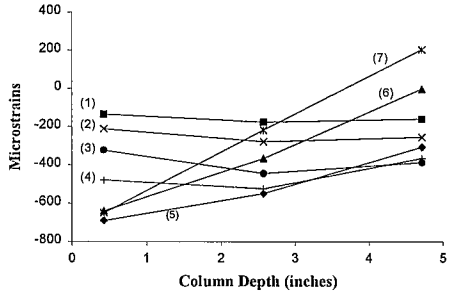

b1) Middle Section of the North Column of Story 1

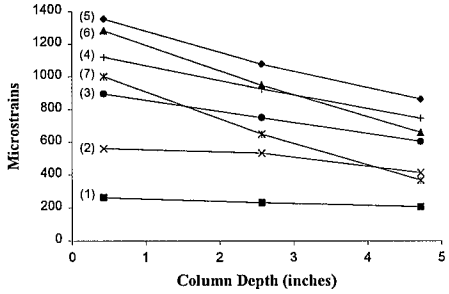

b2) Middle Section of the South Column of Story 1

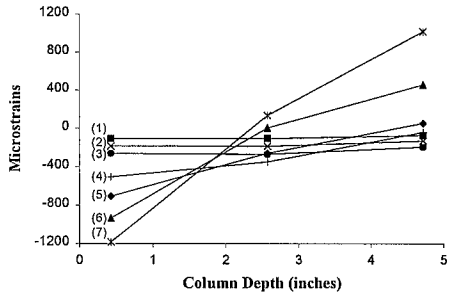

c1) Top Section of the North Column of Story 1

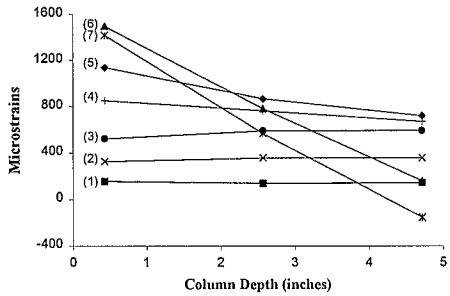

c2) Top Section of the South Column of Story 1

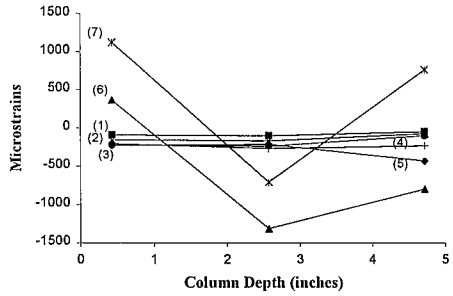

d1) Bottom Section of the North Column of Story 2

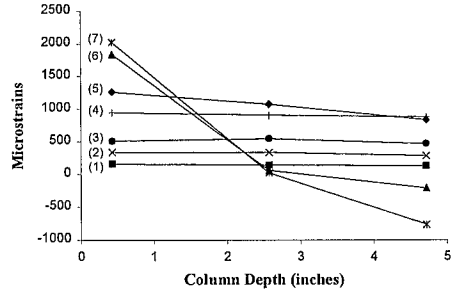

d2) Bottom Section of the South Column of Story2

* (1) – G1-1; (2) – G2-1; (3) – G3-1; (4) – G4-1; (5) – G5-1; (6) – G6-1; (7) – G7-1

Fig. 5.1.6 Steel Column Longitudinal Strain Profiles at Peak Load of First Cycle of Each Loading Group in the North Direction

surpassed the compressive stress from the bending moment when the specimen was loaded in the south direction, while the tensile stress from the bending moment surpassed the compressive stress from the axial force when the specimen was loaded in the north direction. This phenomenon was due to the fact that, at the bottom of the first story, the compressive axial force in the leeward column was lower than the tensile axial force in the windward column, but the overturning moment in the leeward column was higher than that in the windward column, as discussed further in Section 5.1.2. Figure 5.1.3 shows that, in cycle G4-1-C, the shear strain increased rapidly by approximately 12,000 με in the web center when the specimen approached the peak load in the north direction. After yielding, the shear strain kept growing in the next three cycles until the specimen reached the maximum strength in cycle G5-1-C; it then decreased during each cycle thereafter. The maximum shear strain was 25,400 με, showing that strain hardening occurred at the center of the web at this location. At the bottom of the south column in the first story, the recorded strains exhibit similar behavior to those at the bottom of the north column in the first story and are plotted in Figures B.1.13 to B.1.15 of Appendix B. However, Table 5.1.1 shows that the maximum reading from gage C_SC_CF_G1 (on the outside flange) was only 1790 με at cycle G5-1-C, barely surpassing the 1500 με yielding limit. Furthermore, the inside flange did not yield during the entire loading history. The shear strain γ_{xz} in the web center reached its maximum value in cycle G6-1-C. The maximum shear strain was 12,420 με, approximately one half of that in the north column. The large shear deformations at the bottom of both columns were caused by the compressive strut force from the infill wall, which increased with the increasing lateral load and with the yielding and failure of headed studs along the bottom beam-infill interfaces. This transition of the force resisting mechanisms of the specimen is discussed in detail in Chapter 7. Figures 5.1.5 and 5.1.6 show that the slope of the longitudinal strain distribution across the bottom cross section of the first story increased gradually during each loading level and reached its maximum magnitude at the peak load of cycle G5-1. However, at the bottom of the north column, the cross section normal to the

column axis did not remain plane by cycle G5-1. This might be caused by the large shear deformation at the center of the web.

In the middle of the north column in the first story, Table 5.1.1 shows that neither the maximum strain nor the minimum strain of the flange gage surpassed the yielding limit. The maximum value of the shear strain was also only 910 με, far below its yielding limit. It was the same for the middle of the south column in the first story, where both the flanges and the web remained elastic during the entire loading history. The recorded strains in the middle of the north column are plotted in Figures B.1.4 to B.1.6 of Appendix B. The recorded strains in the middle of the south column were plotted in Figure B.1.16 to B.1.18 of Appendix B. Figure 5.1.7 shows the shear strain in the web center in the middle of the north column, which was monitored by stain rosette C_NC_CW_R2. It can be seen that the shear strain in the middle of the north column started to change its direction during cycle G5-1 after the column yielded at its base at cycle G4-1-C, and reached its maximum value at the 1.75% cycles. It was similar for the middle of the south column in the first story (Figure 5.1.8). The reason that the shear strain changed direction is related to the variation of the magnitudes of all the forces acting on this column, and is discussed further in the next section. Figures 5.1.5 and 5.1.6 show that the slope of the normal strain distribution across the middle cross section of the first story was quite small before cycle G5-1, indicating that the axial force was the dominating internal force before the specimen reached its maximum strength. The cross section normal to the column axis remained plane during the entire loading history.

At the top of both columns in the first story, Table 5.1.1 shows that neither the maximum strain nor the minimum strain of the flange gage surpassed the yielding limit. The shear strain remained in the elastic range during the entire loading history. This is in contrast to the substantial shear strain at the bottom of both columns in the first story. As explained in the next section, it is because the critical cross section in the top portion of the column of the first story is just below the centerline of the high strength bolts that connected the vertical leg of the seat angle to the column flange, instead of in the gaged location. The strains at the top of the north column are plotted in Figure B.1.7 to B.1.9 of

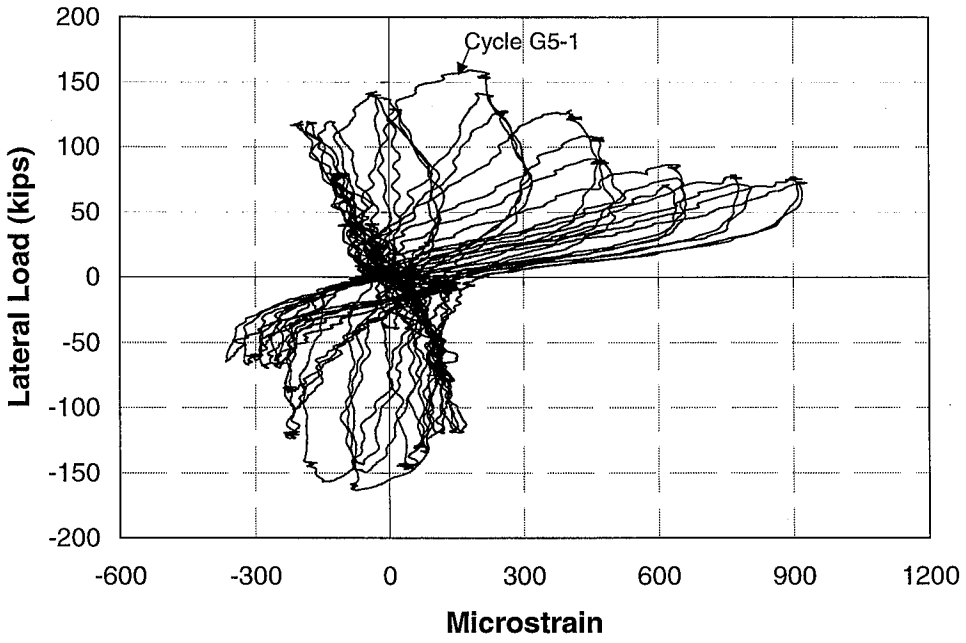

Fig. 5.1.7 Shear Strain from Strain Rosette C_NC_CW_R2

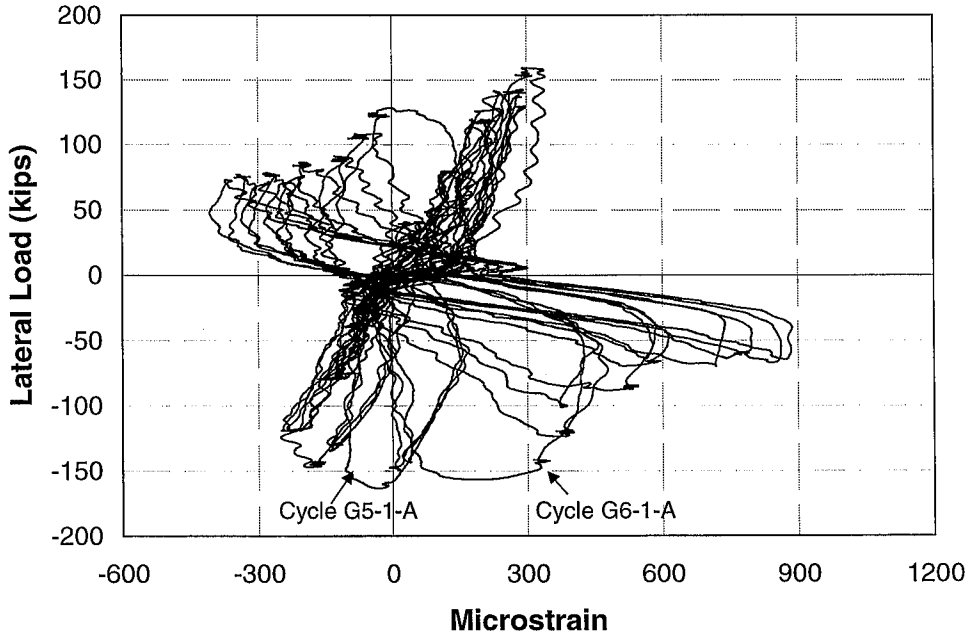

Fig. 5.1.8 Shear Strain from Strain Rosette C_SC_CW_R2

Appendix B. The strains at the middle of the south column are plotted in Figure B.1.19 to B.1.21 of Appendix B.

At the bottom of the north column in the second story, Table 5.1.1 shows that the outside flange yielded in tension during cycle G6-1-A, while the inside flange barely yielded in compression during cycle G9-1-A. None of the strains in either flange entered into the hardening range. Figure 5.1.9 shows that, at cycle G5-1-C, the shear strain increased rapidly by approximately 2500 με in the web center when the specimen approached the peak load in the north direction. The shear strain kept growing in the next three cycles, reaching its maximum value of 29,960 με at cycle G6-1-C, even greater than the shear strain at the bottom of the first story. At the bottom of the south column in the second story, Table 5.1.1 shows the strain in the outside flange reached the yielding limit during cycle G6-1-C, and reached its maximum value of 9910 με in G9-1-C. The inside flange did not yield during the entire loading history. Figure 5.1.10 shows that the shear strain in the web center increased rapidly by approximately 20,000 με during cycle G6-1-A, when the specimen approached its peak load in the south direction. The maximum shear strain was 22,700 με during cycle G6-2-A. Again, the large shear deformation at the bottom of both columns of the second story was caused by the increasing compressive strut force from the infill wall. Figures 5.1.5 and 5.1.6 show that the slope of the normal strain distribution across the bottom cross section of the second story increased substantially after the specimen reached its maximum strength, indicating that bending started to dominate the frame action. The cross section normal to the column axis did not remain plane by cycle G6-1. This may also be related to the large shear deformation at the center of the web.

5.1.2 Characteristics of the Variation of Internal Forces in the Steel Columns

5.1.2.1 Magnitudes of the Internal Forces in the Steel Columns

The internal forces of the steel columns are calculated based on the method discussed in Appendix C. Tables 5.1.2 and 5.1.3 show the internal forces of the steel columns at the cross sections where the strain gages were installed. Table 5.1.2 shows the

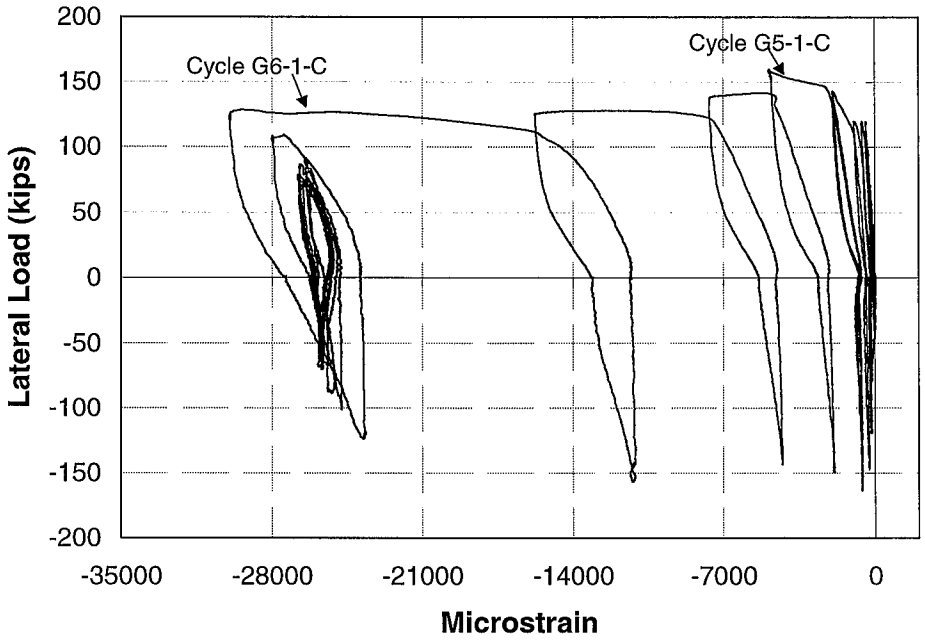

Fig. 5.1.9 Shear Strain from Strain Rosette C_NC_CW_R4

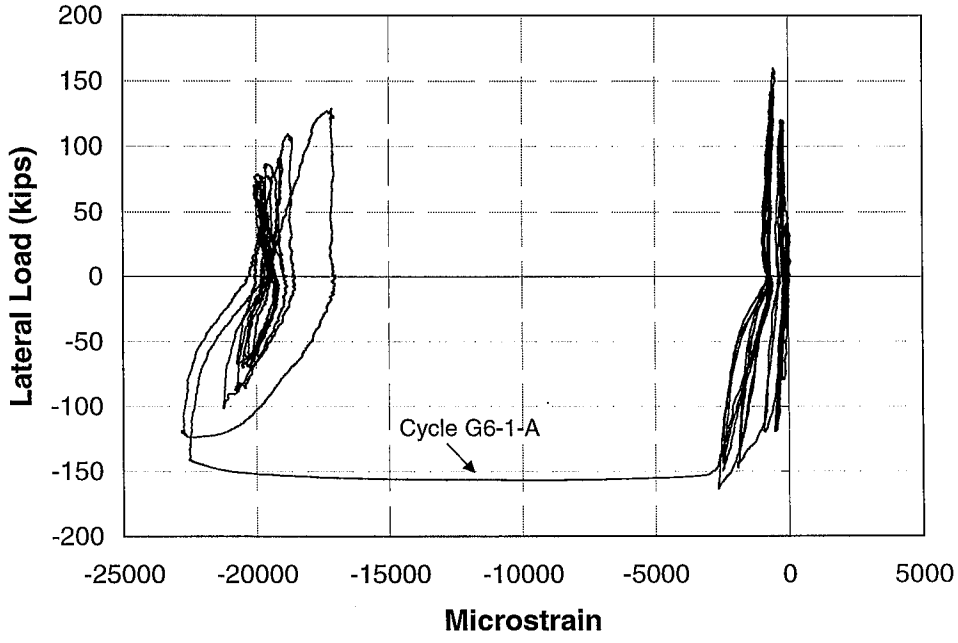

Fig. 5.1.10 Shear Strain from Strain Rosette C_SC_CW_R4

internal forces of the steel columns when the specimen reached the peak load in the south direction, during the first cycle of each group of cycles. Table 5.1.3 shows the internal forces of the steel columns when the specimen reached the peak load in the north direction, during the first cycle of each group of cycles. The yielding of the steel cross sections was determined according to the von Mises yield criterion, as discussed in Appendix C. Once a gaged cross section yielded or the assumption of a linear distribution of the longitudinal strain did not hold for the cross section, the internal forces of the cross section cannot be calculated by using the elastic method proposed in Appendix C. The blanks in Tables 5.1.2 and 5.1.3 mean that the corresponding cross section yielded during the previous quarter loading cycle and the internal forces cannot be obtained thereafter.

To assure consistency among the two columns and two loading directions, the sign convention of the axial force P, shear force V, and bending moment M of the steel column is established as shown in Figure 5.1.11. Furthermore, the lateral force and corresponding overturning moment were defined as negative when the specimen was loaded in the south direction, as well as the corresponding overturning moment. According to the above sign convention, the internal force distributions along the column height in the first story, from the top flange of the bottom beam to the bottom flange of the middle beam, are plotted in Figures 5.1.12 and 5.1.13. The distribution of the axial force, as well as the distribution of the bending moment, is a smooth line connecting three measured values at the base, in the middle and at the top of the column. For the distribution of the shear force, there is an abrupt change at the location of the high strength bolts that connected the seat angle to the column flange. The abrupt change of shear force at this location was caused by the concentrated force from the seat angle of the PR connection. The estimation of the shear force at this location is discussed in the following section. For loading cycles G4-1 and G5-1, only the force distributions from the middle to the top of the column are plotted since the bottom section had yielded in the previous loading cycle.

Table 5.1.2 Internal Forces in the Steel Column at Peak Lateral Load in the South Direction

Cycle No.	Location*[1]	Axial Force (kips)		Moment (kip-inches)		Shear Force (kips)	
		NCol*[2]	SCol*[2]	NCol	SCol	NCol	SCol
G1-1-A (0.05% drift)	S1-Base	40.0	-30.4	-24.1	-31.0	-0.7	-5.9
	S1-Middle	32.3	-29.6	-5.7	0.7	-1.3	-1.1
	S1-Top	22.1	-15.9	3.3	-2.9	-1.3	-0.6
	S2-Base	19.7	-14.4	-5.3	-7.1	0.6	-1.1
G2-1-A (0.2% drift)	S1-Base	83.2	-56.4	-47.2	-70.7	-1.8	-15.3
	S1-Middle	77.8	-50.3	-28.1	-9.5	-1.8	-1.7
	S1-Top	58.8	-34.0	15.8	-2.1	-2.0	-0.9
	S2-Base	49.4	-28.7	-13.5	-11.8	2.0	-2.5
G3-1-A (0.3% drift)	S1-Base	133.4	-54.2	-72.2	-135.5	-2.5	-23.5
	S1-Middle	123.0	-63.0	-44.0	-6.2	-2.4	-3.1
	S1-Top	93.9	-46.4	13.7	-2.1	-5.9	-0.2
	S2-Base	78.2	-35.2	-19.0	-21.5	2.7	-7.1
G4-1-A (0.5% drift)	S1-Base	174.8	***Y***[*3]	-112.7	***Y***	-6.2	***Y***
	S1-Middle	156.5	-75.8	-56.2	-32.6	-0.3	-2.8
	S1-Top	120.0	-58.9	-50.1	-55.4	-7.2	-1.2
	S2-Base	112.2	-40.0	-68.9	-1.4	3.9	-28.0
G5-1-A (0.75% drift)	S1-Base	-	-	-	-	-	-
	S1-Middle	183.6	-106.0	-38.6	-67.0	1.2	-0.5
	S1-Top	144.6	-85.6	-60.5	-78.6	-5.9	-3.8
	S2-Base	167.1	***Y***	-38.7	***Y***	9.0	***Y***

1: S1 represents the first story; S2 represents the second story
2: NCol represents north column, SCol represents south column
3: ***Y*** means that the column web yielded at this loading cycle

Table 5.1.3 Internal Forces in the Steel Column at Peak Lateral Load in the North Direction

Cycle No.	Location	Axial Force (kips)		Moment (kip-inches)		Shear Force (kips)	
		NCol	SCol	NCol	SCol	NCol	SCol
G1-1-C (0.05% drift)	S1-Base	-33.0	41.7	22.3	19.5	4.7	1.9
	S1-Middle	-26.5	38.8	-4.7	10.2	0.5	0.9
	S1-Top	-16.4	23.9	6.4	2.2	0.6	1.2
	S2-Base	-13.7	23.7	8.4	5.7	1.5	-0.3
G2-1-C (0.2% drift)	S1-Base	-51.8	88.1	92.0	52.6	12.6	3.5
	S1-Middle	-41.6	83.7	-8.0	26.9	1.5	2.5
	S1-Top	-28.3	57.5	10.3	-5.8	-0.5	3.9
	S2-Base	-22.4	53.3	15.1	10.2	3.9	-1.9
G3-1-C (0.3% drift)	S1-Base	-65.4	139.8	158.2	90.1	21.4	4.3
	S1-Middle	-64.5	125.0	-11.9	53.1	2.8	2.9
	S1-Top	-40.8	94.7	12.3	-12.9	-1.0	7.6
	S2-Base	-31.5	84.9	22.9	7.7	6.1	-3.2
G4-1-C (0.5% drift)	S1-Base	***Y***	-	***Y***	-	***Y***	-
	S1-Middle	-76.4	155.1	21.0	68.4	0.4	4.3
	S1-Top	-50.4	126.8	85.4	33.7	0.5	3.0
	S2-Base	-39.6	151.7	-4.0	12.0	28.5	-8.3
G5-1-C (0.75% drift)	S1-Base	-	-	-	-	-	-
	S1-Middle	-86.3	183.1	70.5	90.4	-2.6	4.3
	S1-Top	-51.3	151.3	139.6	76.7	1.4	1.6
	S2-Base	***Y***		***Y***		***Y***	

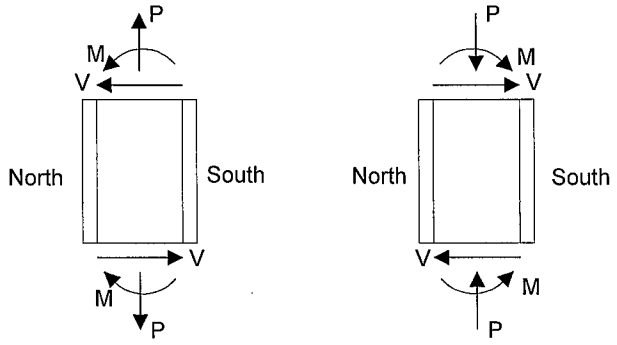

(a) Positive (b) Negative

Fig. 5.1.11 Sign Convention of the Internal Forces in the Columns

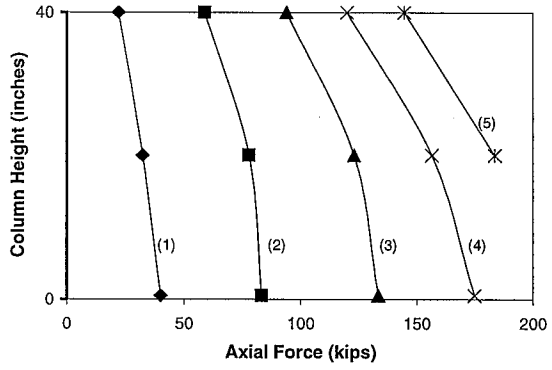

(a1) North Column in Story 1

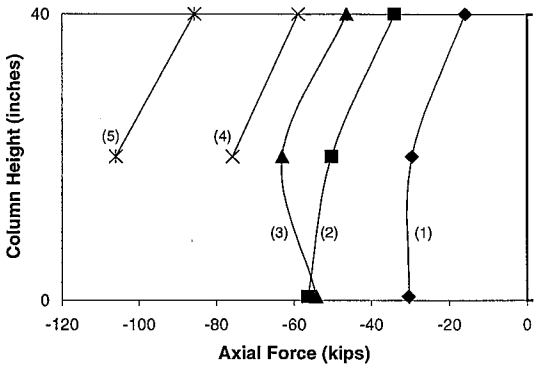

(a2) South Column in Story 1

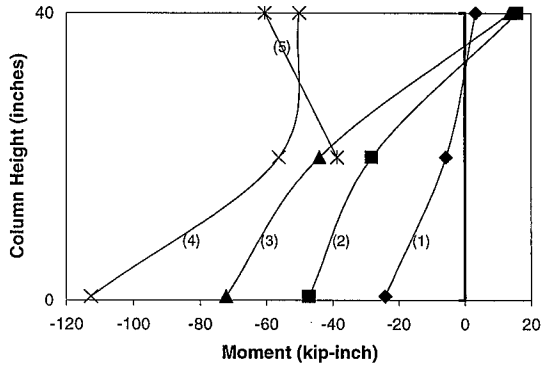

(b1) North Column in Story 1

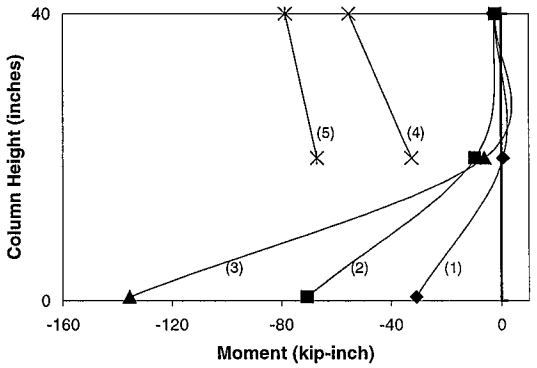

(b2) South Column in Story 1

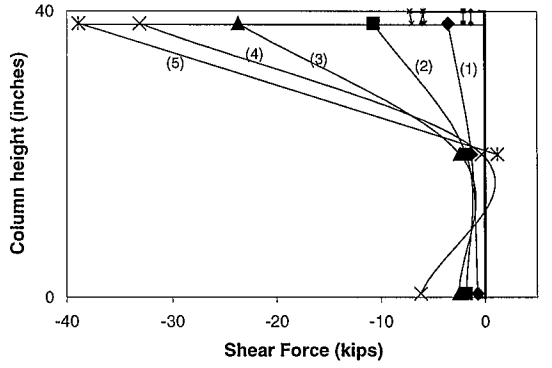

(c1) North Column in Story 1

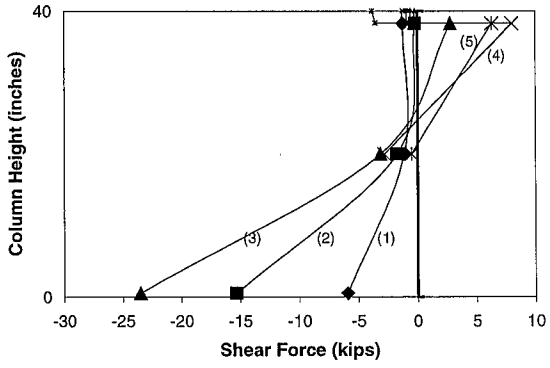

(c2) South Column in Story 1

* (1) – Cycle G1-1; (2) – Cycle G2-1; (3) – Cycle G3-1; (4) – Cycle G4-1; (5) – Cycle G5-1

Fig. 5.1.12 Internal Forces of Both Columns in the First Story at Peak Load in the South Direction

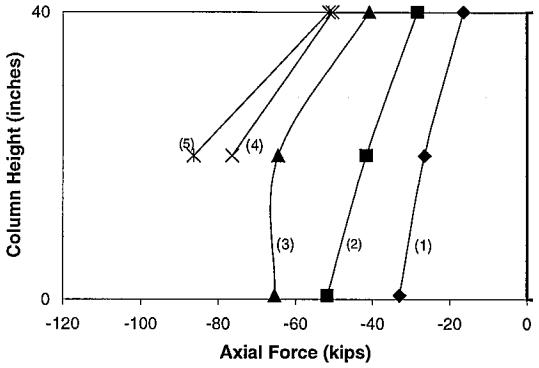

(a1) North Column in Story 1

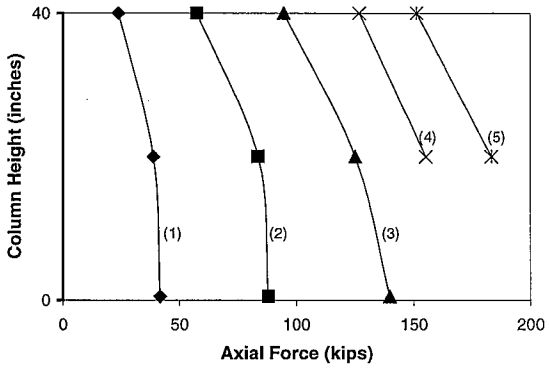

(a2) South Column in Story 1

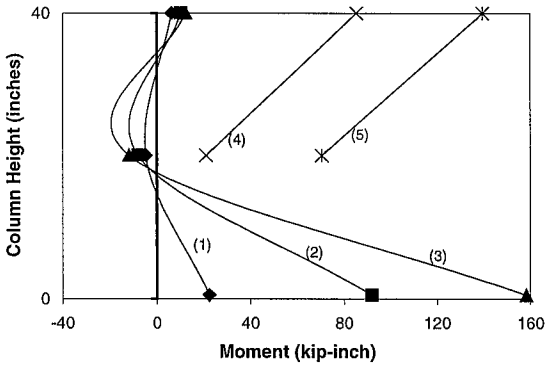

(b1) North Column in Story 1

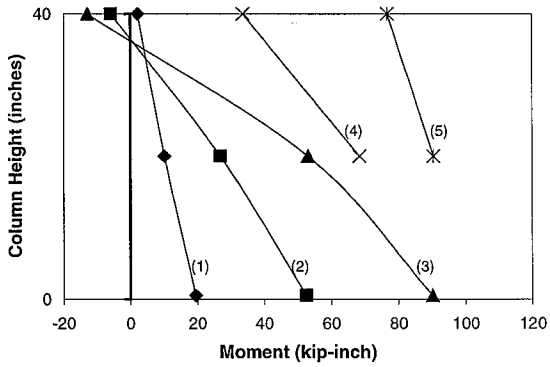

(b2) South Column in Story 1

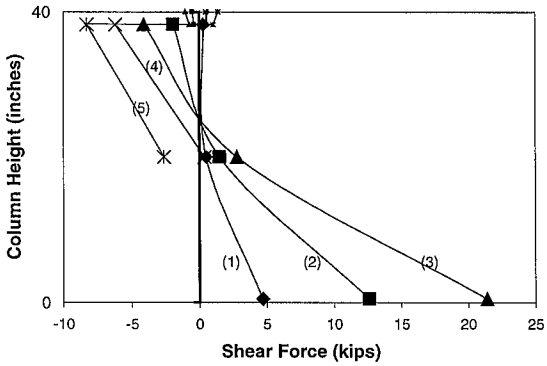

(c1) North Column in Story 1

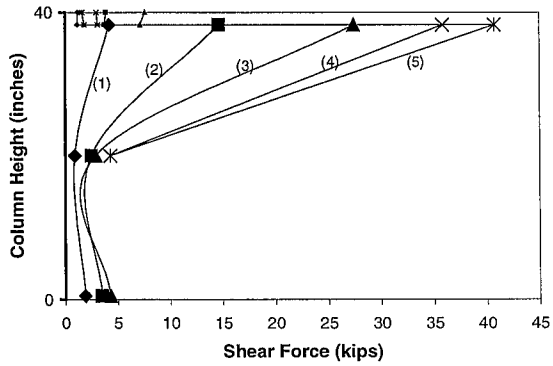

(c2) South Column in Story 1

(1) – Cycle G1-1; (2) – Cycle G2-1; (3) – Cycle G3-1; (4) – Cycle G4-1; (5) – Cycle G5-1

Fig. 5.1.13 Internal Forces of Both Columns in the First Story at Peak Load in the North Direction

5.1.2.2 Estimation of the Shear Forces in the Steel Columns

To estimate the abrupt change of the shear force in the steel column at the location where high strength bolts connected the seat angle to the column flange, the free-body diagrams of both columns in the first story are drawn in Figure 5.1.14. These diagrams correspond to the specimen being loaded in the south direction. Figure 5.1.14 shows three types of lateral force mechanisms along each column: bearing stress, σ_c, from the compressive strut in the infill wall; tensile force of the headed studs, T_{stud}, due to the deformation incompatibility between the steel columns and the infill wall; on the north column, tensile force V_{nsa} from the seat angle of north connection, and on the south column, tensile or compressive force, V_{ssa}, from the seat angle of the south connection. The tensile force from the studs can be assumed linearly distributed along the column due to the close spacing of the studs.

As shown in Figure 5.1.14, P_{nb}, M_{nb}, and V_{nb} are the axial force, bending moment and shear force at the top cross section of the north column (windward column), respectively; and P_{nd}, M_{nd}, and V_{nd} are the axial force, bending moment and shear force at

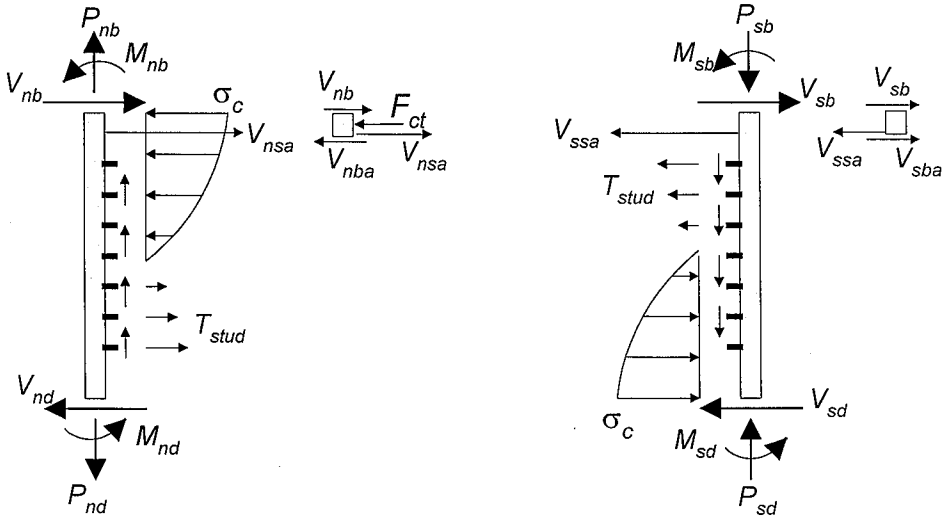

(a) North Column (b) South Column

Fig. 5.1.14 Free-Body Diagrams of the Steel Columns

the bottom cross section. The internal forces at the two cross sections were calculated and are listed in Tables 5.1.2 and 5.1.3. In the north column, the shear force just below the centerline of the bolts connecting the vertical leg of the seat angle to the column flange, V_{nba}, can be written as

$$V_{nba} = V_{nb} + V_{nsa} - F_{ct} \tag{5.1.1}$$

where

F_{ct} = the resultant of the bearing stress just above the centerline of the bolts connecting the vertical leg of the seat angle to the column flange

The resultant bearing force F_{ct} might be expressed as a percentage of the total bearing force, F_c, which is the resultant of the bearing stress along the entire contacted area between the infill wall and column flange. If the distribution is assumed to be parabolic and the bearing length is one-third of the net story height (Liauw, 1983a), then F_{ct} is approximately 20% of F_c for the specimen, based on the actual bolt locations in the seat angle. As a result, Eq. (5.1.1) can be rewritten as

$$V_{nba} = V_{nb} + V_{nsa} - 0.2F_c \tag{5.1.2}$$

An equilibrium equation can be established for all the lateral forces imposed on the north column as follows

$$F_c = V_{nb} + V_{nsa} + T_{stud} - V_{nd} \tag{5.1.3}$$

Substituting Eq. (5.1.3) into (5.1.2) yields

$$V_{nba} = 0.8(V_{nb} + V_{nsa}) + 0.2V_{nd} - 0.2T_{stud} \tag{5.1.4}$$

Table 5.1.2 shows that the shear force at the base of the north column in the first story, V_{nd}, increased up to only 6.2 kips during cycle G4-1-A, so that its effect on the magnitude of V_{nba} is negligible if multiplied by 0.2. It is next necessary to determine whether the stud force should be included in estimating V_{nba}. The behavior of the interface headed studs is discussed in detail in Chapter 6. As shown in Figure 4.4.1, stud SNC1, which is

at the bottom of the north interface of the first story, was instrumented by placing two strain gages on the opposite sides of the stud shank. The axial strain of the stud is plotted in Figure 6.2.5. The figure shows that in cycle G4-1-A, that maximum axial strain increased up to 350 με, representing a tensile force of approximately 1.1 kips if the deformation of stud is still in elastic range. 20% of the tensile force of stud SNC1 is only 0.22 kips. The tensile force of the other studs located above SNC1 is even smaller than 1.1 kips due to less deformation incompatibility between the steel column and the infill wall. Therefore, the effect of stud force can also be neglected in estimating shear force V_{nba}. As a result, Eq. (5.1.4) is reduced to

$$V_{nba} = 0.8(V_{nb} + V_{nsa}) \tag{5.1.5}$$

When the specimen is loaded in the south direction, Eq. (5.1.5) is used to calculated the shear force in the north column, V_{nba}, at the cross section just below the centerline of the bolts connecting the vertical leg of the seat angle to the column flange. In the same loading direction, the shear force in the south column, V_{sba}, at the cross section just below the centerline of the bolts connecting the seat angle to the column flange (Figure 5.1.14) can be calculated as

$$V_{sba} = V_{ssa} - V_{sb} \tag{5.1.6}$$

The shear forces of the top cross sections of both columns, V_{nb} and V_{sb}, have been obtained and are shown in Tables 5.1.2 and 5.1.3. It is next necessary to obtain the tensile or compressive force from the seat angles of the PR connections in order to estimate the shear forces V_{nba} and V_{sba}. Since the end of the beam flange was gaged along the longitudinal axis of the beam, the strain value of the beam flange is used to estimate the axial force in the horizontal leg of the PR connection. The force is calculated as follows:

$$F_{ts} = A_{bf} E_{bf} \varepsilon \tag{5.1.7}$$

where

F_{ts}= axial force in the horizontal leg of the top or seat angle

A_{bf}= area of one flange of the steel beam

E_{bf} = modulus of elasticity of the steel beam flange

ε = longitudinal strain in the beam flange

F_{ts} equals V_{nsa} for the seat angle of the north PR connection and V_{ssa} for the seat angle of the south PR connection. Table 5.1.4 shows the axial forces of the top and seat angles when the specimen reached the peak load in each loading direction.

As a summary, in the diagram of the shear force distribution in Figures 5.1.12 and 5.1.13, the magnitudes of the shear forces at the bottom, in the middle, and at the top of the column in the first story are calculated according to measured strain values from the rosettes on the column web (as per Appendix C). The magnitude of the abrupt change in shear force at the cross section where the bolts connect the seat angle to the column flange is estimated based on either Eq. (5.1.5) or Eq. (5.1.6).

Table 5.1.4 Axial Forces in the Horizontal Leg of Top and Seat Angles (kips)

Loading Direction	Cycle Number	North Joint		South Joint	
		Seat Angle	Top Angle	Seat Angle	Top Angle
South	G1-1-A	2.2	-0.7	-0.6	1.7
	G2-1-A	8.7	-0.2	0.7	6.0
	G3-1-A	17.8	0.6	3.0	15.8
	G4-1-A	25.9	-10.0	9.2	39.2
	G5-1-A	33.0	-13.5	10.1	50.4
North	G1-1-C	0.3	3.0	3.0	-0.2
	G2-1-C	1.4	9.6	10.7	1.1
	G3-1-C	3.1	15.7	19.8	1.6
	G4-1-C	6.7	39.6	32.8	-15.2
	G5-1-C	9.7	48.5	39.1	-13.9

5.1.2.3 Characteristics of the Internal Force Distributions in the Steel Columns

Several observations can be made regarding the internal force distributions along the columns in the first story, as shown Figures 5.1.12 and 5.1.13:

1) The axial force of the windward column was always compressive and that of the leeward column was always tensile, indicating that these two axial forces comprised an important couple to resist the overturning moment. The axial force decreased gradually along the column height due to the decrease in overturning moment.

2) The magnitude of the tensile force in the windward column was greater than that of the compressive force in the leeward column by a large amount. This phenomenon was due to the fact that the concrete infill wall shared more overturning moment with the leeward column on the unseparated side of the beam-infill interface than did the headed studs with the windward column on the separated side of the interface. With the gradual yielding and failing of the headed studs along the interface, the windward column had to carry an increasing amount of tensile force.

3) During the first cycle of the first three groups of cycles, the bending moment along the windward column changed its direction from the base to the top of the column, indicating a double curvature deformation pattern of the column; the bending moment along the leeward column decreased rapidly from the base to the middle of the column. Starting from loading cycle G4-1, the bending moment at the top of the windward column changed its direction by having a large shift in magnitude (the moment increased to –50 kip-inches for the north column in cycle G4-1-A and 34 kip-inches for the south column in cycle G4-1-C). Thus, the deformation pattern of the windward column changed from a double curvature to a single curvature. Also starting from loading cycle G4-1, the bending moment at the top of the leeward column increased rapidly and the deformation pattern of the leeward column has a evident single curvature.

4) For the windward column, the maximum shear force occurred at the cross section just below the centerline of the bolts connecting seat angle to the column flange. For the leeward column, the maximum shear force occurred at the base of the column.

5.2 Performance of the Middle Beam in the Connection Regions

5.2.1 Strain Profiles at the Ends of the Middle Beam

The middle beam was stiffened on both sides by the RC infill wall, with its main function being to transfer the lateral load from the second story to the first story through interface studs in the early loading stages. However, both ends of the beam might be subjected to an increasing amount of shear force and bending moment caused by the compressive stress from the infill wall, and due to the yielding and failure of the interface headed stud connectors. The design of the specimen was targeted to force the majority of the plastic deformation into the PR connections instead of the ends of the beam. Therefore, both ends of the beam were instrumented by using strain gages to monitor the relative behavior of the beam to the PR connection, and also to estimate the force transferred by the PR connections.

As shown in Figure 3.4.8, five strain gages were placed at each end of the middle beam, at a cross section 6 inches away from the surface of the column flange. All five strain gages were oriented along the longitudinal direction of the beam. As a result, Figure 5.2.1 shows the longitudinal strain profile across the beam depth when the specimen reached its peak load in the south direction, while Figure 5.2.2 shows the longitudinal strain profile when the specimen reached its peak load in the north direction. Only the results of the first cycle of each group of cycles were plotted in both figures for simplicity. At the north end, the maximum strain of the bottom flange was approximately 1200 με, achieved during cycle G5-1-A; the maximum strain of the top flange was approximately 1700 με, barely surpassing the yielding limit, achieved during cycle G5-1-C. At the south end, the maximum strain of the bottom flange was approximately 1500 με, achieved during cycle G5-1-C; the maximum strain of the top flange was again approximately 1700 με, barely surpassing the yielding strain, achieved at cycle G5-1-C. Figures 5.2.1 and 5.2.2 show the symmetry of the longitudinal strain distribution in two loading directions. At each end, the magnitude of the slope of the longitudinal strain distribution, as well as the magnitude of the average strain, increased gradually with each group of cycles until loading cycle G5-1. This indicated that the beam ends and thus the

PR connections were subjected to increasing tensile force and bending moment with each group of cycles. The cross section at the south end did not remain plane by cycle G6-1-A, while the cross section of the north end did not remain plane by cycle G6-1-C.

As shown in Figure 3.4.8, one strain rosette was placed near the web angle at each end of the middle beam. The strain readings from three legs of the rosette were used to calculate the shear strain in the web. Figure 5.2.3 shows the shear strain at the center of the north end and Figure 5.2.4 shows the shear strain at the center of the south end. The maximum magnitude of the shear strain was approximately 2200 με at the north end and 2400 με at the south end, achieved at cycle G6-1-A. Although the shear strains were slightly below the yield limit of shear strain, which was approximately 2700 με for the beam web, a few thin yield lines were observed in the beam web near the strain rosette during the test. This minor yielding was induced by the combined tensile stress and shear stress near the web angle. The appearance of the yield lines showed that, as anticipated in specimen design, the shear deformation of the beam web was limited and, as will be shown in the next section, the majority of the plastic deformation in the connection region was contributed by the connection angles.

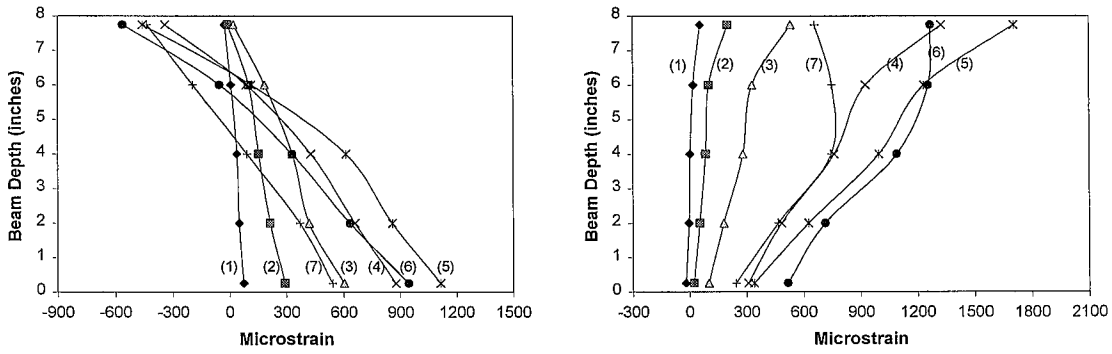

(a) North End of the Middle Beam (b) South End of the Middle Beam

* (1) – G1-1; (2) – G2-1; (3) – G3-1; (4) – G4-1; (5) – G5-1; (6) – G6-1; (7) – G7-1

Fig. 5.2.1 Longitudinal Strain Profile of the Middle Beam at Peak Load in the South Direction

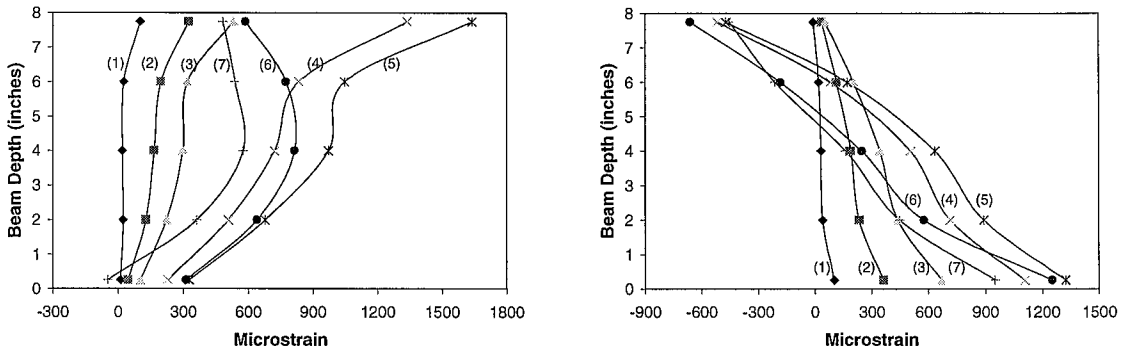

(a) North End of the Middle Beam (b) South End of the Middle Beam

* (1) – G1-1; (2) – G2-1; (3) – G3-1; (4) – G4-1; (5) – G5-1; (6) – G6-1; (7) – G7-1

Fig. 5.2.2 Longitudinal Strain Profile of the Middle Beam
at Peak Load in the North Direction

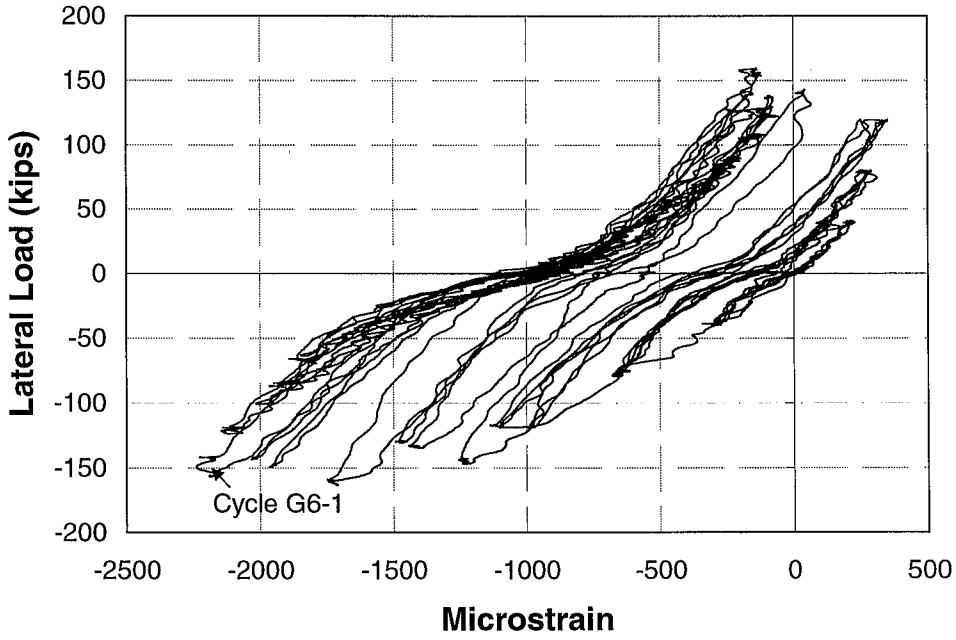

Fig. 5.2.3 Shear Strain from Strain Rosette B_NJ_BW_R1
at the North End of the Middle Beam

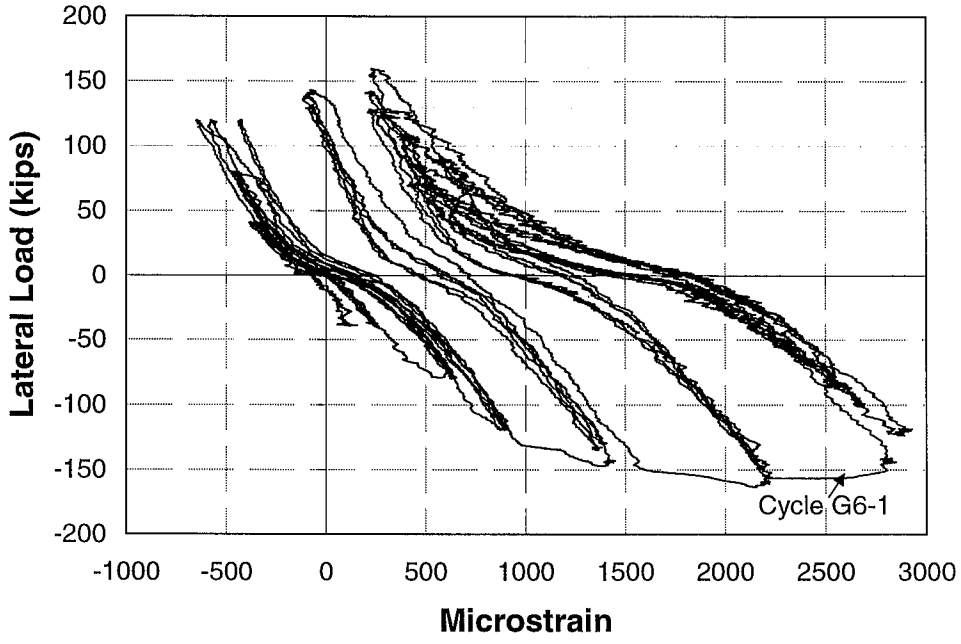

Fig. 5.2.4 Shear Strain from Strain Rosette B_SJ_BW_R1
at the South End of the Middle Beam

5.2.2 Comparison of the Internal Forces at the Two Ends of the Middle Beam

As discussed in the last sub-section, the longitudinal strain profile of each end of the middle beam was measured with two strain gages on the flange and three strain gages on the web. The shear strain profile was measured with one strain rosette near the web double angle. Therefore, the procedure proposed in Appendix C for calculating the internal forces of the steel columns can also be used to estimate the internal forces at both ends of the middle beam. Table 5.2.1 lists the axial force, bending moment and shear force at each end of the beam. For simplicity, only the internal forces at the peak load of the first cycle of each group of cycles are listed. The corresponding sign convention of these internal forces is shown in Figure 5.2.5.

Table 5.2.1 shows that the beam ends were always in tension whenever the specimen reached its peak load in the north direction or in the south direction. The axial force at peak lateral load increased with each group of cycles until the specimen reached its maximum strength during cycle G5-1, and then decreased with each group of cycles.

Figure 5.2.6 compares the axial forces at the two ends of the middle beam versus the total drift of the specimen, where the y-axis is the ratio of the measured axial force P_{pr} at the peak load of the first cycle of each group of cycles to the axial yield strength of the steel

Table 5.2.1 Forces at Ends of Middle Beam

Cycle No.	Loading Direction	Axial Force P_{pr} (kips)		Moment M_{pr} (kip-inches)		Shear Force V_{pr} (kips)	
		NJ*[1]	SJ	NJ	SJ	NJ	SJ
G1-1 (0.05% drift)	S*[2]	3.5	1.4	14.9	10.8	5.4	4.5
	N	4.3	4.4	-11.3	-14.7	-4.2	-7.6
G2-1 (0.2% drift)	S	17.6	10.9	43.7	24.6	13.6	11.5
	N	20.1	21.7	-38.4	-46.9	-5.1	-8.9
G3-1 (0.3% drift)	S	36.1	33.1	85.2	61.9	21.3	17.7
	N	34.2	39.6	-58.1	-89.6	-5.7	-13.1
G4-1 (0.5% Drift)	S	39.7	88.1	184.0	151.4	25.0	28.0
	N	84.0	43.9	-155.5	-237.2	-0.9	-1.4
G5-1 (0.75% Drift)	S	52.0	113.4	238.4	204.3	34.5	***Y***
	N	107.9	59.0	-182.6	-263.6	2.9	-
G6-1 (1.0% Drift)	S	30.0	112.2	226.5	125.9	43.9	-
	N	72.5	28.6	-42.0	-280.7	1.6	-
G7-1 (1.25% Drift)	S	8.7	66.4	154.7	68.5	38.5	-
	N	44.3	20.9	-75.8	-212.6	4.6	-

1: NJ = North connection region; SJ = South connection region
2: S = Loaded in the south direction; N = Loaded in the north direction

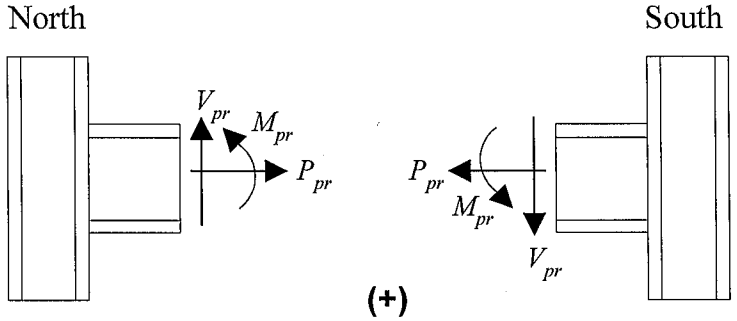

Fig. 5.2.5 Sign Convention of the Internal Forces at Both Ends of the Beam

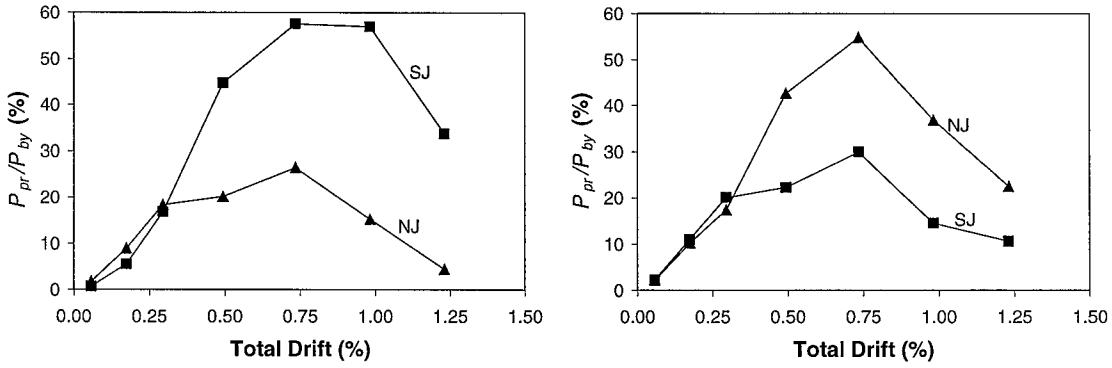

a) Loaded in the South Direction

b) Loaded in the North Direction

Fig. 5.2.6 Variation of the Tensile Force Resisted at the Ends of the Middle Beam

beam P_{by}. It shows that the magnitude of the axial forces at each end were close to each other at the peak load of cycles G1-1, G2-1 and G3-1. However, they show substantial difference at the peak load of cycle G4-1. Starting from cycle G4-1, the axial force at the south end surpassed that at the north end by $0.2P_{by}$ to $0.4P_{by}$ when the specimen was loaded in the south direction, while the axial force at the north end surpassed that at the south end by $0.2P_{by}$ to $0.25P_{by}$ when the specimen was loaded in the north direction. An examination of the force balance of the middle beam indicated that this phenomenon appeared to be related to the sequence of stud failure along the interfaces of the middle beam. Figure 5.2.7 shows the horizontal forces acting on the portion of the middle beam between the gaged cross sections at the two ends, where the directions of the forces are corresponding to the specimen being loaded in the south direction. During the first groups of cycles, the shear force of the headed studs along the top interface was balanced by that along the bottom interface so that the axial force at the two ends were very close to each other. During cycles G3-2, G3-3, and G4-1-A, several of the headed studs failed along the top interface of the middle beam. As a result, the increasing lateral force in cycle G4-1-A was carried by the compressive strut in the infill wall, which imposed an 88 kip tensile force at the south end of the middle at the peak load of this cycle (Table 5.2.1). On the other hand, the headed studs along the bottom interface remained intact and continued to transfer more shear force. Therefore, the axial force was reduced along the middle

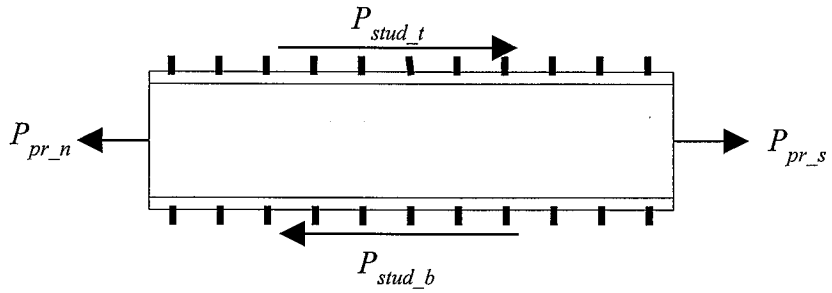

Fig. 5.2.7 Horizontal Forces on the Middle Beam

beam and was only 40 kips at the north end. The same mechanism caused a higher axial force in the north end of the middle beam upon loading reversal. Because the headed studs along the bottom interface of the middle beam failed much later than those along the top interface of the middle beam, as discussed in Section 6. 4, this phenomenon continued in the later loading cycles, with the discrepancy of the axial forces at two ends increasing with each cycle due to the increasing number of failed studs along the top interface of the middle beam.

Table 5.2.1 shows that the bending moment at each end of the middle beam changed its direction upon changing of the loading direction during the test. The bending moments of both ends were positive when the specimen was loaded in the south direction and negative when the specimen was loaded in the north direction. Figure 5.2.8 compares the bending moments at the two ends of the middle beam versus the total drift of the specimen, where the y-axis is the ratio of the measured bending moment M_{pr} at the peak load of the first cycle of each group of cycles to the plastic moment of the steel beam M_{by}. It shows that the bending moment of the north end was always greater than that of the south end when the specimen was loaded in the south direction, and the bending moment of the south end was always greater than that of the north end when the specimen was loaded in the north direction. This phenomenon may relate to the constraint of the infill wall on the middle beam due to the overturning moment effect on the specimen. When the specimen was loaded in the south direction, the overturning moment tended to separate the infill wall and middle beam along the interfaces of the north portion while closing the interfaces of the south portion of the middle beam. Therefore, the north end of

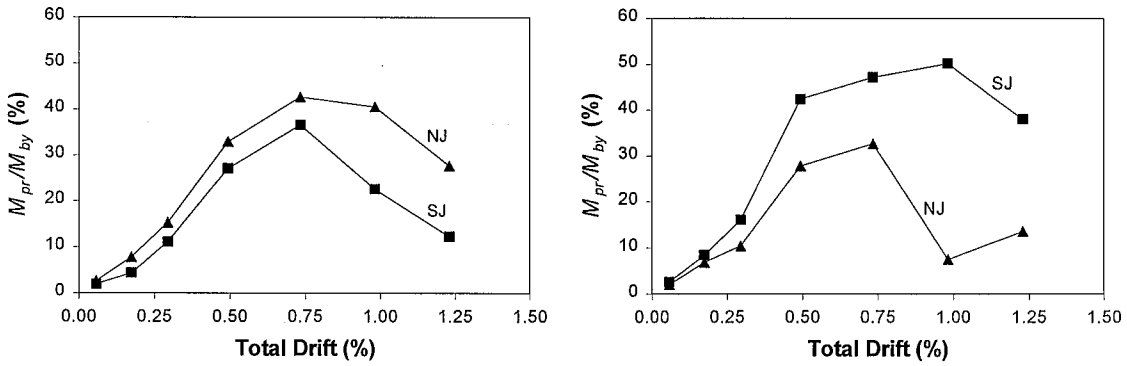

a) Loaded in the South Direction b) Loaded in the North Direction

Fig. 5.2.8 Variation of the Bending Moment Resisted at the Ends of Middle Beam

the beam was able to rotate more freely than the south end due to less constraint from the infill wall. The resulting bending moment was thus greater at the north end than at the south end.

The von Mises criterion proposed in Appendix C was used to determine the yielding of the steel beam at the cross section where the strain rosette was placed. Table 5.2.1 shows that the cross section of the north end did not yield during the entire loading history and that of the south end yielded in cycle G5-1-A. However, as stated in Section 4.4, minor yielding was found near the shear tabs of the middle beam just after the 0.3% loading cycles. The inconsistency between the estimation and the observation was most likely due to the fact that the shear tabs were welded to the web of the steel beam. The welding process generated residual stresses in the beam web near the web double angle, and caused the earlier yielding in the web of the middle beam under combined tensile stress and shear stress. The maximum value of the shear force shown in Table 5.2.1 was 43.9 kips at the north end of the beam, approximately 70% of the nominal shear strength of the beam. In calculating the shear force at the end of the beam, the stress-strain relationship was assumed to be linear during the entire loading history, although yielding in the web did occur starting at the 0.3% cycles, as discussed above. Therefore, the actual shear force at the north end would probably be less than 43.9 kips if the effect of plasticity had been included.

5.3 Behavior of the Partially-Restrained Connections

5.3.1 Behavior of the Top and Seat Angles of the Partially-Restrained Connections

As shown in Figure 3.4.8, at each top or seat angle of the partially-restrained (PR) connections of the middle beam, one strain gage was placed in the middle of the k-line of the vertical leg and two strain gages were placed near the edge of the k-line of the horizontal leg. Figures B.4.1 to B.4.12 (Appendix B.4) show readings of these strain gages versus the total lateral load. The characteristics of these strains are shown in Table 5.3.1. Several observations can be made from Figures B.4.1 to B.4.12.

1) The strain in the k-line region of the vertical leg was less than that of the horizontal leg both for both the seat angle and the top angle. For the seat angle of the north connection, the strain in the k-line region of the vertical leg (gage A_NJ_BA_G1 of Figure B.4.1) never surpasses the yield limit, while those of the horizontal leg (gage A_NJ_BA_G2 of Figure B.4.2 and gage A_NJ_BA_G3 of Figure B.4.3) started a rapid increase of approximately 1000 με during cycle G6-1-A, as the specimen approached its peak load, and kept growing steadily during the later loading cycles. Table 5.3.1 shows that the maximum strain magnitude was 5870 με at gage A_NJ_BA_G2 and 4740 με at gage A_NJ_BA_G3. For the top angle of the north connection, although the strain in the k-line region of the vertical leg (gage A_NJ_TA_G1 of Figure B.4.4) did surpass the yield limit and reached more that 9000 με at the last loading cycle, those of the horizontal leg (gage A_NJ_TA_G2 of Figure B.4.5 and gage A_NJ_TA_G3 of Figure B.4.6) had a substantial and rapid increase during cycle G5-1-C as the specimen reached its peak load and even stretched into the hardening ranges in later cycles. As shown in Figure 5.3.1, this observation contradicts to the assumption that the plastic hinge occurs only along the k-line of vertical leg of the top or seat angle and along the edge of the bolts in the vertical leg (Kim and Chen, 1998). There were two possible reasons for the plastic hinge development along the k-line of the horizontal leg. First, the gap between the beam edge to the surface of the column flange, which was 0.5 inches, was larger than the thickness of the leg and allowed the horizontal leg of the angle to rotate near the k-line. Second, the edge of the beam flange might bend the horizontal leg in resisting shear caused by the

Table 5.3.1 Strain Characteristics of Top and Seat Angles of the PR Connections

Location of each gage group	Individual location	Gage name	Maximum value (με)	Cycle No. at Max. value	Minimum value (με)	Cycle No. at Min. value	Yielding check	Cycle No. if yielded	Hardening check
Seat angle of the north connection	Vertical leg	A_NJ_BA_G1	1280	G5-1-A	-1720	G6-1-C	No		No
	Horizontal leg	A_NJ_BA_G2	5870	G9-2-A	-830	G5-1-C	Yes	G5-1-A	No
		A_NJ_BA_G3	590	G5-1-C	-4740	G9-2-A	Yes	G5-2-A	No
Top angle of the north connection	Vertical leg	A_NJ_TA_G1	9390	G9-2-C	-2610	G6-1-A	Yes	G5-1-D	No
	Horizontal leg	A_NJ_TA_G2	41000	G9-2-C	-1570	G5-1-A	Yes	G5-1-C	Yes
		A_NJ_TA_G3	1300	G5-1-A	-20100	G9-2-C	Yes	G5-1-C	Yes
Seat angle of the south connection	Vertical leg	A_SJ_BA_G1	1700	G5-1-C	-3200	G6-2-A	Yes	G6-1-A	No
	Horizontal leg	A_SJ_BA_G2	14400	G9-2-C	-240	G4-1-B	Yes	G4-2-C	No
		A_SJ_BA_G3	250	G4-3-B	-11000	G9-2-C	Yes	G5-1-C	No
Top angle of the south connection	Vertical leg	A_SJ_TA_G1	9350	G9-2-A	-6330	G7-1-C	Yes	G5-1-C	No
	Horizontal leg	A_SJ_TA_G2	43600	G9-2-A	-1044	G5-1-C	Yes	G5-1-A	Yes
		A_SJ_TA_G3	1231	G5-1-C	-21990	G9-2-A	Yes	G5-1-A	Yes

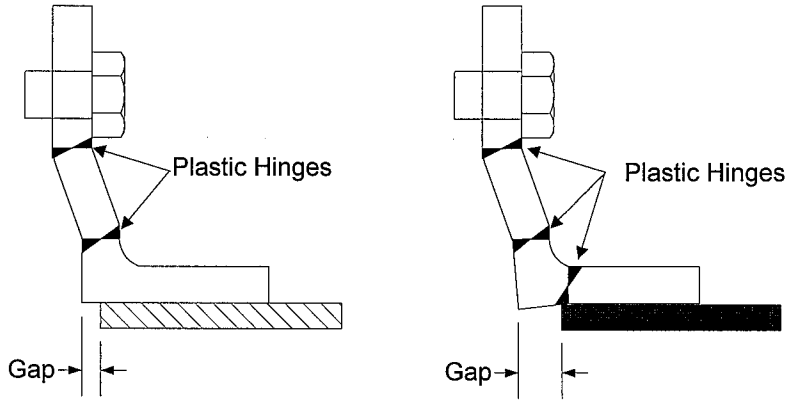

(a) from Kim and Chen (1998) (b) from Present Test

Figure 5.3.1 Locations of the Plastic Hinges in the Angles

compression strut in infill wall. The plastic hinges in the horizontal legs are likely to be prevented in the actual construction since thickness of the top or seat angle is usually larger than the 0.5 inch gap distance.

2) In the same k-line region, the strain in the seat angle was far less than the strain in the top angle of each connection. For example, Table 5.3.1 shows that the maximum reading of strain gage A_lJ_TA_G2 on the top angle was 41,000 με, almost 7 times that of strain gage A_NJ_BA_G2 on the seat angle in the north connection. There are two possible factors responsible for this phenomenon: first, the rupture and crushing of the concrete in the bottom corners of the second story occurred earlier than that in the top corners of the first story so that the top angle lost the restraint from concrete earlier; second, the headed studs along the bottom interface of the second story fractured much earlier than the studs along the top interface of the first story so that the compressive strut force was higher in the second story than in the first story. As a result, the permanent deformation in the top angle was more severe than that in the seat angle after testing.

3) The majority of the yielding along the k-lines of the top and seat angles started during the first cycle of the 0.75% cycles (cycle G5-1) when the specimen achieved its maximum strength. Table 5.3.1 shows only the strain at gage A_SJ_BA_G2 reached its yielding limit during cycle G4-2-C; all the others reached their yielding limit during cycle G5-1.

4) Along the k-line of the horizontal leg of the top and seat angles, the initial yielding was primarily induced by the bending moment. However, after the specimen reached its maximum strength, the axial strain demands also played an important role for the progression of inelasticity in the k-line region of the horizontal legs. The gages on the horizontal leg were placed on the opposite side of each leg. The average of the readings from these two gages was the strain induced by the axial force along the leg. The difference of the readings from these two gages was the strain induced by the bending moment along the k-line. Figure 5.3.2 shows the strain caused by the axial force in the horizontal leg of the top angle of the north connection. Figure 5.3.3 shows the strain caused by the bending moment along the k-line. It can be seen that the strain induced by the bending moment was greater than that induced by the axial force from the beginning, and it also increased faster with each loading level. For example, at cycle G4-3-C, the maximum reading of the axial strain was around 190 με, while the maximum reading of the bending strain has reached 1500 με. The bending strain increased abruptly by approximately 10000 με during cycle G4-1-C, and continued this trend during the remaining loading cycles. The maximum bending strain reached more than 30000 με during the final loading cycles. The axial strain increased abruptly by approximately 2500 με during cycle G5-1-C, and accumulated during the remaining loading cycles. The maximum axial strain reached more than 10000 με during the last loading cycle.

5.3.2 Load–Deformation Relationship of the Partially-Restrained Connections

As discussed in Section 5.2.2, the procedure proposed in Appendix C for calculating the internal forces of the steel columns can also be used to estimate internal forces at both ends of the middle beam. Since the gaged cross section (Figure 3.4.8) at each end of the middle beam was close to the tip of the top and seat angle, the recovered forces may be regarded as the predominant forces transferred through the PR connection to the steel column and the compressive strut in the infill wall. The sign convention of the internal forces at each end of the beam is defined in Figure 5.2.5.

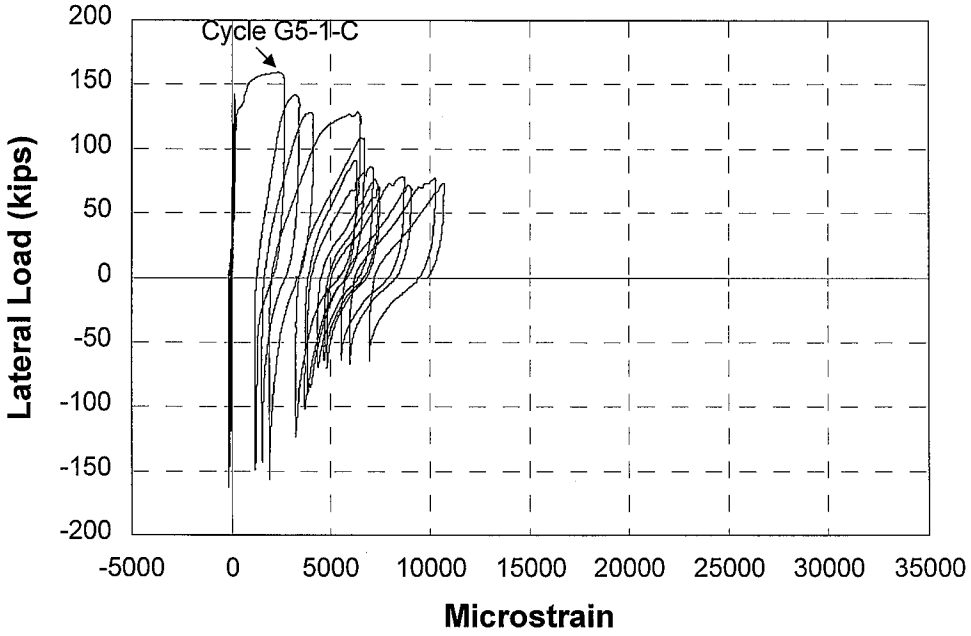

Fig. 5.3.2 "Axial Strain" Induced by the Axial Force along the Horizontal Leg of the Top Angle of the North Connection

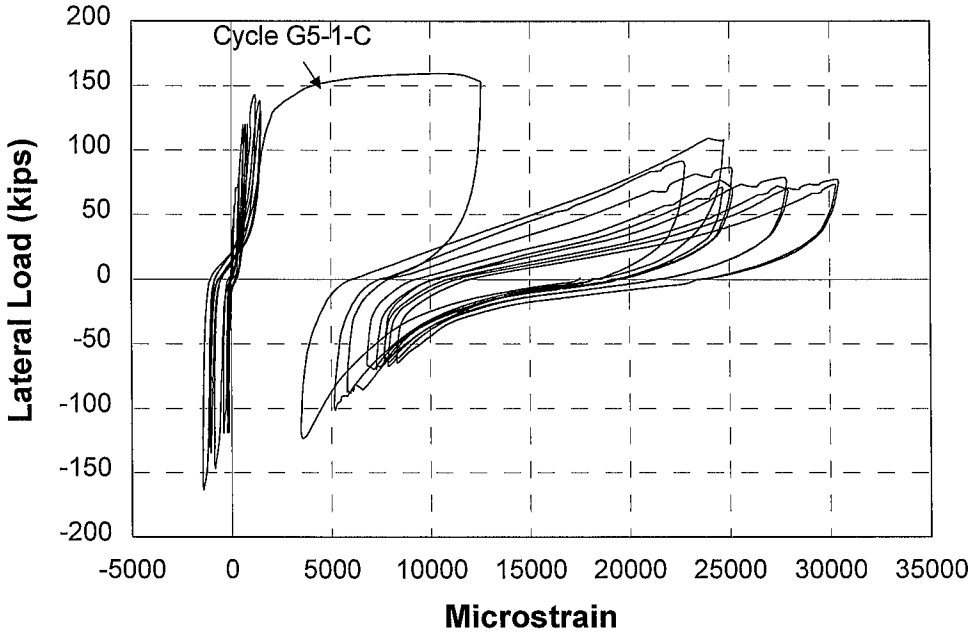

Fig. 5.3.3 "Bending Strain" Induced by the Bending Moment along the k-line of the Horizontal Leg of the Top Angle of the North Connection

As shown in Figure 3.4.7, in the north connection of the middle beam, two LVDTs L_RO_NJ_1 and L_RO_NJ2 were placed along the bottom flange and top flange, respectively, to measure the elongation and rotation of the PR connection. The rotation of the PR connection is calculated as follows:

$$\theta_{PR} = \frac{\Delta_{(L\_RO\_NJ\_2)} - \Delta_{(L\_RO\_NJ-1)}}{h_{PR}} \tag{5.3.1}$$

and the elongation of the PR connection is calculated as follows:

$$\Delta_{PR} = \frac{\Delta_{(L\_RO\_NJ\_2)} + \Delta_{(L\_RO\_NJ-1)}}{2}$$

where

h_{PR} = the distance between the cores of these two LVDTs

$\Delta_{(L\_RO\_NJ\_1)}$ = the readings of LVDT L_RO_NJ_1

$\Delta_{(L\_RO\_NJ\_2)}$ = the readings of LVDT L_RO_NJ_2

The readings of LVDTs L_RO_SJ_1 and L_RO_SJ_2 in the south connection are used to calculate the rotation and elongation of the south PR connection in the same way.

Two types of the load-deformation relationships are considered simultaneously for the PR connection in the S-RCW system: a moment–rotation relation and an axial force–elongation relation. Figure 5.3.4 shows the moment–rotation relation of the north PR connection of the middle beam, and Figure 5.3.5 shows that of the south PR connection. Figure 5.3.6 shows the axial force–elongation relation of the north PR connection of the middle beam, and Figure 5.3.7 shows that of the south PR connection. The readings were truncated after the 1.25% cycles because the holders of LVDTs L_RO_NJ2 and L_RO_SJ_2 were loosened by falling concrete during the 1.25% cycles. For clarity and simplicity, only cycles up to the 0.75% drift level are plotted in Figure 5.3.3 to 5.3.6. The entire history of each relation is shown in Appendix B. Several observations can be made about the hysteretic behavior of the PR connections from the figures:

1) Figures 5.3.4 and 5.3.5 show the PR connections were very stiff in rotation during the early loading cycles due to the restraint from the concrete. For the north PR connection, up to cycle G3-2, the change of rotation was close to zero when the specimen was loaded in the north direction, and the moment varied almost linearly with the rotation by a stiffness of approximately 240,000 kip-inches/radian, when the specimen was loaded in the south direction. For the south PR connection, also up to cycle G3-2, the change of the rotation was close to zero when the specimen was loaded in the south direction, and the moment varied almost linearly with the rotation by a stiffness of approximately 180,000 kip-inches/radian, when the specimen was loaded in the north direction.

2) Figures 5.3.6 and 5.3.7 show the PR connection was also very stiff in elongation. Both connections were in tension during the entire loading history. The tensile force varied almost linearly with the elongation by a stiffness of approximately 14,000 kips/inch.

3) The north PR connection experienced a large increase of rotation and elongation with an abrupt decrease of stiffness when the specimen approached its peak cycle during cycles G4-1-C and G5-1-C. The south PR connection experienced a large increase of rotation and elongation with an abrupt decrease of stiffness when the specimen approached its peak load during cycles G4-1-A and G5-1-A. The drop of both rotation and tensile stiffness during cycle G5-1 coincided with the yielding along the k-lines of horizontal legs of the top and seat angles (Section 5.3.1). Therefore, it can be concluded that the plastic mechanism of the PR connections of the middle beam has formed during the first cycle of 0.75% cycles.

4) The maximum capacity of the north PR connection was achieved during cycle G5-1-C, with the bending moment approximately equaling 180 kip-inches and the axial tensile force approximately equaling 105 kips. The maximum capacity of the south PR connection was achieved during cycle G5-1-A, with the bending moment approximately equaling 200 kip-inches and the axial tensile force approximately equaling 110 kips.

5) Figures 5.3.4 and 5.3.5 show that the substantial increase of the rotation with an abrupt drop of the rotational stiffness always occurred when the moment put the top

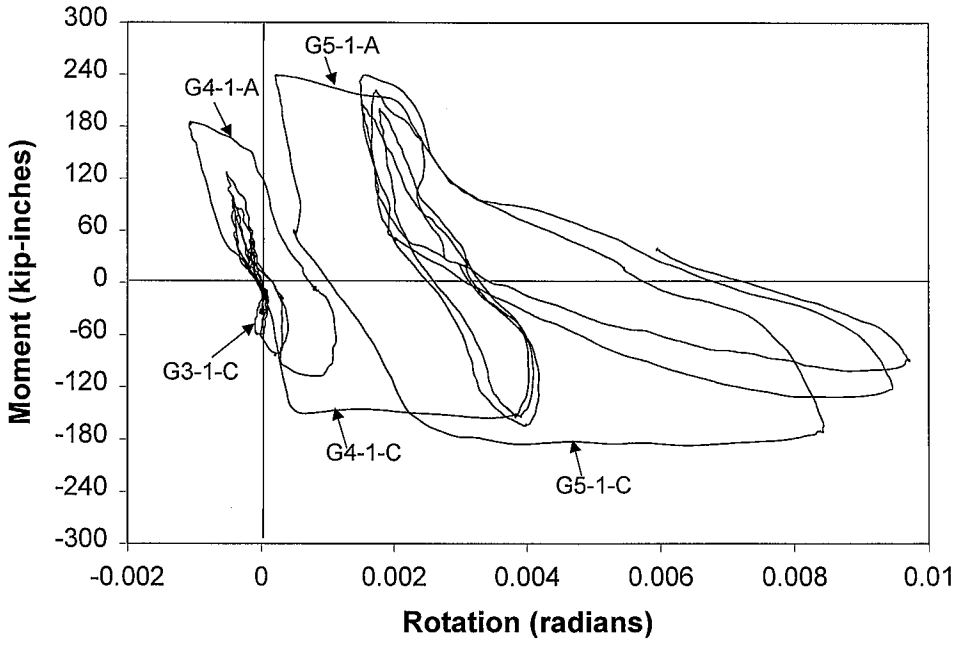

Fig. 5.3.4 Rotation versus Moment for the North PR Connection

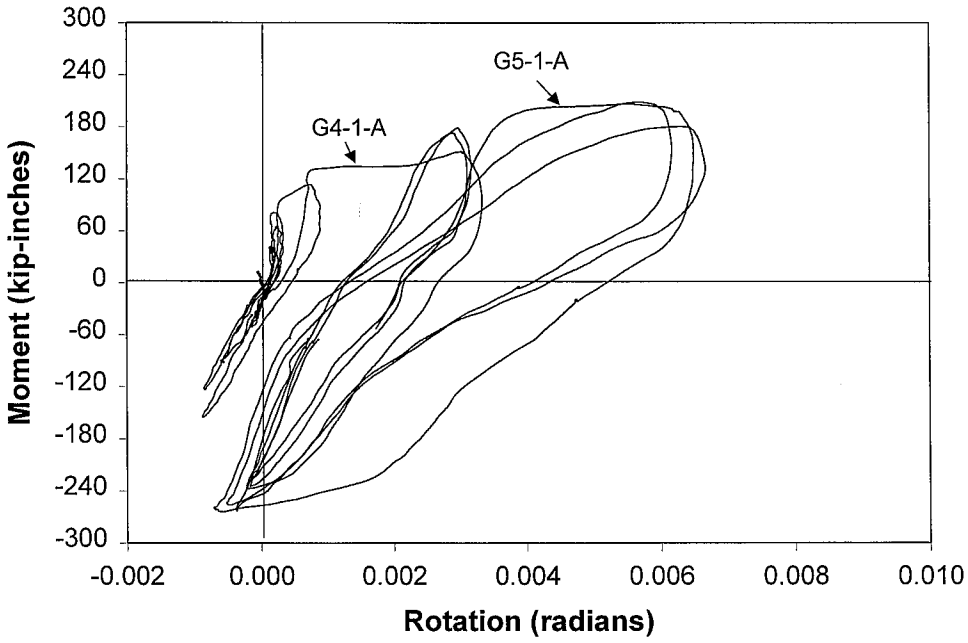

Fig. 5.3.5 Rotation versus Moment for the South PR Connection

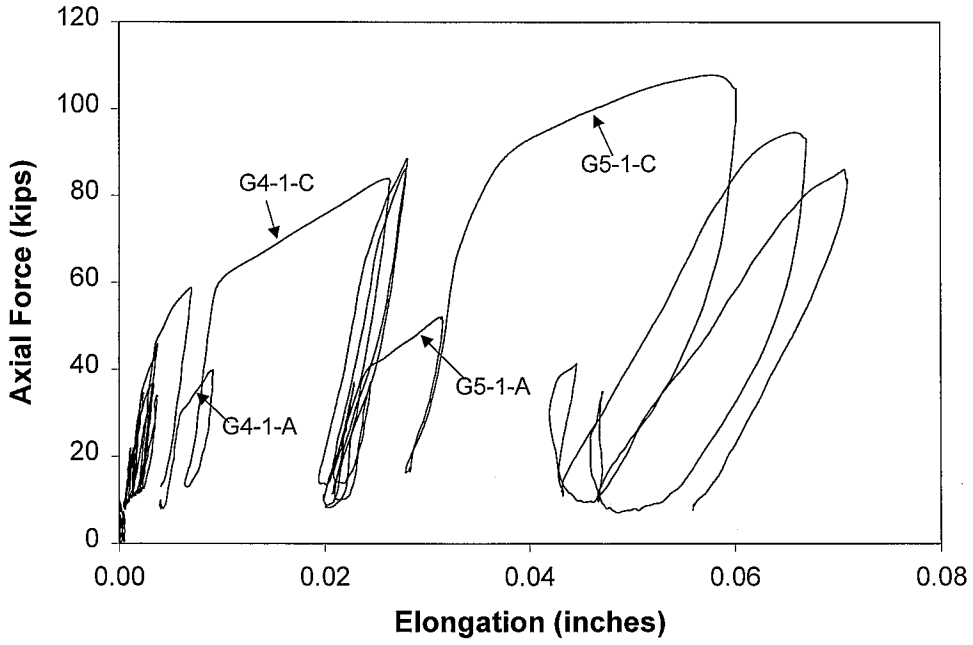

Fig. 5.3.6 Elongation versus Axial Force for the North PR Connection

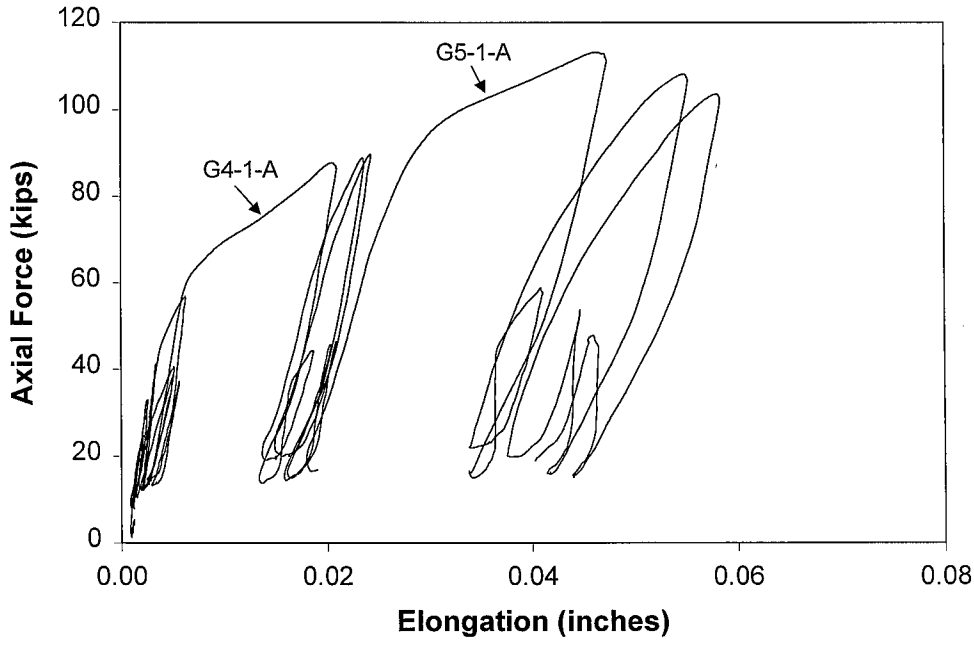

Fig. 5.3.7 Elongation versus Axial Force for the South PR Connection

angle in tension and the seat angle in compression. This behavior might be related to the fact that the concrete around the top angle was disrupted earlier than the concrete around the seat angle. The deformation of the top or seat angle in tension tends to be restrained by the corner concrete due to the compressive strut action. Because of the earlier disruption of the concrete around the top angle, the compressive stiffness of the concrete there decreased faster than that around the seat angle. As a result, the top angle was subjected to less restraint when in tension and had a larger deformation than the seat angle.

5.4 Deformation of the Panel Zones

In each column panel zone at the level of the middle beam, two 0.1 inch LVDTs were installed diagonally to measure the deformation of the panel zone. Figure 3.4.7 shows that orientation of LVDTs L_PD_NC_1 and L_PD_NC_2 in the panel zone of the north column. LVDTs L_PD_SC_1 and L_PD_SC_2 in the panel zone of the south column were orientated in the same way as L_PD_NC_1 and L_PD_NC_2, respectively. Different from all the other LVDTs, these four 0.1 inch LVDTs were calibrated so that the positive reading represented shortening and the negative reading represented elongation. Figures 5.4.1 and 5.4.2 show the readings of LVDTs in the panel zone of the north column. Figures 5.4.3 and 5.4.4 show the readings of the LVDTs in the panel zone of the south column.

It can been seen that, before cycle G5-1, the panel zone of the north column elongated along both diagonal directions when the specimen was loaded in the south direction and shortened along both diagonal directions when the specimen was loaded in the north direction. The reason was that the axial force was the dominant internal force in this panel zone before cycle G5-1. This panel zone elongated along the column axis under tensile force when the specimen was loaded in the south direction and shortened along the column axis under compressive force when the specimen was loaded in the north direction. At cycle G5-1, there was a sudden elongation along LVDT L_PD_NC_1 and further shortening along LVDT L_PD_NC_2 when the specimen approached its peak

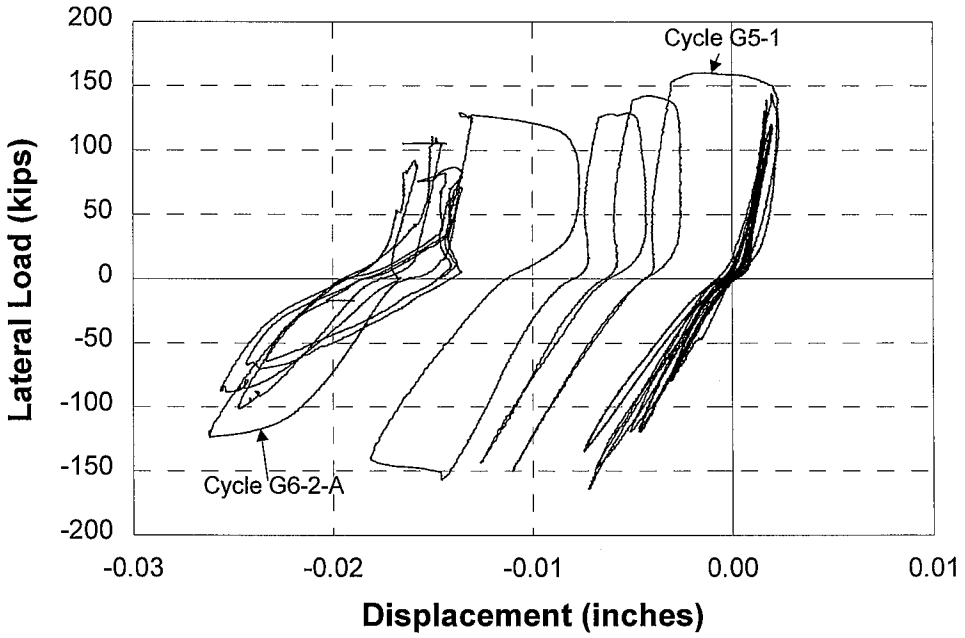

Fig. 5.4.1 Reading of LVDT L_PD_NC_1 in the Panel Zone of North Column

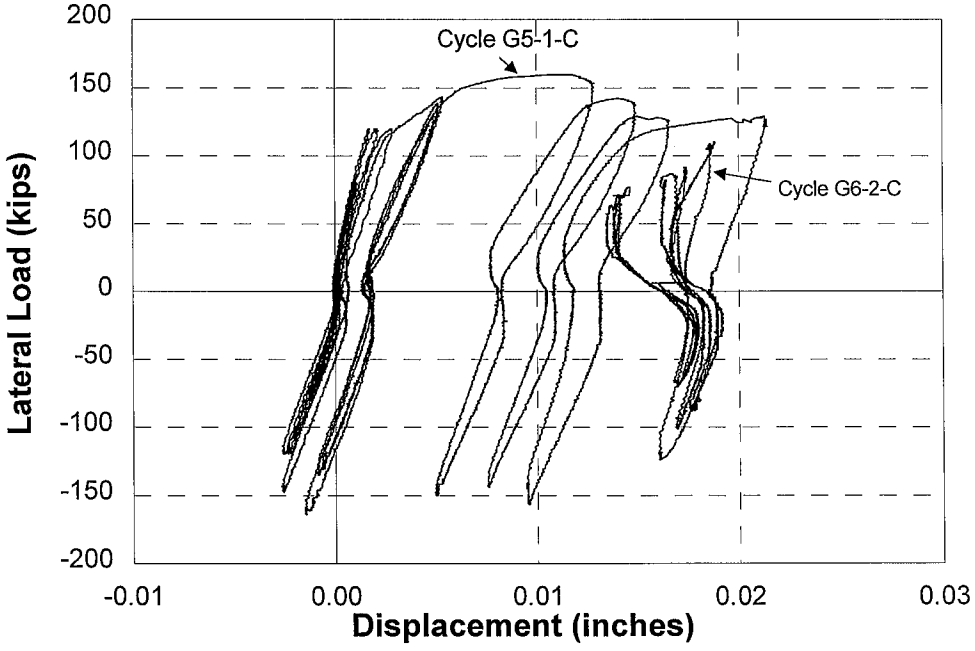

Fig. 5.4.2 Reading of LVDT L_PD_NC_2 in the Panel Zone of North Column

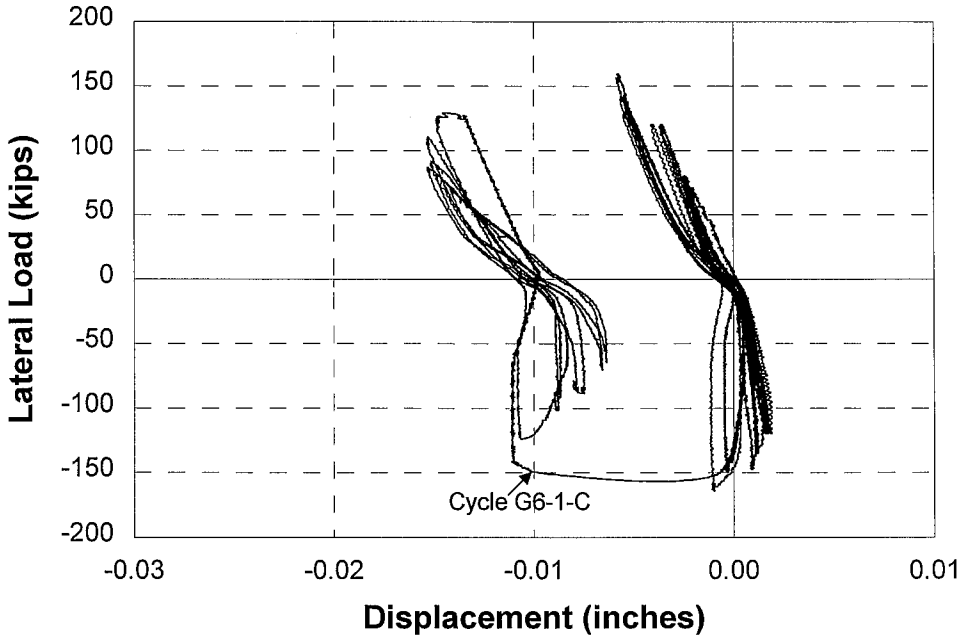

Fig. 5.4.3 Reading of LVDT L_PD_SC_1 in the Panel Zone of South Column

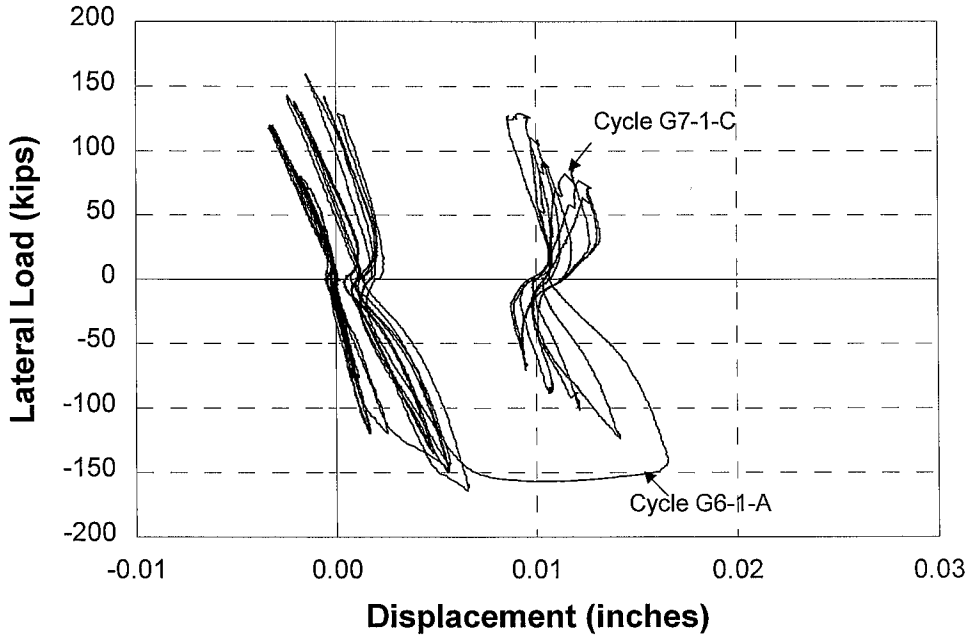

Fig. 5.4.4 Reading of LVDT L_PD_SC_2 in the Panel Zone of South Column

strength in the north direction. This was induced by the sudden shear yielding in the web at the base of the north column of the second story. The panel zone continued to elongate along the direction of LVDT L_PD_NC_1 and shorten along the direction of LVDT L_PD_NC_2 during the next three cycles due to the continued increase of shear deformation at the base of the north column in the second story. The deformation pattern of the panel zone started to change by cycle G6-2. It elongated along the direction of L_PD_NC_1 and shortened along the direction of L_PD_NC_2 when the specimen was loaded in the south direction. In contrast, it shortened along the direction of L_PD_NC_1 and elongated along the direction of L_PD_NC_2 when the specimen was loaded in the north direction. This phenomenon indicated that the bending moment started to increase at the north end of the middle beam and the panel zone started to behave in shear, as would a panel zone in a PR steel frame.

As mentioned in Section 3.4, one strain rosette was placed at the center of each column-middle beam panel zone. Figure 5.4.5 shows the shear strain from the strain rosette C_NC_PZ_R1 at the center of the north column-middle beam panel zone. It can be seen that before the specimen reached its maximum strength during cycle G5-1, the panel zone had no discernible pattern due to the complexity of the strain state in this region. A typical panel zone deformation pattern started to form by the 1.0% cycles, just as that indicated by the LVDTs readings. Figure 5.4.5 also shows that the maximum shear strain was 2500 με, indicating minor yielding accumulated in the panel zone during the entire loading history, which can also be proven by the appearance of yield lines in the center of the panel zone, as shown in Figure 5.3.2.

The behavior of the panel zone of the south column in the first story was similar to that of the north column, except that the magnitude of deformation was smaller.

5.5 Behavior of the Reinforced Concrete Infill Walls

5.5.1 Deformation of the Reinforced Concrete Infill Walls

As shown in Figure 3.4.2, two linear position transducers (LPTs) were installed diagonally in the infill wall of each story to measure the diagonal deformation of the infill

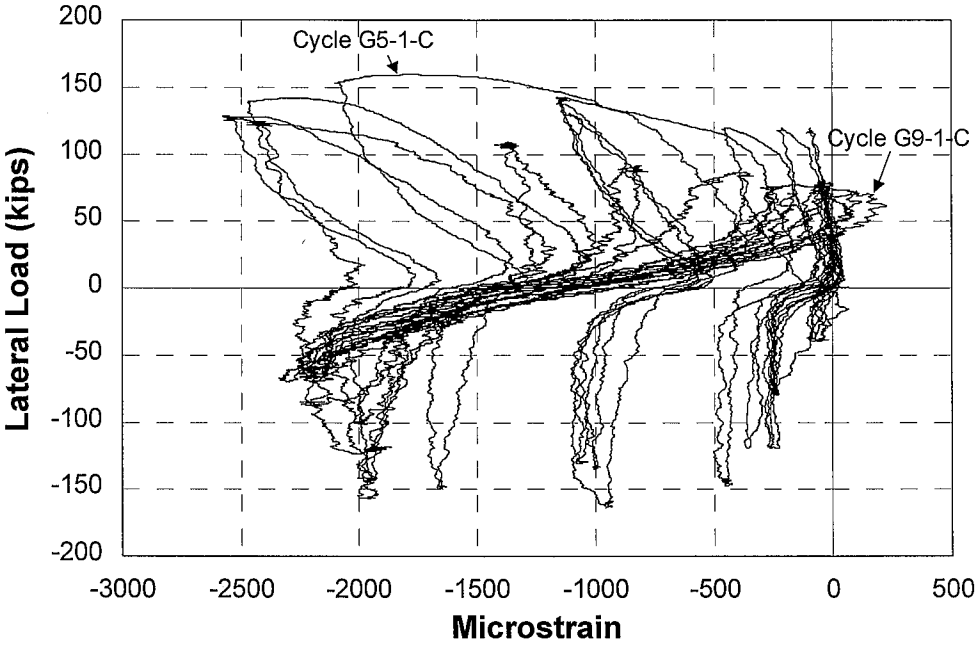

Fig 5.4.5 Shear Strain from Rosette C_NC_PZ_R1
at the Center of the Panel Zone of the North Column

walls. LPT1 and LPT2 were installed in the first story and LPT 3 and LPT4 were installed in the second story. Figures 5.5.1 to 5.5.3 show the readings of these LPTs versus the total lateral load, with a positive reading indicating elongation and a negative reading indicating shortening. LPT-4 did not function properly during the test and its results will not be reported. The reading of LPT-3 in the second story was recorded until it fell off during cycle G6-1-A. The readings of LPT-1 and LPT-2 were recorded until they were removed before the 1.25% cycles.

The diagonal length of the infill wall in the direction of LPT-1 increased when the specimen was loaded in the south direction and decreased when the specimen was loaded in the north direction, while the diagonal length in the direction of LPT-2 varied in the opposite way. This behavior indicated a typical shear distortion pattern of the infill wall. The same observation can be applied to the second story. In the first story, the magnitude of the peak diagonal deformation increased with each group of cycles until the specimen reached its maximum interstory drift during cycle G6-1. Figure 5.5.1 shows that the first

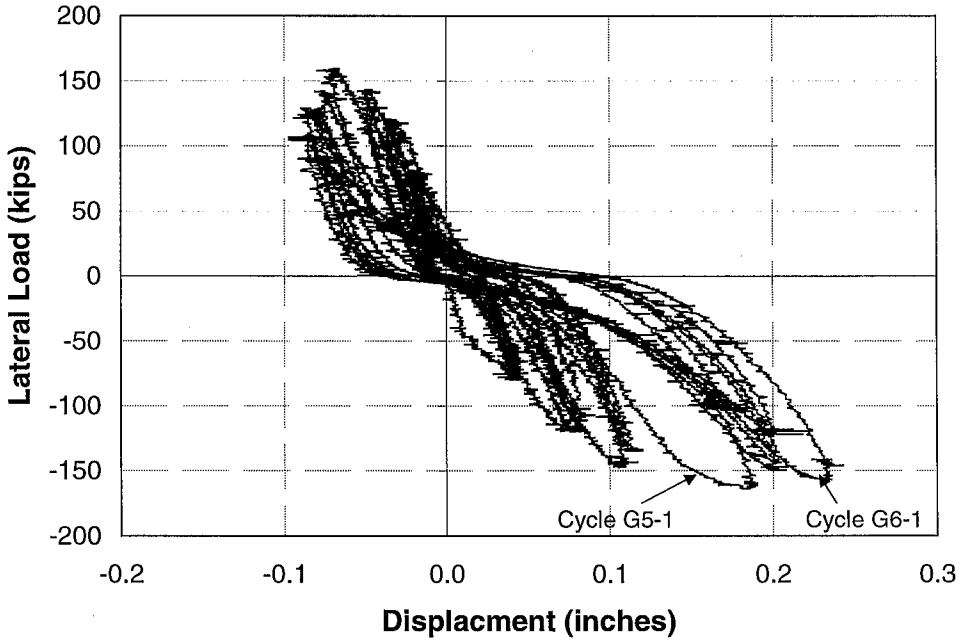

Fig. 5.5.1 Diagonal Deformation of the Infill Wall
along the Direction of LPT-1 in the First Story

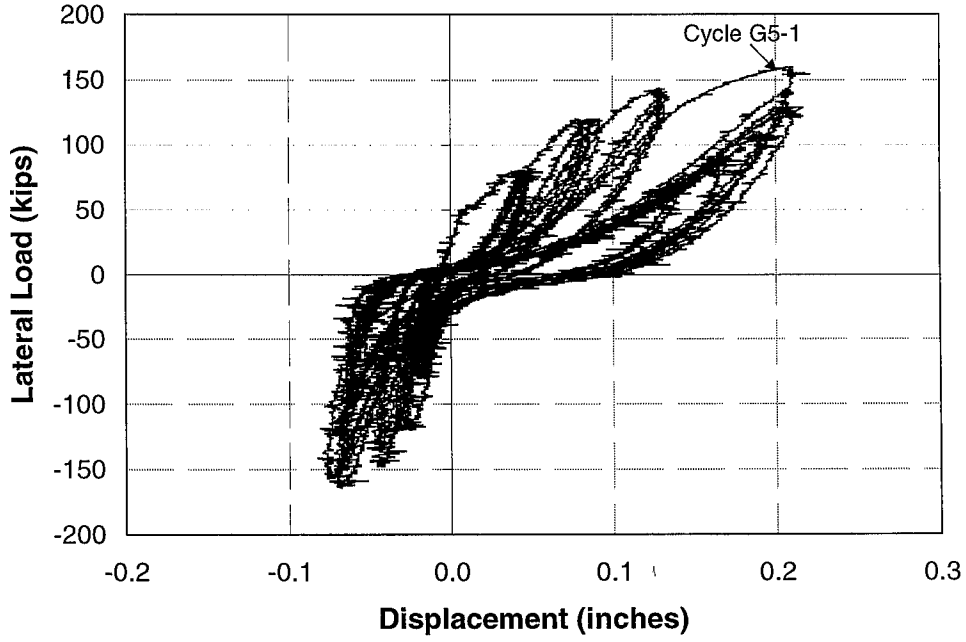

Fig. 5.5.2 Diagonal Deformation of the Infill Wall
along the Direction of LPT-2 in the First Story

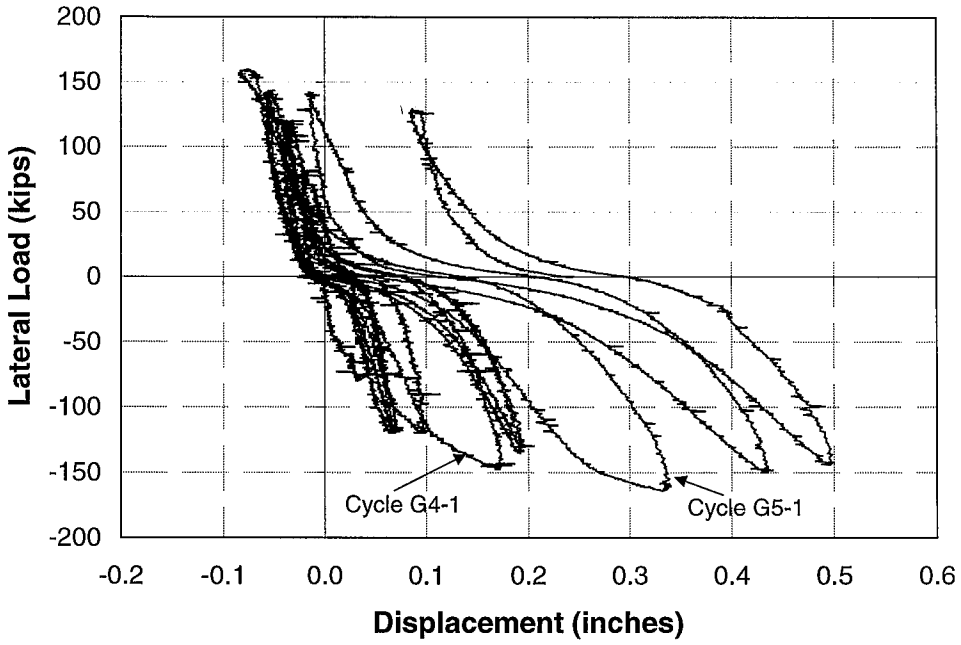

Fig. 5.5.3 Diagonal Deformation of Infill Wall
along the Direction of LPT-3 in the Second Story

instance of a large increase in the LPT-1 reading occurred during cycle G5-1-A. Figure 5.5.2 shows that the first instance of a large increase in the LPT-2 reading occurred during cycle G5-1-C. In the second story, the first instance of a large increase in the LPT-3 reading occurred earlier, in cycle G4-1-A, and continued during the following 0.75% cycles. For example, the diagonal elongation in the direction of LPT-3 at the peak load of cycle G4-1-A was 0.17 inches, nearly 80% greater than that of cycle G3-3-A, although the peak load of cycle G4-1-A was only 25% greater than that of cycle G3-3-A. The large increase in the reading of the LPTs might be related to the vertical cracking in the corner regions, which was discussed in Section 4.3. As an example, Figure 4.3.3 shows a typical vertical crack in the north bottom corner region of the second story. It can be observed that, due to the discontinuity of the reinforcement at the joint of the vertical and horizontal reinforcement cages, the vertical crack expanded and extended upwards to the column-infill wall interface when the frame was loaded in the south direction. The holders of LPTs were installed close to the corners (see Figure 5.5.4). As such, the

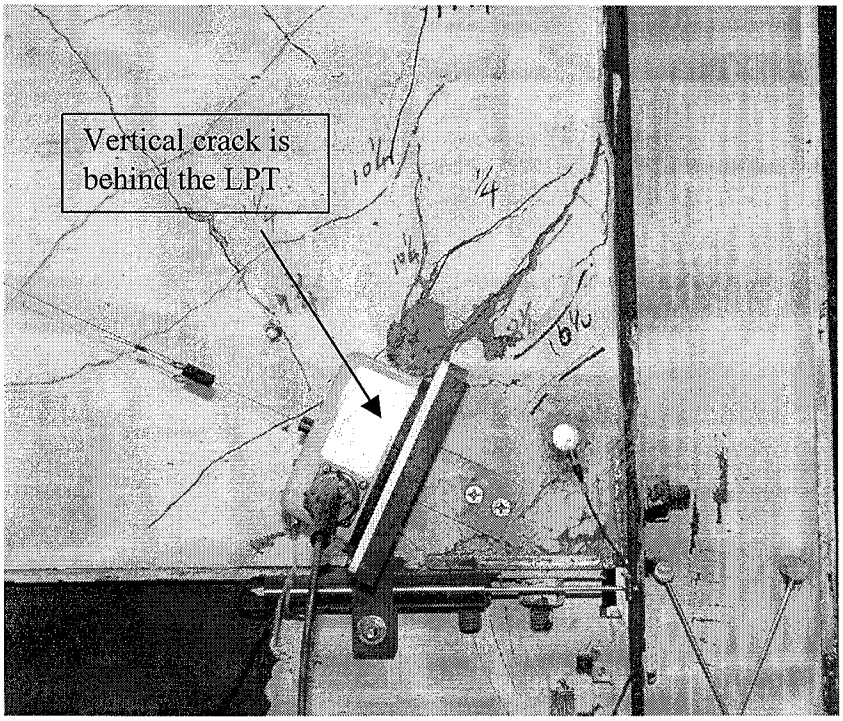

Fig. 5.5.4 Location of the LPT

vertical corner crack was located within the measurable range of the LPT and became one of the major contributions of measured diagonal deformation of the infill wall. In the second story, the vertical cracking first initiated at the joint of the vertical and horizontal reinforcement cages in the bottom corner regions during cycle G4-1 and then initiated at the same locations of the top corner regions during cycle G5-1. In the first story, the vertical cracking first initiated at the top corner regions during cycle G5-1. Therefore, the occurrence of the vertical cracking was coincident to the large increase in LPT readings mentioned above. The vertical cracking in the bottom corner regions of the second story was the most severe one. Figure 5.5.3 shows that the reading of LPT-3 did not decrease into the negative range when the specimen was loaded in the north direction during cycle G5-3-C. This may be caused by the fact that the cracks in the north bottom corner of the second story open up in cycle G5-3-A did not fully close after opening in prior cycles.

The gross shear deformation of the infill wall was calculated approximately based on the following equation:

$$\gamma_w = \frac{|\Delta_{LPT,1}| + |\Delta_{LPT,2}|}{2} \frac{\sqrt{(b_{LPT})^2 + (h_{LPT})^2}}{b_{LPT} h_{LPT}} \tag{5.5.1}$$

where

$\Delta_{LPT,1}$ = the diagonal displacement of the infill wall along the direction of LPT-1;

$\Delta_{LPT,2}$ = the diagonal displacement of the infill wall along the direction of LPT-2;

b_{LPT} = the horizontal distance between the fixed points of two LPT holders;

h_{LPT} = the vertical distance between the upper fixed point and lower fixed point of one LPT.

Figure 5.5.5 shows the gross shear deformation of the first story infill wall versus the total lateral load. The gross shear deformation was symmetrical in the two loading directions. It can be observed that the rate of the gross shear deformation increased gradually along the envelope of the load–shear distortion curve. If 85% of the lateral load is assumed to be carried by the shear deformation of the infill wall, the approximate peak–peak effective shear modulus of the infill wall in the first story can be obtained using the following equation:

$$G_w = \frac{1.2(0.85)\sum P}{A_w \sum \gamma_W} \tag{5.5.2}$$

where

$\sum P$ = sum of the absolute values of the peak loads in the two loading directions during each loading cycle

$\sum \gamma_W$ = sum of the absolute values of the peak shear deformations in the two loading directions during each loading cycle

A_w = cross sectional area of the infill wall

Figure 5.5.6 shows the ratio of the effective shear modulus G_w to the elastic shear modulus of the concrete G_c for the first loading cycle of each group of cycles, where the elastic shear modulus of concrete G_c is taken as 42% of the elastic modulus of the concrete, E_c, and the value of E_c is reported in Section 3.2.2. It can be observed that the

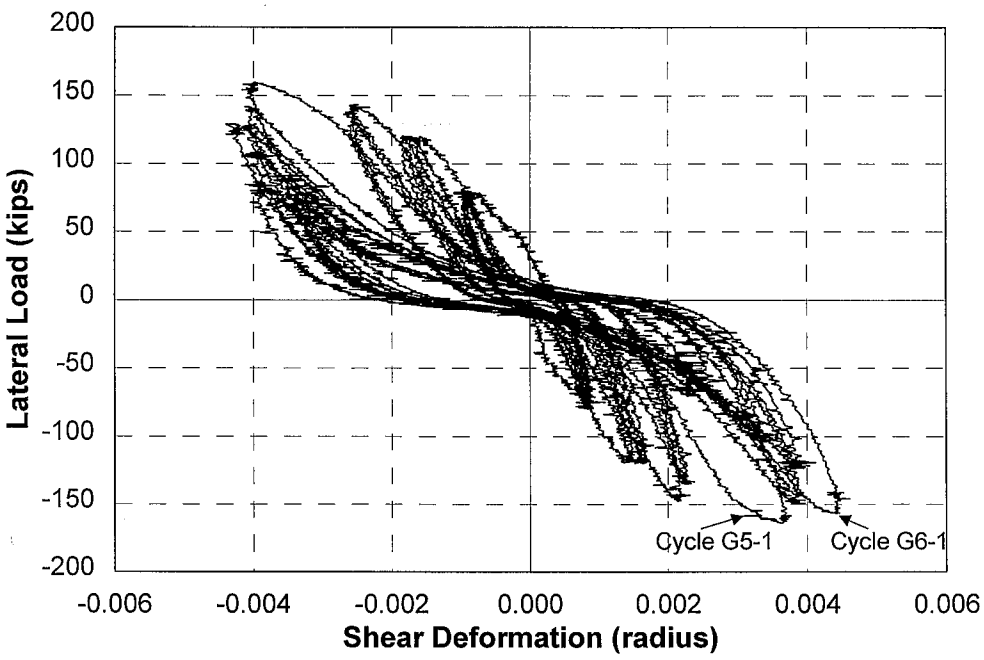

Fig. 5.5.5 Gross Shear Deformation of the Infill Wall in the First Story

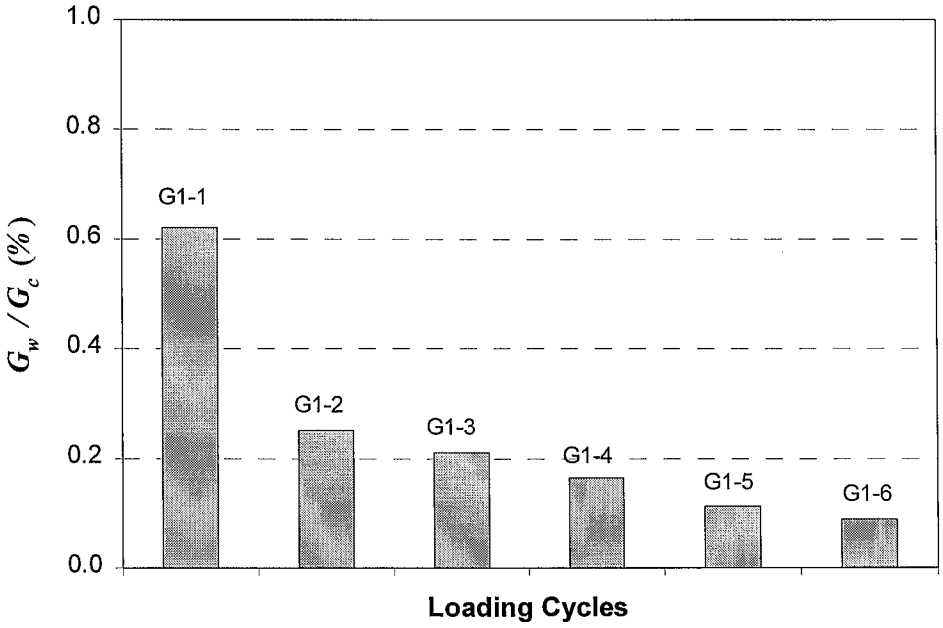

Fig. 5.5.6 Ratio of the Effective Shear Modulus G_w to the Elastic Shear Modulus of the Concrete G_c in the First Story

effective shear modulus of the infill wall was approximately 60% of the elastic shear modulus of the infill concrete for the first loading cycle G1-1. It quickly dropped to 25% for the loading cycle G2-1 when the peak lateral load increased approximately from 40 kips to 80 kips. The effective shear modulus then decreased gradually with each group of cycles and was only 11% of the elastic shear modulus of the wall concrete for cycle G5-1, when the specimen reached its maximum strength during the entire loading history.

Another interesting issue is the percentage of the interstory drift associated with the gross shear deformation of the infill wall, γ_w. Figure 5.5.7 shows that percentage for the first story at the peak load of the first cycle of each loading group, where the percentage is the average value in the two loading directions. It can be seen that the percentage of the interstory drift associated with the gross shear deformation of the infill wall increased steadily with each group of cycles. For the first loading cycle G1-1, approximately 30% of the interstory drift was associated with the shear deformation of the infill wall. When the specimen reached its maximum strength of the entire history in

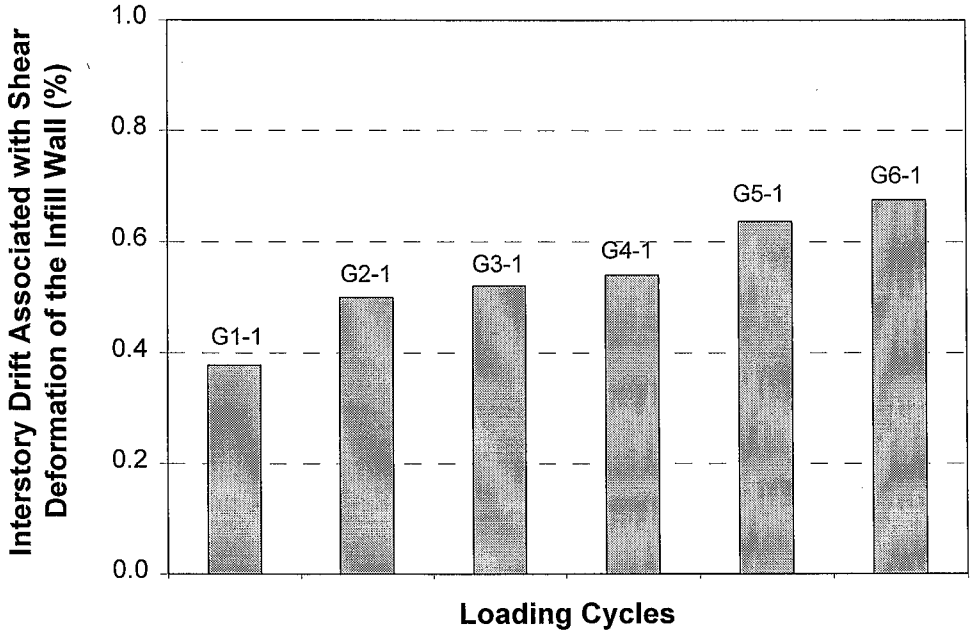

Fig. 5.5.7 Percentage of the Interstory Drift Caused
by the Shear Deformation of the Infill Wall in the First Story

loading cycle G5-1, this percentage increased up to 53%. However, it should be noted that 53% of the first story drift is much smaller than 53% of the total drift because the first story contribution to the total drift was getting smaller by the 0.75% cycles (Section 4.6).

5.5.2 Strain in the Reinforced Concrete Infill Walls

The gross longitudinal strains along the diagonal directions of the infill wall can be evaluated as follows:

$$\varepsilon_{w\_d} = \frac{\Delta_{LPT}}{\sqrt{(b_{LPT})^2 + (h_{LPT})^2}} \tag{5.5.3}$$

where Δ_{LPT}, b_{LPT}, and h_{LPT} are defined in Eq. (5.5.1). Figures 5.5.8 and 5.5.9 show the gross longitudinal strain in the direction of LPT1 and LPT2 in the first story, respectively. Figure 5.5.10 shows the gross longitudinal strain along the direction of LPT3. These figures show that, when the specimen was loaded in the south direction, the infill wall was in tension (positive gross diagonal strain) along the diagonal directions of LPT1 in the first story and LPT3 in the second story, and was in compression (negative gross diagonal strain) along the diagonal directions of LPT2 in the first story. The opposite held when the specimen was loaded in the north direction. The tensile gross strain in one loading direction was always greater than the compressive gross strain in the other direction at the same load level. This is understandable since the tensile gross strain was primarily caused by the opening of cracks while the compressive gross strain was the result of compressive deformation of concrete. When the specimen reached its maximum strength in the south loading direction of cycle G7-1, the gross compressive strain was 790 με in the direction of LPT2; when the specimen reached its maximum strength in the reversed north loading direction of cycle G7-1, the gross compressive strain was 800 με in the direction of LPT1 and 950 με in the direction of LPT3. These strains are less than the strain at the compressive strength of the infill concrete, which is usually between 2000 με to 3000 με. However, this does not prove that the concrete did not crush when

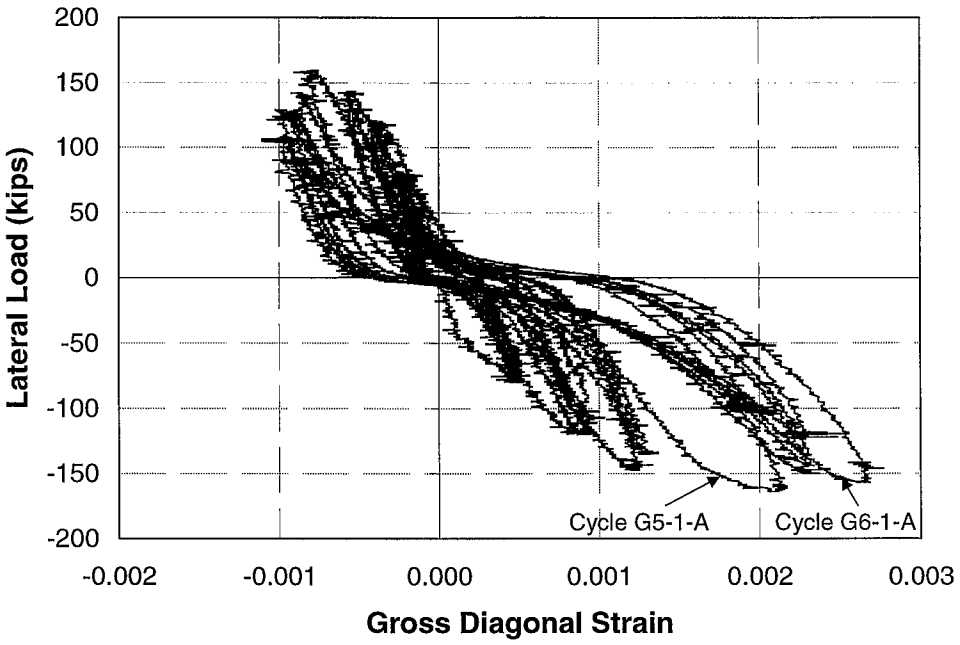

Fig. 5.5.8 Gross Longitudinal Strain of the Infill Wall along the Direction of LPT-1 in the First Story

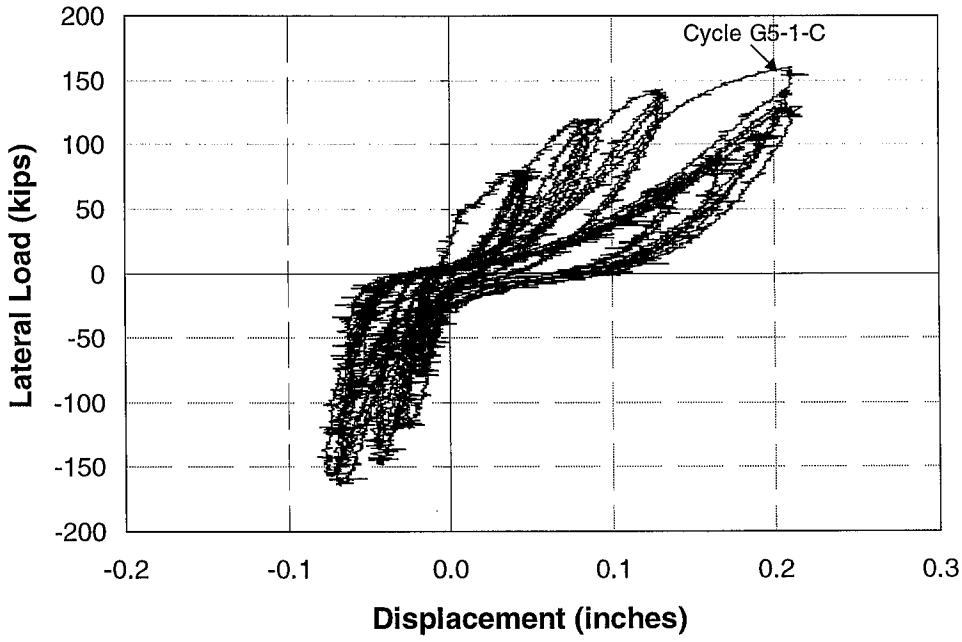

Fig. 5.5.9 Gross Longitudinal Strain of the Infill Wall along the Direction of LPT-2 in the First Story

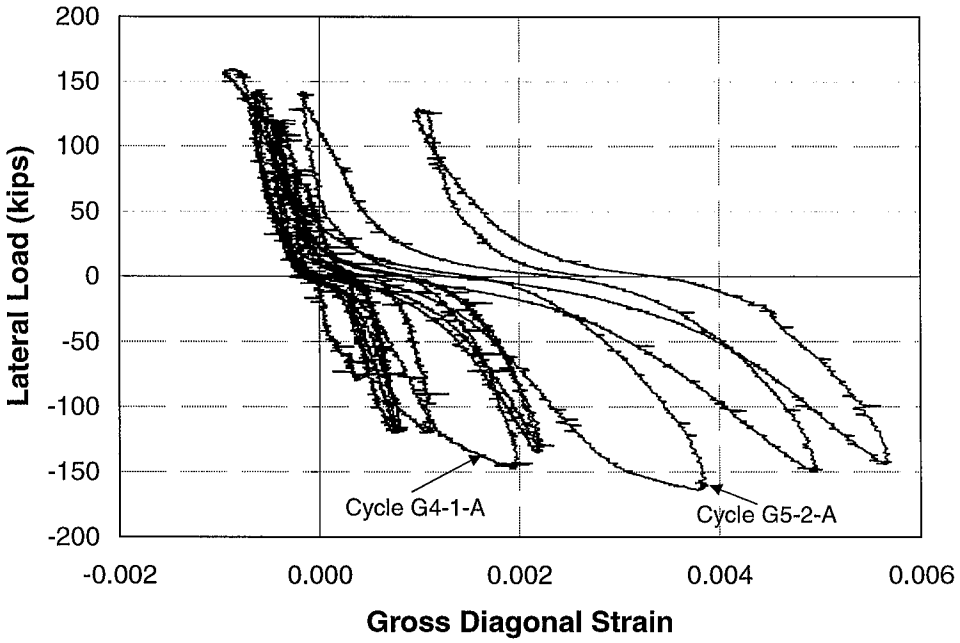

Fig. 5.5.10 Gross Longitudinal Strain of the Infill Wall
along the Direction of LPT-3 in the First Story

the specimen reached its maximum strength, since the longitudinal strain was not uniformly distributed along the diagonal direction of the infill wall.

In order to obtain the strain and stress distribution of the RC infill walls, nine surface strain rosettes were placed uniformly along both diagonal directions of the infill wall in the first story, as shown in Figure 5.5.11. Rosettes W1, W3, W5, W7, W9 were placed along the diagonal direction of LPT1, and rosettes W2, W4, W5, W6, W8, were placed along the diagonal direction of LPT2. Unfortunately, most of these surface gages were broken during the early loading cycles because the cracking happened to go through these gages. Along the diagonal direction of LPT1, rosette W1 and W7 even lost readings during the first loading cycle G1-1. Therefore, only the strains from the rosettes placed along the direction of LPT2 were used to calculate the longitudinal strains in that direction and compared to the estimated gross diagonal strain. Table 5.5.1 shows a close match between the strains given by the strain gages and the gross strain given by LPTs

during first three groups of cycles, proving the results of the LPTs can be used in an overall evaluation of the infill wall behavior.

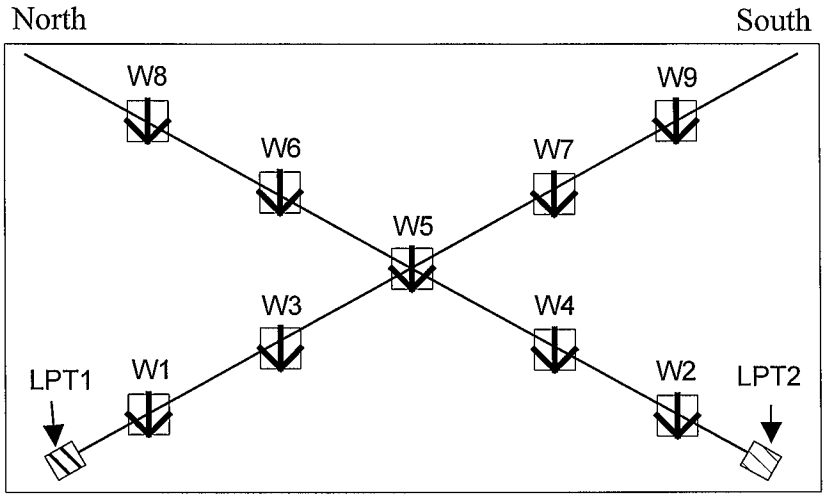

Fig. 5.5.11 Locations of the Strain Rosettes and LPTs in the First Story

Table 5.5.1 Comparison of the Gross Diagonal Strains and the Measured Strains from Strain Rosettes (με)

Cycle No.	W2	W4	W5	W6	W8	Average	Gross Strain (from LPT-2)
G1-1-A	-87.4[*1]	-53.2	-57.2	-69.1	-38.2	-61.0	-40.00
G2-1-A	-122.0	-151.2	-[*2]	-140.6	-199.1	-153.2	-200.00
G3-1-A	-167.9	-	-	-	-424.0	-295.9	-300.00

1: Negtive sign means it is in compression
2: "-" means the strain rosette died in the correponding cycle

Chapter 6

Behavior of Interface Headed Stud Connectors

This chapter compares the "axial" and "bending" strain demands of the interface headed stud connectors, discusses the slip and separation demands along the interfaces, and determines the deformation capacity of the headed studs due to the low-cycle fatigue.

6.1 Yielding of the Gaged Headed Studs

In order to fully understand the behavior of the headed stud connectors in this composite system, a number of studs were monitored by placing two strain gages on the opposite sides of each stud shaft, as close to the base as possible. Figure 4.5.1 shows the designation of each gaged stud, which takes the first three letters from the corresponding strain gage names as defined in Figure 3.4.4. The recorded strain for each gaged stud is plotted versus loading time in Appendix B.3.

The headed studs along the beam-infill wall interfaces fractured after undergoing a limited number of cycles (≤ 25 cycles). It is desirable to determine whether plastic deformation was involved in the low-cycle fatigue failure. If so, the strain instead of the stress should be the dominant factor in decreasing the fatigue life of the studs (Masubuchi, 1980) and further analysis of the strain history of the studs is warranted.

Each gaged stud was checked for yielding and the result is listed in Table 6.2.1. The strain gages of studs SMB4 and SSC3 were broken during the casting of the infill

Table 6.2.1 Yielding of the Headed Stud Connectors

Stud Location	Stud Name	Yield Check	First Yield Gage	Cycle No. When Yielded
Bottom Interface of Story 1	SBB1	Yes	SBBSBG1-a	G2-1-C
	SBB2	Yes	SBBSBG2-a	G2-1-C
	SBB3	Yes	SBBSBG3-b	G2-1-B
	SBB4	Yes	SBBSBG4-b	G2-1-A
Top Interface of Story 1	SMB1	Yes	SMBSBG1-a	G2-1-A
	SMB2	Yes	SMBSBG2-a	G2-1-A
	SMB3	Yes	SMBSBG3-a	G2-2-A
	SMB4	Bad gage		
	SMB5	Yes	SMBSBG5-b	G2-2-C
	SMB6	Yes	SMBSBG6-b	G2-1-C
Bottom Interface of Story 2	SMB7	Yes	SMBSBG7-a	G3-3-A
	SMB8	No	SMBSBG8-a	
	SMB9	Yes	SMBSBG9-b	G3-2-C
	SMB10	No	SMBSBG10-a	
North Interface of Story 1	SNC1	Yes	SNCSBG1-b	G1-2-D
	SNC2	Yes	SNCSBG2-a	G2-1-C
	SNC3	Yes	SNCSBG3-b	G3-1-A
	SNC4	Yes	SNCSBG4-a	G2-1-A
South Interface of Story 1	SSC1	Yes	SSCSBG1-b	G2-1-A
	SSC2	Yes	SSCSBG2-a	G2-1-A
	SSC3	Bad gage		
	SSC4	Yes	SSCSBG4-a	G3-1-C

wall so that the yielding status of these two studs could not be determined. Only studs SMB8 and SMB9, which were located along the bottom interface of the second story, did not yield before the studs failed during the test. All the other studs yielded in the gaged location no matter if they fractured or not during the test. The majority of yielding occurred during the 0.2% cycles and the remaining occurred during the subsequent 0.3% cycles. Therefore, the strain demands of the studs should be examined with regard to their low-cycle fatigue lives because the studs started to undergo plastic deformation early in the test.

6.2 Axial and Bending Strain Demands on the Headed Studs

6.2.1 Axial and Bending Strain Behavior of the Headed Studs

Because of the effects from overturning moment and the deformation incompatibility between the steel frames and infill wall, the interface headed stud connectors, especially those located in the corner regions, are subjected not only to shear force but also to axial force. The axial tensile force in the headed stud is believed to have a more profound effect on the strength and ductility of the headed stud than the axial compressive force, since the latter tends be relieved from the studs through the compression between the concrete and the flanges of the steel sections. This phenomenon has been mentioned by Liauw and Kwan (1983a, 1983b), but has never been quantitatively addressed due to the lack of experimental data. Therefore, one purpose of the test was to determine the proportions of the strength demands from the axial force and the shear force, as well as the slip and separation demands on the headed studs. Since both the force and the deformation are related to the strains in the studs, the first step herein is to fully understand the characteristics of the strain demands from the shear force and the axial force, respectively, and how they varied with stud location. In the specimen, each gaged stud had two strain gages placed on opposite sides, just above the base. As shown in Figure 6.2.1, the average of the measured strains from these two gages indicates the strain mainly induced by the axial force along the shaft and is defined as the "axial strain"; the difference between the measured strains from these two gages indicates the strain mainly induced by the shear force and bending moment and is defined as the "bending strain". This section examines the axial strain and bending strain of four typical headed studs, SBB1, SMB7, SMB2 and SNC1, respectively. As shown in Figure 4.5.1, stud SBB1 was located in the north corner of the bottom interface of the first story, stud SMB7 was located in the north corner of the bottom interface of the second story, stud SMB2 was located in the

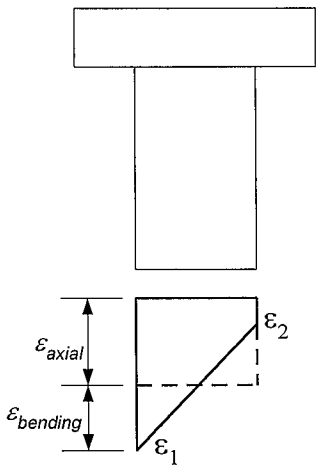

Fig. 6.2.1 Axial and Bending Strains

north portion of the top interface of the first story, and stud SNC1 is located in the bottom corner of the north interface of the first story.

Figure 6.2.2 shows the time history of the axial strain and the bending strain of stud SBB1 in the north corner of the bottom interface of the first story. The bending strain of all studs was calculated in the same way: $\varepsilon_{bending} = (\varepsilon_a - \varepsilon_b)/2$, where ε_a is the measured strain from gage "a" and ε_b is the measured strain from gage "b" of each stud. It can be seen that, until cycle G4-1-A, the axial strain increased in the positive direction when the specimen was loaded in the south direction and increased in the negative direction when the specimen was loaded in the north direction, indicating that this stud was in tension when the specimen was loaded in the south direction and in compression when the specimen was loaded in the north direction. During the first three groups of cycles, the peak values of the negative axial strain were close to each other, approximately equaling 750 με, while the peak values of the positive strain increased with each group of cycles. When the specimen was loaded in south direction, the stud stretched in the location of gage "a" and compressed in the location of gage "b". Therefore, the bending strain $\varepsilon_{bending}$ increased in the positive direction. In contrast, the bending strain $\varepsilon_{bending}$ increased in the negative direction when the specimen was loaded in the north direction. During the first three groups of cycles, the bending strain was primarily negative, indicating the stud bent more severely when the specimen was loaded in the north direction than when the specimen was loaded in the south direction. This is probably due to the stud being subjected to the force of the compression strut in the RC infill wall when the specimen was loaded in the north direction. During cycle G4-1-A, both the axial strain and the bending strain increased substantially in their positive directions and their peak values were close to each other, approximately equaling 1800 με. During most of the cycles shown in Figure 6.2.2, the range of the bending strain was 1.5 to 2 times that of the axial strain, indicating the axial strain might be an important factor in the low cycle fatigue failure of stud SBB1. Figure 6.2.2 also shows that the stud was in combined tension and shear when failure occurred.

Figure 6.2.3 shows the time history of the axial strain and the bending strain of stud SMB7 in the north corner of the bottom interface of the second story. Similar to the axial strain of stud SBB1, the axial strain of stud SMB7 was positive when the specimen was loaded in the south direction and negative when the specimen was loaded in the north direction. During the first three groups of cycles, the peak values of the negative axial strain were close to each other, while the peak values of the positive axial strain increased with each group of cycles. The peak value of the positive axial strain dropped after cycle G3-2 when the specimen was loaded in the south direction. This possibly occurred because of the cracking nearby along the intersection of the vertical reinforcing cage and the horizontal reinforcing cage, which might have released some of the confinement of this stud. Figure 6.2.3 shows that the range of the bending strain was close to that of the axial strain during the first group of cycles, approximately 2 times that of the axial strain during the second group of cycles, and 2 to 3 times that of the axial strain during the third group of cycles. This indicated that the axial strain might also be an important factor in the low cycle fatigue failure of stud SMB7.

Figure 6.2.4 shows the time history of the axial strain and the bending strain of stud SMB2 in the north portion of the top interface of the first story. The corner stud SMB1 was not chosen because it did not fail in the test. During the first four groups of cycles, both the peak value and the range of axial strain were far less than those of the bending strain for each cycle. For example, the strain range in cycle G4-1 was approximately 600 $\mu\varepsilon$ for the axial strain, but was nearly 5500 $\mu\varepsilon$ for the bending strain. Figure 6.2.5 shows the time history of the axial strain and the bending strain of stud SNC1 along the north interface of the first story. During the first three groups of cycles, both the peak value and the range of axial strain were far less than those of the bending strain. However, Figures 6.2.4 and 6.2.5 show there is a large permanent "set" in the axial strain of the two studs, accumulated during the 0.75% cycles and 1.0% cycles for stud SMB2 and during the 0.5% cycles for stud SNC1. However, the bending cycles still dominate the loading during these cycles. The permanent "set" in the axial strain is possibly related to the localized crushing of concrete on the top of the stud head. During a

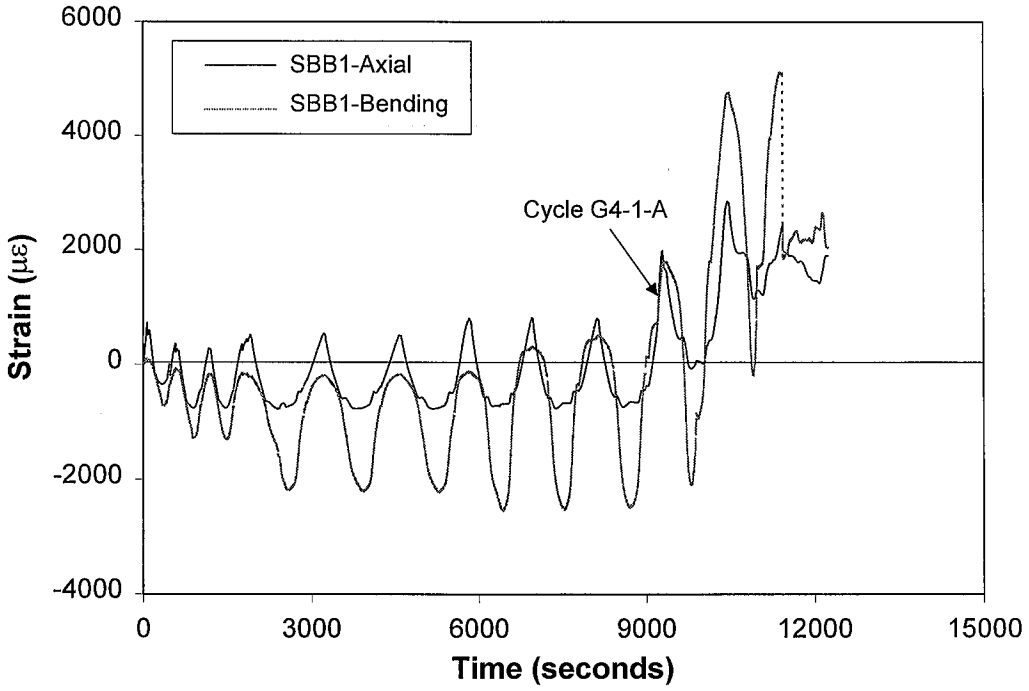

Fig. 6.2.2 Axial Strain and Bending Strain of Stud SBB1

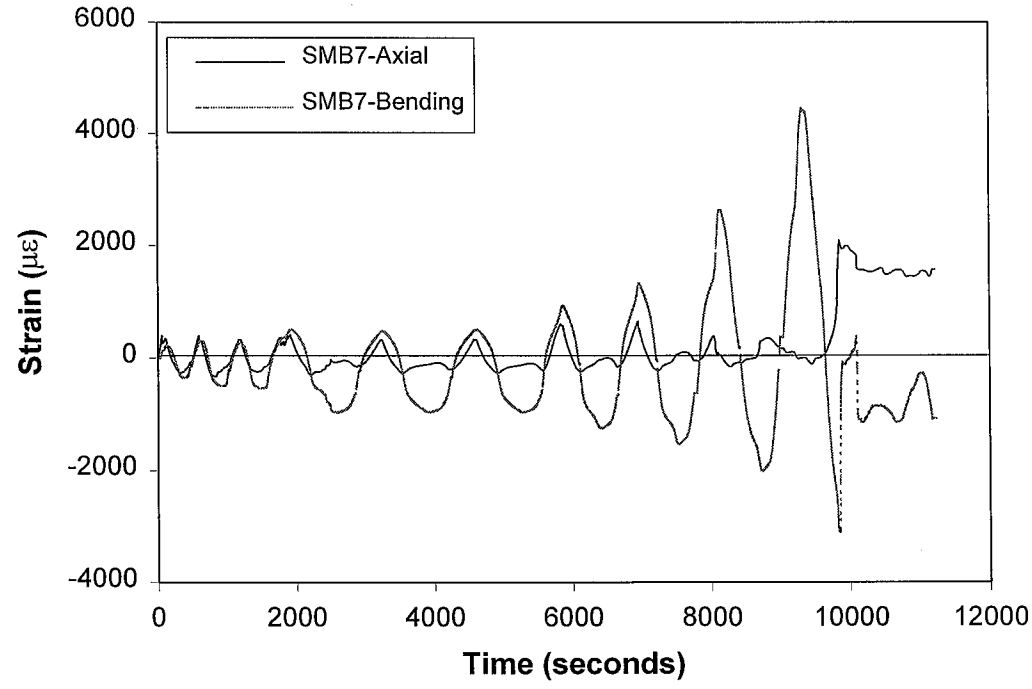

Fig. 6.2.3 Axial Strain and Bending Strain of Stud SMB7

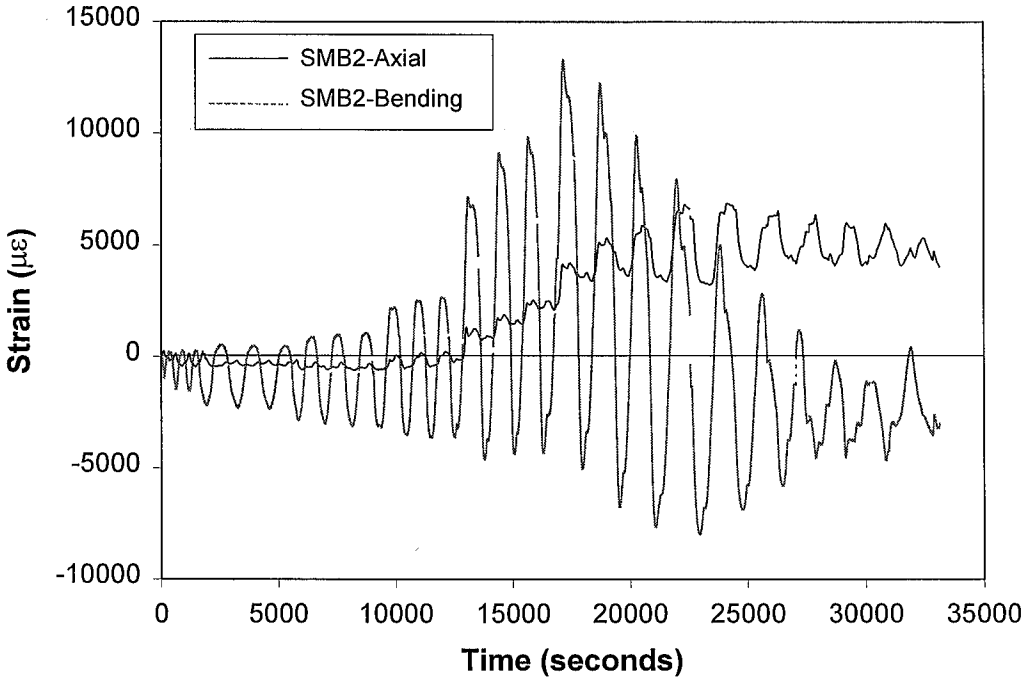

Fig. 6.2.4 Axial Strain and Bending Strain of Stud SMB2

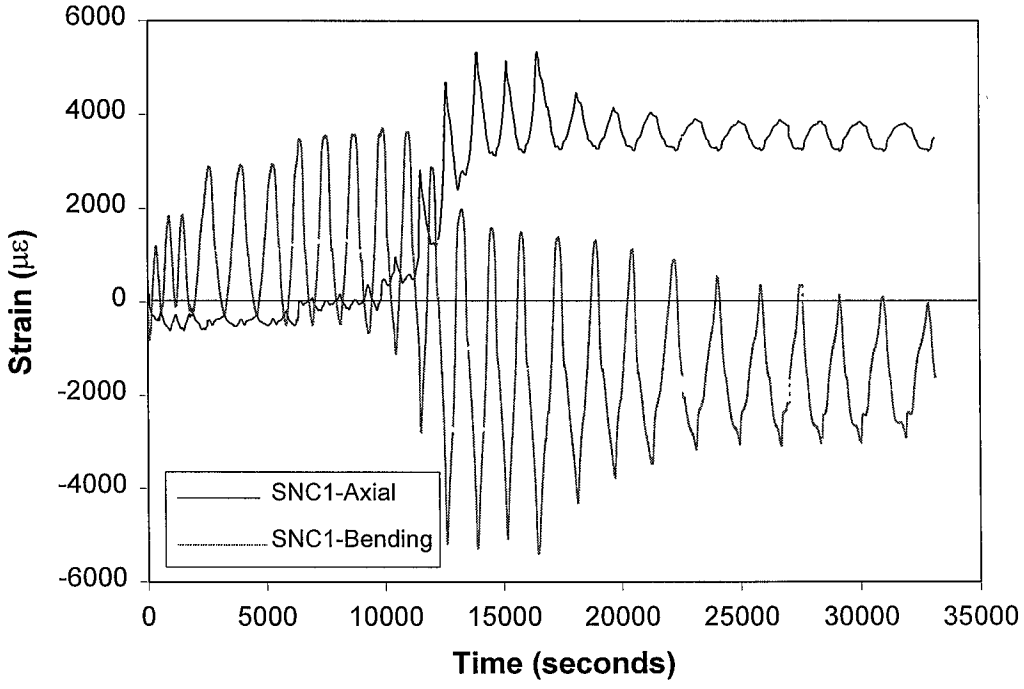

Fig. 6.2.5 Axial Strain and Bending Strain of Stud SNC1

certain loading period, the concrete on the top of the stud head started to crush under increasing concentrated compressive stress. The stud then yielded when undergoing unloading and loading in tension. When the stud was back loaded in compression, the crushed concrete on the top of the stud head did not have sufficient stiffness to drive the axial strain back to the magnitude in the previous cycle, resulting a residual tensile strain in the stud. The residual tensile strain continued to accumulate during the following cycles and led to a large permanent "set" observed in the strain history diagram.

6.2.2 Comparison of the Axial Strain Demands for the Headed Studs

This section compares the axial strain of the headed studs located along different interfaces of the specimen. From each interface, two gaged studs in the corner region were chosen as representative.

Figure 6.2.6 compares the axial strain histories of studs along the bottom interface of the both stories. Studs SBB1 and SBB2 were located in the north corner of the bottom interface of the first story. Studs SMB7 and SMB8 were located in the north corner of the bottom interface of the second story. During each cycle of the first three loading groups, the positive peak axial strains of studs SBB1 and SMB7 were close to each other, with that of stud SBB1 slightly greater than that of stud SMB7; the positive peak axial strain of studs SBB2 and SMB8 were also close to each other. However, during each cycle, the positive peak axial strains of studs SBB2 and SMB8 were only 1/4 to 1/5 of those of studs SMB1 and SMB7. This phenomenon indicated that, along the same bottom interface of each story, the closer to the corner, the larger tensile force a stud has to resist and the larger separation a stud had to undergo. Figure 6.2.6 also shows that, during each cycle of the first loading groups, stud SBB1 had the largest negative peak axial strain, stud SBB2 had the second largest negative peak axial strain, and studs SMB7 and SMB8 had similar, lower negative peak axial strains. This comparison further indicated that, along the bottom interface, the lower the story and the closer to the corner, the larger was the variation range of the stud axial strain.

Figure 6.2.7 compares the axial strain histories of the studs along the bottom and the top interfaces of the first story. Studs SMB1 and SMB2 were located in the north corner of the top interface of the first story. The axial strain histories of studs SMB1 and SMB2 were only plotted up to the 0.5% cycles in this figure since studs SBB1 and SBB2 failed during the 0.5% cycles. Figure 6.2.7 shows that the axial strains of studs SMB1 and SMB2 are primarily in the negative region, indicating the studs SMB1 and SMB2 were in compression during these groups of cycles. Furthermore, during each loading cycle, the axial strain variation of stud SMB1 was approximately one half of that for stud SBB1, and the strain variation of stud SMB2 was even less. This comparison indicated that the effect of the axial force and deformation might be negligible for the studs along the top interface of the infill wall, at least during the first four groups of cycles.

Figure 6.2.8 compares the axial strain histories of the studs along the bottom interface and along the north interface of the first story. Studs SNC1 and SNC2 were located in the bottom corner of the north interface of the first story. During the first three groups of cycles, the strain variation of studs SNC1 and SNC2 was quite small as compared to those of studs SBB1 and SBB2 along the bottom interface, indicating the effect of axial force might be negligible for the studs along the north and south interfaces of the infill wall during the early loading cycles.

The entire strain histories of studs SMB1, SMB2, SNC1 and SNC2 are shown in Figure 6.2.9. It can be observed that axial strains of studs SNC1 and SNC2 started to increase in the positive direction during the 0.5% cycles, and reached their maximum value during the 0.75% cycles; the axial strain of stud SMB2 started to increase during the 0.75% cycles and reached its maximum value during 1.25% cycles. A large permanent "set" of the axial strain was accumulated for each of these three studs. The reason that the axial strain of the studs along the top and side interfaces was very small during the early loading stages but became significant later is possibly related to the deformation patterns of the specimen. The deformation of the specimen can be decomposed into two major patterns, as shown in Figure 6.2.10. Figure 6.2.10.(a) shows the specimen deflecting by bending and shear as a composite cantilever. Figure

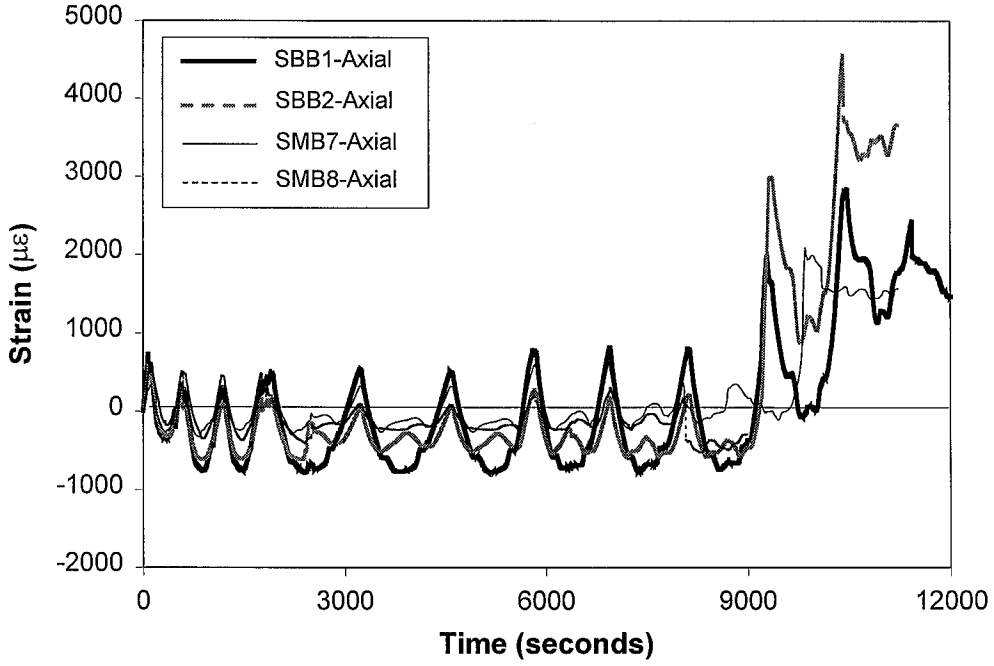

Fig. 6.2.6 Axial Strains of the Studs along the Bottom Interface of Both Stories

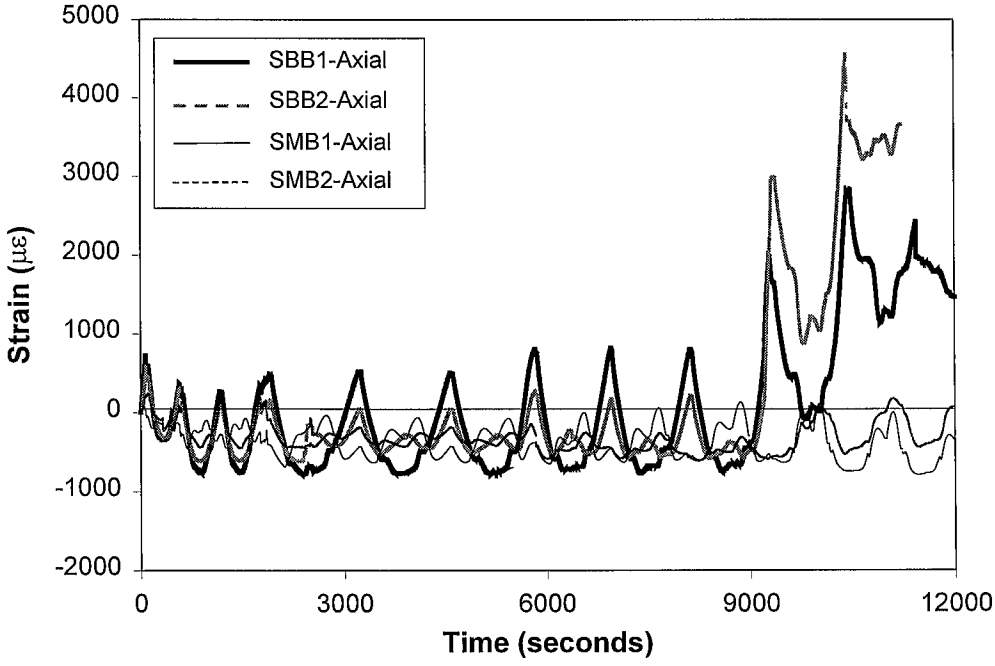

Fig. 6.2.7 Axial Strains of the Studs along the Bottom Interface and Top Interface of the First Story

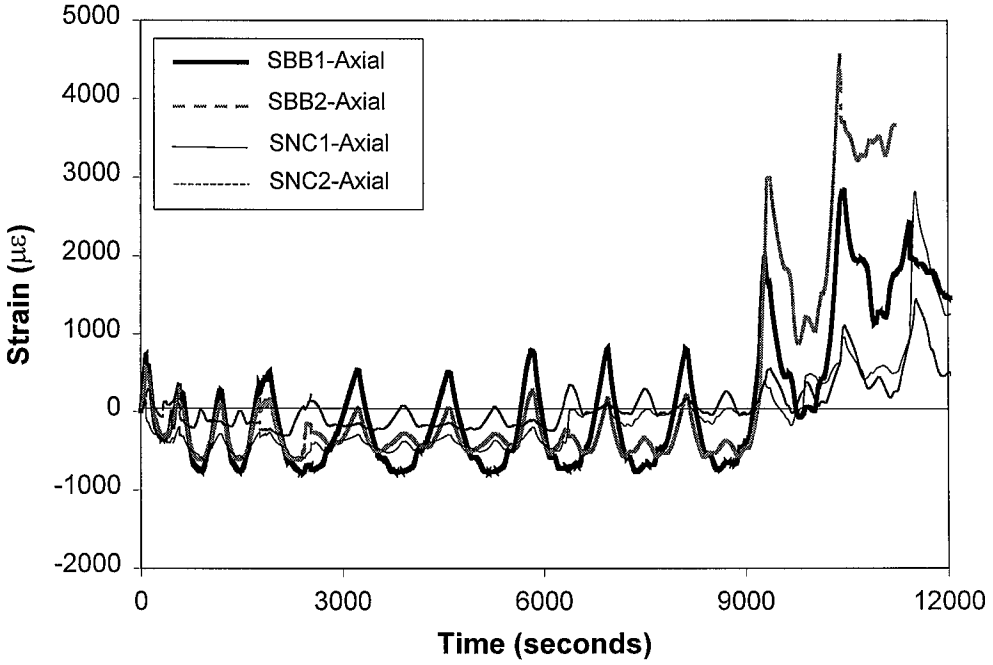

Fig. 6.2.8 Axial Strains of the Studs along the Bottom Interface and North Interface of the First Story

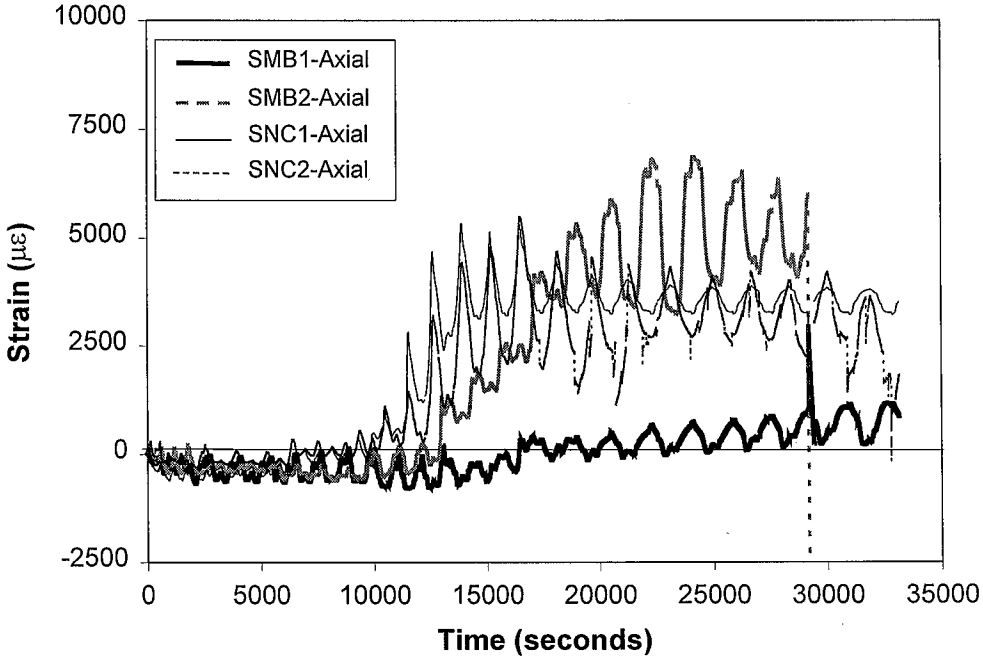

Fig. 6.2.9 Axial Strains of the Studs along the Top Interface and the North Interface of the First Story

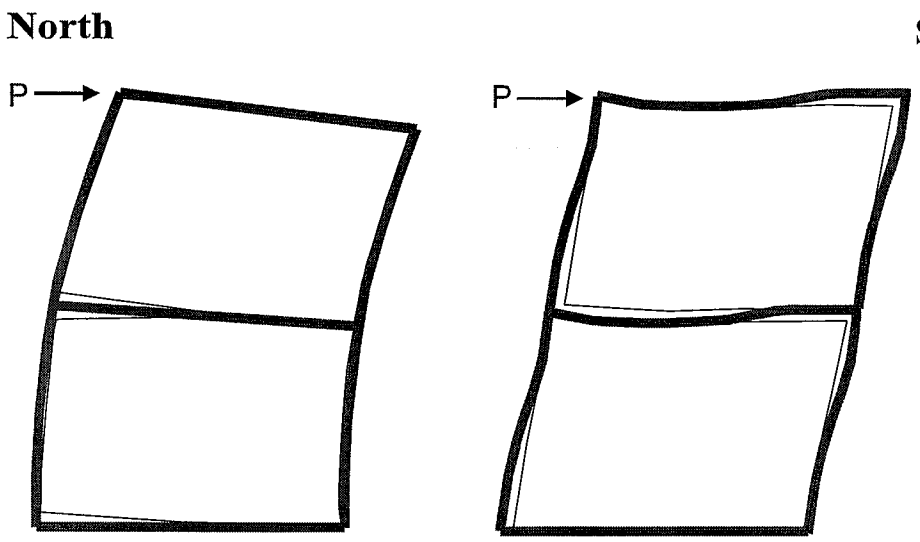

a) "Bending" + "Infill Shear" b) "Truss" + "Frame Shear"

Fig. 6.2.10 Deformation Pattern for the Specimen

6.2.10.(b) shows the specimen deflecting by bending as a truss and shearing as a moment frame. When the specimen was pushed in the south direction, the north portion of the top interface of the first story tended to separate due to the cantilever bending action shown in deformation pattern (a), and to close up due to the deformation incompatibility between the steel frame and infill wall shown deformation pattern (b). At the same time, the south portion of the top interface of the first story tended to close up due to the bending action and to separate due to the deformation incompatibility. Therefore, in the early loading stages, the axial strain demands were quite small for the studs along the top interfaces because of the counteraction of these two deformation patterns. In a contrast, the studs along the bottom interfaces had to endure higher strain demands due to the combined action of the cantilever bending and deformation incompatibility, as shown in Figure 6.2.10. With the increasing cycle numbers and lateral load, the headed studs along the bottom interfaces likely failed first (see Section 6.4.1). As a result, the cantilever bending action degraded as load history progressed and the specimen started to deflect in bending as a "truss" and in shearing as a "moment frame" predominantly, which led to the increasing degree of deformation incompatibility and placed higher and higher axial

strain demands on the studs along the top and side interfaces of the infill wall. As proof, for stud SMB2, the large increase of tensile strain during the 0.75% cycles occurred when the specimen was loaded in the north direction. For studs SNC1 and SNC2, the increase of the tensile strain during the 0.5% cycles occurred when the specimen was loaded in the south direction.

6.2.3 Comparison of the Bending Strain Demands for Headed Studs

This section compares the bending strain of the same used in the previous section. In Figures 6.2.11 to 6.2.13, the bending strains of the studs along bottom interface of both stories were calculated as $\varepsilon_{bending} = (\varepsilon_a - \varepsilon_b)/2$, while the bending strains of the studs along the top and north interfaces of the first story were calculated as $\varepsilon_{bending} = (\varepsilon_b - \varepsilon_a)/2$, in order to achieve the same trend in the plots for comparison.

Figure 6.2.11 compares the bending strain histories of the studs along the bottom interface of both stories. It shows that the variation of the bending strains of studs SBB1 and SBB2 along the bottom interface of the first story were quite consistent, as well as those of studs SMB7 and SMB8 along the bottom interface of the second story. In each cycle of the first three groups of cycles, the bending strain ranges of studs SMB7 and SMB8 were slightly less than those of studs SBB1 and SBB2.

Figure 6.2.12 compares the bending strain histories of the studs along the bottom and top interfaces of the first story. Again, it shows that the variation of the bending strain of studs SMB1 and SMB2 along the top interface of the first story were also quite consistent. In each cycle of the first groups of cycles, the bending strain ranges of studs SMB1 and SMB2 were approximately the same as those of studs SBB1 and SBB2.

Figure 6.2.13 compares the bending strain histories of studs along the top interface and north interface of the first story. During the first four groups of cycles, the bending strain ranges of studs, SNC1 and SNC2, along the north interface were close to those of the studs, SMB1 and SMB2, along the top interface of the first story. However, the bending strain ranges of studs SNC1 and SNC2 decreased gradually after they reached their maximum value during the 0.75% cycles, while the bending strain of stud

SMB2 had a large increase during the 0.75% and 1.0% loading cycles. The bending strain range of stud SMB2 was approximately 2 to 3 times those of the studs SNC1 and SNC2, 3 to 4 times those of the studs SNC1 and SNC2.

It should be noted that it may not be fair to compare the bending strains of the studs along different interfaces according to the readings of corresponding strain gages, especially when the strains are small. The reason is that the magnitude of the bending strain of the stud is related to the positions of the strain gages. The farther the strain gages are from the base of the stud, the smaller the bending strain. The distance from the centers of the strain gages to the base of each stud (gage height) were measured after installation of strain gages and are listed in Table 3.4.1. The table shows that the gage heights of studs SMB7 and SMB8 were 5/16 inches, 1/16 inches larger than the gage heights of studs BB1 and SBB2, which were 1/4 inches. Therefore, the slightly smaller recorded bending strains of studs SMB7 and SMB8 do not necessarily mean that studs SMB7 and SMB8 along the bottom interface of the second story underwent smaller interface slips than studs SBB1 and SBB2 along the bottom interface of the first story.

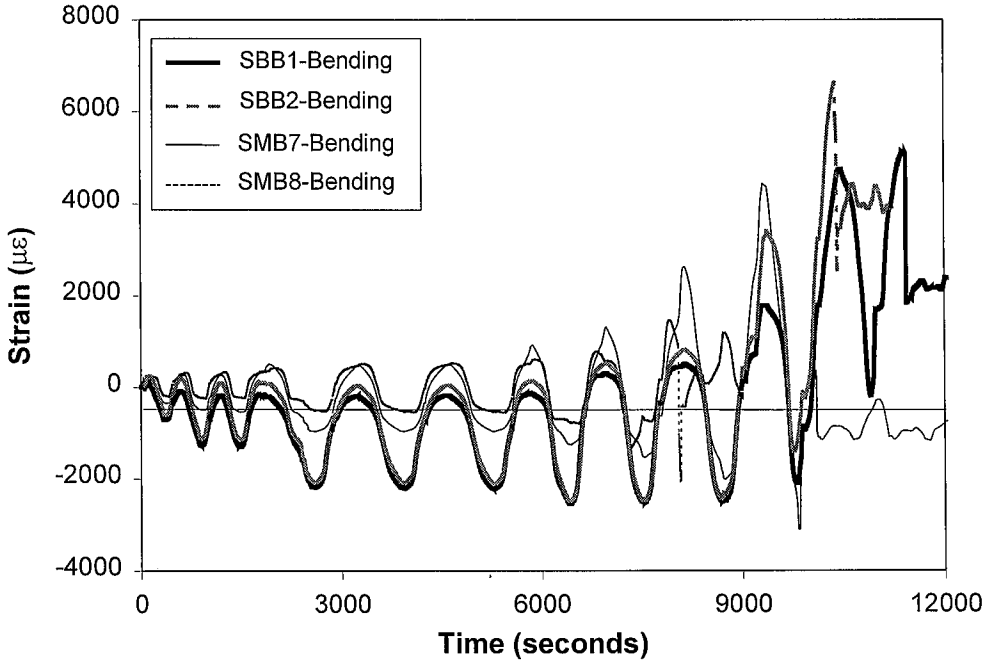

Fig. 6.2.11 Bending Strains of the Studs along the Bottom Interfaces of Both Stories

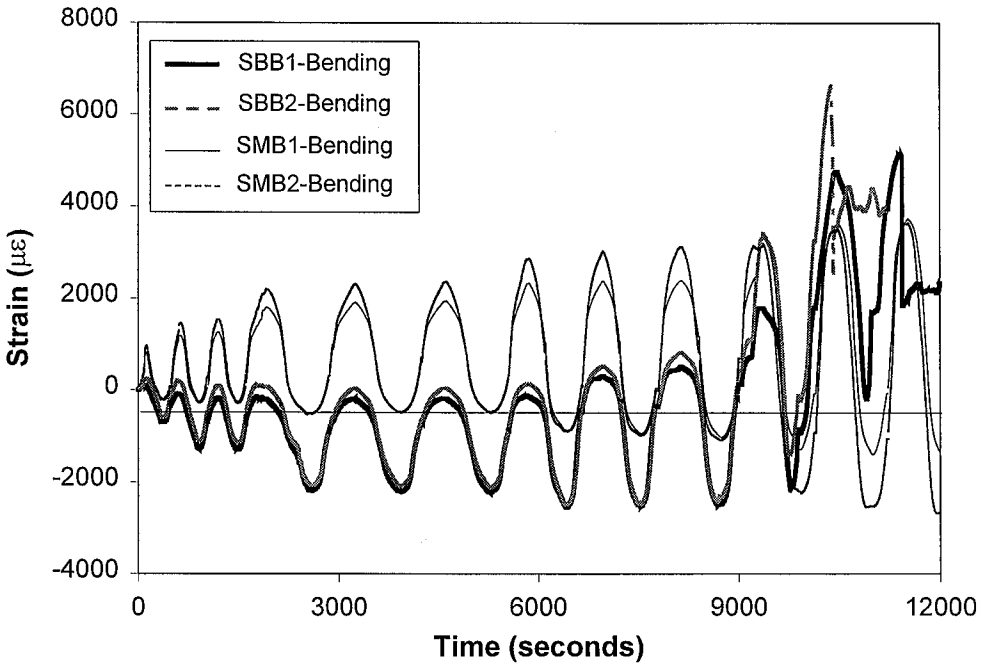

Fig. 6.2.12 Bending Strains of the Studs along the Bottom and the Top Interfaces of the First Story

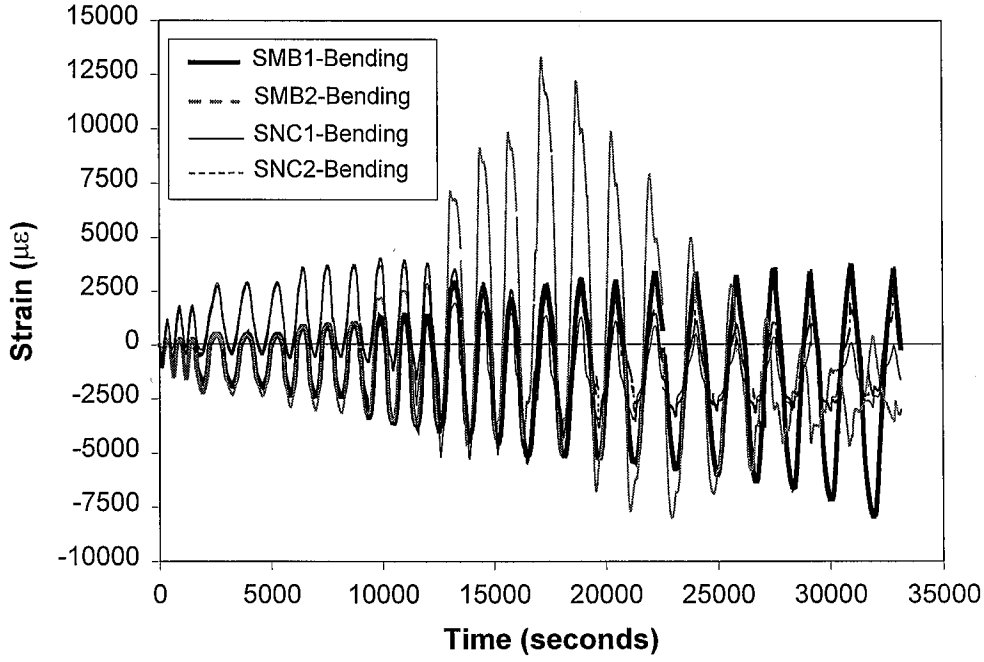

Fig. 6.2.13 Bending Strains of the Studs along the Top and North Interfaces of the First Story

6.2.4 Summary of Axial and Bending Strain Demands

According to the discussions from the previous section, the strain demands on the interface headed stud connectors can be summarized as follows:

1) The headed studs along the bottom interface of the infill walls had the highest tensile strain demands and largest variation range of the axial strain in each cycle.

2) The axial strains of the studs along the top interfaces and side interfaces are negligible during the first three loading groups, but a permanent "set" of the axial strains was accumulated during later cycles for these studs.

3) There was not much difference between the bending strain demands on the headed studs along different interfaces before the studs along the bottom interfaces started to fail.

4) The bending strain range of studs along the side interfaces decreased after the specimen reached its maximum load, but the bending strain range of the studs along top interface of the first story continued growing and dominated the stud response.

6.3 Interface Slip and Separation

There were 29 LVDTs placed along the interfaces between the steel frame and the RC infill walls to measure the slip and separation of the interfaces. The slip or separation readings of these LVDTs are plotted versus the applied lateral load in Appendix B.2. The reading of each "slip" LVDT at the peak story drift of each loading cycle is listed in Table B.2.1 of Appendix B.2. The reading of each "separation" LVDT at the peak story drift of each loading cycle is listed in Table B.2.2 of Appendix B.2.

6.3.1 Interface Slip Demands

6.3.1.1 Difference in Slip Demands in Two Loading Directions

The difference of the readings from the slip LVDTs in the north and south loading directions indicated that slip demands on the interface headed stud connector were quite different in the two loading directions, especially for the studs near to the corner regions. Since the studs failed primarily due to low-cycle fatigue and strain range is the

determining factor in low-cycle fatigue, the average of the absolute values of the slip readings in the two directions, instead of the absolute value of the maximum slip reading, is more meaningful to represent the slip demand of the stud.

Figure 6.3.1 shows the ratio of the readings in the two loading directions from the slip LVDTs along the bottom interface of the first story, at the peak interstory drift of each loading cycle. Figure 6.3.2 shows the ratio of the readings in the two loading directions from the slip LVDTs along the top interface of the first story, at the peak interstory drift of each loading cycle. As shown in Figure 6.3.3, the slip LVDTs LSLBI_1 and LSLBI_2 were along the north portion and south portion of the bottom interface of the first story, respectively; and the slip LVDTs LSLTI_1 and LSLTI_2 were along the north portion and south portion of the top interface of the first story, respectively. When the specimen was loaded in the south direction, besides carrying approximately uniform shear force transferred through the middle beam, the studs in the south portion of the bottom interface (where LVDT LSLBI_2 was located) and in the north portion of the top interface (where LVDT LSLTI_1 was located) had to resist an additional horizontal component of the strut force in the infill wall. This resulted in larger readings in LVDTs LSLBI_2 and LSLTI_1 when the specimen was loaded in the south direction, as shown in Figure 6.3.1.(b) and Figure 6.3.2.(a). For the same reason, at locations of LVDTs LSLBI_1 and LSLTI_2, the slips were larger when the specimen was loaded in the north direction than in the south direction. Among the four slip LVDTs along the beam–infill wall interfaces of the first story, LVDT LSLBI_2 had the largest disparity of slip readings between the two loading directions. After 0.2% cycles, at the location of LVDT LSLBI_2, the slip in the north loading direction was less than 20% of the slip in the south loading direction, which may explain why the studs along the south portion of the bottom interface of the first story did not fail in the test.

Figure 6.3.4 shows the distribution of the average slip along the bottom interface of the first story, top interface of the first story and the bottom interface of the second story, respectively, by using the test data from the two LVDTs installed along each interface. The average slip is the average of the absolute values of the peak slip readings

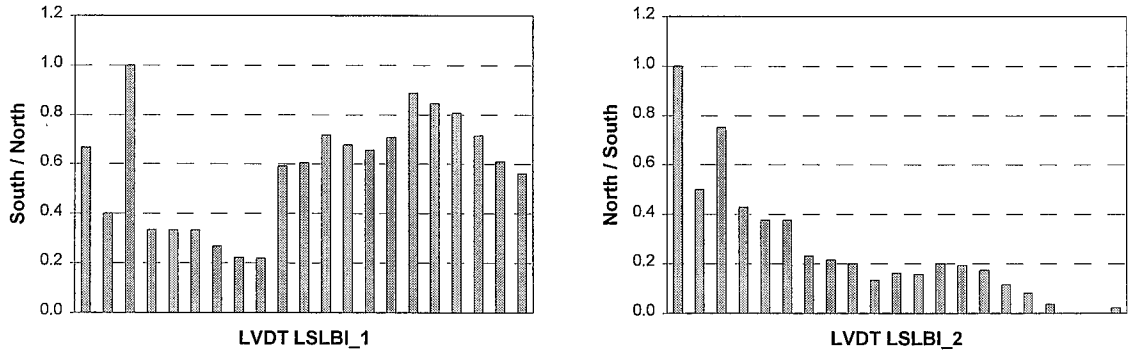

Fig. 6.3.1 Ratio of the LVDT Readings in the Two Loading Directions along the Bottom Interface of the First Story at Peak Interstory Drift per Cycle

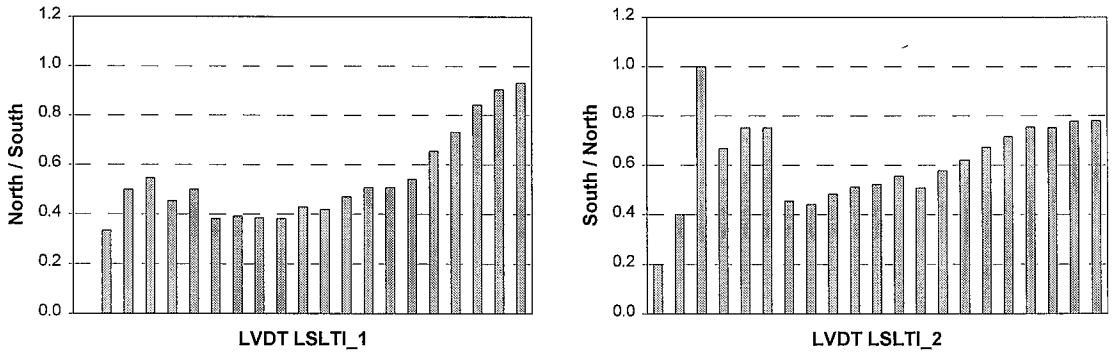

Fig. 6.3.2 Ratio of the LVDT Readings in the Two Loading Directions along the Top Interface of the First Story at Peak Interstory Drift per Cycle

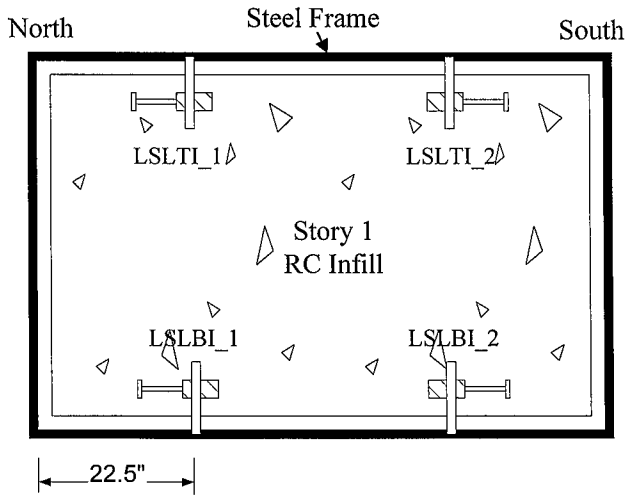

Fig. 6.3.3 Slip LVDTs along the Beam-Infill Wall Interfaces in the First Story

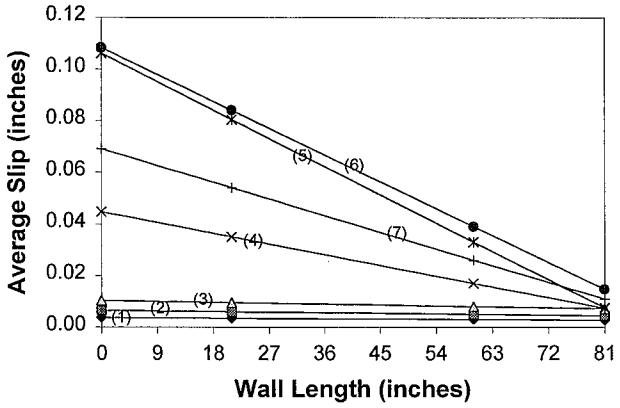

a) Bottom Interface of Story1

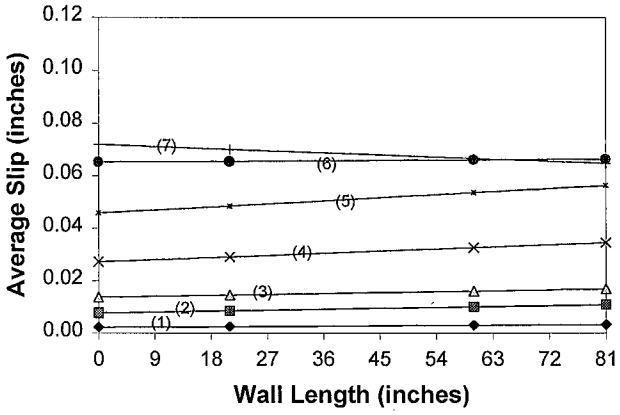

b) Top Interface of Story 1

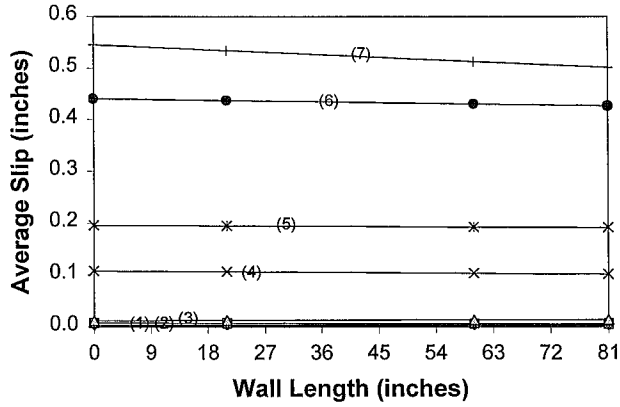

c) Bottom Interface of Story 2

* (1) – Cycle G1-1; (2) – Cycle G2-1; (3) – Cycle G3-1; (4) – Cycle G4-1; (5) – Cycle G5-1; (6) – Cycle G6-1; (7) – Cycle G7-1

Fig. 6.3.4 Distribution of the Average Slip along the Beam–Infill Interfaces

in the north and the south loading directions during each loading cycle, providing a direct correlation to the strain ranges seen in the stud. The distribution was obtained by using a straight line to fit the average slips from the two LVDTs along each interface. It can been observed that along the bottom interface of the first story, the average slip decreased from the north corner to the south corner, while along the top interface of the first story and the bottom interface of the second story, the average slip was approximately constant.

6.3.1.2 Comparison of Slip Demands

Figures 6.3.5 and 6.3.6 compare the interface slips of the first story at the peak interstory drift in the south loading direction and in the north loading direction, respectively. Figures 6.3.7 and 6.3.8 compare the interface slips of the second story similarly. The interface slips shown in these figures are the slips in the middle of the interfaces because only one slip LVDT was installed in the middle of the column–infill interfaces. Since the majority of the studs along the beam–infill wall interfaces fractured during the test, the slips along bottom and top interfaces of both stories are compared in Figures 6.3.9 and 6.3.10. The following observations can be drawn from these figures:

1) The headed stud connectors along the beam–infill wall interfaces of the second story were subjected to the highest slip demand. During the first two groups of cycles, Figures 6.3.7 and 6.3.8 show that the slips along the bottom and the top interfaces of the second story were comparable to the slip of either the north or the south interface of the second story. From cycle 8 (cycle G3-2), the slip along the bottom–infill interface of the second story became much larger than the slips along other interfaces of the second story. It continued to increase quickly during the following groups of cycles, surpassing 0.1 inches during cycles 10 to 12 (0.5% cycles), surpassing 0.2 inches and approaching 0.3 inches during cycles 13 to 15 (0.75% cycles), and surpassing 0.5 inches during cycles 16 to 18 (1.0% cycles). The slips along the top interface of the second story started to accelerate its increasing pace from cycle 16 (cycle G6-1), surpassing 0.1 inches during cycle 17 (cycle G6-2) and 0.2 inches during cycle 18 (cycle G6-3), and approaching 0.5 inches during the subsequent 1.25% cycles. It is unlikely that the studs can survive any

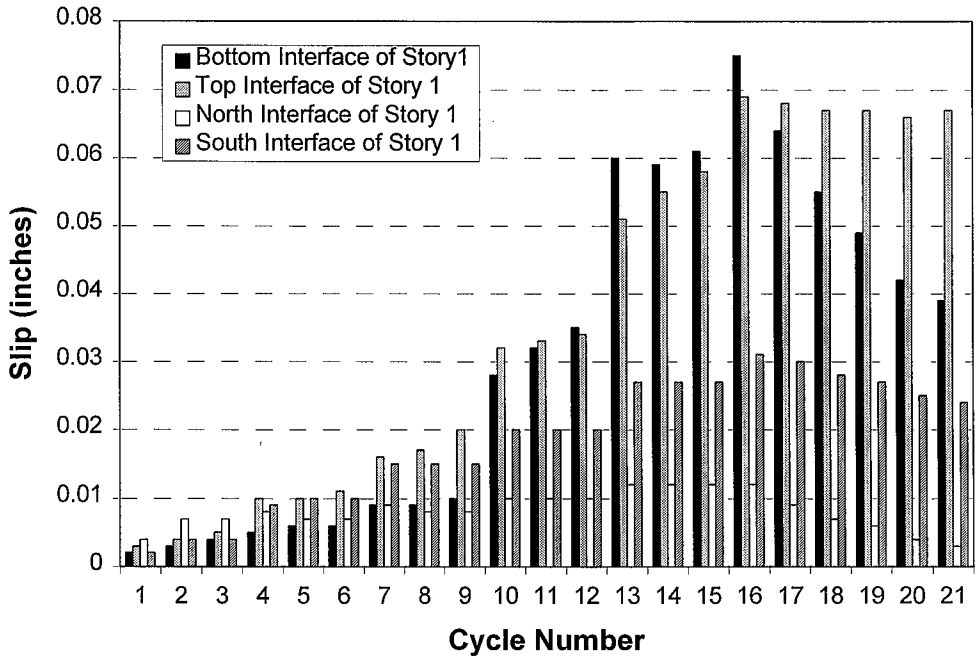

Fig. 6.3.5 Comparison of the Interface Slips in the First Story at Peak Interstory Drifts in the South Direction

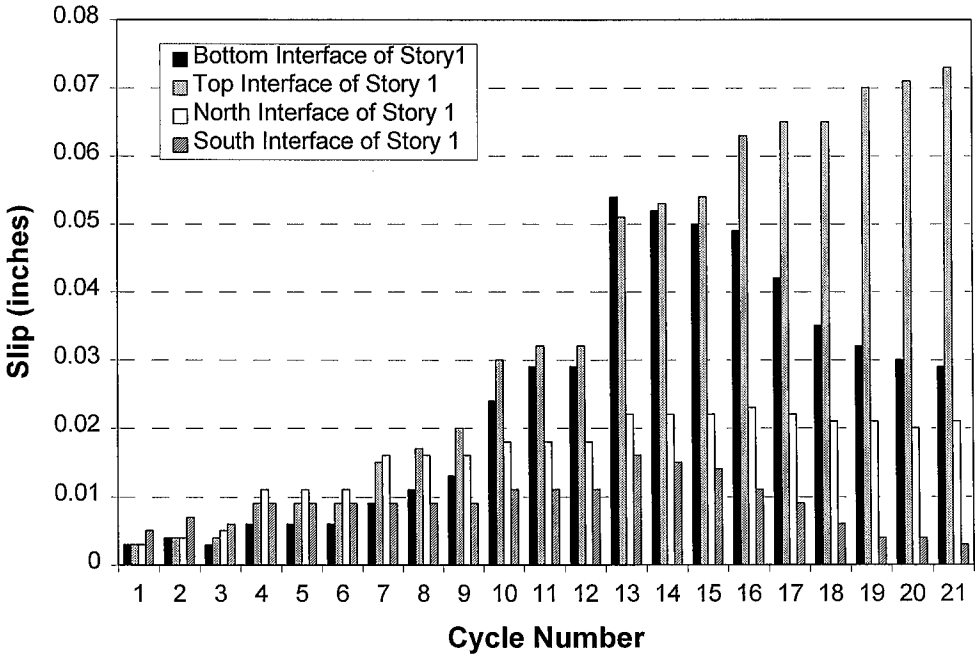

Fig. 6.3.6 Comparison of the Interface Slips in the First Story at Peak Interstory Drifts in the North Direction

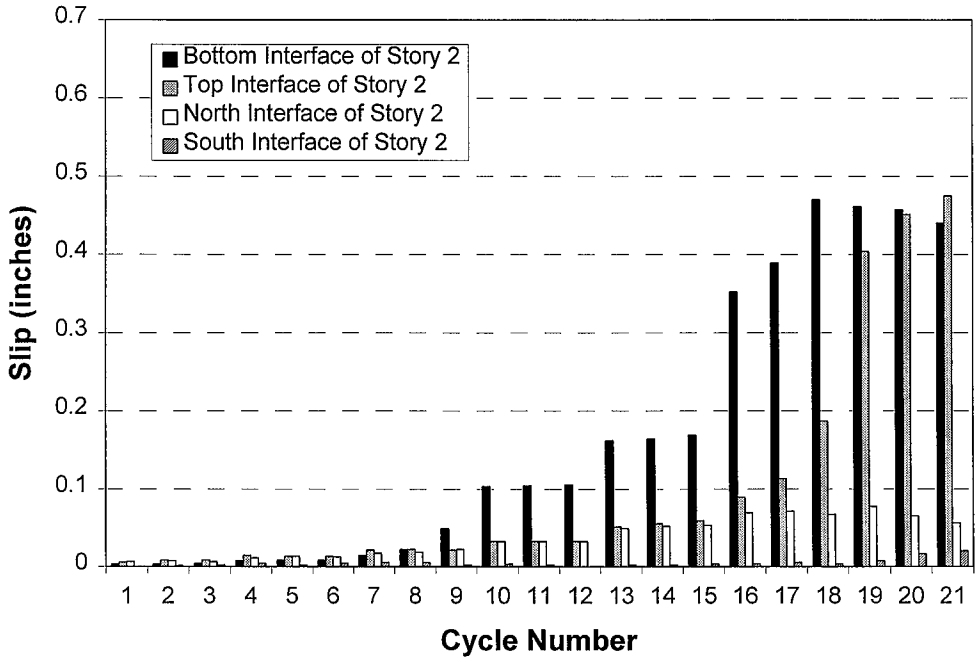

Fig. 6.3.7 Comparison of the Interface Slips in the Second Story at Peak Interstory Drifts in the South Direction

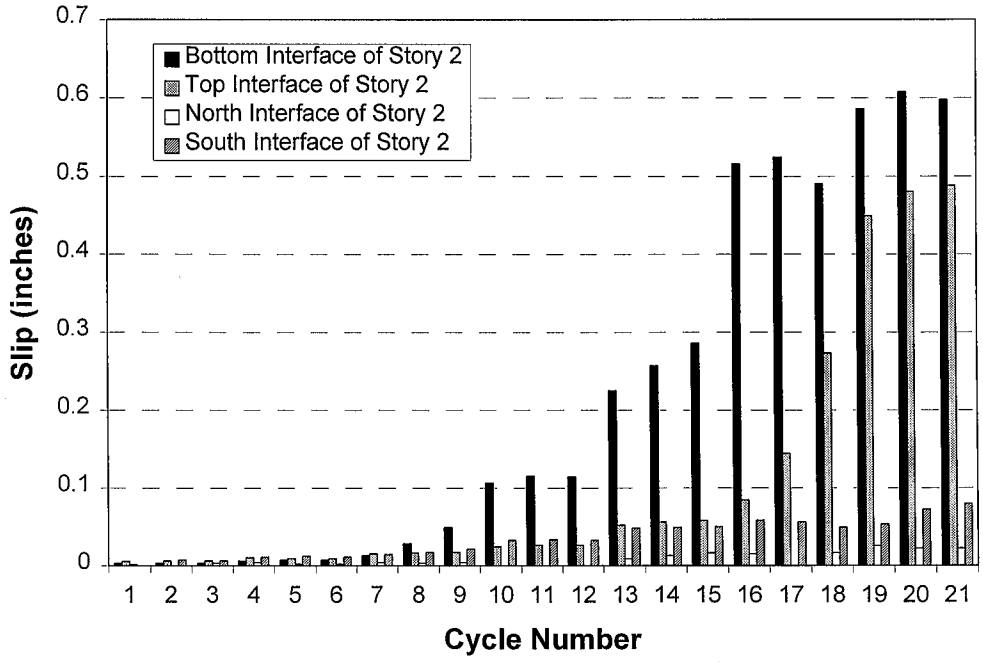

Fig. 6.3.8 Comparison of the Interface Slips in the Second Story at Peak Interstory Drifts in the North Direction

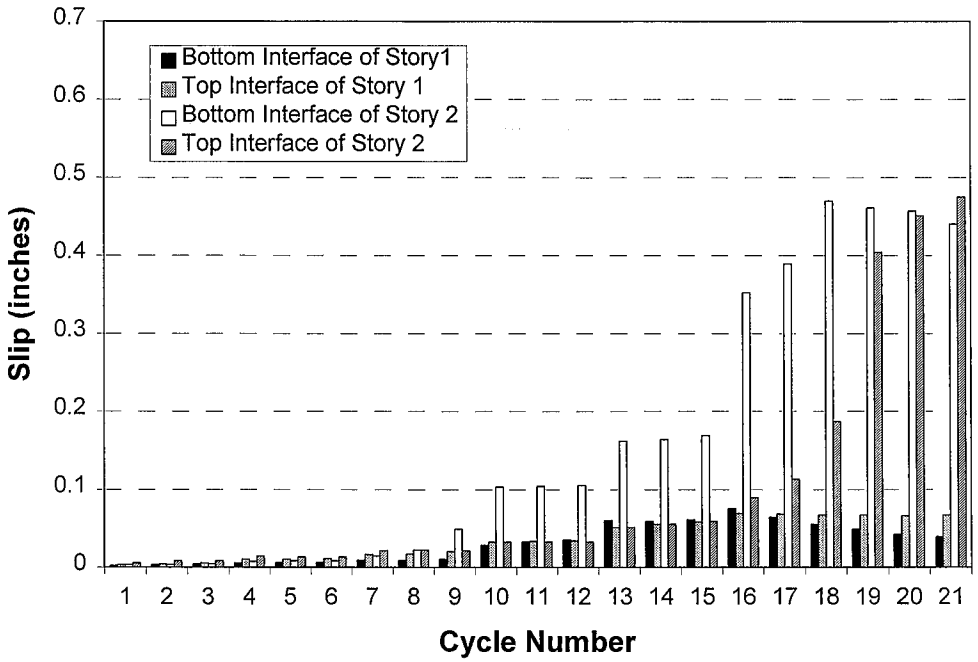

Fig. 6.3.9 Comparison of Slips along Beam-Infill Interfaces at Peak Interstory Drifts in the South Direction

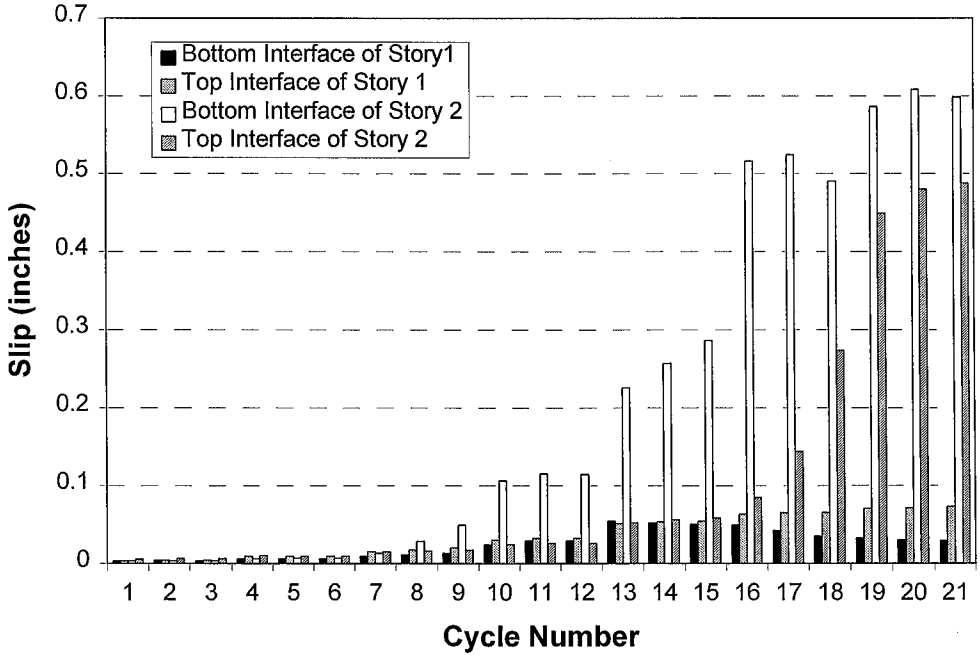

Fig. 6.3.10 Comparison of Slips along Beam-Infill Interfaces at Peak Interstory Drifts in the North Direction

slip beyond 0.5 inches (Saari, 1998). Therefore, the studs along the bottom interface of the second story were likely to fail by the time they reached the 1.25% cycles and the studs along the top interface of the second story were likely to fail by the time they reached the 1.5% cycles.

2) The studs along the beam–infill interfaces of the first story were hit moderately hard. As shown in Figures 6.3.9 and 6.3.10, the slips along the bottom and top interfaces of the first story increased steadily with each group of cycles, and were comparable to those along the top interface of the second story until cycle 16 (cycle G6-1). The slips along the bottom and top interfaces reached their maximum values during cycle 16, which were between 0.05 inches to 0.075 inches. After that, the slips along the bottom interface at the peak interstory drift decreased slowly while the slips along the top interface at the peak interstory drift maintained their values.

3) The studs along the column–infill interfaces of the second story were hit moderately hard in one direction. As shown in Figures 6.3.7 and 6.3.8, at the peak interstory drifts, the slips along the south interface of the second story were far below the slips along the north interface of the second story when the specimen was loaded in the south direction, while the slips along the north interface were far below the slips along south interface when the specimen was loaded in the north direction. Until cycle 16 (cycle G6-1), the larger one of these two slips was close to the slip along the top interface of the second story during each loading cycle.

4) The headed studs along the north and the south interfaces of the first story were subjected to the lowest slip demand. The maximum slip along these two interfaces at the peak interstory drift was only approximately 0.03 inches, or one half of the maximum slip along the north and the south interfaces of the second story at the peak interstory drift. The largest slips, those along the beam-infill interfaces in the second story, were approximately 50 times larger than those along the north and south interfaces in the second story.

6.3.1.3 Relationship Between Interstory Drift and Interface Slip

One of the most important objectives of the test was to determine the slip demands on the interface stud connectors in this composite system. A possible way to estimate the slip demand is to relate the interface slips to the interstory drift. Figure 6.3.11 plots the average slips from each slip LVDT along the top and bottom interfaces of the first story versus the average interstory drifts of the first story, where the average slips are the averages of the absolute values of each slip LVDT readings at the peak interstory drifts in the two loading directions. Figure 6.3.12 plots the average slips from each slip LVDT along the top and bottom interfaces of the second story versus the average interstory drifts of the second story. Figure 6.3.11 plots the average peak slips up to the 1.0% cycles because the average peak slip started to decrease thereafter. Figure 6.3.12 plots the average peak slips up to the 1.5% cycles because the slip readings were out of measurable range of the slip LVDTs thereafter. As seen from Figure 6.3.11, the average slip at the location of LVDT LSLBI_2 (south portion of the bottom interface) was lower than the average slips at other three LVDT locations. A trend of exponential growth of the average slip with the average interstory drift can be observed. Figure 6.3.12 shows that, in the second story, the average slips at the bottom interface (LSLBII_1 and LSLBII_2) increased approximately linearly with the interstory drift after the interstory drift surpassed about 0.4%, while again a trend of exponential growth can be observed for the average slip along the top interface of the second story. Based on the above observations, an exponential function was used to approximate the relation between the interface slips and interstory drifts, as shown in Figure 6.3.13. It can be seen that this exponential curve represents an upper bound for the estimation of the interface slips before 0.75% interstory drift, but may underestimate the interface slips between the 0.75% and 2% interstory drift.

6.3.1.4 Effect of the Axial Extension of the Partially-Restrained Connections

The extension of the PR connections generated the horizontal gap that allowed the infill panels to slip and comprised part of the interface slip demand. In order to determine

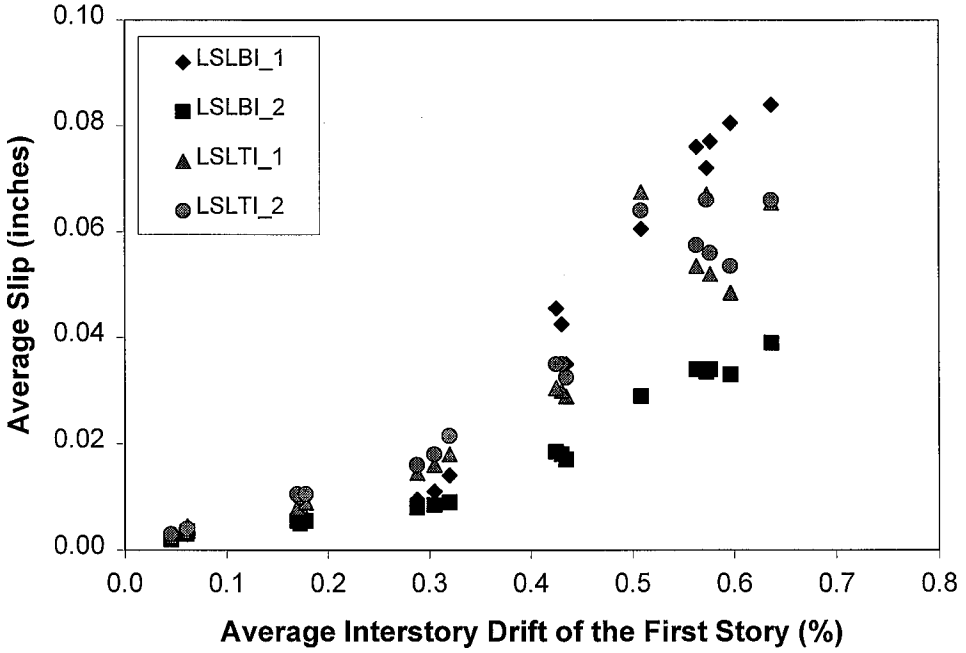

Fig. 6.3.11 Relationship of Average Interstory Drift and Average Interface Slip in the First Story

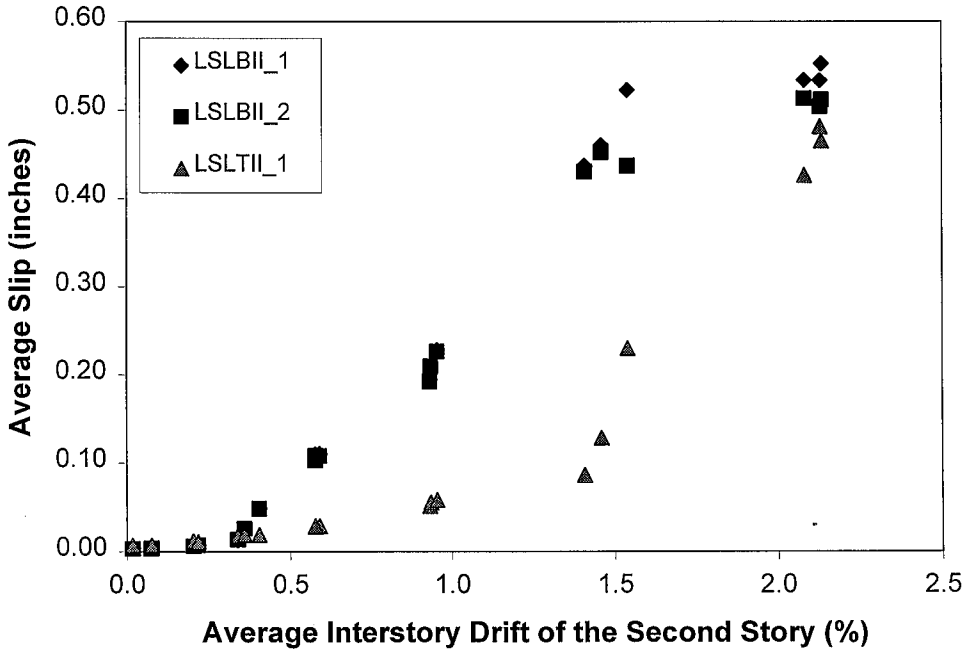

Fig. 6.3.12 Relationship of Average Interstory Drift and Average Interface Slip in the Second Story

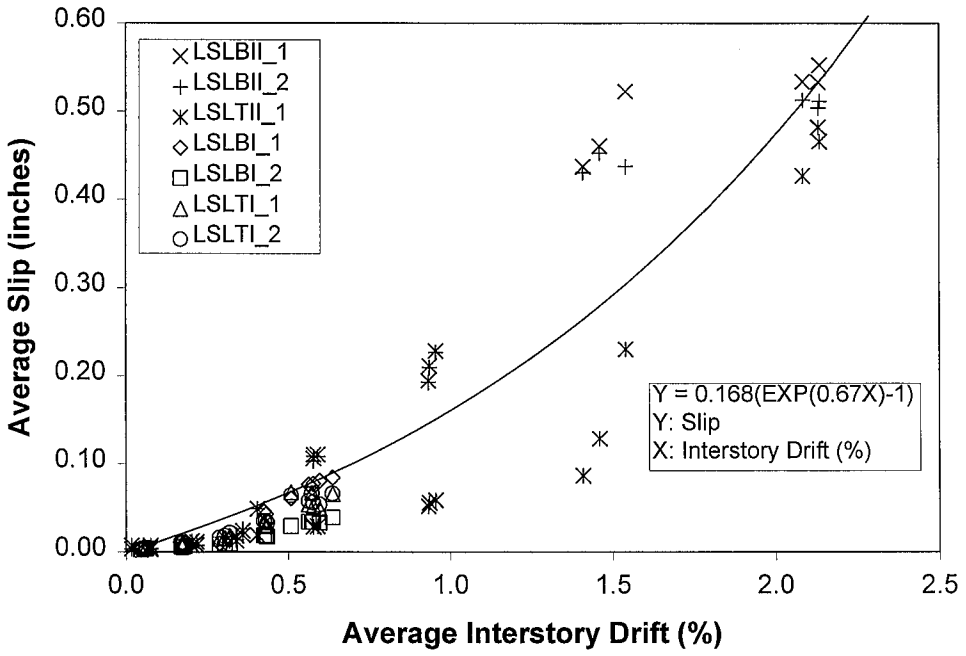

Fig. 6.3.13 Relationship of Average Interstory Drift and Average Interface Slip

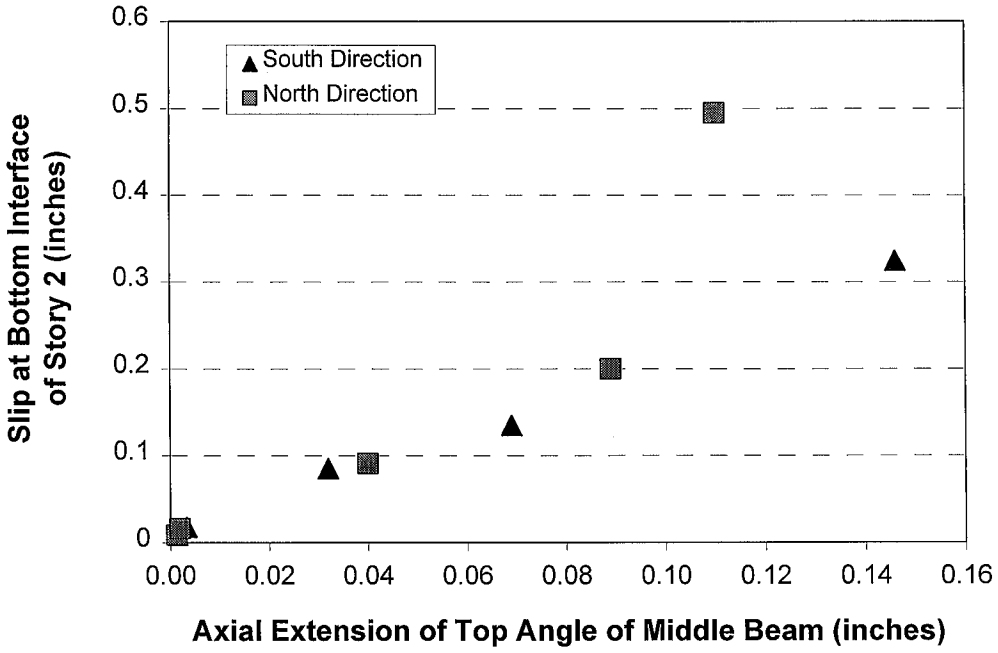

Fig. 6.3.14 Axial Extension of the PR Connections versus Beam-Infill Interface Slip

such an effect quantitatively, Figure 6.3.14 plots the axial extension of the top angle of the PR connections of the middle beam versus the slip along the bottom interface of the second story, at the peak load of the first cycle of each loading group. The extension of the top angles was measured by two LVDTs attached to the top flange of the middle beam (see Figure 3.4.7). Figure 6.3.14 shows the relationship up to cycle G6-1 since these two LVDTs malfunctioned after this cycle.

It can be observed from Figure 6.3.14 that, during the first three groups of cycles, the axial extension of the top angles of the PR connections comprised less than 20% of the interface slip demands. However, this contribution increased up to 40-50% during the later two groups of cycles.

6.3.2 Separation Demands on the Headed Studs

As shown in Figure 3.4.5, there were three separation LVDTs placed along every beam-infill wall interface except for the top interface of the second story, where only two separation LVDTs were used, and there were two separation LVDTs placed along every column-infill wall interface. The purpose of using these separation LVDTs is to determine the variation of separation demands along the steel frame and infill wall interfaces. Unfortunately, the readings of the separation LVDTs were found to be unreliable after the test and could only be used as qualitative evidence for evaluating the behavior of the separation demands.

After the test, the readings of six separation LVDTs along the beam-infill interfaces were used to calculate the axial strain of the nearby studs and compared to the results of direct strain measurement. Figure 6.3.15 compares the axial strains in stud SBB2, which was located in the north portion of the bottom interface of the first story. The thin line represents the axial strain obtained by calculating the average of the readings from two strain gages placed on opposite sides of the stud shaft. The coarse line represents the axial strain obtained by dividing the readings of the separation LVDT LSEBI_1 by the stud shaft length, 2.22 inches. Relating the interface separation to the axial strain of the stud is based on two assumptions. First, the stud and the separation

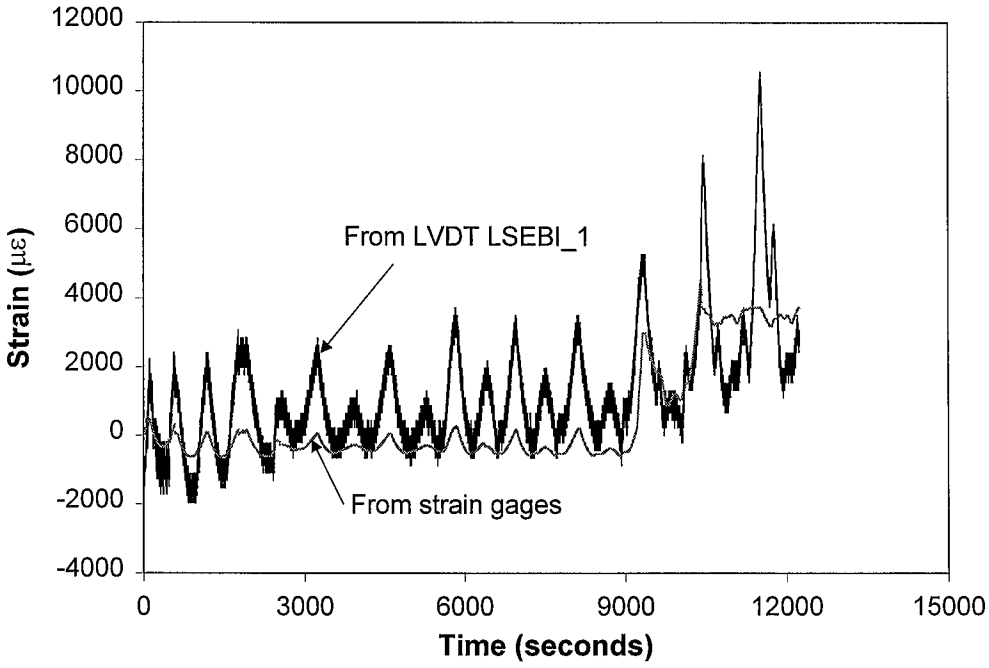

Fig. 6.3.15 Comparison of the Axial Strains in Stud SBB2 Obtained from Two Experimental Approaches: LVDTs and Strain Gages

LVDT are in the same location along the interface. In this case, the separation LVDT LSEBI_1 was only 0.5 inches away from the location of stud SBB2 and the two can be considered approximately in the same location. Second, interface separation is induced by the elongation of the headed stud, and deformation of the concrete below the stud headed is negligible. This assumption was proven to be correct for the cast-in-place headed studs that were loaded in tension and failed by shaft fracture (Cook et al., 1992). The comparison in Figure 6.3.15 shows that although the strain history obtained from the LVDT synchronized with the strain history from the strain gages, a large disparity existed between the two sets of curves, with the strains computed from the LVDT data being considerably larger than those obtained from the strain gages. The axial strain limits for each cycle obtained from the LVDT data was approximately five times that obtained from the strain gages.

Figure 6.3.16 compares the axial strains in stud SMB8, which was located in the north portion of the bottom interface of the second story. It can be seen that the strain

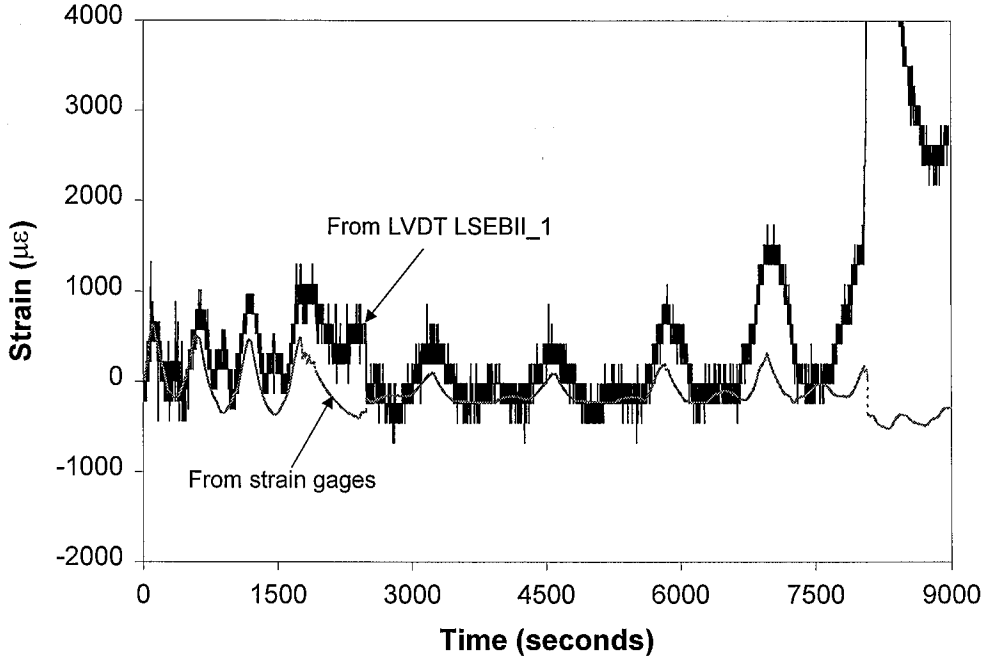

Fig. 6.3.16 Comparison of the Axial Strains in Stud SMB8 Obtained from Two Experimental Approaches: LVDTs and Strain Gages

history obtained from the LVDT also synchronized with the strain history from the strain gages, and the two sets of values were closer to each other than those of stud SBB2, but they cannot be considered equivalent.

Figure 6.3.17 compares the axial strains in stud SMB2, which was located in the north portion of the top interface of the second story. Lack of synchronization, as well as a large disparity, were observed between the strain history obtained from the LVDT data and that from the strain gages.

Influence from the interface slip might be the primary factor responsible for the disparity and lack of synchronization between the two sets of strain histories obtained from different experimental approaches. As seen from the setup of the separation LVDT in Figure 3.4.6, friction between the aluminum plate and rounded head of the LVDT rod might have prevented the rod head from sliding freely on the surface of the aluminum plate that was mounted the beam flange. As a result, the LVDT rod might have not remained perpendicular to the aluminum plate during the loading history, and extension

of the rod due to the interface slip is, therefore, inexorably combined with the separation readings. Interface slips were also three orders of magnitude larger than interface separations (see Section 6.4.2). Thus, even a small angle of inclination for the rod translates to a large difference in axial movement of the rod.

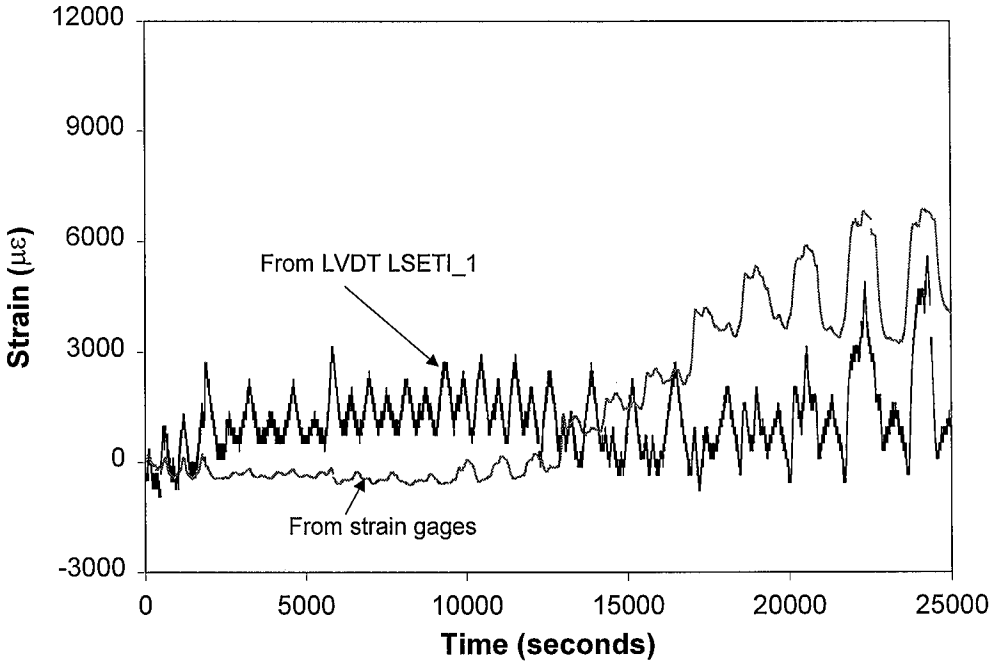

Fig. 6.3.17 Comparison of the Axial Strains in Stud SMB2 Obtained from Two Experimental Approaches: LVDTs and Strain Gages

6.4 Deformation Capacity of the Headed Studs

6.4.1 Failure Sequence of the Gaged Headed Studs

It is important to identify the time and sequence of failure of headed stud connectors, which not only helps to understand how the composite interaction between the steel and the RC infill wall deteriorated during the loading history, but also enables the estimation of deformation capacity of headed studs under cyclic loading. In the specimen, a limited number of studs in different representative locations were instrumented by strain gages, as shown in Figure 4.5.1. It was assumed that gaged studs

failed by fracture as long as the measured strain traces vanished or stopped providing reasonable measurements. Table 6.4.1 lists the designation of each gaged stud that fractured during the test, together with the cycle when failure occurred and the corresponding interface slips. In the table, the "interface slip when fracture occurred" and the "maximum interface slip before fracture" of a particular stud are the slip values measured by the nearest LVDT to that stud. Several observations can be made from the table:

Table 6.4.1 Gaged Studs that Fractured During Testing

Stud Location	Stud Desig-nation	Failure Sequence	Gage Reading Description	Interface Slip when Fracture Occurred (inches)	Maximum Interface Slip before Fracture (inches)
Bottom interface of story 1	SBB1	6	Signal vanished during cycle G4-3-A	0.025	0.053 during cycle G4-2-C
	SBB2	5	Signal vanished during cycle G4-2-A	0.019	0.044 during cycle G4-1-C
Top interface of story 1	SMB2		Provided signal during the entire loading history		
	SMB3	8	Signal vanished during cycle G7-3-A	0.063	0.085 during cycle G6-1-A
	SMB4		One gage malfunctioned before testing, the other provided signal during the entire loading history		
	SMB5	7	Signal vanished during cycle G6-3-C	0.057	0.079 during cycle G6-1-C
Bottom interface of story 2	SMB7	4	Signal vanished during cycle G4-1-C	0.069	0.121 during cycle G4-1-A
	SMB8	1	Possibly signal vanished during G3-3-A	0.034	0.027 during cycle G3-2-C
	SMB9	2	Possibly signal vanished during G3-3-C	0.024	0.041 during cycle G3-3-A
	SMB10	3	Signal vanished during cycle G4-1-A	0.045	0.056 during cycle G3-3-C

1) The gaged studs along the bottom interface of the second story fractured first, then the gaged studs along the bottom interface of the first story fractured, and the gaged studs along the top interface of the first story were the last ones to fracture. It is inconclusive when the studs along the top interface of the second story fractured because these studs were not gaged.

2) The fracture of the gaged studs along the bottom interfaces of both stories occurred before the specimen reached its maximum strength in cycle G5-1. The fracture of the gaged studs along the top interface of the first story occurred after the specimen reached its maximum strength in cycle G5-1.

3) The studs usually fractured at a slip that was smaller than the maximum slip in the previous loading cycle. This phenomenon further indicated that stud fracture was due to low-cycle fatigue.

6.4.2 Deformation Capacity of the Headed Studs

The deformation capacity of the interface headed studs might be diminished by two factors: 1) cyclic loading, and 2) combined axial deformation and slip demands. This section attempts to determine quantitatively the effect of these factors according to the available information provided by gaged studs that fractured during the test.

The first step is to determine the effect on stud deformation capacity of combined axial deformation and slip demands. In Table 6.4.2, the two columns under the title "Maximum Slip" list the values of the maximum slip achieved by the gaged studs before they fractured during the test, and the values of their corresponding axial deformation; the two columns under the title "Maximum Separation" list the values of maximum separation achieved by the studs before they fractured during the test, and the values of corresponding slip. The slip at the location of each stud was determined by interpolating or extrapolating the measured slips from the two slip LVDTs along the same interface containing the studs. The axial deformation of each stud was obtained by multiplying the axial strain of that stud with stud shaft length. It was necessary to estimate separation in this manner because the separation LVDT data was determined not to have the required

accuracy (see Section 6.3.2). The table shows that the occurrence of the maximum slip was not accompanied by the occurrence of the maximum separation, and the stud could be either in compression or in tension when the stud reached its maximum slip. Furthermore, the fracture of the stud did not necessarily occur at either maximum slip or maximum separation. Therefore, the maximum slip demand or the maximum separation demand is not a good index to evaluate the combined effect of axial deformation and the slip demands. As discussed in the previous sections in this chapter, the interface headed studs of this composite steel frame-RC infill wall specimen failed by low-cycle fatigue. Masubuchi (1980) stated that, with low-cycle fatigue, the strain range is the dominant factor with decreasing fatigue life. Since the strain of the stud is related to the deformation of the stud and the loading cycles have varied magnitudes, the "average deformation range" of the stud can be considered to be a better index in evaluating the combined effect of axial deform and slip demands. The average deformation range of the stud is calculated in the same way as "average stress range" is commonly calculated in high-cycle fatigue problems, or:

$$\Delta_a = \frac{1}{2}\left(\sum \frac{1}{n}\Delta^3\right)^{1/3} \tag{6.4.1}$$

where

Δ_a = half of the average deformation range, either half of the average slip range, Δ_{as}, or half of the average axial deformation, Δ_{aa}, inches

Δ = deformation range, either the slip range or separation range, in one cycle

n = total slip or separation cycles before the stud fractured

The two columns under the title "Average Deformation Range" list values of the average slip range and average axial deformation range for each gaged stud that fractured during the test. To consider the interaction between the slip and axial deformation, the "half-average" slip range, Δ_{as}, and "half-average" axial deformation range, Δ_{aa}, for each stud were normalized by Δ_{su} and Δ_{au}. These normalized deformation ranges are plotted in Figure 6.4.1. The first normalization factor, Δ_{su}, is half of the required slip range for the

Table 6.4.2 Slip and Separation Information of
the Gaged Studs that Fractured during Testing (inches)

Stud	Location	Maximum Slip		Maximum Separation		Average Deformation Range	
		Slip	Axial	Slip	Separation	Slip(Δ_{as})	Axial(Δ_{aa})
SBB1	Bottom interfaces	0.071	0.0028	0.032	0.0061	0.027	0.0017
SBB2		0.051	0.0027	0.023	0.0101	0.018	0.0013
SMB7		0.134	0.0000	0.061	0.0046	0.051	0.0008
SMB8		0.027	-0.0001	0.003	0.0013	0.024	0.0006
SMB9		0.039	0.0005	0.028	0.0023	0.025	0.0006
SMB10		0.062	-0.0005	0.006	0.0018	0.025	0.0008
SMB3	Top interfaces	0.084	0.0142	0.062	0.0192	0.047	0.0018
SMB5		0.085	0.0040	0.048	0.0096	0.044	0.0023

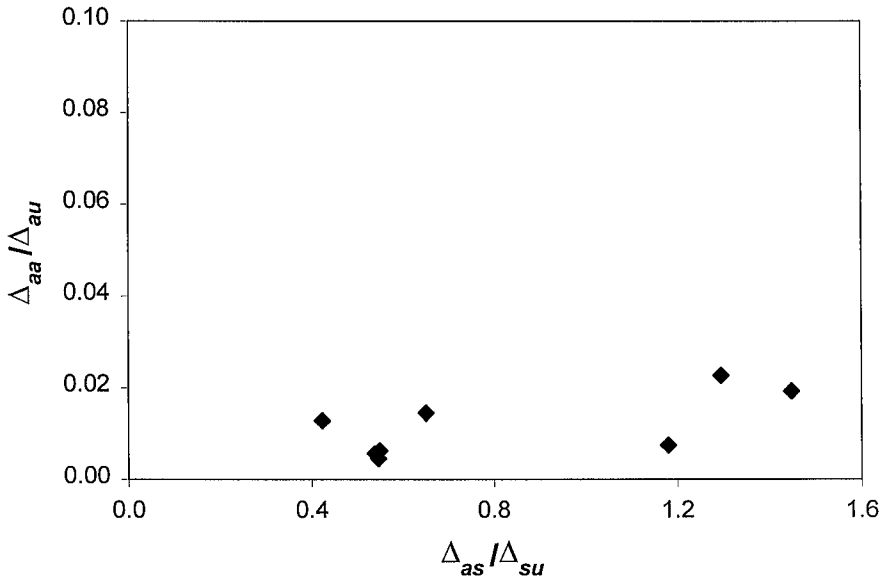

Fig. 6.4.1 Deformation Capacity of the Headed Studs

stud to fracture under cyclic shear loading alone with cycle number equal to that experienced during the actual test. The second factor, Δ_{au}, is half of the required axial deformation range for the stud to fracture under pure cyclic axial deformation with the cycle number equal to that experienced during the actual test. The normalization factors, Δ_{su} and Δ_{au}, may be related to ε_t, the required strain range for a smooth steel specimen, made of the same material as the stud, to fracture under axial cyclic loading with the cycle number equal to that experienced by the stud.

Figure 6.4.2 shows the deformation pattern of a failed stud under shear, which was observed by Saari (1998), indicating two plastic hinges might form in the shaft, one at the base and the other at a height of h_s from the base. If the elastic bending deformation and shear deformation of the stud are neglected and the length of the plastic hinges is assumed to equal $d_s/2$ (see Figure 6.4.2), then the slip, Δ_s, can be related to the maximum strain at the surface of the shaft, ε_m, as follows:

$$\Delta_s = h_s\theta = h_s\left(\frac{\varepsilon_m}{d_s/2}\right)\frac{d_s}{2} = \frac{h_s}{2}(2\varepsilon_m) \tag{6.4.2}$$

It is reasonable to assume that, for a stud with sufficient embedment length, the distance between the two plastic hinges is only determined by the diameter of stud as:

$$h_s = C_1 d_s \tag{6.4.3}$$

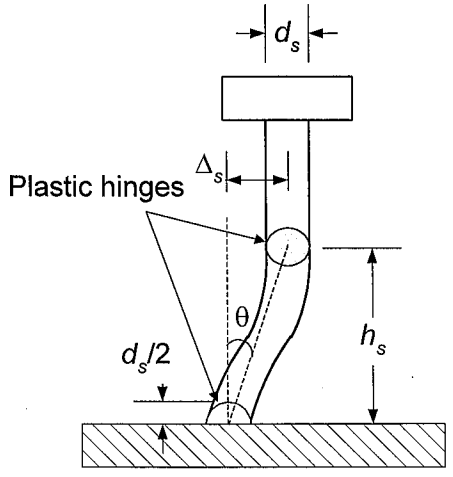

Fig 6.4.2 Failure Mechanism of a Headed Stud

where

C_1 = a constant

Therefore, Eq. (6.4.2) can be rewritten as:

$$\Delta_s = \frac{h_s}{2}(2\varepsilon_m) = \frac{C_1 d_s}{2}(2\varepsilon_m) = C_s(2\varepsilon_m)d_s \tag{6.4.4}$$

Replacing Δ_s with Δ_{su}, and $2\varepsilon_m$ with ε_t in Eq. (6.4.4) yields

$$\Delta_{su} = C_s \varepsilon_t d_s \tag{6.4.5}$$

In Eq. (6.4.5), the value of constant C_s can be determined according to the monotonic shear test of the headed studs confined in RC infill wall (Sarri, 1998). Under the monotonic shear loading, the maximum strain range ε_t at the surface of the stud shaft is equal to $2\varepsilon_u$, where ε_u is the elongation of the stud material. Saari (1998) conducted a series of tests to investigate the strength and deformation capacity of headed stud connectors between the RC infill wall and steel frames. One of them applied monotonic shear loading to headed studs with 3/4 inch in diameter. In that test, the slip capacity of the headed stud was 0.36 inches. The ultimate tensile elongation of that stud material was measured as approximately 25% in the mill reports provided by the supplier, Stud Welding Associates. Substituting $\Delta_{su} = 0.36$ inches, $\varepsilon_t = 2*0.25 = 0.5$ and $d_s = 0.75$ inches into Eq. (6.4.5) yielded the constant $C_s = 0.96$.

In Eq. (6.4.5), the value of ε_t can be obtained from the S-N diagram provided by Masubuchi (1980), in which S represents the strain range and N represents the cycle number. Masubuchi (1980) concluded from his research that the low-cycle fatigue of different types of steel materials followed the same S-N diagram, and furthermore, the low-cycle fatigue of different types of metals had close S-N diagrams. According to Masubuchi (1980), the relationship of total strain range versus cycles for failure of steel material can be approximately expressed as

$$\log \varepsilon_t = -0.4145 \log N - 0.5242 \tag{6.4.6}$$

By assuming the tensile strain is uniform along the stud shaft, factor Δ_{au} can be related to ε_t as:

$$\Delta_{au} = 0.5\varepsilon_t l_s \tag{6.4.7}$$

where

l_s = length of stud shaft

Figure 6.4.1 shows that the majority of values of Δ_{aa}/Δ_{au} are between 0 to 0.02, and the values of Δ_{as}/Δ_{su} are between 0.4 to 1.6. This indicates that the influence of axial deformation is negligible on the deformation capacity of headed studs in this specimen. Furthermore, because of the axial deformation demands are so small, the failure of studs is largely determined by the cyclic slip demands. Note that while the value of $C_s = 0.96$ is quite approximate, variation in this value does not lead to a change in this conclusion.

The second step towards estimating stud cyclic deformation capacity is to determine the effect of cyclic loading on the slip capacity of the headed stud since the axial deformation demand is considered being negligible. Based on the assumption that the slip capacity varies linearly with the maximum strain range in the stud (see Eq. (6.4.5)), the reduction of slip from monotonic loading to cyclic loading is determined solely by the number of cycles. For example, a stud undergoing 20 cycles before it fractures has a maximum strain range equal to approximately 86000 με according to Eq. (6.4.6). This is approximately 20% of the monotonic capacity, $2\varepsilon_u$, if the elongation of the stud material, ε_u, is defined as 20%. As a result, 20 cycles will decrease the stud slip capacity by approximately 80%.

The slip capacity obtained from the second step is a constant value of slip range that a stud is able to undergo before it fractures after a certain number of cycles. In an actual earthquake, the acceleration of ground movement is random, thus, the variation of interface slip is also random. Therefore, in order to evaluate the slip capacity in design, the "design" earthquake specification should include an effective number of cycles, and the mean value of the magnitude of the ground movement.

Chapter 7

Force Distribution in the Structural System

This chapter presents the force transfer mechanisms of the specimen, and calculates the proportions of the lateral force and overturning moment resisted by major components of the structural system.

7.1 Lateral Force Distribution

Figure 7.1.1 shows a schematic diagram of the idealized lateral force transfer paths in the composite steel frame-RC infill wall specimen. It can be seen that the lateral load is transferred to the base through three mechanisms: shear stud–infill wall interaction; diagonal compression struts due to the interaction between the steel frame and infill walls; and deformation of the steel frame alone. The percentage of the lateral force resisted by each mechanism is determined in this chapter for the purpose of evaluating the relative importance of these mechanisms at various loading stages.

7.1.1 Lateral Force Transferred by the Headed Studs

The lateral force along the cross sections at interfaces between the middle beam and the infill wall (sections A-A and B-B in Figure 7.1.1) was resisted by the steel column, the seat or top angles and the beam headed studs along the interfaces. The lateral force along the cross section at the bottom interface of the first story (section D-D in

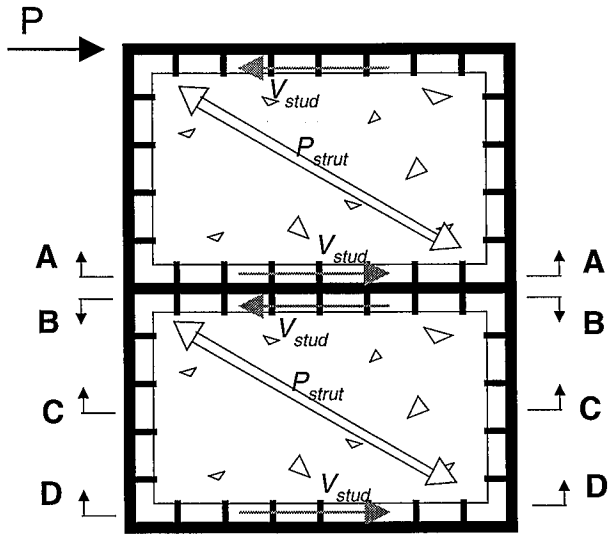

Figure 7.1.1 Lateral Shear Force Transfer Mechanism of the Specimen

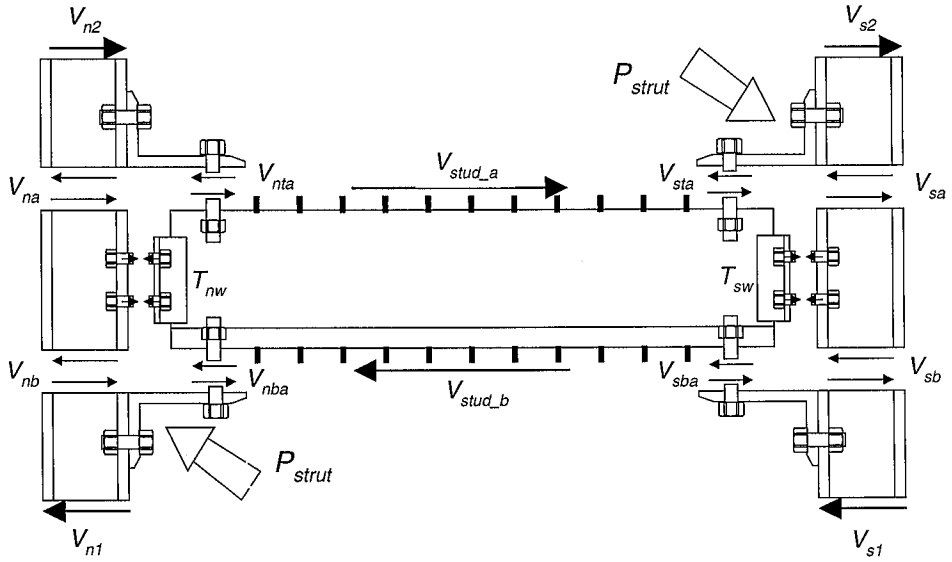

Figure 7.1.2 Lateral shear Force Transfer along Sections A-A and B-B

Figure 7.1.1) was resisted by the steel column and the beam headed studs since there were no top angles there. Figure 7.1.2 shows a schematic diagram of the lateral force distribution along section A-A and section B-B on both sides of the middle beam. The

Possible friction force due to the bearing between the steel beams and the infill wall in the corner region is neglected. It can be seen that the portion of lateral force transferred through the studs along the top interface of the beam most likely flowed into the studs along the bottom interface of the beam directly. The portion of the lateral shear force transferred through the compression strut was divided into two components: one that flowed into the panel zone region through shear in the column, and the other that flowed into the middle beam through tension in the top angle or seat angle of the PR connection. An equilibrium equation for lateral force is established along section A-A:

$$P = V_{stud\_a} + V_{na} + V_{sa} + V_{nta} + V_{sta} \tag{7.1.1}$$

where

P = total applied lateral force, kips

V_{stud_a} = lateral force resisted by the headed studs along A-A section, kips

V_{na} = shear force at the bottom of the north column in the second story, kips

V_{sa} = shear force at the bottom of the south column in the second story, kips

V_{nta} = axial force in the horizontal leg of the top angle of the north connection, kips

V_{sta} = axial force in the horizontal leg of the top angle of the south connection, kips

As discussed in Section 5.2, the shear forces at the bottom of the steel columns in the second story, V_{na} and V_{sa}, were estimated using measured shear strains at the center of the column web (see Appendix C). Tables 5.1.2 and 5.1.3 show these two shear forces at the peak lateral load in the south and north directions, respectively. The axial forces in the horizontal legs of the top angles, V_{nta} and V_{sta}, were assumed to equal the axial forces in the top flanges of the middle beam and were computed according to Eq. (5.1.7). Table 5.1.4 shows these forces at the peak lateral load in both directions. Therefore, the lateral force resisted by the interface studs along the middle beam V_{stud_a} can be written as:

$$V_{stud\_a} = P - (V_{na} + V_{sa} + V_{nta} + V_{sta}) \tag{7.1.2}$$

The same procedure can be used to calculate the lateral force resisted by the headed studs along the bottom interface of the middle beam (section B-B), V_{stud_b} and the lateral force resisted by the headed studs along the bottom interface of the first story (section D-D).

Figures 7.1.3 and 7.1.4 show the percentage of the lateral force resisted by the interface studs along sections A-A, B-B, and D-D, at the peak load of the first cycle of each group of cycles, but is unrecoverable after the column at the corresponding section yielded. It can be observed that, initially, the headed studs along the bottom interface of the second story shared the highest percentage of the lateral load among three interfaces (approximately 91% for the studs along the bottom interface of the second story, 88% along the top interface of the first story, and 83% along the bottom interface of the first story). The lateral force resisted by the studs along the bottom interface of the first story dropped by 4-5% in next two groups of cycles. The percentage of the lateral force resisted by the studs along the top interface of the first story also dropped slightly during the next two groups of cycles, but was maintained at about 80% for loading cycle G4-1 and G5-1. Figures 7.1.3 and 7.1.4 shows that the percentage of the lateral force resisted by the studs along the bottom interface of the second story dropped a little from cycle G1-1 to cycle G3-1, but quickly dropped by approximately 30% from the cycle G3-1 to G4-1.

To further evaluate the strength of the headed studs as a group, Figure 7.1.5 shows a plot of the lateral force resisted by the studs versus the average slip along the top interface of the first story at the peak lateral load during the first cycle of each group of cycles. Figure 7.1.6 shows a plot of the lateral force resisted by the studs versus the average slip along the bottom interface of the second story. The curve linking these peak values represents a possible envelope of the hysteretic shear force–slip relationship of the interface headed studs as a group. Figure 7.1.5 shows that, along the envelope, the shear stiffness of the stud group along the top interface of the first story decreased gradually before the average slip reached approximately 0.015 inches in cycle G3-1. The stud group then started to quickly lose its shear stiffness, approaching zero at 0.05 inches of

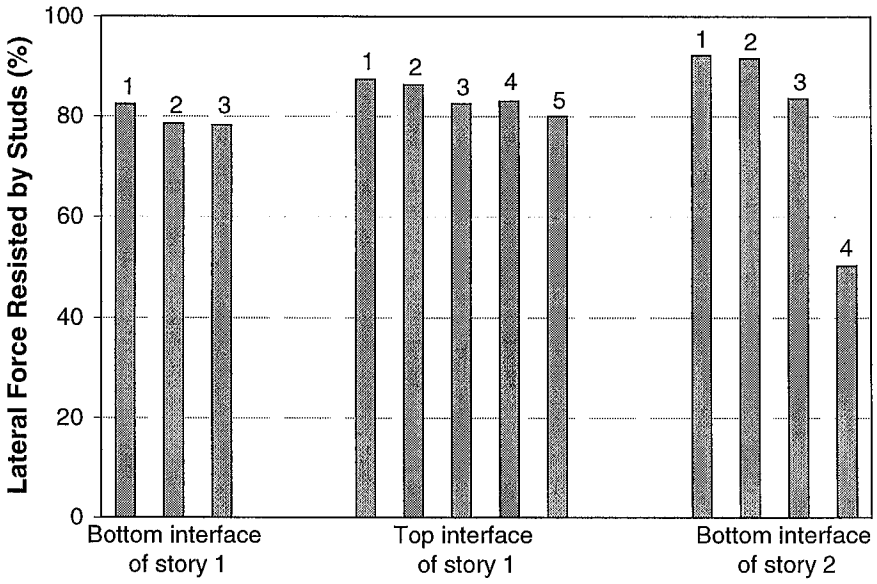

* 1 – G1-1-A; 2 – G2-1-A; 3 – G3-1-A; 4 – G4-1-A; 5 – G5-1-A

Fig. 7.1.3 Percentage of the Lateral Load Resisted by Interface Studs at Peak Load in the South Direction

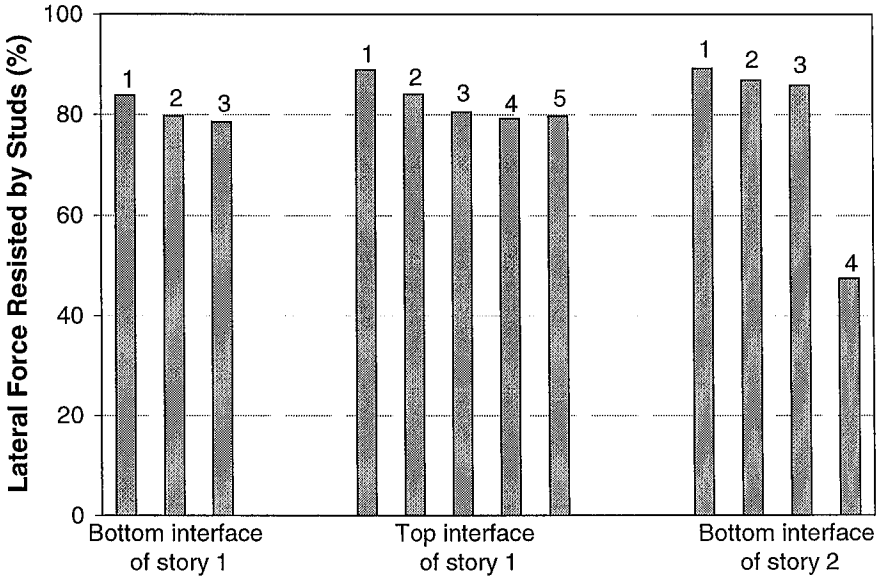

* 1 – G1-1-C; 2 – G2-1-C; 3 – G3-1-C; 4 – G4-1-C; 5 – G5-1-C

Fig. 7.1.4 Percentage of the Lateral Load Resisted by Interface Studs at Peak Load in the North Direction

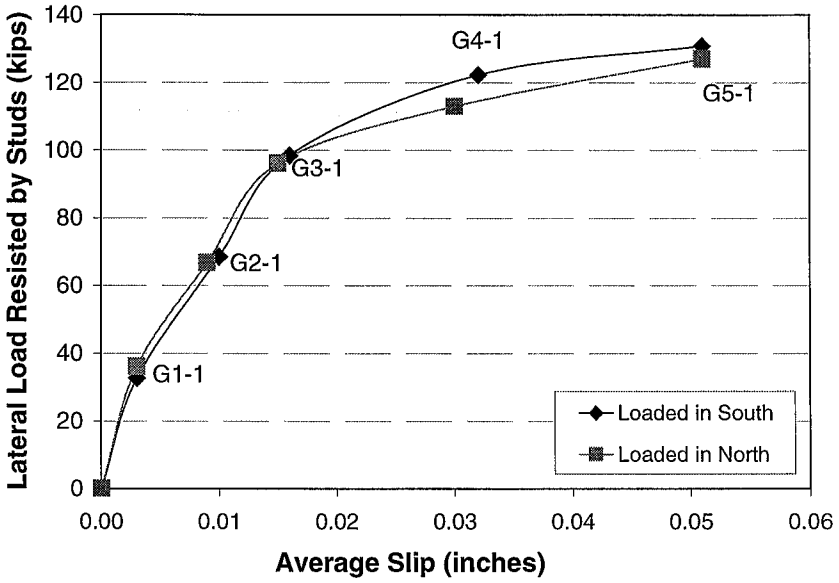

Fig. 7.1.5 Lateral Load Resisted by Studs versus Average Slip along the Top Interface of the First Story

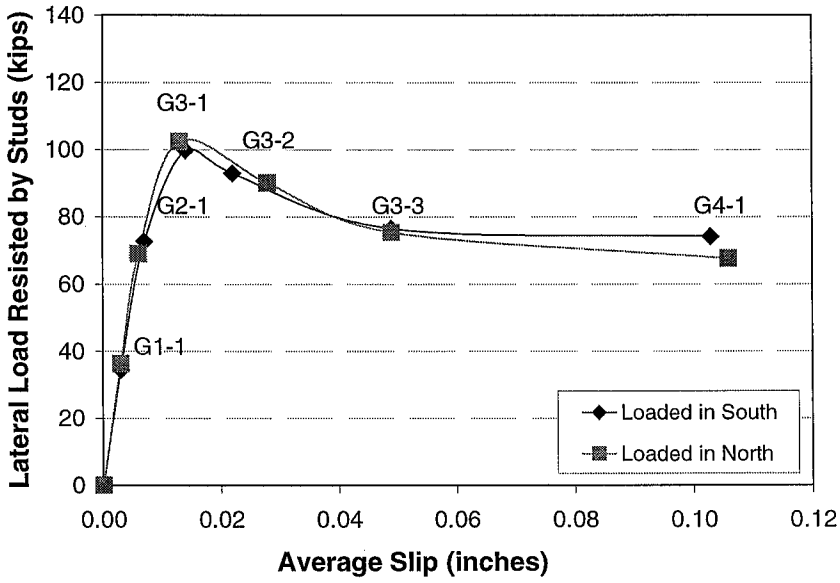

Fig. 7.1.6 Lateral Load Resisted by Studs versus Average Slip along the Bottom Interface of the Second Story

slip. Therefore, it is reasonable to designate the maximum strength of the stud group along the top interface of the first story as approximately 130 kips, approximately 1.85 times the design strength of the stud group. Figure 7.1.6 shows that, along the envelope, the shear stiffness of the stud group along the bottom interface of the second story was close to that of the stud group along the top interface of the first story until cycle G3-1. However, the maximum shear strength of the stud group there was achieved at cycle G3-1 at approximately 100 kips. The shear strength then dropped about 25% during the next two loading cycles, indicating that some of the studs along this interface failed during these loading cycles. There was little decrease of the shear strength during the next cycle, G4-1, although the average slip increased by more than 100% to reach 0.1 inches.

7.1.2 Lateral Force Transferred by the Compression Strut

Figure 5.1.14 shows that, when the specimen was loaded in the south direction, the horizontal component of the compressive strut along the up-north interface of the first story can be written as

$$F_c = V_{nb} + V_{nsa} + T_{stud} - V_{nd} \tag{5.1.3}$$

As discussed in Section 5.1.2, the shear force at the bottom of the north column and tensile force of the studs along the bottom portion of the north column were negligible. Therefore, when the specimen was loaded in the south direction, the shear force resisted by the compressive strut was approximately equal to the sum of the shear at the top of the north column in the first story, V_{nb}, and the axial force in the horizontal leg of the seat angle, V_{nsa}. Similarly, the lateral force resisted by the compressive strut in the infill wall of the first story should also approximately equal the shear force at the bottom of the south column, V_{sd}, when the specimen was loaded in the south direction. As a result, it is reasonable to assume that the average of $(V_{nb}+V_{nsa})$ and V_{sd} is the approximate lateral load resisted by the diagonal strut in the first story infill wall when the specimen is loaded in the south direction. Similarly, the average value of sum of the shear at the top of the south column and in the first story and the axial force in the horizontal leg of the seat

angle (V_{sb}+V_{ssa}), and shear at the bottom of the north column, V_{sd}, is the approximate lateral load resisted by the diagonal strut in the first story infill wall when the specimen was loaded in the north direction. There is no average for the second story since only the forces along the bottom of the second story were obtained. Figure 7.1.7 and Figure 7.1.8 show the percentage of the lateral load resisted by the diagonal strut in the infill wall of each story. In the first story, this percentage increased steadily from 10% in the first cycle to 25% when the specimen reached its maximum strength. In the second story, this percentage increased rapidly to 50% after cycle G3-1, indicating the diagonal strut become one of the major mechanisms to transfer the lateral load. As stated above, this is likely due to the loss of shear strength of the stud group along the bottom interface of the second story.

7.1.3 Lateral Force Resisted by the "Shear" Deformation of Steel Frame

Figures 7.1.3, 7.1.4, 7.1.7 and 7.1.8 show that, along sections at steel beam-infill wall interface, the headed studs and the compression strut transferred the majority of the lateral force. The steel frame was also gaged in the middle of the steel columns of the first story (section C-C in Figure 7.1.1). The result indicated that the steel columns only resisted 1-3% of the total lateral force along section C-C. It can be concluded that the lateral force resisted by the "shear" deformation of steel frame is negligible before the crushing of concrete occurred.

After the peak load, as the concrete was crushed and the compression strut deteriorated in the second story, both steel columns in the second story started to resist the shear force through the shear deformation of steel frame. After the 1.25% cycles, the maximum lateral load was stabilized to be 70 to 80 kips, which was approximately equal to the sum of the nominal shear strengths of the two steel columns, $2(0.6F_{yw}A_w)$=83 kips.

7.2. Overturning Moment Distribution

Since the axial force and bending moment of each column were obtained in Section 5.2, it is feasible to calculate the overturning moment resisted by the steel

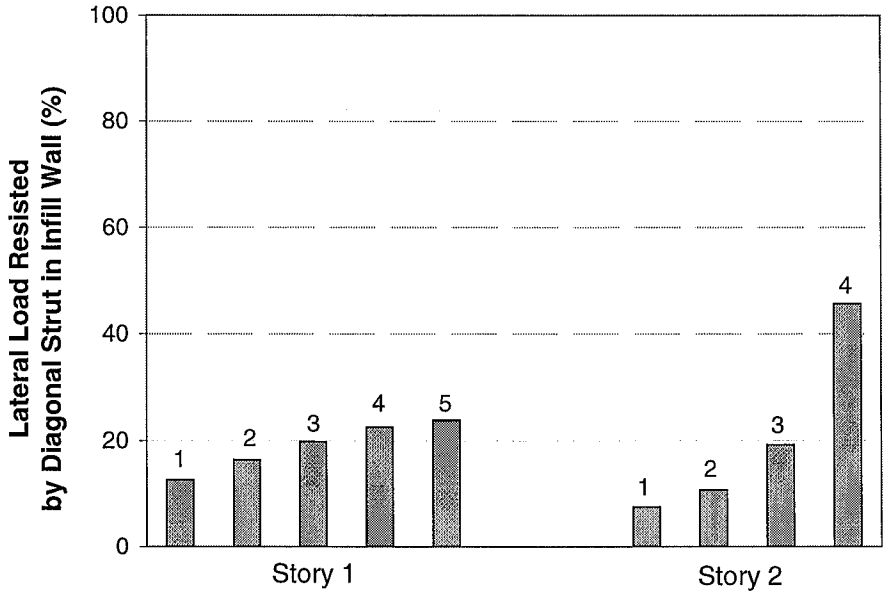

Fig. 7.1.7 Percentage of the Lateral Load Resisted by Diagonal Strut in Infill Wall at Peak Load in the South Direction

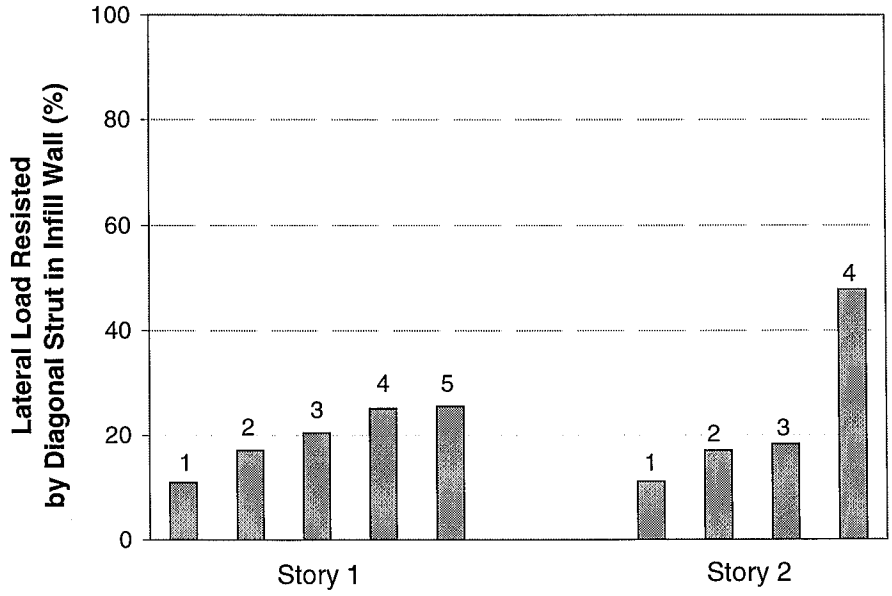

Fig. 7.1.8 Percentage of the Lateral Load Resisted by Diagonal Strut in Infill Wall at Peak Load in the North Direction

columns if the neutral axis of each cross section of the entire specimen can be determined. It is difficult to determine the location of the neutral axis of sections A-A and B-B (Figure 7.1.1) because of the complicated deformation pattern of the middle beam. However, for sections C-C and D-D, it is reasonable to assume that the deformation of these gaged sections is planar, as shown in Figure 7.2.1. As a result, three equations were established to solve the distances x_{nc} and x_{sc}:

$$\varepsilon_{nc} = \frac{N_{nc}}{EA_c} \tag{7.2.1}$$

$$\varepsilon_{sc} = \frac{N_{sc}}{EA_c} \tag{7.2.2}$$

$$x_{nc} + x_{sc} = L_c \tag{7.2.3}$$

where

N_{nc} = axial force in the north column, kips

N_{sc} = axial force in the south column, kips

ε_{nc} = axial strain at the center of the north column

ε_{sc} = axial strain at the center of the south column

A_c = cross section area of the column, inch^2

E = modulus of elasticity of the steel column, ksi

x_{nc} = distance from the neutral axis to the centerline of the north column, inches

x_{sc} = distance from the neutral axis to the centerline of the south column, inches

L_c = distance between the centerlines of the two columns, inches

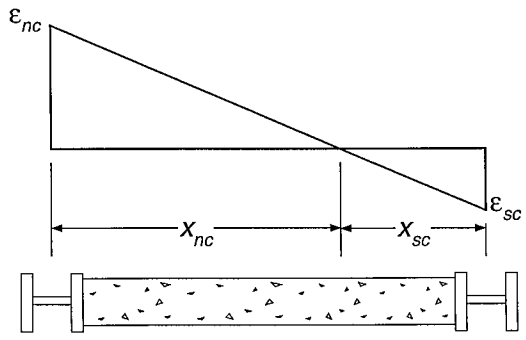

Figure 7.2.1 Section Deformation

The resulting x_{nc} and x_{sc} are:

$$x_{nc} = \frac{N_{nc}}{N_{nc} + N_{sc}} L_c \tag{7.2.4}$$

$$x_{sc} = \frac{N_{sc}}{N_{nc} + N_{sc}} L_c \tag{7.2.5}$$

Therefore, the overturning moment resisted by the steel columns was

$$M_{sct} = N_{nc} x_{nc} + N_{sc} x_{sc} + M_{nc} + M_{sc} \tag{7.2.6}$$

Substituting Eq. (7.2.4) and Eq. (7.2.5) into Eq. (7.2.6) yields

$$M_{sct} = \frac{(N_{nc}^2 + N_{sc}^2)}{N_{nc} - N_{sc}} * L_{sc} + M_{nc} + M_{sc}$$

where

M_{nc} = bending moment in the north steel column, kip-inches

M_{sc} = bending moment in the south steel column, kip-inches

The percentages of the overturning moment resisted by combined bending moment and axial force in the steel columns are shown in Figures 7.2.2 and 7.2.3. These figures show that, at the bottom of the first story, the percentage of overturning moment resisted by steel columns was approximately 80%. In the middle of the first story, the percentage of overturning moment resisted by steel columns varied from about 85% in cycle G1-1 to nearly 100% in cycle G5-1. It is not a surprise that this calculated percentage was higher in the middle of the first story than in the bottom, because in determining the neutral axis of section C-C, the interface slip between the steel columns and the infill wall was neglected. As a result, the location of the neutral axis was moved to the compression side of section C-C and the overturning moment was magnified a little. Therefore, it is reasonable to conclude that in the early loading cycles, the overturning moment resisted by the steel columns was approximately 80%, with the remainder resisted by the infill wall.

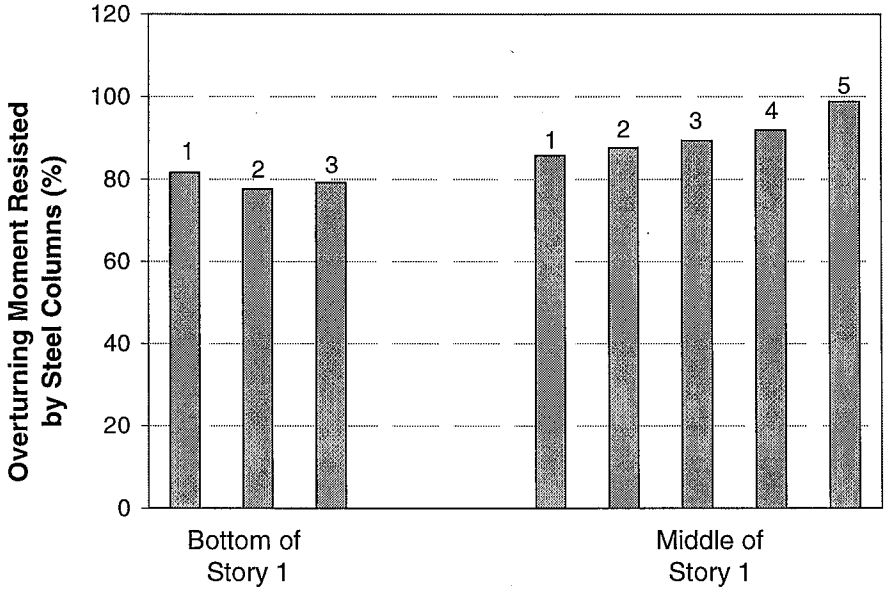

* 1 – G1-1-A; 2 – G2-1-A; 3 – G3-1-A; 4 – G4-1-A; 5 – G5-1-A

Figure 7.2.2 Percentage of the Overturning Moment Resisted by Steel Columns at the Peak Load in the South Direction

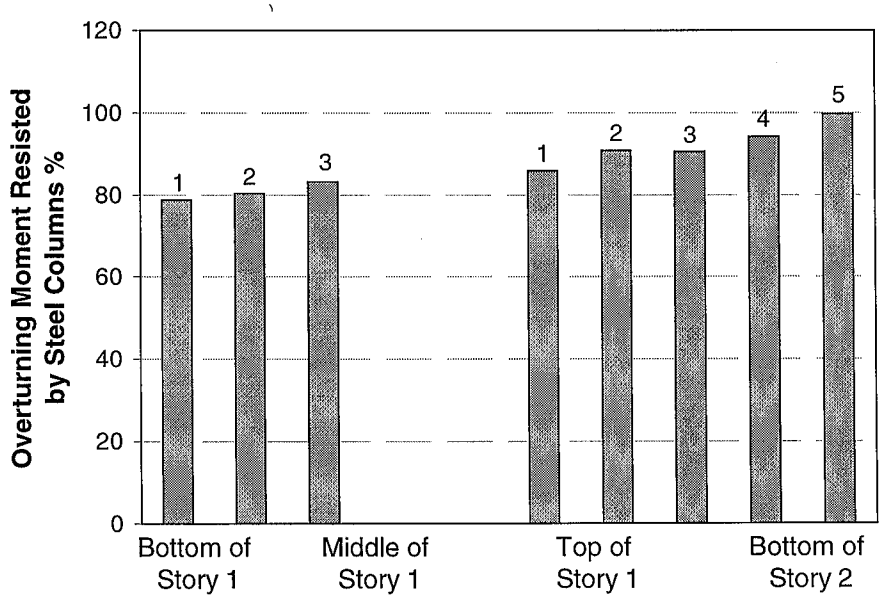

* 1 – G1-1-C; 2 – G2-1-C; 3 – G3-1-C; 4 – G4-1-C; 5 – G5-1-C

Figure 7.2.3 Percentage of the Overturning Moment Resisted by Steel Columns at the Peak Load in the North Direction

Figures 2.2.2 and 2.2.3 also show that, as the headed studs fail progressively, the steel frame carried more and more overturning moment. When few studs remained at the bottom interface of the second story during cycle G5-1, the frame was basically carrying all the overturning moment.

Chapter 8

Finite Element Analysis

This chapter compares the finite element analysis results with the test data, with the purpose of establishing a reasonable finite element model for analysis and design.

8.1 Finite Element Model of the Specimen

As stated in the seismic design provisions of NEHRP (1997), unless otherwise required, the design of a structure (sizing of individual members and connections) is based on the internal forces resulting from a linear elastic analysis using the prescribed lateral design force. This prescribed lateral force is calculated by dividing the force that would be associated with elastic response by a response modification factor, often symbolized as R. The elastic deformation of the structure under this design force is then amplified by a deflection amplification factor C_d to estimate the anticipated deformation likely experienced by the structure under severe levels of ground motion, and this deformation should not exceed the deformation limit specified in NEHRP (1997). This approach was employed in the design of the prototype structures, with the response modification factor R equaling 6 and the deflection amplification factor C_d equaling 5.5, as proposed in NEHRP (1997) for special composite reinforced concrete shear walls with steel elements.

The specimen was an approximately one-third scale model of the bottom two

stories of the six-story prototype structure. The prescribed lateral design load for the specimen was approximately 70 kips (see Section 3.1.1). However, lateral force at the limit state of "elastic" response of a structure, where the first significant yield of the structure occurs, usually has a higher value than the prescribed force (NEHRP, 1997). Discussions in Section 4.6 suggests that the lateral force at the limit state of "elastic" response of the specimen can be considered as approximately 80 kips according to its load–drift relationships. This implies that under the 80 kip lateral force, a reasonable elastic finite element model should give a close estimation of the internal forces of individual members, as well as the deformations in the actual specimen. These internal forces can then be used to design the individual members, and the deformation at the design force level can then be amplified to estimate the drift likely experienced by the structure under severe levels of ground motion.

The finite element model of the specimen is shown in Figure 8.1.1. The principles involved in the modeling of the specimen are basically the same as those used in the modeling of the prototype structure: the steel frame was modeled using beam elements and the infill wall was modeled using membrane elements in the commercial software program SAP2000 (CSI, 1996); each stud was modeled using a beam element; the mesh size of the infill wall was chosen so that a headed stud was located at each of the nodes along the perimeter; the PR connection was not modeled and, instead, the beam-to-column connection was assumed to be rigid. However, the eccentricity of the stud location was further included in the modeling of the specimen. Figure 8.1.2 shows the modeling of the interface where the studs are located. A rigid element was connected perpendicular to either the column or the beam. The length of the rigid element was approximately the same as the distance from the centerline of the frame element to the flange surface, so that the displacement at the end of the rigid element could represent the displacement of the flange surface. One end of the headed stud element was linked to the end of the rigid element and the other end was linked to the joint of the infill wall element. Since the headed studs were fully embedded into the concrete and there was no obvious gap along the interface before the test, the length of headed stud element was set

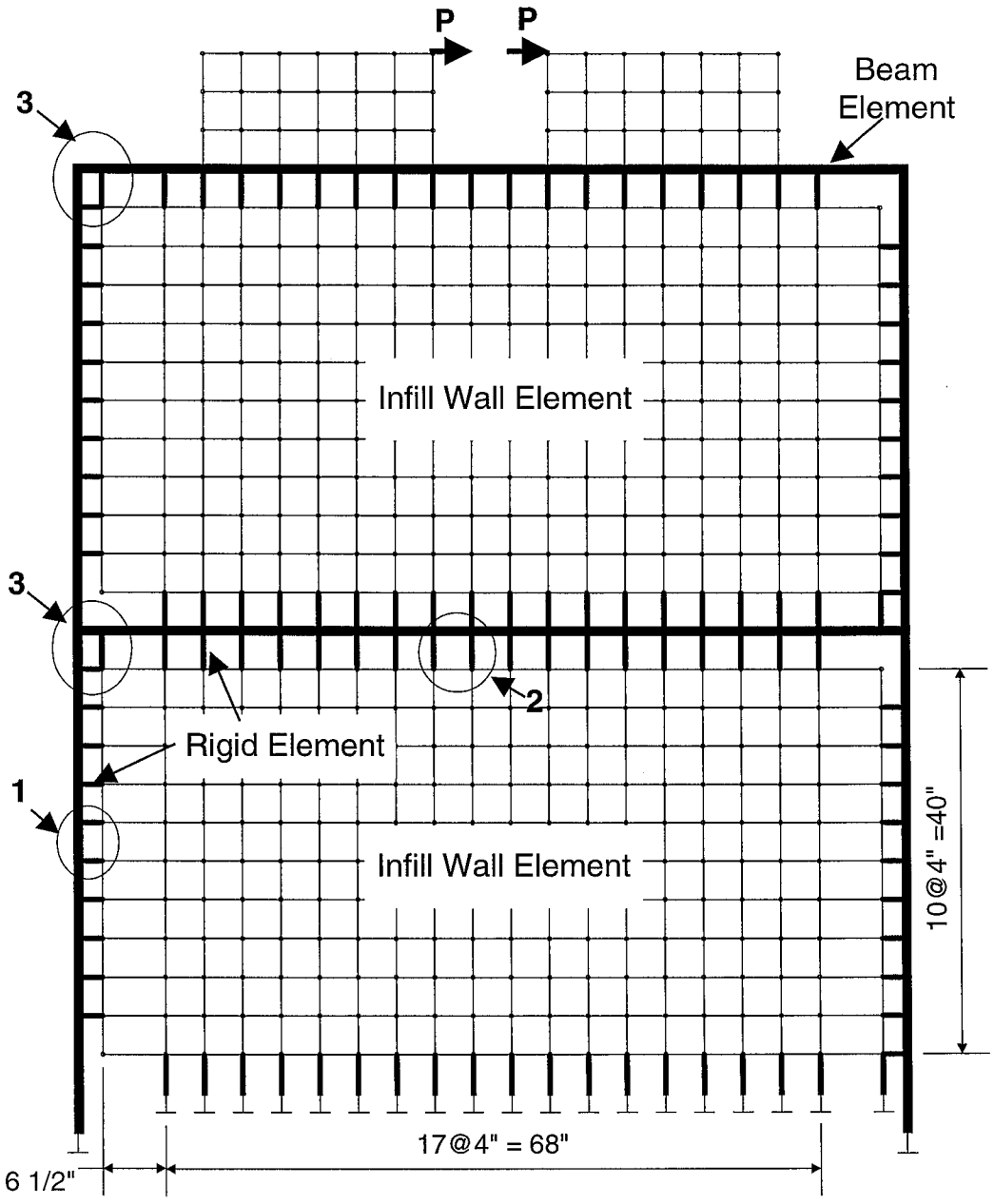

* Detailing of (1), (2) and (3) see Figure 8.1.2

Fig. 8.1.1 Finite Element Model of the Specimen

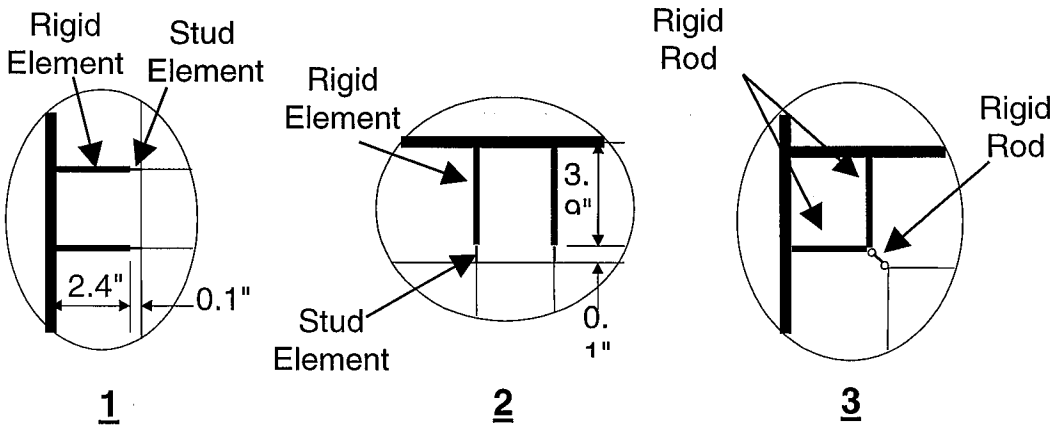

Fig. 8.1.2 Modeling of Interface Studs

only as 0.1 inches. It can be seen from Figure 8.1.2 that, although in the specimen there were no headed studs in the north-top corner in the first story and in the north-top corner in the second story, in the model, two rigid rods were connected to the beam and the column and connected to each other at their other ends. Another rigid rod was then linked to the intersection point and the corner joint of the infill wall to transfer the compression force in the corner region, which existed when the specimen was pushed to the south. The same modeling technique was applied to the south-bottom corners of both stories based on the same reason.

The forces from two actuators were applied to two loading beams W8×40 welded to the top flange of the top beam W8×13. Therefore, the bending deformation of the top beam of the specimen was highly restrained by the loading beams. To model this behavior, two sets of membrane elements were connected along the top beam, with each having infinite stiffness. The heights of these two membranes were the same as the distance from the centerline of the top beam to the centerline of the actuator. It was assumed that the load was equally transferred to the two membranes, through tension and compression, respectively.

As for the boundary conditions, it was assumed that the column was fixed at the bottom, at the same height as the centerline of the bottom beam. It is a reasonable assumption since the stiffness of the bottom portion was strongly enhanced by the two

stiffener plates welded along the tips of the column flanges to form a box section (see Section 3.3). The bottom ends of the rigid element along the bottom interface of the first story were assumed to be fixed since the bottom beam was welded to the foundation plate.

The dimensions of the headed stud connector used in the specimen were as follows: length = 2.5 inches; diameter of the shank = 3/8 inches; thickness of the stud head = 9/32 inches.

As discussed in the finite element analysis of the prototype structures (see Section 2.3.3), based on the experimental results from Cook et al. (1992), the axial tensile stiffness of one stud was calculated as: $K_{ts} = EA/L$= 1442.8 kips/inch, implying that the stud behaves elastically under the lateral force at the limit state of "elastic" response of the structure and the crushing of concrete around the stud is neglected. The stud element was a beam element with a 0.1 inch length. When the stud element was in tension, it had the same axial stiffness as K_{ts} calculated above. When the stud element was in compression, the concrete and the steel frame compressed against each other in the actual structure. Therefore, much less deformation was expected in the stud element. To achieve this in the modeling, the axial area of a stud element was set to approach infinity (i.e., a very high value) when it was in compression. A few iterative steps were needed for the analysis to determine whether the studs were in compression or in tension.

Equation (2.3.2) shows the shear load-slip relationship of an embeded headed stud subjected to shear force, as proposed by Ollgaard et al. (1971). This relationship is plotted in Figure 8.2.1, where the shear load is normalized by the nominal shear strength of the stud, Q_{sn}. At the limit state of "elastic" response of the specimen, the shear stiffness of the headed stud was defined in the same way as the effective lateral stiffness of the entire structural system (see Section 4.6). As shown in Figure 8.1.3, the shear stiffness is taken as a secant to the capacity curve at a shear force equal to $0.6Q_y$=(0.6)(0.85Q_{sn})= 0.51Q_{sn}, where Q_y=0.85Q_{sn} is defined as the yield strength of a headed stud loaded in shear, and $0.6Q_y$ is taken as the load at which the secant stiffness is defined (this corresponds to methodology used in Section 4.6 to define the secant stiffness of the

system as a whole). The slip of a headed stud at a shear of $0.51Q_{sn}$ is equal to 0.011 inches.

According to Eq. (2.3.3), at a given slip level, the secant shear stiffness $K_{ss} = Q/\Delta$ is proportional to the nominal shear strength of the stud, Q_{sn}, which is given by AISC (1993) as:

$$Q_{sn} = 0.5A_{sc}\sqrt{f_c' E_c} \leq F_u A_{sc} \tag{8.1.1}$$

Contrary to Eq. (3.1.1), the strength reduction factor due to the cyclic loading is not included in the nominal shear strength if the nominal shear strength is used for estimating the shear stiffness. This is so because cyclic loading typically reduces the strength and the slip capacity of a shear studs but has little effect on its secant stiffness (i.e., the envelope of the cyclic loading history is close to the monotonic loading history). The nominal shear strength of a headed stud with 3/8 inches in diameter is approximately 6 kips if the nominal compressive strength properties of concrete, 3.5 ksi, and the corresponding modulus of elasticity, 3370 ksi, are used in Eq. (8.1.1).

As in the finite element analysis of the prototype structure, it was assumed that, under shear force, the stud element deforms as if both ends of the stud element were fixed. As a result, the shear stiffness of the stud element is:

$$K = \frac{12EI}{L^3} \tag{8.1.2}$$

This stiffness should be equal to the secant shear stiffness K_{ss} of the stud.

8.2 Evaluation of the Finite Element Analysis

Table 8.2.1 lists the secant shear stiffness of a headed stud at the slip of 0.011 inches (at the shear of $0.51Q_{sn}$). In order to legitimize using this secant shear stiffness as the shear stiffness of a headed stud at the limit state of "elastic" response of the specimen, the following sections compare the measured response with the computational responses for finite element models A to D, in which the secant shear stiffnesses, K_{ss}, of a headed stud were calculated at slips of 0.005 inches, 0.0075 inches, 0.011inches, and 0.02 inches,

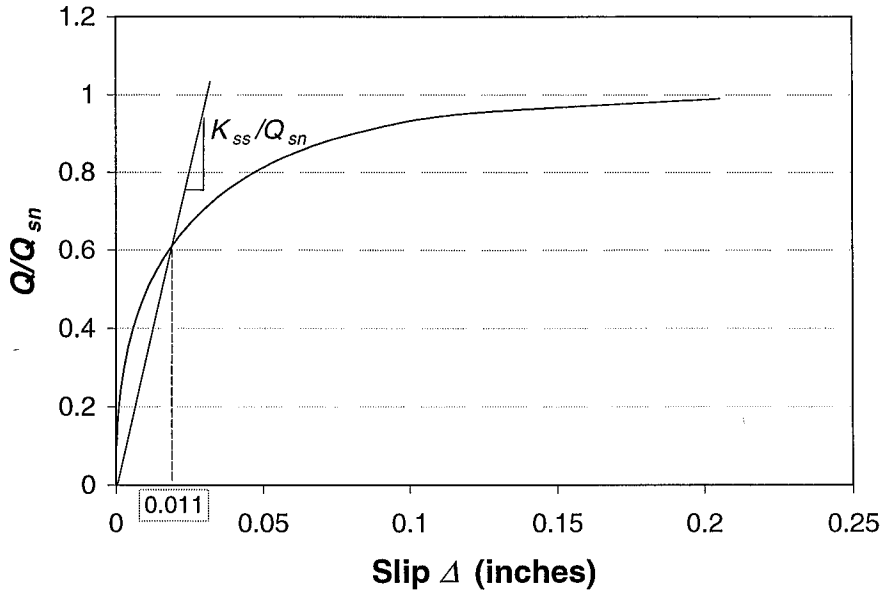

Fig. 8.1.3 Definition of the Shear Stiffness of a Headed Stud
at the Limit State of "Elastic" Response of the Structural System

Table 8.2.1 Shear Stiffness of the Stud with 3/8 inches in Diameter

Slip Δ (inches)	Shear Force (kips)	Secant shear stiffness K_{ss} (kips/inch)
0.005	2.25	449.9
0.0075	2.62	349.6
0.011*[1]	**3.06**	**278.2**
0.02	3.71	185.9

1: defined shear stiffness at the limit state of "elastic" response of the specimen

respectively (see Table 8.2.1). The total applied lateral load in the finite element model is 78.8 kips, which was the same as the peak load of cycle G2-1-A, was regarded to be sufficiently close to 80 kips, the lateral force at the limit state of "elastic" response of the specimen. In these finite element models, the nominal modulus of elasticity of steel is

equal to 29000 ksi and the nominal modulus of elasticity of concrete is equal to $57\sqrt{f_c'} = 57\sqrt{3500} = 3370$ ksi.

8.2.1 Comparison of Interface Slips

Table 8.2.2 lists the interface slips from the analyses of finite element models A to D, together with the measured responses of the specimen at the peak load of cycle G2-1-A (see Section 6.3). The computational result is an average value of the slips of all studs along the same interface. The measured response is an average value of the readings from two "slip" LVDTs along the same interface. The measured response shows that the interface drift along the bottom story in the first story was the smallest due to the boundary conditions, which is also reflected in the results of the finite element analysis. The finite element analysis shows that the interface slips along the top interface in the first story, bottom interface of the second story and the top interface of the second story are almost the same, while the slip along the top interface in the first story slightly greater than the other two. However, the test data shows variations of the slips along these three interfaces. In order to evaluate which value of the secant shear stiffnesses gives a best estimation of the overall interface slips, "Slip Error" in Table 8.2.2 is calculated in accordance with the following equation:

$$Error = \frac{\sqrt{\frac{\sum_i (S_{FE,i} - S_{M,i})^2}{4}}}{\frac{\sum_i S_{M,i}}{4}} \times 100\% \qquad (8.2.1)$$

where

$S_{FE,i}$ = average slip along one of the interfaces from the finite element analysis

$S_{M,i}$ = average slip along one of the interfaces from actual measurement

Although case B gives the minimum value of "Slip Error", the error of case C is only 5% more than that of case B. Therefore, regarding the estimation of the interface slips, the secant shear stiffness K_{ss} = 278.2 kips/inch at the shear of $0.51Q_{sn}$ can be considered a

reasonable estimate for the secant shear stiffness of studs at the limit state of "elastic" response of the specimen.

8.2.2 Comparison of Interstory Drifts

Figure 8.2.1 compares the interstory drifts of the specimen at the peak load of cycle G2-1-A (see Section 4.2) with those from the finite element analyses. It can be seen that the finite element analyses underestimate the interstory drifts by a large percentage, and decreasing the shear stiffness of the studs has a small effect on the estimated interstory drifts. For example, the second story interstory drift increases by only 27% from case A to case D, while the secant shear stiffness of the headed stud decreases almost by 70%. However, even in case D, the interstory drift is still less than the test result by 42% for the first story and by 30% for the second story. This is understandable because the increase of interstory drift from models A to D only comes from the increase of interface slip, which is not the major source of interstory drift. One possible reason that the finite element analysis underestimating the interstory drift is because the

Table 8.2.2 Comparison of the Interface Slip from the Test with Those from the Finite Element Analyses

Location*[2]	Measured	A*[1]	B	C	D
Slip of BS1(inches)	0.005	0.0068	0.0083	0.0098	0.0130
Slip of TS1 (inches)	0.010	0.0079	0.0097	0.0116	0.0156
Slip of BS2 (inches)	0.007	0.0075	0.0091	0.0109	0.0146
Slip of TS2 (inches)	0.014	0.0075	0.0091	0.0109	0.0146
Error of Slip (%)		39.3	34.9	39.4	68.8

1: A - K_{ss} = 449.9 kips/inch associated with a 0.005 inch slip
B - K_{ss} = 349.6 kips/inch associated with a 0.0075 inch slip
C - K_{ss} = 278.2 kips/inch associated with a 0.011 inch slip
D - K_{ss} = 185.9 kips/inch associated with a 0.02 inch slip
2: BS1 – Bottom interface of the first story
TS1 – Top interface of the first story
BS2 – Bottom interface of the second story
TS2 – Top interface of the second story

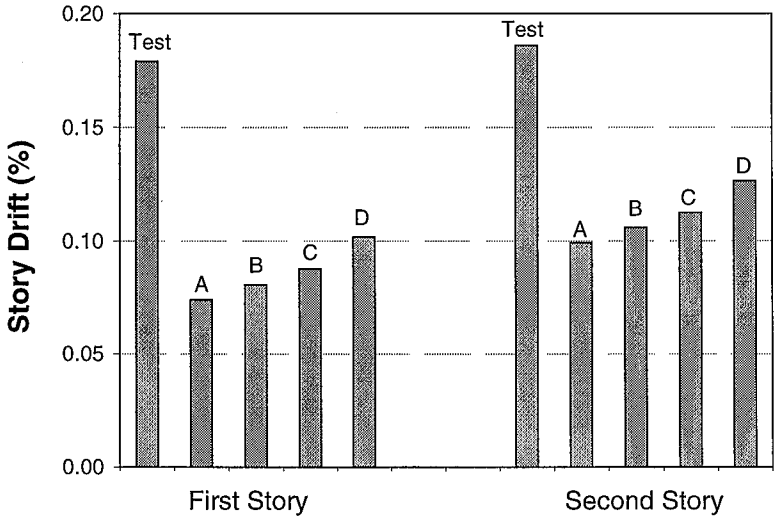

Fig. 8.2.1 Comparison of Interstory Drift from the Test with Those from the Finite Element Analyses

influence of the cracking in the RC infill wall was not included in the modeling. Figure 4.2.1 shows that more than half of the total major cracks formed in cycle G2-1-A, and the cracking decreased both the shear and flexural stiffness of the infill wall by a certain degree. Another possible reason is that a certain number of studs at the north–bottom interfaces of both stories yielded under combined tensile and shear forces. As a result, they were unable to maintain their elastic tensile stiffness.

8.2.3 Comparison of Lateral Forces Resisted by the Studs

Table 8.2.3 shows the lateral load resisted by the studs along three interfaces in both the specimen (see Section 7.1) and the finite element models. Along the top interface of the first story, the discrepancy between the analytical results from the finite element models and the measured responses in the test is the smallest, and along the bottom interface of the second story, the discrepancy is the largest. The lateral load resisted by the studs diminishes with the decrease of the secant shear stiffness of the studs. Along the top interface of the first story, the computational result is less than the measured response by approximately 7% for case A, 11% for case B, 15% for case C, and 24% force case D. Along the bottom interface of the second story, the computational

result is less than the measured response by approximately 17% for case A, 21% force case B, 25% force case C, and 32% for case D. Although the shear stiffness is increased by 60% from case C to case A, the lateral force resisted by the studs only increased by 12% for the bottom interface of the first story, and by 10% for the bottom interface of the second story.

Therefore, if the secant shear stiffness of the stud at a shear of $0.51Q_{sn}$ is used as the shear stiffness of the stud at the limit state of "elastic" response of the structure for the analysis model of Section 8.1, the lateral force resisted by the studs will be underestimated by 15-25%, implying that the lateral force resisted by the steel column will be overestimated by 15-25%. Changing the shear stiffness of the headed studs would not affect this percentage very much.

Table 8.2.3 Comparison of the Lateral Load Resisted by the Studs from the Test with Those from the Finite Element Analyses (kips)

Location	Measured	A	B	C	D
BS1	62.3	54.9	52.2	49.1	43.4
TS1	68.5	63.5	60.8	57.9	52.1
BS2	72.3	59.7	57.1	54.5	48.9

8.2.4 Comparison of Axial Forces in the Steel Columns

Table 8.2.4 lists the axial forces of the steel columns in both the specimen (Section 5.1.2) and the finite element models. Both the measured response and the finite element analysis show that the north column was in tension and the south column was in compression when the specimen was loaded in the south direction. However, for the north column, the finite element analysis underestimates the maximum tensile axial force by 28% at the bottom of the column in the first story, and by 35% at the bottom of the column in the second story. For the south column, the maximum compressive axial force at the bottom of the first story predicted using the finite element analysis is very close to the measured response. Figure 8.2.2 shows the axial forces along the south column in the first story. The axial forces are normalized by being divided by the maximum value at the

bottom. It can be observed that along the lower portion of the steel column, the axial force from the finite element analysis decreases faster than that in the specimen; along the top portion of the steel column, the axial force in the specimen decreases faster than that from the finite element analysis.

Since the tensile force in the north column is underestimated, the finite element model tends to overestimate the overturning moment resisted by the infill wall. The possible reason for this behavior is that, in the specimen, a certain number of studs at the north bottom interfaces of both stories might have yielded under combined tensile and shear forces, so that they were unable to maintain their elastic tensile stiffness, as assumed in the finite element modeling.

Table 8.2.4 Comparison of the Column Axial Force from the Test with Those from the Finite Element Analyses

Location*[1]	Measured		A		B		C		D	
	NC*[2]	SC	NC	SC	NC	SC	NC	SC	NC	SC
BS1	83.2	-56.4	59.1	-55.4	58.2	-55.3	57.5	-55.3	56.6	-55.4
MS1	77.8	-50.3	48.8	-44.9	49.3	-45.1	49.9	-45.4	51.0	-45.9
TS1	58.8	-34.0	44.7	-40.6	45.7	-41.3	46.7	-41.9	48.8	-43.2
BS1	49.4	-28.7	31.8	-24.5	31.2	-24.2	30.5	-23.9	29.5	-23.5

1: MS1 – Middle of the First Story, others are the same as in Table 8.2.2
2: NC – North Column; SC – South Column

8.2.5 Summary

Evaluation of the finite element analysis reveals several problems of the present finite element models, which are similar to the one used for prototype structure design:

1) The models underestimate the interstory drift by a large percentage, and the magnitude of the shear stiffness of the headed studs has limited influence on interstory drift.

2) The secant stiffness of a headed stud at the load of $0.51Q_{sn}$ gives a reasonable estimation of the interface slips.

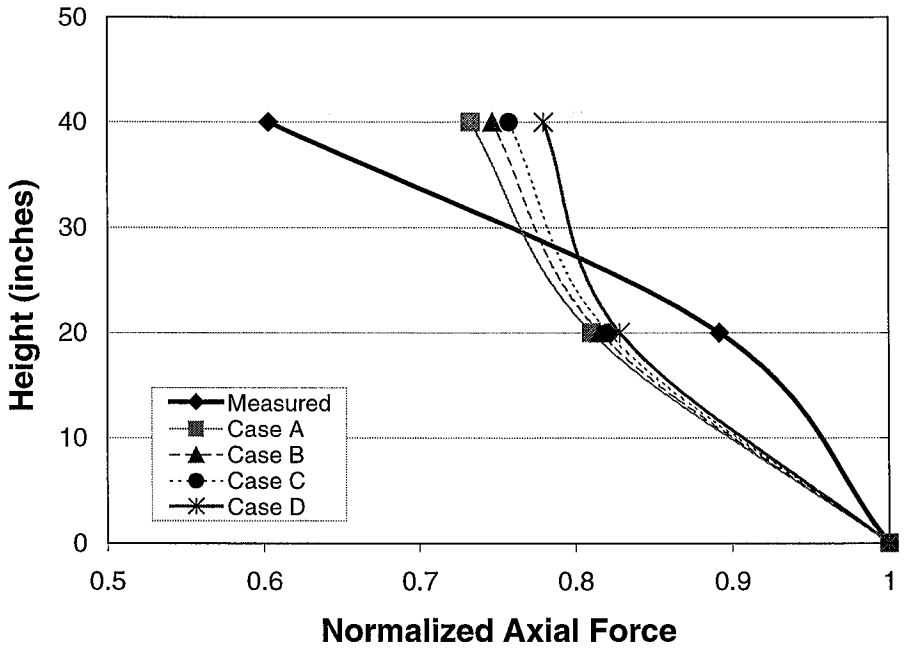

Fig. 8.2.2 Normalized Axial Force in the South Column of the First Story

3) The models underestimate the percentage of the lateral load resisted by the headed studs in general, and the magnitude of the shear stiffness of the headed studs has a small influence on this percentage.

4) The models provide a close assessment of the compressive axial force resisted by the leeward column, but underestimate the tensile axial force resisted by the windward column.

8.3 Modification of the Finite Element Model

Based on the discussions in the last section, two approaches were used to modify the original finite element model, as follows:

1) The modulus of elasticity of the wall material, namely concrete, was decreased by 75% to include the loss of shear stiffness of the concrete wall due to cracking in the RC wall and possible yielding in the reinforcing steel. This approach was based on the evaluation of the actual shear stiffness of the RC infill wall after the test (see Section 5.5).

As shown in Figure 5.5.6, in cycle G2-1, the effective shear modulus of the infill wall was approximately 25% of the elastic shear modulus of the infill wall. Since the shear modulus is linearly related to the modulus of elasticity in the elastic finite element model, the modified modulus of elasticity of the concrete is taken as 840 ksi, 25% of the nominal modulus of elasticity of the concrete, 3370 ksi.

2) The axial stiffness of the tensile stud along the bottom interface of each story was neglected. The intent of this approach was to counteract the overestimation of the overturning moment resisted by the infill wall. Iteration was required to determine which studs were in tension.

Two modified finite element models were analyzed to evaluate the above two approaches. Model E is the same as the original Model C except that the modulus of elasticity of concrete in the wall element was decreased by 75%, as proposed in item 1. Model F further modifies Model E by neglecting the axial stiffness of the tensile studs along the bottom interface of both stories, as proposed in item 2.

Table 8.3.1 compares the interface slips of the specimen with those of the three models. It shows that decreasing the modulus of elasticity of the concrete by 75% (Model E) increases the interface slip slightly, and neglecting the axial stiffness of the tensile studs has little influence on the interface slip (Model F). The combination of the two modifications increased the error of the estimation of the interface slips by approximately only 5% compared to model C.

Figure 8.3.1 compares the interstory drifts of the specimen with those of the three finite element models. It shows that decreasing the modulus of elasticity (model E), and thus the shear modulus of the concrete, greatly improved the assessment of the interstory drift, and neglecting the tensile stiffness of the studs along the bottom interface further increased the interstory drift a little. The combined combination of the two approaches resulted in a first story interstory drift 17% less than the measured one, and a second interstory drift approximately the same as the measured one.

Figure 8.3.2 compares the lateral force resisted by the interface studs. It can be observed that decreasing the modulus elasticity of the concrete (model E) increased the

Table 8.3.1 Comparison of the Interface Slips from the Test with Those from the Modified Finite Element Analyses

Location	Measured	C*[1]	E	F
Slip of BS1 (inches)	0.005	0.0098	0.0111	0.0109
Slip of TS1 (inches)	0.010	0.0116	0.0123	0.0122
Slip of BS2 (inches)	0.007	0.0109	0.0118	0.0117
Slip of TS2 (inches)	0.014	0.0109	0.0117	0.0116
Error of Slip		39.4	46.8	45.6

1: C - K_{ss} = 278.2 kips/inch associated with a 0.011 inch slip
E - same as model C except that the modulus of elasticity of concrete of the wall element material was decreased by 75%
F – same as model E except that the axial stiffness of the tensile studs along the bottom interfaces of both stories was neglected

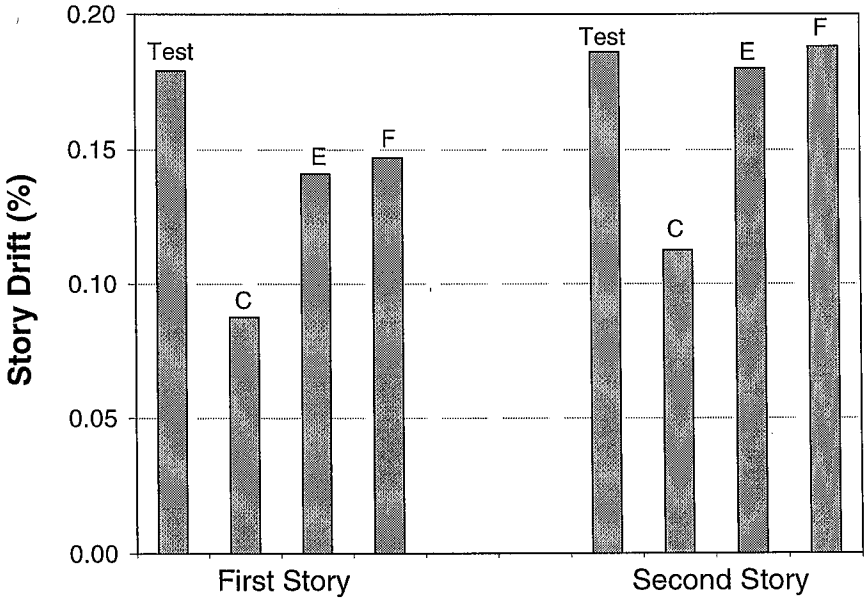

Fig. 8.3.1 Comparison of Interstory Drift from the Test with Those from the Modified Finite Element Analyses

lateral force resisted by the studs by a small percentage, and neglecting the tensile stiffness of the studs (model F) along the bottom interface has little effect. The combination of the two approaches (model F) underestimated the lateral force resisted by the studs by approximately 11% for the studs along the bottom interface of the first story, 10% for the studs along the top interface of the first story, and 19% for the studs along the bottom interface of the second story.

Table 8.3.2 shows the axial forces in both columns in the three finite element models. It can be seen that reducing the modulus of elasticity of the concrete increased the tensile axial force in north column by approximately 20%. Neglecting the tensile stiffness of the studs along the bottom interface further increased the calculated axial force in north column. As a result, the combination of the two modifications gave a close assessment of the axial tensile force in the north column. However, the reduction in modulus of elasticity of the concrete resulted in an overestimate of the compressive axial force in the south column.

8.4 Conclusion

Overall, the finite element model proposed in the present study provides a reasonable estimation of both the internal forces in the steel and concrete members, as well as the drifts of the structure, at the limit state of "elastic" response of the specimen. In doing so, the shear stiffness of a headed stud at the design level can be determined as a secant at a shear of 51% (i.e., approximately 50%) of the nominal shear strength of the headed studs, the effective modulus of elasticity of the concrete wall element should be taken as 25% of the nominal modulus of elasticity of the concrete, and the tensile stiffness of the headed studs along the bottom interfaces should be neglected. It should be noted that this finite element model will underestimate the lateral shear force resisted by the interface studs by 10-20%, which in turn conservatively overestimates the maximum shear force in the steel columns by 10-20%. Furthermore, this model gives a conservative estimation of the compressive force in the leeward column.

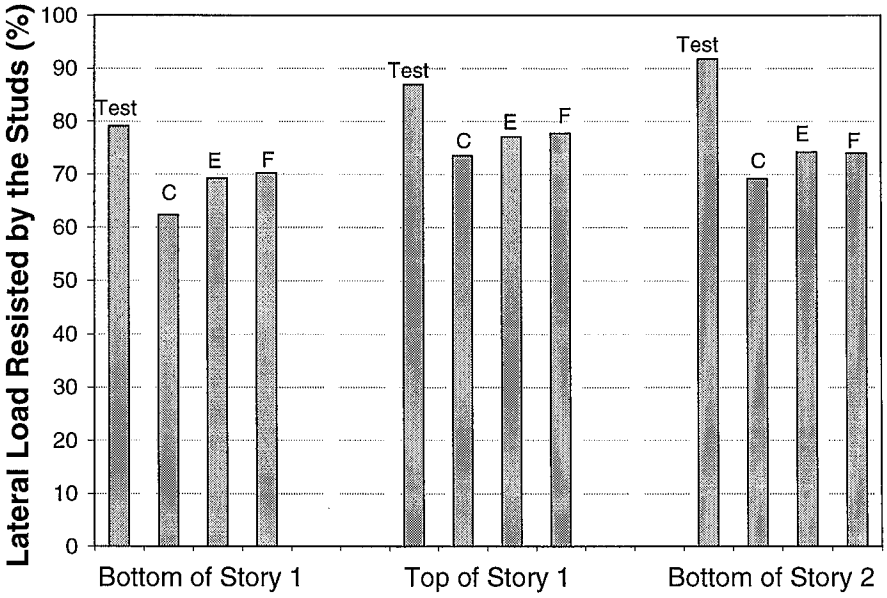

Fig. 8.3.2 Comparison of Lateral Force Resisted by the Interface Studs from the Test with those from the Modified Finite Element Analyses

Table 8.3.2 Comparison of the Column Axial Force from the Test with Those from the Modified Finite Element Analyses (kips)

Location	Measured		C		E		F	
	NC	SC	NC	SC	NC	SC	NC	SC
BS1	83.2	-56.4	57.5	-55.3	69.2	-78	84.7	-76.6
MS1	77.8	-50.3	49.9	-45.4	58.9	-66.5	69.1	-67
TS1	58.8	-34.0	46.7	-41.9	51.6	-57.8	59.6	-57.7
BS1	49.4	-28.7	30.5	-23.9	35.5	-40.2	45.6	-39.4

Chapter 9

Plastic Mechanism Analysis

This chapter evaluates the plastic analysis mechanisms for one-story infilled frames proposed by other researchers by using experimental data obtained from the literature, and establishes a plastic mechanism for analysis of the two-story composite steel frame-reinforced concrete infill wall specimen test conducted in the present research.

9.1 Evaluation of Existing Plastic Mechanism Models

As discussed in Section 1.3.2, different approaches have been tried to predict the maximum strength of infilled steel frames subjected to lateral load since the 1960's. One of these approaches is plastic mechanism analysis, in which the collapse modes and collapse loads for an infilled steel frame are dependent on the bending strength of the steel members and crushing stress of the infill wall material. Among all the researchers, only Liauw and Kwan (1983a, 1983b) have established plastic mechanisms for infilled steel frames both with and without interface connectors, with the backing of static lateral loading tests and finite element analysis. This section evaluates the plastic mechanisms proposed by Liauw and Kwan (1983a, 1983b) by using experimental results from cyclic loading tests on one-story, one-bay RC infilled steel frames obtained from the literature.

The plastic mechanisms defined by Liauw and Kwan (1983b) for a one-story, one-bay infilled steel frame having interface connectors are shown in Figure 9.1.1. They include the following aspects of behavior at the limit of useful response to lateral loading: 1) Corner crushing with yielding of the infill/beam connectors and plastic hinges forming at two joints and in the columns (mode 1, Figure 9.1.1.(a)); 2) Corner crushing with yielding of the infill/column connectors and plastic hinges forming at two joints and in the beams (mode 2, Figure 9.1.1.(b)); 3) Diagonal crushing with yielding of the

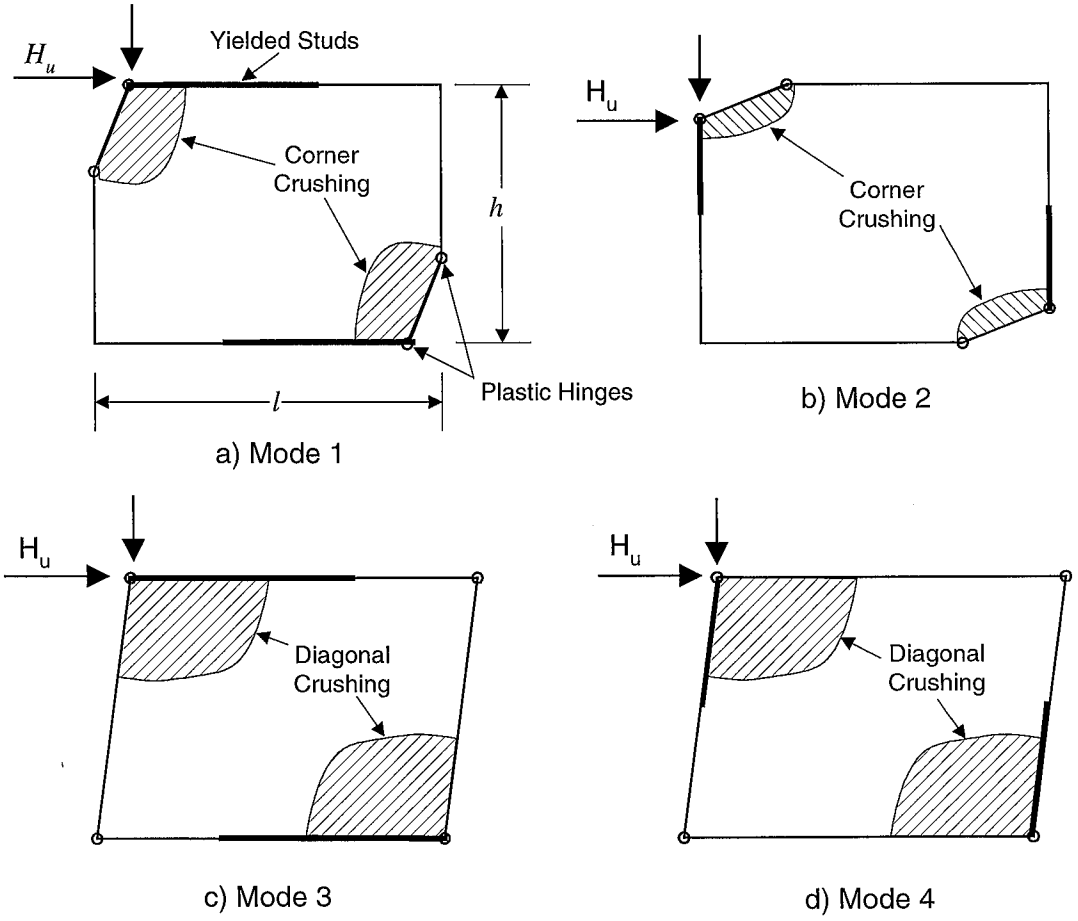

Figure 9.1.1 Failure Modes of a Single Story Infilled Steel Frame Having Interface Connectors [after Liauw and Kwan (1983)]

infill/beam connectors and plastic hinges forming at four joints (mode 3, Figure 9.1.1.(c)); 4) Diagonal crushing with yielding of the infill/column connectors and plastic hinges forming at four joints (mode 4, Figure 9.1.1.(d)).

These plastic mechanisms were primarily based on experimental observations of small models, having a scale approximately equal to 1:10 to 1:12. The steel frames in these test models comprised 0.87 inches × 0.87 inches solid square steel bars, which have different section characteristics if compared to rolled wide flange sections. Furthermore, the interface connectors were J hooks or U hooks bent from wire, instead of using headed studs. Because these parameters differ from the test conducted in this research, and also to further confirm the validity of equations of Liauw and Kwan (1983a, 1983b), these mechanisms are evaluated in the present study by using additional experimental results of larger-scale one-story specimens with headed studs as interface connectors.

The parameters of the tests used for verification are listed in Tables 9.1.1 and 9.1.2. These tests have been conducted by two groups of researchers in Japan since 1980 (Makino et al., 1980; Makino, 1984; Hayashi and Yoshinaga, 1985, 1986, 1987, 1994). These tabulated specimens are all one-story and one-bay, comprising steel members with wide flange sections and reinforced concrete infill walls. The reinforcement ratio of the RC infill walls was approximately 0.5%. The specimens have either the strong axis of the steel columns or the weak axis of the steel columns oriented in the plane of the infill wall. The stud spacing varied from approximately 4.5 inches to 12 inches. In each test, each column was subjected to a static gravity load equal to one-third of its axial yielding strength, while cyclic lateral loading was added on the top joint. In Tables 9.1.1 and 9.1.2, l = center-to-center spacing of columns; h = story height (center-to-center spacing of beams); t = thickness of the RC infill wall; f_c' = compressive strength of the concrete; F_y = yield strength of the frame steel; Q_{sn} = nominal shear strength of a single headed stud; d = distance between adjacent studs.

The nominal shear strength of a single headed stud in these specimens was calculated according to the following formula:

$$Q_{sn} = \phi 0.5 A_{stud} \sqrt{f_c' E_c} \tag{9.1.1}$$

where

$$\phi = \sqrt{t/11.8}$$

t = wall thickness, inches

Equation (9.1.1) was established by Makino (1984) according to the shear tests on the same studs as those used in their infilled steel frame specimens. Because the studs used in these specimens were not confined by reinforcement cages, the strength reduction factor, ϕ, was used to take into account the limited confinement provided by the concrete alone.

The analytically predicted maximum lateral loads of the four different failure modes of Figure 9.1.1 for each of the specimens are tabulated in Table 9.1.3. In the table, the error of the analytical prediction is calculated as follows:

$$\text{Error}(\%) = (100\%) * \left(\frac{H_{u,analy} - H_{u,test}}{H_{u,test}} \right) \tag{9.1.2}$$

Comparison of the results of the four failure modes with the experimental peak load shows that mode 3 is the predicted governing failure mode for all of the Japanese tests except for specimen D8, for which the mode 1 and mode 3 had almost the same maximum lateral load. The predicted failure modes were consistent with the observed modes in the tests. Figure 9.1.2 shows the error of the analytically predicted maximum lateral load for the specimens having the strong axis of the steel columns oriented in the plane of the infill wall, and Figure 9.1.3 shows the error of the analytically predicted maximum lateral load for the specimens having the weak axis of the steel columns oriented in the plane of the infill wall. Figure 9.1.2 shows that the plastic mechanisms proposed by Liauw and Kwan (1983b) overestimate the maximum lateral load of the specimens having the strong axis of the steel columns oriented in the plane of the infill wall by approximately 20% on average. Figure 9.1.3 shows that the plastic mechanisms proposed by Liauw and Kwan (1983b) underestimate the maximum lateral load of the

Table 9.1.1 Parameters for Steel Frame-RC Infill Wall Specimens from Japan

Reference	Specimen Designation	Specimen Number	Interface Connectors	Number of Connectors		Frame[*1] section	Column[*2] Orientation
				Beam	Column		
Makino (1984)	A2	1	Studs	3	2	a	X
	B2	2	Studs	3	2	a	Y
	C2	3	None	-	-	b	X
	C4	4	Studs	3	2	b	X
	C6	5	Studs	5	3	b	X
	C8	6	Studs	3	2	b	X
	C9	7	Studs	3	2	b	X
	C10	8	Studs	9	5	b	X
	C11	9	None	-	-	b	X
	C12	10	Studs	3	2	b	X
	C13	11	Studs	3	2	b	X
	D2	12	None	-	-	b	Y
	D3	13	Studs	3	2	b	Y
	D4	14	Studs	5	3	b	Y
	D5	15	Studs	3	2	b	Y
	D6	16	Studs	9	5	b	Y
	D7	17	None	-	-	b	Y
	D8	18	Studs	3	2	b	Y
Hayashi et al. (1985)	SRCV1-2X	19	Welded reinforcing bar	-	-	c	X
Hayashi et al. (1986)	SRCV1-7X	20	Studs	5	3	d	X
Hayashi et al. (1987)	SRCV2-7X	21	Studs	5	2	d	X
	SRCV1-2Y	22	Studs	3	3	c	Y
Hayash et al. (1994)	SRCV2-7X	23	Studs	6	3	d	X

1: a = both the columns and beams are fabricated from H-4.92×4.92×0.26×0.35 (wide flange section - depth × width × web thickness × flange thickness, in inches)
b = both the columns and beams are fabricated from H-4.92×4.92×0.18×0.24
c = both the columns and beams are fabricated from H-3.94×3.94×0.24×0.32
d = the columns are fabricated from H-3.94×3.94×0.24×0.32, and the beams are fabricated from H-5.90×2.95×0.20×0.28

2: X = Strong axis of the steel column is oriented in the plane of the infill wall
Y = Weak axis of the steel column is oriented in the plane of the infill wall

Table 9.1.2 Parameters for Steel Frame-RC Infill Wall Specimens from Japan

Specimen Designation	Specimen Number	Frame Dimension (inches)			f_c' (ksi)	F_y (ksi)		Q_{sn} (kips)	d (inches)	M_p(kip-ft)	
		l	h	t		Column	Beam			Column	Beam
A2	1	47.2	39.4	2.4	1.9	46.7	46.7	3.1	11.8	35.1	35.1
B2	2	47.2	39.4	2.4	2.6	46.7	46.7	4.0	11.8	16.7	35.1
C2	3	47.2	39.4	2.4	3.1	46.7	46.7	-	-	24.9	24.9
C4	4	47.2	39.4	2.4	2.6	46.7	46.7	4.0	11.8	24.9	24.9
C6	5	47.2	39.4	2.4	2.4	46.7	46.7	3.8	7.9	24.9	24.9
C8	6	47.2	39.4	2.4	3.3	46.7	46.7	4.7	11.8	24.9	24.9
C9	7	47.2	39.4	2.4	2.8	46.7	46.7	4.2	11.8	24.9	24.9
C10	8	47.2	39.4	2.4	3.2	46.7	46.7	1.0	4.7	24.9	24.9
C11	9	47.2	39.4	2.4	3.3	46.7	46.7	-	-	24.9	24.9
C12	10	47.2	39.4	2.4	3.2	46.7	46.7	4.6	11.8	24.9	24.9
C13	11	47.2	39.4	2.4	3.1	46.7	46.7	5.9	11.8	24.9	24.9
D2	12	47.2	39.4	2.4	2.3	46.7	46.7	-	-	11.4	24.9
D3	13	47.2	39.4	2.4	2.3	46.7	46.7	3.6	11.8	11.4	24.9
D4	14	47.2	39.4	2.4	2.3	46.7	46.7	3.6	7.9	11.4	24.9
D5	15	47.2	39.4	2.4	2.6	46.7	46.7	4.0	11.8	11.4	24.9
D6	16	47.2	39.4	2.4	2.7	46.7	46.7	0.9	4.7	11.4	24.9
D7	17	47.2	39.4	2.4	2.7	46.7	46.7	-	-	11.4	24.9
D8	18	47.2	39.4	3.1	2.7	46.7	46.7	4.7	11.8	11.4	24.9
SRCV1-2X	19	43.3	43.3	2.0	3.7	47.1	47.1	-	-	20.5	20.5
SRCV1-7X	20	63.0	45.3	2.0	2.7	52.6	47.6	3.7	9.8	22.9	24.1
SRCV2-7X	21	63.0	45.3	2.0	3.5	46.0	52.5	4.6	9.8	20.0	26.5
SRCV1-2Y	22	43.3	43.3	2.0	2.4	50.6	50.6	3.4	9.8	10.7	22.0
SRCV2-7X	23	82.6	45.3	2.0	3.7	50.7	45.7	4.8	11.2	22.0	23.1

Table 9.1.3 Comparison of the Analytical Maximum Lateral Load with the Test Results

Specimen Designation	Specimen Number	Maximum Lateral Load (kips)						Error (%)
		Plastic Analysis Theory					Test	
		Mode 1	Mode 2	Mode 3	Mode 4	Minimum		
A2	1	93.3	109.5	78.9	90.5	78.9	76.8	2.7
B2[*1]	2	79.6	112.9	70.0	86.4	70.0	69.0	1.5
C2	3	94.2	113.0	79.0	-	79.0	65.4	20.8
C4	4	95.9	111.8	80.8	97.4	80.8	72.6	11.3
C6	5	96.3	111.0	81.5	96.2	81.5	78.0	4.5
C8	6	107.4	125.1	92.3	113.1	92.3	69.7	32.4
C9	7	99.1	115.5	83.9	101.7	83.9	69.9	20.0
C10	8	100.2	118.2	85.0	105.6	85.0	77.8	9.2
C11	9	97.0	116.3	81.9	-	81.9	72.2	13.4
C12	10	105.1	122.5	90.0	109.9	90.0	69.0	30.4
C13	11	135.4	157.7	125.2	158.8	125.2	100.5	24.6
D2[*1]	12	54.0	81.7	48.8	-	48.8	65.6	-25.6
D3[*1]	13	63.0	89.8	57.9	72.3	57.9	73.5	-21.2
D4[*1]	14	66.7	92.7	61.5	75.2	61.5	71.5	-13.9
D5[*1]	15	83.3	111.8	80.8	97.4	80.8	80.0	1.0
D6[*1]	16	63.7	93.1	60.1	77.5	60.1	79.1	-24.0
D7[*1]	17	58.7	88.8	55.1	-	55.1	77.8	-29.2
D8[*1]	18	79.2	112.6	80.4	103.2	79.2	97.3	-18.7
SRCV1-2X	19	88.8	88.8	79.3	79.3	79.3	74.3	6.8
SRCV1-7X	20	90.9	118.6	78.9	112.4	78.9	61.9	27.4
SRCV2-7X	21	102.9	180.0	88.7	179.8	88.7	66.1	34.2
SRCV1-2Y[*1]	22	56.5	68.1	53.1	53.1	53.1	59.3	-10.4
SRCV2-7X	23	113.6	180.2	104.2	225.2	104.2	71.6	45.5

1: the specimen has column weak axes in the plane of the walls

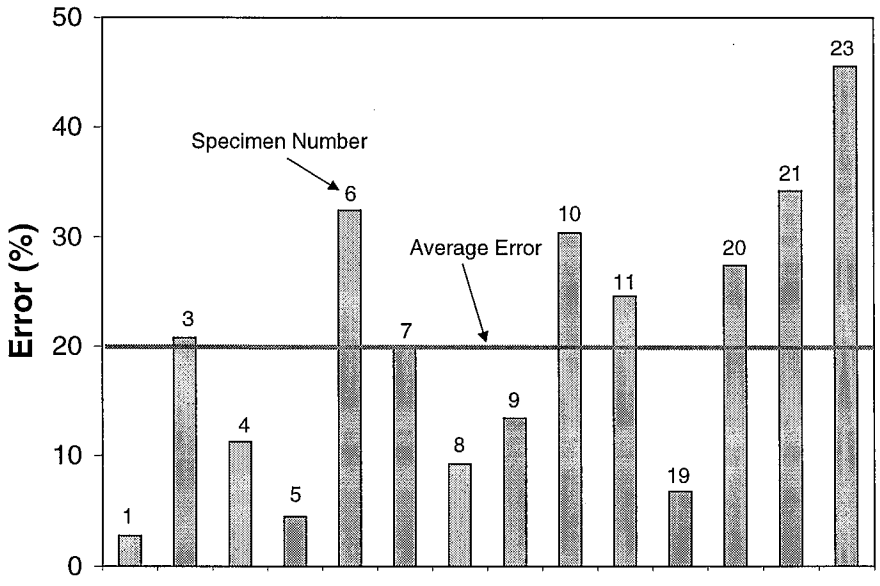

Fig. 9.1.2 Error of Predicted Maximum Lateral Load for Japanese Infilled Steel Frames with Strong Axis of Steel Columns Oriented in the Plane of the Infill Wall

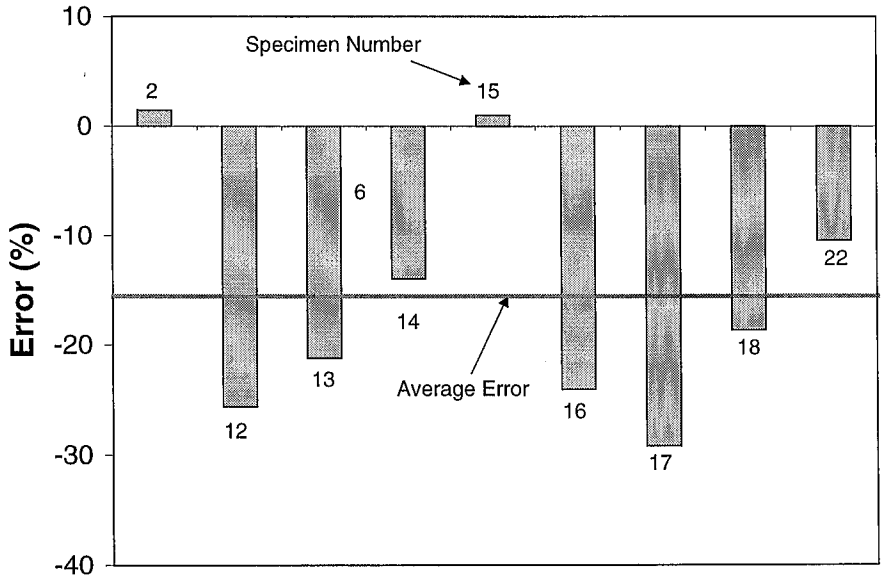

Fig. 9.1.3 Error of Predicted Maximum Lateral Load for Japanese Infilled Steel Frames with Weak Axis of Steel Columns Oriented in the Plane of the Infill Wall

specimens having the weak axis of the steel columns oriented in the plane of the infill wall by approximately 15% on average. It can be concluded that the plastic mechanism analysis is not conservative for infilled steel frames having the strong axis of the steel columns oriented in the plane of the infill wall.

There are several possible reasons that might contribute to the overestimation of the maximum lateral load of the specimens having the strong axis of steel columns oriented in the plane of the infill wall: 1) Liauw and Kwan (1983a, 1983b) assumed that the crushing of the concrete initiated when the maximum stress in the corner region reached the compressive strength of the concrete. It was recommended by Macgregor (1997) that $0.85f_c'$ is a more appropriate value for the crushing strength of concrete in a nodal region bounded by compressive struts and bearing plates. 2) The reduction of the plastic moment capacity of the frame members due to the shear force and, particularly, the axial force, was not recognized by Liauw and Kwan (1983a, 1983b). The effect of shear force on the plastic moment capacity of a steel cross section can usually be neglected if the shear force is less than the nominal yielding strength of the steel column (ASCE-WRC, 1971). However, for strong axis bending of steel members, the influence of axial force should not be neglected if the axial force is larger than 15% of the nominal compressive yielding strength of this cross section (ASCE-WRC, 1971). 3) The depth of the steel members was neglected so that the infill wall was slightly oversized in the plastic mechanism calculations of Liauw and Kwan (1983b). In the next section, the above three factors will be considered in establishing the plastic mechanism for the two-story composite steel frame-RC infill wall specimen tested in the present project.

The plastic mechanisms proposed by Liauw and Kwan (1983a, 1983b) will further underestimate the maximum lateral strength of the Japanese specimens having the weak axis of the steel columns oriented in the plane of the infill wall, if all three of the factors mentioned above are included in the models. A possible reason that the maximum lateral strengths of these specimens were underestimated was the particular construction detailing in the column-infill wall interface. As shown in Figure 9.1.4, except for specimen B2 (No. 2), the infill wall in the other Japanese specimens having the weak axis

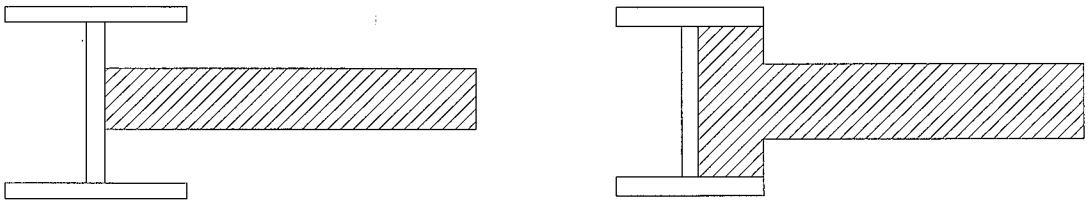

(a) Specimen B2 (b) Other Specimens

Figure 9.1.4 Interface Detailing of Japanese Specimen with Weak Axis of Steel Columns Oriented in the Plane of the Infill Wall

oriented in the plane of the infill wall was enlarged to fill the area surrounded by the column flanges and web. As a result, the crushing stress of the concrete along the column-infill wall interfaces might be increased due to the confinement from the steel flanges and web. This effect is not further explored since the specimen tested in the present project had the strong axis of the steel columns oriented in the plane of the infill wall.

9.2 Application of Plastic Mechanism Analysis to the Test Specimen

The plastic mechanism of a one-bay, multistory composite steel frame-infill wall structural system with PR connections is established by modifying the plastic mechanisms of the one-story, one bay infilled steel frame shown in Figure 9.1.1. The proposed modifications include modeling the PR connection, adopting a reasonable value for concrete crushing strength, specifying a more accurate value for the contact length between the column and infill, modeling the location and length of the yielded studs along the beam-infill interface, and incorporating the coupling effect of the axial force and bending moment in the steel members.

Figure 9.2.1 shows the mechanism of a two story structural system, the same as the one tested in the present project. With the adoption of the PR connections to link the steel columns and steel beams, the plastic hinges are forced to form in the PR connection regions as long as the moment capacity of the PR connection, M_{ppr}, is ensured to be less

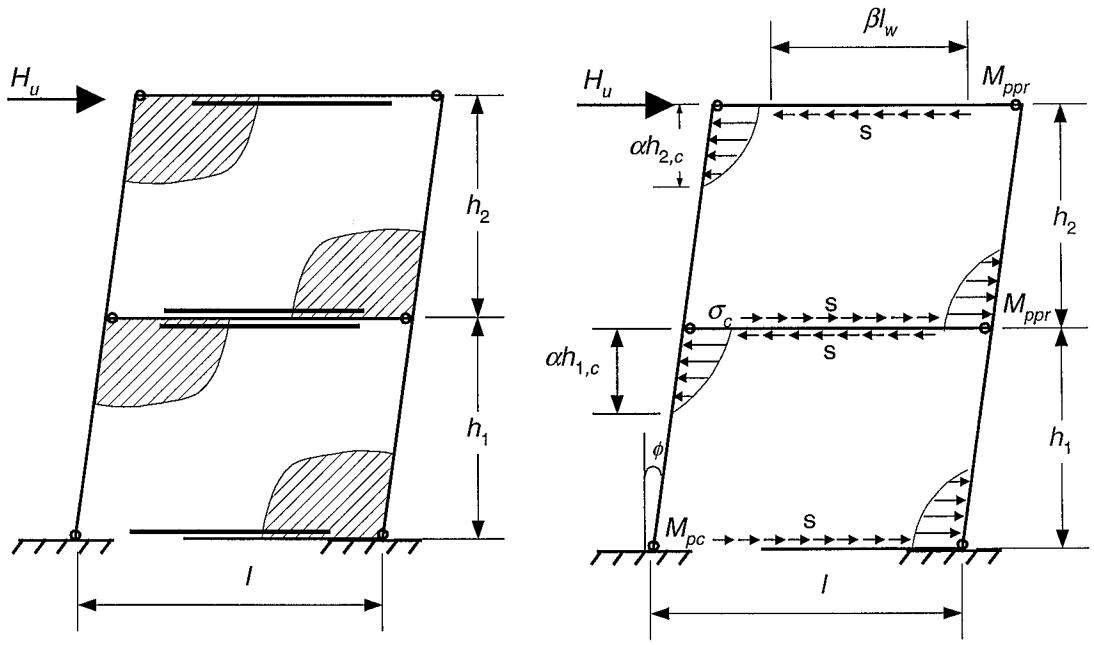

a) Failure Mode b) Force Distribution on the Frame

Figure 9.2.1 Plastic Mechanism of the Two-Story Structural System

than the reduced plastic moment capacity of the steel columns, M_{pc}, at the beam-to-column joint. As a result, this plastic mechanism has plastic hinges at the bases of the two columns, four plastic hinges in the PR connections and diagonal crushing of concrete in each story.

Different from the mechanisms shown in Figure 9.1.1, the yielded studs along the beam-infill wall interface exist in the middle portion of the interface because the cyclic loading tends to fracture the studs in both corner regions. It is assumed that the number of remaining yielded studs along each beam-infill wall interface is the same.

The derivation of the maximum lateral load of a one-bay, two-story composite steel frame-RC infill wall system as follows uses the virtual work method, with an iterative step to include the effect of axial force on the maximum moment capacity moment of the columns. In Figure 9.2.1.(b), the steel frame is in equilibrium under the interactive forces between the steel frame and infill wall and the lateral force. It shows that the external work done by lateral load is:

$$W_{ext} = H_u(h_1 + h_2)\phi \tag{9.2.1}$$

where

h_1 = height of the first story, inches

h_2 = height of the second story, inches

The internal work done by the rotation of the plastic hinges is:

$$W_{\text{int}1} = 2M_{pc} + 4M_{ppr} \tag{9.2.2}$$

It is assumed that the distribution of the contact pressure along the column-infill wall interfaces is parabolic and the system achieves its maximum strength when the maximum pressure reaches the crushing strength of the concrete, σ_c. Therefore, the internal work done by the compressive stress from the concrete in one infill panel, i, is:

$$\begin{aligned} W_{\text{int}2}^{i} &= \frac{2}{3}\sigma_c t\alpha h_{i,c} \times [(h_{i,c} - \frac{3}{8}\alpha h_{i,c})\phi - (\frac{3}{8}\alpha h_{i,c})\phi] \\ W_{\text{int}2} &= \left(\frac{2}{3} - \frac{1}{2}\alpha\right)\alpha t\left[(h_{1,c})^2 + (h_{2,c})^2\right]\sigma_c\phi \end{aligned} \tag{9.2.3}$$

where

σ_c = crushing strength of the concrete, equal to $0.85f_c'$, ksi

t = thickness of infill wall, inches

$h_{i,c}$ = clear height of the infill wall in story i, inches

The internal work done by the shear force of the interface headed studs is:

$$W_{\text{int}3} = h_{1,c}\phi s\beta l_w + h_{2,c}\phi s\beta l_w \tag{9.2.4}$$

where

$s = Q_{sn}/d$ = linear shear strength of the interface headed studs, kips/inch

l_w = clear infill wall spacing, inches

If $h_{1,c} = h_{2,c} = h_c$, then the total internal work is:

$$W_{\text{int}} = 2(M_{pc} + 2M_{ppr})\phi + 2\left(\frac{2}{3} - \frac{1}{2}\alpha\right)\alpha t h_c^2 \sigma_c \phi + 2h_c s\beta l_w \phi \tag{9.2.5}$$

Setting $W_{int} = W_{ext}$ yields the maximum lateral load of the two-story structural system

$$H_u = (M_{pc} + 2M_{ppr})/h + \left(\frac{2}{3} - \frac{1}{2}\alpha\right)\alpha t \frac{h_c^2}{h}\sigma_c + \frac{h_c}{h} s\beta l_w \tag{9.2.6}$$

An iterative procedure can be adopted to include the effect of the axial force on the moment capacity of the steel column and to refine the estimation of the maximum lateral strength of the structural system as follows:

1) In the first step, the effect of the axial force is neglected and moment capacity of the steel column is assumed to be fully achieved. The maximum lateral load of the system can then be obtained according to Eq. (9.2.6).

2) In the second step, the lateral force is used to calculate the overturning moment along the base section of the structural system. Based on the experimental result shown in Section 7.1.2, it is assumed that 80% of the overturning moment is resisted by the steel column. The axial force at the base of the steel column is then estimated as

$$P_c = \frac{0.8H_u(2h)}{l} \tag{9.2.7}$$

Equation (9.2.7) assumes that the axial forces are the same for the windward column and the leeward column. This is not true according to the experimental results in Section 5.1.2. However, it reflects the average value of the axial forces in the two columns.

The axial force P_c is then used to modify the moment capacity of the steel column having the strong axis oriented in the plane of the infill wall according to the following equation (ASCE-WRC, 1971):

$$\frac{M_{pc}}{M_p} = 1 - \frac{\left[\frac{P_c}{P_y}\left(1+\frac{2b_f t_f}{t_w d_w}\right)\right]^2}{\left(1+\frac{4b_f t_f d_f}{t_w d_w^2}\right)} \qquad (9.2.8)$$

$$0 \le \frac{P_c}{P_y} \le \frac{1}{1+\frac{2b_f t_f}{t_w d_w}}$$

or

$$\frac{M_{pc}}{M_p} = \frac{2\left(\frac{d}{d_w}\right)\left(1-\frac{P_c}{P_y}\right)\left(1+\frac{2b_f t_f}{t_w d_w}\right)}{1+\left(1+\frac{d}{d_w}\right)\frac{2b_f t_f}{t_w d_w}} \qquad (9.2.9)$$

$$\frac{1}{1+\frac{2b_f t_f}{t_w d_w}} \le \frac{P_c}{P_y} \le 1.0$$

where

M_p = plastic moment capacity of the steel column without the effect of axial force, kip-inches

P_y = yielding strength of the steel column under axial force, kips

The other parameters are shown in Figure 9.2.2

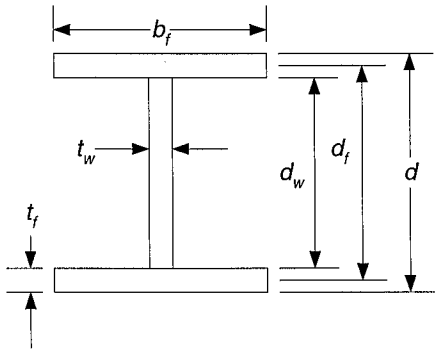

Figure 9.2.2 Dimension Parameters of Wide-Flange Section

Equation (9.2.8) is for the case that the neutral axis of the cross section under combined axial force and bending moment is located in the web and Eq. (9.2.9) is for the case that the neutral axis of the cross section under combined axial force and bending moment is located in the flange.

3) In the third step, the reduced moment capacity is substituted into Eq. (9.2.6) to obtain the modified maximum lateral load of the structural system.

This iterative process can be repeated until the difference of the two results is negligible, e.g., 2%.

Two parameters have to be determined in Eq. (9.2.6): α for the contact length between the RC infill wall and steel frame, and β for the length of the remaining studs along the infill wall-beam interfaces. It was very difficult to measure the actual contact length $\alpha h_{i,c}$ during the test. Liauw and Kwan (1983b) noticed that α varied from 1/3 to 1/2 from the calibration of their experimental results and they chose $\alpha = 1/3$ as a conservative approach to estimate the maximum lateral load of the structure. They also noticed that the interface connectors used in their specimen were pulled out from the concrete along the steel frame-infill wall interface so that the column-infill interface separated early during the test, which did not occur to the headed stud connectors used in the present project. As a result, the contact length in the present specimen should be larger than that in the specimens tested by Liauw and Kwan (1983b). Therefore, $\alpha = 1/2$ is adopted for the composite structural system tested in the present project and will be verified using the test result. It was reasoned in Section 4.4 that approximately 26 studs failed before the specimen reached its maximum lateral load. If the failed studs are assumed to be equally distributed along the four beam-infill interfaces, approximately two-thirds of the studs remain along each interface when the specimen reached its maximum lateral load. As a result, β is set as 2/3 for the specimen tested in the present project. It would be ideal if all the studs remain intact during the entire loading history so that β can be simply set as 1. More importantly, the specimen can increase its maximum lateral strength and diminish the loss of lateral strength at larger lateral displacement.

Based on Eqs. (9.2.1) to (9.2.9), the maximum lateral strength of the specimen is calculated according to this iterative plastic mechanism analysis. The dimension of the specimen tested in the present study is shown in Figure 3.1.1: For the overall dimensions, l = 86 inches, l_w = 81 inches, h = 48 inches, h_c = 40 inches; for the wall thickness, t = 3.5 inches. The average compressive strength of the concrete is approximately 3750 ksi (see Tables 3.2.2 and 3.2.3). The moment capacity of the PR connection, M_{ppr}, is approximately 190 kip-inches (see Section 5.3.2). The plastic moment capacity of the steel column without coupling of the axial force, M_p, is approximately 525 kips-inches. Eq. (3.1.1) is used to calculate the shear strength of a single ϕ3/8 headed stud. The shear strength of a single stud is approximately 5.1 kips if the actual material properties of the concrete are substituted into Eq. (3.1.1). Therefore, the linear shear strength of the studs is 1.275 kips/inch based on the 4 inch stud spacing. Substituting all the parameters into Eq. (9.2.6) yields the maximum lateral load of the specimen

$$\begin{aligned} H_u &= (M_{pc} + 2M_{ppr})/h + \left(\frac{2}{3} - \frac{1}{2}\alpha\right)\alpha t \frac{h_c^2}{h}\sigma_c + \frac{h_c}{h} s\beta l_w \\ &= (525 + 2(190))/48 + \frac{5}{24}(3.5)\frac{40^2}{48}(0.85)3.75 + \frac{40}{48}(1.275)\frac{2}{3}(81) \\ &= 18.85 + 77.47 + 57.38 = 153.7 \text{ kips} \end{aligned}$$

Equation (9.2.8) is then used to estimate the average axial force in the two columns, which is:

$$\begin{aligned} P_c &= \frac{0.8H_u(2h)}{l} \\ &= \frac{0.8(153.7)(2\times 48)}{86} = 137.3 \text{ kips} \end{aligned}$$

Since $\dfrac{1}{1+\dfrac{2b_f t_f}{t_w d_w}} = 0.21 \le \dfrac{P_c}{P_y} = 0.55 \le 1.0$, the reduced moment capacity of the steel

column due to the effect of the axial force is calculated according to Eq. (9.2.9). The result is M_{pc}= 0.56M_p =294 kips-inches.

In the second iteration, the reduced maximum moment of the steel column is substituted into Eq. (9.2.6) and the maximum lateral load of the specimen is the

$$H_u = (M_{pc} + 2M_{ppr})/h + \left(\frac{2}{3} - \frac{1}{2}\alpha\right)\alpha t \frac{h_c^2}{h}\sigma_c + \frac{h_c}{h} s\beta l_w$$
$$= (294 + 2(190))/48 + 77.47 + 57.38$$
$$= 14.04 + 77.47 + 57.38 = 148.9 \text{ kips}$$

The third iteration step is not needed since the maximum lateral load is reduced only by 3% due to the effect of the axial force in the steel column. For the 148.9 kips lateral load, the steel frame alone contributes 9.5% of the maximum lateral strength, the compression along the column-infill wall interface contributed 52% of the maximum lateral strength, and the shear studs contributed 38.5% of the maximum lateral strength of the specimen.

The maximum lateral strength of the specimen was achieved during the first cycle of the 0.75% cycles (cycle G5-1). It was 164 kips when the specimen was loaded in the south direction and 159.5 kips when the specimen was loaded in the north direction, and the average value is 161.8 kips. Therefore, the plastic mechanism shown in Figure 9.2.1 underestimates the maximum lateral load by 8%. In theory, the plastic mechanism analysis should provide an upperbound estimation for the maximum lateral strength. However, it should be noted that friction between the beam and the infill is neglected in the proposed plastic mechanism (see Figure 9.2.1) although it exists, particularly near the corner regions due to the compression strut in infill wall. This neglect of friction leads to a slightly conservative analysis approach, with α = 1/2 being a reasonable value for estimating the contact length.

It may be argued that the failure mode in Figure 9.2.1 is not the one observed in the test because the extensive damage was concentrated in the second story while only little spalling of the concrete was observed at the top corners of the first story after the

test. However, four pieces of evidence suggest that the failure mode in Figure 9.2.1 reasonably illustrates the specimen at its maximum strength: 1) the columns yielded at their bases (see Table 5.1.1); 2) the plastic hinges started to form in the PR connections of the middle beam in the 0.5% cycles and reached their maximum capacity during the first cycle of 0.75% cycles; 3) the ratio of the second story interstory drift to the first story interstory drift was quite consistent during the first five groups of cycles (see Figure 4.5.4) and; 4) during the first cycle of the 0.75% cycles, the energy dissipated in the second story was only approximately 1.2 times that dissipated in the first story.

Chapter 10

Design Recommendations

This chapter assesses the preliminary design guidelines as proposed in Chapter 2 based on the experimental results, provides design recommendations for each component of this composite structural system, and modifies an existing model for estimating the strength capacity of the PR connections.

10.1 Assessment of the Preliminary Design Recommendations

The desirable failure mode of the steel frame with composite RC infill wall structural system is interpreted at the beginning of Section 2.2. The tentative design guidelines proposed in that section are primarily intended to ensure that the composite structural system provides sufficient strength at the prescribed design force level. Special detailing approaches were adopted for two distinct components of the specimen in order to enhance the energy dissipation capacity of this structural system: 1) PR connections comprising the top and seat angles and a double web angle were adopted to ensure that the plastic hinges formed in the PR connections; 2) confining reinforcement cages were incorporated in the concrete at the interfaces to increase the strength and deformation capacity of the headed stud connections. This section assesses these preliminary design recommendations based on the actual performance of the specimen. The results of this assessment follow:

1) At the prescribed design force level, the specimen succeeded in achieving the performance goals specified in the tentative design guidelines:

The experimental results show that the infill wall resisted nearly 100% of the lateral load (80% from headed studs along the beam-infill wall interfaces and 20% from the compressive strut through compressive interaction along the column-interface), as was intended.

The steel frame of the specimen was designed according to the results of elastic, linear finite element analysis. At design force level, the measured maximum shear force in the steel columns was 20% of the lateral load, 10% less than the design value. However, it should be noted that the steel columns exhibited extensive shear yielding at the bottom of the second story with the increasing compression strut force from the infill wall. Therefore, it may not be a sound approach to design the column to just resist shear force at the design force level. The shear failure at the maximum load level should also be prevented.

The steel columns and the infill wall shared the overturning moment, but the steel columns resisted 80% of this moment through their coupled axial forces, 20% larger than the design value. The bending moment in the columns was only 10% of their plastic moment capacity at the design force level, 10% less than the design value. Despite the discrepancy between the design values and measure values, both columns were able to provide sufficient strength for the interaction of axial force and bending moment at the design force level.

2) The tentative design guidelines ensured that the specimen had sufficient reserve strength over the prescribed design force. The maximum lateral strength of the specimen is approximately twice the prescribed design force. This overstrength was primarily provided by the increasing compressive strut force between the steel columns and the infill wall and yielding of the PR connections.

3) The PR connection behaved successfully as designed. The PR connections started to form plastic hinges by the 0.5% cycles, thus providing a basis for the development of a desirable failure mode of this structural system (Figure 9.2.1).

However, the plastic moment capacity of the PR connection was approximately 25% smaller than predicted, indicating that there can be improvement in the plastic mechanism (Kim and Chen, 1998) used in the specimen design. The double web angles of the PR connections provided sufficient strength to resist the shear force.

4) The confined headed stud connectors succeeded in ensuring the composite action of the steel frames and the infill wall. The headed studs were designed to resist 100% of the lateral load at the design load. In the test, the headed studs along the beam-infill interfaces transferred approximately 80% of the lateral load, indicating that the studs had at least 20% reserve strength. The headed studs along the column-infill interfaces were intact during the entire loading history. Although the headed studs along the beam-infill interface failed gradually after the design force level, the magnitude of the lateral force transferred through the headed studs was maintained, if not increased, until at least the 0.5% cycles, which ensured the increasing shear deformation of the infill wall before the specimen reached its maximum strength. Although the stud failures were by low-cycle fatigue in general and associated with the slip demands, only strength requirements for the headed studs are addressed in the preliminary design recommendations. Therefore, it will be ideal to increase the slip capacity of the headed studs, thus further increasing the overstrength of the system and improving the energy dissipation ability of the system through continued yielding of the headed studs and continued yielding of the reinforcing bars in the infills.

5) The specimen had a ductility index $\mu = 4$ for the second story and $\mu = 3$ for the entire structure. The second story interstory drift was able to surpass 3% with the lateral load being maintained at approximately 50% of the maximum strength of the specimen. It will be ideal to increase the strength of the system at larger drifts, thus further enhancing the energy dissipation capacity of the system. Figure 10.1.1 illustrates the impact of two possible mechanisms on the lateral force-deformation of the specimen. It is discussed in Section 4.2 that the disruption in the corner concrete of the second story was initiated due to the combined tensile ripping and compressive crushing after the specimen reached its maximum strength. This disruption in the corner concrete deteriorated the compressive

strut mechanism in the infill wall of the second story and was one of the primary reasons for the quick drop in the lateral strength. The second possible reason was the continued fracture of the headed stud along the beam-infill wall interface after the specimen reached maximum strength.

6) The specimen exhibited a weak second story mechanism that did not sufficiently develop the energy dissipation capacity of the first story at larger drifts. This phenomenon is not primarily related to the preliminary design philosophy, but rather to the highly restrained boundary conditions at the base of the test setup.

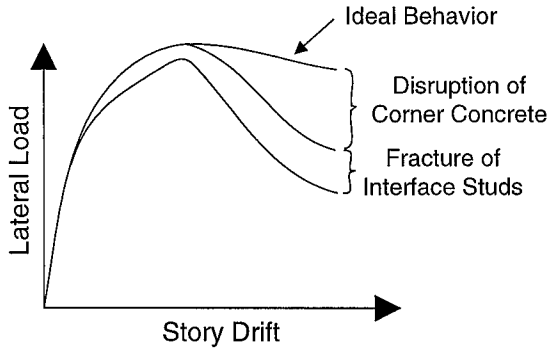

Fig. 10.1.1 Mechanisms Responsible for Decrease in Lateral Strength

10.2 Design Recommendations for Future Experimental Study

As discussed in Section 2.2, it is recommended that the bare steel frame of this composite structural system should be designed to carry design gravity load. Therefore, the following design recommendations are targeted at the composite system subjected to the lateral load combination.

10.2.1 Design Recommendations for the Steel Columns

The design of the steel columns is targeted at two load levels: the prescribed design load level and the maximum load level.

At the prescribed design force level, the internal forces in the steel column can be estimated by using an appropriate analytical method, such as the finite element method proposed in Section 8.3.

At the maximum load level, the steel columns should have sufficient shear strength to resist the force from the compressive strut. Eq. (9.2.6) gives the maximum lateral load of a two-story structural system. Following the same procedure illustrated in Section 9.2, the maximum lateral load of an n-story structural system can be obtained by the following equation:

$$H_u = (\frac{2M_{pc}}{n} + 2M_{ppr})/h + \left(\frac{2}{3} - \frac{1}{2}\alpha\right)\alpha t \frac{h_c^2}{h}\sigma_c + \frac{h_c}{h}s\beta l_w \qquad (10.2.1)$$

According to Eq. (10.2.1), the maximum required shear force in the column can be approximately estimated as:

$$V_{cu} = (\frac{M_{pc}}{n} + M_{ppr})/h + \left(\frac{2}{3} - \frac{1}{2}\alpha\right)\alpha t \frac{h_c^2}{h}\sigma_c \qquad (10.2.2)$$

The first part of the right side of Eq. (10.2.2) is the shear force induced by the deformation of steel frame alone, and the second part is the shear force induced by the compressive strut. Although the discussion in Section 5.2.1 indicated that the maximum shear force in the connection region of the column can be reduced due to the presence of PR connections, it is conservative to neglect that effect and simply take the result of Eq. (10.2.2) as the maximum required shear force in one steel column. Since the maximum shear force is localized in the corner region and the shear demand decreases after the concrete crushes at the maximum lateral load, hardening in the web steel may be used to resist the maximum shear force. According to Eq. (10.2.2), the maximum shear force in the column of the specimen tested in the present project was equal to 85.5 kips, more than twice that of the nominal shear strength of the steel column, 41.6 kips. The measured ultimate tensile strength of the column web steel was approximately 74.4 ksi, 1.63 times its static yield strength, 45.6 ksi. If limited hardening in the column web is allowed and the maximum shear stress is specified as $1.4(0.6f_{sy})$, the web area needs to be increased from 1.39 inch^2 in the present specimen to 2.22 inch^2 in order to have sufficient strength to resist the maximum shear force in the column.

10.2.2 Design Recommendations for the Steel Beams

The steel beam is designed at one load level: the maximum load level.

At the maximum load level, the steel beam web shall have sufficient strength to resist the vertical component of the compressive strut force from the RC infill wall and limited hardening in the beam web is also allowed. As shown in Figure 7.1.1, it can be assumed that the maximum shear force in the steel column is the horizontal component of the compressive strut force, so that the maximum shear force in the steel beam is:

$$V_{bu} = \frac{h_c}{l_w} V_{cu} = \frac{h_c}{l_w}\left[\left(\frac{M_{pc}}{n} + M_{ppr}\right)/h + \left(\frac{2}{3} - \frac{1}{2}\alpha\right)\alpha t \frac{h_c^2}{h}\sigma_c \right] \qquad (10.2.3)$$

According to Eq. (10.2.3), the maximum shear force in the beam of the specimen tested in the present project is equal to 42 kips, less than the nominal shear strength of the beam, 58.9 kips, indicating the beam in the present specimen has sufficient shear strength for the maximum shear requirement.

10.2.3 Design Recommendations for the Partially-Restrained Connections

The PR connection is also designed at one load level: the maximum load level.

At the maximum load level, the PR connection needs to have sufficient shear strength to resist the vertical component of the compressive strut force as determined by Eq. (10.2.3). It is assumed that all the shear force is resisted by the double web angles of the PR connection.

At the maximum load level, both the ratio of the plastic moment capacity of the PR connection to that of steel column and the ratio of the plastic moment capacity of the PR connection to that of the steel beam should be less than 1.0. This requirement can be expressed in the following equation,

$$M_{ppr} < M_{pc}, \text{ and } M_{ppr} < M_{pb} \qquad (10.2.4)$$

In calculating the plastic moment capacities of these three steel components at the maximum load level, the effect of the axial force should be included. The plastic

mechanism analysis method can be utilized to estimate the axial force in the three components. Figure 10.2.1 shows the equilibrium of the vertical forces on the windward column and leeward column. For example, at the level of the second floor, the axial force in the windward column below the beam can be calculated as

$$P_c = nV_{bu} + sh_c - P_{g1} \tag{10.2.5}$$

where

P_{g1} = axial force in columns at the level of the first floor due to gravity load, kips

and the axial force in the leeward column below the beam can be calculated as

$$P_c = (n-1)V_{bu} + sh_c + P_{g1} \tag{10.2.6}$$

The larger value from Eq. (10.2.5) and Eq. (10.2.6) should be used in Eq. (9.2.8) or Eq. (9.2.9) to estimate the plastic moment capacity of the steel column.

The axial force in the PR connection is the same as that in the steel beam. Figure 10.2.2 shows the equilibrium of the horizontal forces in the windward column to middle beam joint of the structural system shown in Figure 9.2.1. It can be seen that

$$P_b \text{ or } P_{pr} = V_1 - V_2 \tag{10.2.7}$$

where

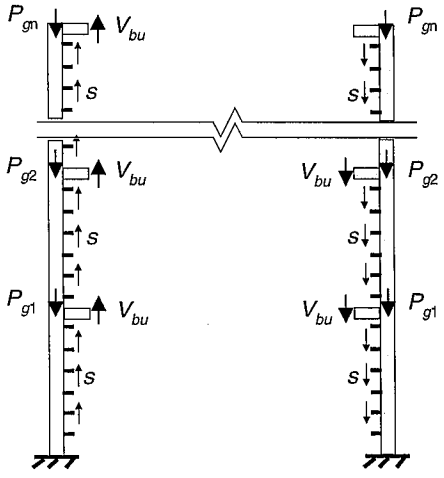

a) Windward Column b) Leeward Column

Fig. 10.2.1 Equilibrium of Vertical Forces in Columns

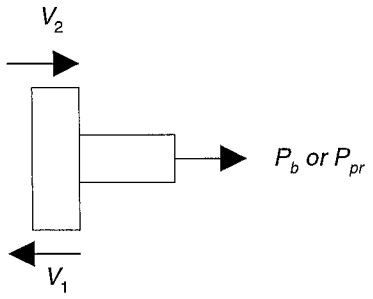

Fig. 10.2.2 Force Equlibrium in Joint

P_b = axial force in the steel beam when the structure reaches its maximum lateral strength

P_{pr} = axial force in the PR connection when the structure reaches its maximum lateral strength

V_1 = the shear force at the top of the windward column in the first story when the structure reaches its maximum lateral strength

V_2 = the shear force at the bottom of the windward column in the second story when the structure reaches its maximum lateral strength

V_1 is essentially the maximum shear force in the steel column, V_{cu}. In Section 5.1.2, the experimental result shows that the shear force at the bottom of the windward column in the second story was very small compared to the shear force at the top of the windward column in the first story. Therefore, shear force V_2 is neglected and the axial force in either the steel beam or the PR connection can be simply taken as

$$P_b = P_{pr} = V_{cu} = (\frac{M_{pc}}{n} + M_{ppr}) / h + \left(\frac{2}{3} - \frac{1}{2}\alpha\right)\alpha t \frac{h_c^2}{h}\sigma_c \qquad (10.2.8)$$

The plastic moment capacity of the PR connection has to be assumed in using Eq. (10.2.8). After the axial force is obtained, Eq. (9.2.8) or Eq. (9.2.9) can be used to determine the plastic moment capacity of the steel beam, and the method proposed in Section 10.3 can be used to design the PR connection according to the presumed plastic moment capacity and calculated axial force.

10.2.4 Design Recommendations for the Reinforced Concrete Infill Walls

The RC infill wall is designed at one load level, the prescribed design force level, at which RC infill wall shall have sufficient strength to resist 100% of the total lateral force. Additional detailing is proposed to ensure that the corner concrete crushes gradually after the structure reaches its maximum strength.

As discussed in Section 4.2, the corner concrete has to endure tensile ripping in

one direction and compressive crushing in the other direction. Because there was a discontinuity of the reinforcing cages in the corner (Figure 4.2.2), cracking initiated at that location and extended upwards due to the ripping from increasing shear force of the corner beam studs and the increasing tensile force from the column studs. As a result, the concrete at the corner region was quickly disrupted before the specimen underwent large displacement. The rapid disruption of the corner concrete is one of the primary reasons for the quick drop in the lateral strength of the specimen at large displacement. Therefore, it is suggested that in the future construction, the longitudinal bars of the horizontal reinforcing cages be extended into the vertical reinforcing cages, as shown in Figure 10.2.3, to prevent the growth and extension of vertical cracking in the corner of the infill wall. For clarity, the longitudinal bars in the horizontal reinforcing cages are represented in Figure 10.2.3 by thicker lines than those indicating wall steel in the infills.

10.2.5 Design Recommendations for the Headed Stud Connectors

The interface headed stud connectors should be designed to meet both a strength requirement and a deformation requirement.

It is reasonable to require the headed stud connectors to have sufficient strength to resist 100% of the lateral force, although it transferred only 80% of the lateral load during the test. This requirement gives the headed studs reserve strength to continue transferring lateral force, and more importantly, reserve slip to undergo the increasing interface slip at large drift. In estimating the shear strength of the headed studs, the effect of the axial force should be included.

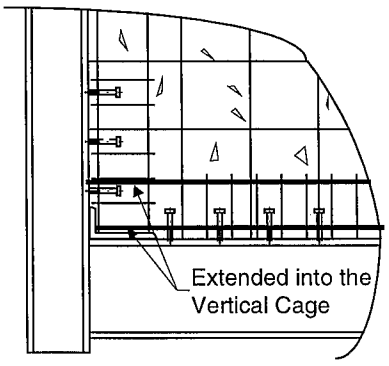

Fig.10.2.3 Detailing of Reinforcing Cages in the Corner

As discussed in the last section, fracture of the interface headed stud connectors reduced the overstrength of the system, reduced the energy dissipated through yielding of the reinforcing bars in RC infill walls, and in part resulted in the decrease in lateral strength of the system after reaching its peak. Therefore, it is important to delay the fracture of the headed studs in order to improve system behavior. Analysis of the experimental results (Chapter 6) shows that fracture of the headed studs was due to low-cycle fatigue failure, and it was mainly related to the interface slip demands in this system. Two approaches can be used to delay the fracture of the interface studs: either increase the slip capacity of the stud itself or reduce the interface slip of the system.

The experimental results showed that studs along the top interface of the first story survived longer than the studs along the bottom interface of the second story. The fractured surface of the studs (Section 4.5) also indicated that the studs along the top interface underwent larger deformation than the studs along the bottom interface, and they appeared to have behaved in a more ductile manner. The two different fracture types for the failed studs are likely related to the interface conditions in either story. First, it is reasoned that a thin layer of the concrete along the top surface of the infill wall was weaker due to the casting procedure so that the concrete surrounding the base of the studs along top interface crushed at an earlier cycle than those along the bottom interfaces. Furthermore, a small gap might exist along the top interface because of shrinkage of the concrete. As a result, the base of the stud shaft might have lost concrete confinement after a few cycles and the section just above the weld collar became the critical one. A series of push-out tests on the headed studs conducted in the University of Minnesota demonstrated that placing a polymer cone around the base of the headed stud (the same mechanism as a weak layer of concrete) can enhance ductility by as much as 60%. Therefore, it is suggested that in the future construction, a thin layer of soft material can be placed at the interface between the steel frame and the RC infill wall to enhance the ductility of the headed stud connectors, or cones or cylinders of plastic be placed around the base of each stud. Further research is needed regarding enhancing the deformation capacity of the headed stud connectors.

Another approach is to reduce the interface slip demands of the system. One method is to place more headed studs along the beam-infill wall interface to limit the interface slip requirement of the headed studs and enforce more shear deformation of the RC infill wall. Another method is to reduce the axial extension of the PR connection. For the specimen in the present research, the axial extension of the PR connection contributed approximately 40-50% of the interface slip demands by the 0.5% cycles (see Section 6.3.1.4). Furthermore, the plastic moment capacity of the PR connection was less than the designed value by approximately 25%. Therefore, larger sizes of angles can be used and/or the location of the high-strength bolts can be alternated to reduce the prying deformation of the angles, increase the moment capacity, and reduce the axial extension demands of the PR connection.

10.3 Estimating the Strength of the PR Connections

Section 5.3.2 concluded that the north PR connection reached its maximum strength in loading cycle G5-1-C, with the moment approximately equaling 180 kip-inches and the axial tensile force approximately equaling 105 kips; the south PR connection reached its maximum strength in loading cycle G5-1-A, with the moment approximately equaling 200 kip-inches and the axial tensile force approximately equaling 110 kips. The maximum strength of the north PR connection is slightly lower than that of the south PR connection because it was achieved one-half cycle later.

To verify the failure mechanism proposed by Kim and Chen (1998), the moment capacity of the PR connection subjected to pure bending and the tensile capacity of the PR connection subjected to pure tensile force were calculated again using the actual yield strengths of the PR connection components. The static yield strength of the top and seat angles was 52.7 ksi and that of the double web angles was 39.6 ksi. Following the procedures in Appendices A.3 and A.4, the estimated nominal moment capacity of the PR connection subjected to pure bending was 430.4 kip-inches, and the nominal tensile capacity of the PR connection subjected to pure tensile force was 104.6 kips. Both were close to the original estimated strength obtained in Appendix A. When the PR connection

reached its maximum strength in cycle G5-1, although the actual moment was only approximately 40% of the estimated moment capacity of the PR connection, the actual tensile force was larger than the tensile capacity of the PR connection. Therefore, the failure mechanism proposed by Kim and Chen (1998) for the PR connection in the bare steel frame likely underestimates the maximum strength of the PR connection used in the infill steel frame. The major reason is that the contribution of the surrounding concrete was not included in the failure mechanism of Kim and Chen (1998). For example, when the north PR connection of the middle beam reached its maximum strength in cycle G5-1-C, it rotated around a rotation center in the seat angle (the k line of the horizontal leg of the seat angle) so that the top angle deformed as shown in Figure 3.1.3. At the same time, the axial force from the middle beam further deformed the top angle in the same way. However, the compressive force from the concrete restrained the deformation of the top angle. As a result, the failure mechanism of the top angle was formed under the combined tensile force in the horizontal leg and the compressive stress from concrete, as shown in Figure 10.3.1. This failure mechanism is modeled with the formation of two plastic hinges. One is along the edge of the nut and the other along the toe of the fillet of the vertical leg. At the same time, the concrete also reaches its effective compressive strength uniformly along the vertical leg of the top angle. The virtual work equation for the top angle at the failure state may thus be estimated by:

$$M_{pt1}\theta + M_{pt2}\theta = V_{pt} g_2 \theta - \left[\frac{1}{2} f_{ce} (g_2\theta) g_2 l_{tv} + f_{ce} (k - t_t)(g_2\theta) l_{tv} \right] \qquad (10.3.1)$$

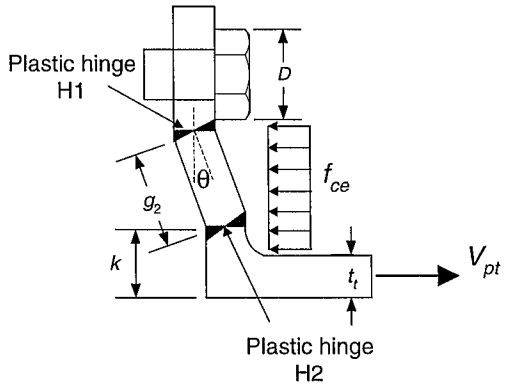

Fig. 10.3.1 Failure Mechanism of the Top Angle of North Connection

where

M_{pt1} = plastic moment of hinge 1 with coupling of the shear force

M_{pt2} = plastic moment of hinge 2 with coupling of the shear force

g_2 = distance between two plastic hinges

V_{pt} = tensile force in the horizontal leg

f_{ce} = effective compressive strength of the concrete

k = distance from the heel to the toe of fillet of the angle

t_t = thickness of the angle

l_{tv} = width of the angle

As stated in Kim and Chen (1998), the bending moment-shear interaction formula for the yielding state proposed by Drucker (1956) is used to include the effect of the shear force on the moment capacity. That is:

$$\frac{M_{pt,i}}{M_0}+\left(\frac{V_{pt,i}}{V_0}\right)^4=1 \tag{10.3.2}$$

where

$V_{pt,i}$ = plastic shear force in the location of hinge i with coupling of moment

$M_{pt,i}$ = plastic moment in the location of hinge i with coupling of shear

M_0 and V_0 are the plastic bending moment and the plastic shear force without coupling, respectively, and they are

$$M_0=\frac{F_y l_{tv}(t_t)^2}{4} \tag{10.3.3}$$

$$V_0=\frac{F_y l_{tv} t_t}{2} \tag{10.3.4}$$

where

F_y = yielding strength of the angle

Based on force equilibrium, V_{pt1} and V_{pt2} can be related to V_{pt} as follows:

$$V_{pt1} = V_{pt} - (g_2 + k - t_t) l_{tv} f_{ce} \tag{10.3.5}$$

$$V_{pt2} = V_{pt} - (k - t_t) l_{tv} f_{ce} \tag{10.3.6}$$

From Eqs. (10.3.1) to (10.3.6), V_{pt} can be simplified as

$$\frac{2g_2}{t_t}\left(\frac{V_{pt}}{V_0}\right) - \frac{c_1 + c_2}{t_t}\left(\frac{g_2 l_{tv} f_{ce}}{V_0}\right) + \left(\frac{V_{pt} - c_2 l_{tv} f_{ce}}{V_0}\right)^4 + \left(\frac{V_{pt} - c_1 l_{tv} f_{ce}}{V_0}\right)^4 = 2 \tag{10.3.7}$$

where

$$c_1 = g_2 + k - t_t$$
$$c_2 = k - t_t$$

V_{pt} can be determined by using an iterative procedure in Eq. (10.3.7). For the L5×3×5/16×5 angle used in the PR connection of the specimen, the dimensions used in Eq. (10.3.7) are given in Appendix A. As for the effective crushing strength of the concrete, MacGregor (1997) recommended it to be $0.85f_c'$ in the node region bounded by compressive strut and bearing areas. The average compressive strength f_c' of the concrete in the specimen was approximately 3.75 ksi. Using the actual yielding strength in the angle in Eq. (10.3.4) gives $V_0 = 41.2$ kips. As a result, the tensile force V_{pt} in the horizontal leg at the failure state is equal to 37.2 kips, 40% greater than that in the PR connection of a bare steel frame.

Figure 10.3.2 shows the free body diagram of the PR connection in the infilled steel frame at the failure state, when the PR is subjected to pure bending. It can be seen that the moment capacity of this PR connection is the combination of the moment capacities provided by the top angle, the seat angle and the double web angles:

$$M_{u,PR} = M_{ut} + M_{us} + M_{uw} \tag{10.3.8}$$

where

M_{ut} = the moment capacity contributed by the top angle

M_{us} = the moment capacity contributed by the seat angle

M_{uw} = the moment capacity contributed by the double web angles

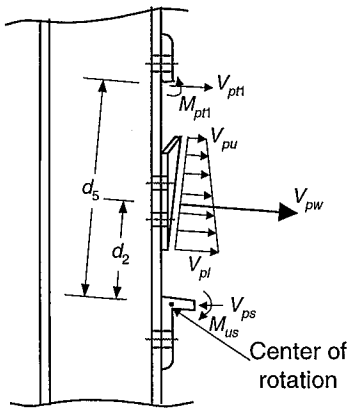

Fig.10.3.2 Free-Body Diagram of the PR Connection at Failure State When Subjected to Pure Bending

Due to the influence of the concrete, the moment capacity of the top angle is given by

$$M_{ut} = V_{pt1} d_5 - M_{pt} \tag{10.3.9}$$

where

$$d_5 = d + \frac{t_s}{2} + (k + g_2)$$

Equation (10.3.5) gives V_{pt1} = 22.7 kips and Eq. (10.3.2) gives M_{pt1} = 5.8 kip-inches. According to Eq. (10.3.9), the contribution of the top angle to the moment capacity is 207.1 kips-inches. Since the web angle and the seat angle are not affected by the concrete in the infill wall, the moment capacities contributed by these two can still be calculated using the procedures proposed by Kim and Chen (1998). The contributions of the double web angles and the seat angle to the moment capacity are 182.6 kip-inches and 6.4 kip-inches, respectively. Therefore, including the restraining effect of the concrete, the total moment capacity of the PR connection is 391.2 kip-inches.

When the PR connection in the infilled steel frame reaches its tensile capacity under pure tensile force, the top and seat angles have the same failure mechanisms as shown in Figure 10.3.1. Therefore, the tensile forces in the horizontal legs of both the top and seat angles are equal to 37.2 kips. The failure mechanism of the double web angles are the same as those in the PR connections in a bare steel frame since no concrete surrounds the double web angles. The tensile force provided by the double web angles

can be calculated according to the procedure in Appendix A.4 and the result is 26.0 kips. Therefore, including the restraining effect from the concrete, the total tensile capacity of the PR connection is 120.2 kips.

The test data can be used to calibrate the moment-tensile interaction equation of the PR connection in the infilled steel frame. It is assumed that the interaction equation is of the form:

$$\left(\frac{M_{PR}}{M_{u,PR}}\right)^{\alpha}+\left(\frac{T_{PR}}{T_{u,PR}}\right)^{\beta}=1 \qquad (10.3.10)$$

Figure 10.3.3 shows the interaction equation with different sets of α and β. Two pairs of the test data for the PR connections of the middle beam are also plotted in Figure 10.3.3. It can be observed that the two pairs of test data are located between the interaction equation with α=1.75 and β=1.75 and the interaction equation α=2.25 and β=2.25. The equation with α=1.75 and β=1.75 gives a slightly conservative estimation compared to the test data. Therefore, it is recommended that interaction equation is of the form:

$$\left(\frac{M_{PR}}{M_{u,PR}}\right)^{1.75}+\left(\frac{T_{PR}}{T_{u,PR}}\right)^{1.75}=1 \qquad (10.3.11)$$

More experimental data are needed to further verify Eq. (10.3.11) for estimating the maximum strength capacity of the PR connections in the RC infilled steel frame.

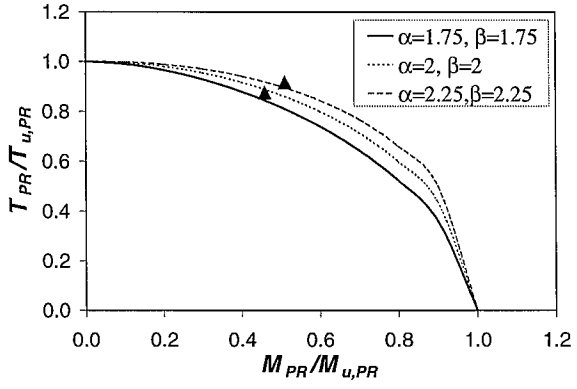

Fig.10.3.3 Moment and Axial Force Interaction Equation of the PR Connection

Chapter 11

Conclusions

In order to validate the use of partially-restrained steel frames with composite reinforced concrete infill walls as an alternative structural system for seismic design, this research investigates the seismic behavior of this composite system by conducting a one-bay, two-story, one-third scale experiment of the complete structural system, proposing a finite element model for use in design, and establishing a rational plastic mechanism analysis procedure to verify lateral load strength.

11.1 Summary of Experimental Program

This facet of the research was designed to investigate the seismic behavior of composite steel frame-reinforced concrete infill wall structural system. To initiate this research, a series of prototype structures were analyzed and designed according to currently available U.S. seismic design provisions so as to identify member sizes for acceptable seismic performance. The design studies identified a 6-story prototype structure with PR connections as the focus of this research.

The two-story, one bay test specimen was meant to represent the bottom two levels of the six-story prototype structure at an approximate one-third scale. The story dimensions were 86 inches of width and 48 inches of height, measured from center to center of steel members. The steel columns comprised W5x19 wide-flange shapes, while

the girders comprised W8x13 wide-flange shapes. All column and girder material was A572 Grade 50 steel. The RC infill wall was 3.5 inch thick, with nominal compressive strength targeted at 3.5 ksi. The infill reinforcement comprised two-layers of #2 deformed bars, with reinforcement ratio equaling 0.5% in each direction.

The beams and columns were joined using PR connections. These PR connections comprised top and seat angles and double web angles. The PR connections were designed to resist 50% of the plastic moment of the girder, and 100% of the shear capacity of the girder.

The headed studs, which were 3/8 inches in diameter and 2.5 inches in length, were used to connect the steel frames and the RC infills at the interfaces. The headed studs were placed at a 4-inch spacing, and were intended to resist 100% of the lateral shear at design force level of the system. Confining cages, comprising #2 deformed bars as the horizontal bars and W3.5 wire as ties, were used to enhance the strength and ductility of the headed stud connectors.

The test specimen was subjected to a cyclic loading history, including three cycles at total drifts of 0.05%, 0.20%, 0.35%, 0.50%, 0.75%, 1.00%, and 1.25%, followed by two cycles each at total drifts of 1.50% and 1.75%.

11.2 Observations from Experimental Study

The experimental results are summarized according to the global and local behavior of the specimen.

11.2.1 Global Behavior

The main conclusions derived from the global response of the specimen pertain to strength, drift capacity, ductility, and distribution of forces between the frame and panel. These are:

1) The specimen provided sufficient system overstrength. The specimen was sized to resist approximately 70 kips prescribed design lateral load. The maximum load of the specimen was approximately 160 kips, 2.3 times the design lateral load. The yield

strength of the specimen was defined as 85% of the maximum load, 1.9 times the design lateral load.

2) The second story interstory drift was able to surpass 3% without collapse of the structure. Approximately 50% of the lateral strength was lost when the total drift of the specimen was increased from 0.75% to 1.25%. The decrease in the lateral strength was primarily induced by the quick disruption of the corner concrete in the second story and failure of the headed stud connectors along the beam-panel interfaces.

3) The ductility index, μ, is approximately equal to 4 for the second story and 3 for the entire structure. The first story was unable to exhibit the same level of the ductility, and consequently it did not dissipate the same amount of energy as the second story. The primary factor responsible for this behavior was the fixity of the first-story columns, which is an artifice of the test setup used.

4) The lateral shear force was resisted primarily by the compression strut and interface headed stud connectors. At the design lateral force level, the headed studs resisted 80-90% of the total lateral load, and the remaining 10-20% was resisted by the compression strut. The compression strut was required to resist increasing amounts of lateral shear force as the number of stud failure increased.

5) The overturning moment was shared by the steel frame and the RC infill wall. At the design lateral force level, the steel frame resisted approximately 80% of the overturning moment. The steel frame was required to resist increasing amounts of overturning moment as the number of stud failure increased.

11.2.2 Local Response of the Steel Frame and the Reinforced Concrete Infill Walls

The main observations derived from the local responses of the steel frame and the infill wall pertain to deformation demands of major components, internal force distribution in the steel columns, and strength capacity of the PR connections. These are:

1) The steel column flanges exhibited moderate yielding in and near the connection regions, but extensive shear yielding occurred to the steel column web due to the increasing compression strut force. As designed, the steel beam had minor shear

yielding in the connection region so that the plastic deformation of the connection was contributed primarily by the connection angles.

2) The axial forces in the two columns comprised an important couple to resist overturning moment. The ratio of the tensile force in the windward column to the compressive force in the leeward column was greater than 1, and this ratio increased with increasing drift demands. It was more than 2 when the specimen reached its maximum strength.

3) The maximum shear force in the column occurred in the connection region, at the cross section just below or above the centerline of the bolts connecting the seat angle to the column flange.

4) As designed, the RC infill wall exhibited approximately uniform shear deformation until the headed studs failed and the corner concrete crushed. The percentage of the interstory drift induced by the gross shear deformation of the infill wall increased with increasing drift demands. In the first story, this percentage reached more than 50% when the specimen achieved its maximum strength.

5) The load-deformation response envelope of the PR connections exhibited bilinear (elastic-plastic) behavior. The plastic hinges in the PR connections started to form before the specimen reached its maximum lateral strength, and the plastic mechanism of the PR connections was fully achieved in the 0.75% cycles when the specimen reached its maximum lateral strength.

6) The plastic moment capacity of the PR connection was decreased by approximately 60% due to the coupled axial force. The confining concrete around the top and seat angle increased axial tensile strength of the PR connection by approximately 20%.

11.2.3 Behavior of the Interface Headed Stud Connectors

The observations derived from the behavior of the interface headed stud connectors pertain to interface slip demands, stud axial strain demands, stud yielding, stud fracture, and interface concrete confinement. These are:

1) The headed studs connectors along the beam-infill wall interfaces had higher slip demands than the headed stud connectors along the column-infill wall interfaces. Furthermore, the slip demands were approximately equal in the two loading directions for the studs along the beam-infill interfaces, but had a large difference in the two loading directions for the studs along column-infill interfaces.

2) The headed studs along the bottom interface of each infill appeared to have the highest forces based upon strain data. These forces likely were sufficiently large to reduce the shear strength of the studs. However, failure of studs was likely controlled more directly by strain demands leading to low-cycle fatigue fracture. The majority of the studs that failed did so by low-cycle fatigue. The fractured studs were along the beam-infill interfaces. With respect to the low-cycle fatigue failure of the studs, it appeared that the slip demands far outweighed the axial deformation demands.

3) The headed studs along the top interface of each panel exhibited a more ductile failure pattern that the headed studs along the bottom interface, indicating that isolating the studs from the concrete at the base may be an effective approach for increasing their slip capacity.

4) The headed studs along the beam-infill wall interface were well confined by the reinforcing cages, but the corner concrete along the column-infill wall interfaces crushed substantially at limited interstory drift demands, indicating more confining steel is needed in these locations.

11.3 Observations from Plastic Mechanism Analysis and Finite Element Analysis

The observations from the plastic mechanism analysis and finite element analysis pertain to the advantages of the modified plastic mechanism and the feasibility of the proposed finite element model. These are:

1) The plastic mechanism analysis methods proposed by Liauw and Kwan (1983a, 1983b) overestimate the lateral strength of the infilled steel frames with the strong axis of the steel columns oriented in the plane of infill wall by approximately 20%. The modified

model in the present study (Chapter 9) captures the failure pattern at the peak load, and provides a closer but conservative estimation by adopting a reasonable value for concrete crushing strength, by specifying a more accurate value for the contact length between the column and infill, by treating the yielding of the studs along the beam-infill interface more accurately, and by incorporating the coupling effect of the axial force and bending moment in the steel members.

2) The finite element model proposed in the present study (Chapter 8) provides reasonable estimates of internal forces in both the steel and concrete members, as well as the drift of the structure at the design force level of the system. In doing so, the shear stiffness of a headed stud at the design level can be defined as the secant at a shear of approximately 50% of the nominal shear strength of the headed studs. In addition, the effective modulus of elasticity of the concrete wall element should be taken as 25% of the nominal modulus of elasticity of the concrete, and the tensile stiffness of the headed studs along the bottom interfaces should be neglected. This type of elastic analysis is suitable for use in design at the design force level.

11.4 Conclusions on the SRCW System

The following conclusions can be derived from the present study on the SRCW system:

1) This system offers a lot of potential as a lateral framing system for buildings located in earthquake-prone regions. The composite action provided by the confined headed stud connectors is able to mobilize beneficial characteristics of both the RC infill and steel boundary members. The relatively light steel frame joined using PR connections maximizes the system economy, and still ensures the system integrity at large deformations. Some presumed advantages of this system, such as the development of an ideal failure mode for maximizing energy dissipation capacity, require additional verification.

2) This system has ample strength to resist the lateral forces from earthquake and ample stiffness to control system drift. Adequate redundancy is provided to the system by

alternate load paths, such as shear stud-infill interaction, truss action due to steel frame-infill interaction, and deformation of the steel frame.

3) Improvement is needed for reducing the post-peak strength degradation observed in the present study. The improvement should focus on mitigating the ripping/crushing damage to corner regions of the concrete infills, and increasing the low-cycle fatigue life of the interface head stud connections.

11.5 Recommendations

11.5.1 Design

Under the gravity load combinations, the bare steel frame should be sized to resist 100% of the gravity load.

Under the lateral load combinations, it is proposed that the composite structural system be designed at two load levels, the prescribed design load level and the maximum load level.

At the design load level, the finite element model described in Chapter 8 can be used to estimate the system drift and the internal forces in major components. At the design load level, the steel column should provide sufficient strength capacity, the RC infill should be sized to resist 100% of the lateral load, the headed stud connectors should be designed to transfer 100% of the lateral load and, and the effect of the axial force should be included in estimating the shear strength of the headed studs.

At the maximum load level, the steel column and steel beam should provide sufficient shear strength to resist the compression strut force by utilizing the hardening of steel. The moment capacity of the PR connection should be less than the moment capacity of the steel column in the connection region. The effect of the axial force should be considered in estimating the moment capacity for both the steel columns and the PR connections.

Reinforcing cages should be provided around the headed studs to increase the strength and ductility of the headed stud. Continuity of the reinforcement at the intersection between the horizontal cages and vertical cages shall be guaranteed.

11.5.2 Research

Additional experimental and analytical research is needed for further improving the seismic behavior of this composite structural system.

In future experimental work, it is recommended that plastic inserts (cones or cylinders) should be placed around the base of each stud to increase the slip capacity of the studs. At the same time, relatively larger angles should be used for the PR connections to reduce the axial deformation of the PR connections, thus reducing the slip demands along the beam-infill interfaces. The number of studs should also be increased to further reduce the slip demands. Further research is needed for determining optimal geometry for the plastic inserts, reasonable angle sizes for the PR connections, and optimal number of studs. In addition, better confinement should be implemented to ensure gradual crushing of the concrete located in the corner regions of the infills. Furthermore, less reinforcement should be used for the RC infills without sacrificing tight bar spacing requirements to reduce the stiffness and increase the shear deformation of the infills. It is also suggested that the degree of fixity at the specimen base be reduced below what was used in the present test setup so that it better represents actual construction practice.

Future analytical research, such as development of nonlinear finite elements suitable for analyzing this system, should quantify the effect of each component on the system behavior and provide insight for optimal design of this composite structural system.

Appendix A

Design of Partially-Restrained Connections in the Specimen

The design of the partially-restrained (PR) connection complied with the following criteria:

1) The web angle has at least the same shear strength as that of the beam.
2) Under combined axial tension and bending moment, the nominal moment capacity of the PR connection shall be approximately 50% of the nominal moment capacity of the beam.
3) All the bolts shall be sized to ensure the formation of the plastic mechanism of the PR connection.

A36 steel was used for both the top and seat angles and the double web angles. A36 steel was also used for the beams. Since the exact material properties of the beam and connection components were unknown during design, and A36 steel usually has an actual strength larger than its specified minimum yield strength, the design yield strength of the A36 steel was specified as $1.3 \times 36 = 46.8$ ksi for the beam and the PR connection. The nomenclature of typical dimensions of each angle in the PR connection is shown in Figure A.1.

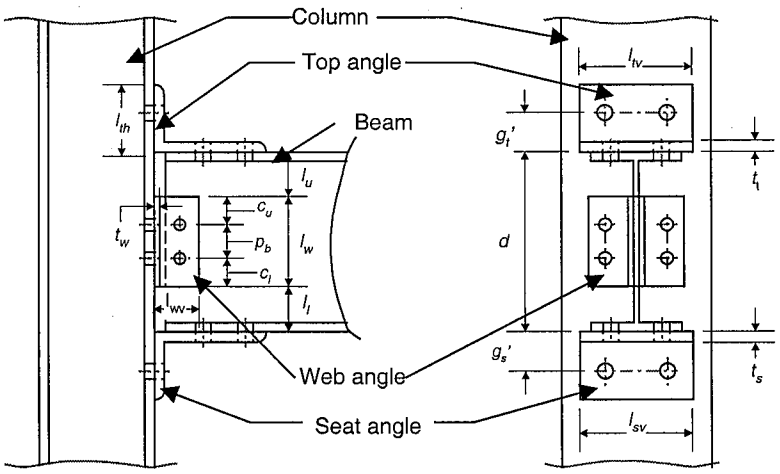

Fig. A.1 Nomenclature of Typical Dimensions of Each Angle in the PR Connection

1. Design the double-web angle

a. Determine the shear force to be resisted by the double web-angle

Assuming the double web angle has the same design shear strength as that of the W8×13 beam, the required shear force is:

$$V_u = \phi 0.6 A_w F_{yw} = 0.9 \times 0.6 \times 0.23 \times 7.99 \times 36 \times 1.3 = 46.4 \text{ kips}$$

where

ϕ = resistance factor

A_w = web area, inch^2

F_{yw} = specified minimum yield stress of the web, ksi

b. Calculate the number of bolts connecting the double web-angle to the column flange

Use an A490, ϕ1/2 inch bolt:

$$\phi R_n = 0.75 F_v A_b = 0.75 \times 60 \times 0.1963 = 8.8 \text{ kips}$$

$$n \geq \frac{V_u}{\phi R_n m} = \frac{46.4}{8.8 \times 2} = 2.6 \approx 3$$

where

F_v = nominal shear strength of the bolt, ksi

A_b = nominal shear area of the bolt, inch^2

m = number of shear planes

Therefore, use three A490 ϕ1/2 inch bolts to connect each angle.

c. Choose the thickness of the double web angle

i. Consider the bearing strength

Use A36 steel and assume $L_e > 1.5d_b$ and $s \geq 3d_b$:

$$\phi R_n = \phi(2.4F_u t_w d_b) = 0.75 \times 2.4 \times 58 \times t_w \times 0.5 = 52.2t_w \geq \frac{V_u}{6}$$

$$t_w \geq \frac{46.4}{6 \times 52.2} = 0.15 \text{ inches}$$

where

F_u = specified minimum tensile strength of the angle steel, ksi

t_w = thickness of the web angle, inches

d_b = diameter of the bolt, inches

ii. Consider the rupture strength

Assume the length of the double web angle is 5 inches:

$$\phi R_n = 0.75(0.6F_u A_{nv}) = 0.75 \times 0.6 \times 58 \times t_w \times (5 - 3 \times \frac{9}{16})$$

$$= 86.45t_w \geq V_u / 2$$

$$t_w \geq \frac{46.4/2}{86.45} = 0.27 \text{ inches}$$

where

A_{nv} = net area subjected to shear, inch^2

Therefore, choose the thickness of the web angle t_w = 5/16 inches

d. Calculate the size of the weld connecting the double web angle to the girder web

The double web angle must be welded to girder web because there is not enough clearance for bolting.

Use a 1/4 inch E70 fillet weld:

$$\phi R_n = 0.75 F_w A_w = 0.75 \times 0.6 \times 70 \times 0.707 \times 0.25 \times l_{wd}$$
$$= 5.56 l_{wd} \geq V_u / 2$$
$$l_{wd} \geq 4.17 \text{ inches}$$

where

F_w = nominal strength of the weld electrode material, ksi

A_w = shear area of the weld, inches

l_{wd} = length of the weld, inches

Therefore, the length of the web angle shall be greater than 4.17 inches.

e. Choose the angle sizes

Based on the clearance requirement and the strength requirement, choose a L2×2×5/16×5 angle as the double-web angle.

2. Design the top and seat angles

The top and seat angles were sized so that the PR connection had a moment capacity approximately 50% of that of the middle beam when it was subjected to combined bending moment and tensile force. The failure mechanism and analytical procedures proposed by Kim and Chen (1998) were used to predict the maximum strength of the PR connection subjected to pure bending, as well as the maximum strength of the PR connection subjected to pure tensile force [see also (CTBUH, 1993)]. With consideration of both the strength requirement and the clearance requirement, a L5×3×5/16×5 was chosen for the top and seat angles. The procedures to estimate the strength of the PR connections are detailed in the following sections.

3. Moment Capacity of the PR Connection Subjected to Pure Bending

Figure A.2.(a) shows the failure mechanism of the PR connection subjected to pure bending. It can be seen that the vertical leg of the top angle and the legs of the double web

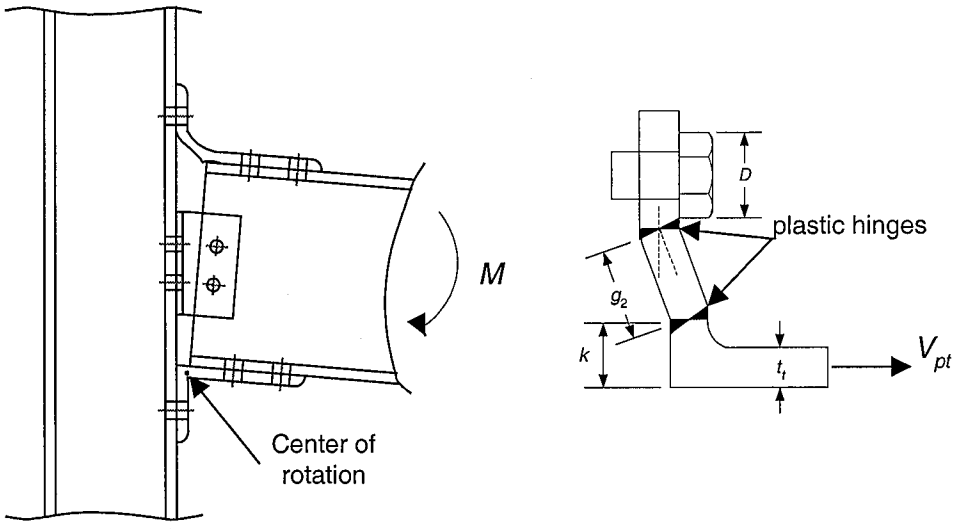

(a) (b)

Fig. A.2 Failure Mechanism of the PR Connection Subjected to Bending [after Kim and Chen (1998)]

angles attached to the columns are pulled off the column flange. The horizontal leg of the seat angle bends as a cantilever beam. The entire PR connection rotates around the rotation center in the seat angle. As proposed by Kim and Chen (1998), the moment capacity of the PR connection subjected to pure bending is the combination of moment capacities provided by the top angle, the seat angle, and the double web angle

$$M_{u,PR} = M_{ut} + M_{us} + M_{uw} \tag{A.1}$$

where

M_{ut} = the moment capacity contributed by the top angle, kip-inches

M_{us} = the moment capacity contributed by the seat angle, kip-inches

M_{uw} = the moment capacity contributed by the double web angle, kip-inches

The moment capacity contributed by each component is calculated as follows. The derivations of the equations are not given for simplicity and can be found in Kim and Chen (1998).

a. Calculate M_{ut}

$$M_{ut} = M_{pt} + V_{pt} d_2 \tag{A.2}$$

where

V_{pt} = plastic shear force in the vertical leg, kips

d_2 = distance from V_{pt} to the center of rotation (see Figure A.2), inches

The plastic moment in the top angle, M_{pt}, and the plastic shear force in the vertical leg of the top angle, V_{pt}, are achieved when two plastic hinges formed in the top angle, as seen in Figure A.2.(b). V_{pt} is calculated from the follow equation:

$$\left(\frac{V_{pt}}{V_o}\right)^4 + \frac{g_2}{t_t}\left(\frac{V_{pt}}{V_o}\right) = 1 \tag{A.3}$$

where

V_o = plastic shear force of the top angle without coupling, kips

t_t = thickness of the top angle, inches

g_2 = distance between two hinges, inches

V_o and g_2 are estimated as follows:

$$V_o = \frac{F_y l_{tv} t_t}{2} = \frac{36 \times 1.3 \times 5 \times 5/16}{2} = 36.35 \text{ kips}$$
$$g_2 = 1.75 - \frac{D}{2} - k = 1.75 - \frac{1.0625}{2} - \frac{13}{16} = 0.41 \text{ inches} \tag{A.4}$$

where

l_{tv} = width of the top angle, inches

D = width of nuts across flat sides for bolt fasteners, inches

k = distance from heel to toe of fillet of an angle, inches

Substituting V_o and g_2 into Equation (A.3) yields

V_{pt} = 23.2 kips

This V_{pt} can then be used to size the bolts connecting the top angles to the column and beam flanges.

The plastic moment of the top angle without coupling, M_{pt}, is:

$$M_{pt} = \frac{V_{pt} g_2}{2} = \frac{23.2 \times 0.41}{2} = 4.76 \text{ kip-inches}$$

The arm of V_{pt}, d_2, is:

$$d_2 = d + \frac{t_s}{2} + k = 8 + 0.15625 + 0.8125 = 8.97 \text{ inches}$$

where

d = depth of the beam, inches

t_s = thickness of the seat angle, inches

Therefore,

$$M_{ut} = M_{pt} + V_{pt} d_2 = 4.76 + 23.2 \times 8.97 = 212.86 \text{ kip-inches}$$

b. Calculate M_{us}

$$M_{us} = F_y l_{sv} (t_s)^2 / 4 = 36 \times 1.3 \times 5 \times (5/16)^2 \div 4 = 5.71 \text{ kip-inches}$$

where

l_{sv} = width of the seat angle, inches

c. Calculate M_{uw}

Similar to the top angle, the web angle reaches its maximum capacity when two yield lines form along the leg attached to the column flange:

$$M_{uw} = 2 V_{pw} d_4 \qquad \text{(A.5)}$$

The resultant of the plastic shear force in a single web angle, V_{pw}, is:

$$V_{pw} = (V_{pu} + V_{pl}) l_w / 2 \qquad \text{(A.6)}$$

where the plastic shear force per unit length at the top edge of the web angle, V_{pu}, can be calculated from the following equation:

$$\left(\frac{V_{pu}}{V_{ow}}\right)^4 + \frac{g_y}{t_w}\left(\frac{V_{pu}}{V_{ow}}\right) = 1 \qquad \text{(A.7)}$$

where

V_{ow} = plastic shear force per unit length of the web angle without coupling, kips/inch

t_w = thickness of the web angle, inches

g_y = distance between two hinges at the top edge of the web angle, inches

V_{ow} and g_y can be calculated as:

$$V_{ow} = \frac{F_y t_w}{2} = \frac{36 \times 1.3 \times 5/16}{2} = 7.31 \text{ kips/inch}$$

$$g_y = g_c - k = 1.25 - \frac{11}{16} = 0.5625 \text{ inches}$$

where

g_c = distance from bolt center to angle edge

Substitute the values into Equation (A.7):

$$V_{pu} = 3.8 \text{ kips/inch}$$

The plastic shear force per unit length at the bottom edge of the web angle, V_{pl}, is equal to V_{ow}, therefore

$$V_{pw} = (V_{pu} + V_{pl}) l_w / 2 = (3.8 + 7.31) \times 5 \div 2 = 27.77 \text{ kips}$$

The arm of V_{pw}, d_4, can be calculated as:

$$d_4 = l_w \frac{2V_{pu} + V_{pl}}{3\left(V_{pu} + V_{pl}\right)} + l_l + t_s / 2$$

$$= 5 \times \frac{2 \times 3.8 + 7.31}{3(3.8 + 7.31)} + 1.5 + 0.15625 = 3.89 \text{ inches}$$

The moment contributed by the web angle is:

$$M_{uw} = 2V_{pw}d_4 = 2\times 27.77\times 3.89 = 216.05 \text{ kip-inches}$$

The total moment capacity of the PR connection is:

$$M_{u,PR} = M_{ut} + M_{us} + M_{uw} = 212.86 + 5.71 + 216.05 = 434.82 \text{ kip-inches}$$

4. Tensile Capacity of the PR Connection Subjected to Pure Tensile Force

When the PR connection is subjected to pure tensile force, each component deforms in the same way as the top angle shown in Figure A.1.(a). The vertical legs of both the top and seat angle, as well as the legs of the double web angles attached to the column, are pulled off the surfaces of the column flanges. Therefore, the tensile strength of the PR connection is reached when the failure mechanism shown in Fig.A.2.(b) forms in each component. As a result, the tensile strength is the combination of the plastic shear force of each component.

The plastic shear force of one leg of the web angle, V_{pw}, can be calculated using the same approach as calculating V_{pt} of the top angle. The result is

$$V_{pw} = 32 \text{ kips}$$

The plastic shear force of the seat angle is the same as that of the top angle since they have the same size.

The total tensile capacity is:

$$T_{u,PR} = V_{pt} + V_{st} + 2V_{pw} = 23.2\times 2 + 32\times 2 = 110.4 \text{ kips}$$

5. Effect of the Axial Force on the Moment Capacity of the PR Connection

The corner crushing of the infill wall will induce a non-uniform bearing force on the top portion of the boundary column. This bearing force may induce a significant amount of tensile force in the PR connection. In design, the tensile force of the PR connection can be conservatively assumed to equal the shear capacity of the column at the ultimate stage. Therefore, the axial force of the PR connection is:

$$T_{PR} = V_n \textit{ of the column} = 0.6\times 50\times 1.2\times 5.15\times 0.27 = 50.0 \text{ kips}$$

Again, the minimum yield strength of the column steel is multiplied by a factor of 1.2 to consider the likely overstrength of the actual material. Furthermore, the moment-axial force interaction equation of the PR connection is assumed to be linear, so that:

$$\frac{M_{PR}}{M_{u,PR}} + \frac{T_{PR}}{T_{u,PR}} = 1 \tag{A.8}$$

Therefore,

$$M_{PR} = M_{u,PR}(1 - \frac{T_{PR}}{T_{u,PR}}) = M_{u,PR}(1 - \frac{50.0}{116}) = 0.57 M_{u,PR}$$

The uncoupled moment capacity of the beam is:

$$M_{u,pb} = Z_b F_{yb} = 11.4 \times 1.3 \times 36 = 533.52 \text{ kip–inches}$$

where

Z_b = plastic modulus of the beam, inch^3

F_{yb} = specified minimum yield stress of the beam, ksi

The axial force at the end of the beam is assumed to be 50.0 kips, the same as that imposed on the PR connection. Eq. (9.2.8) is used to include the effect of the axial force on the moment capacity of the beam. As a result, the coupled moment capacity of the beam, M_{pb}, is 87% of the uncoupled moment capacity of the beam, $M_{u,pb}$. Therefore,

$$M_{PR} = 0.57 M_{u,PR} = 247.84 \text{ kip–inches} \approx 0.55 M_{pb}$$

Appendix B

Documentation of Instrument Readings

Appendix B documents the readings of the strain gages and LVDTs during the entire loading history in the following sequences:

Appendix B.1 – the hysteretic lateral load-strain relationships of the column strain gages (Figures B.1.1 to B.1.24)

Appendix B.2 – 1) the reading of each "slip" LVDT at the peak story drift of each loading cycle (Tables B.2.1 and B.2.2)

2) the reading of each "separation" LVDT at the peak story drift of each loading cycle (Tables B.2.3 to B.2.6)

3) the hysteretic lateral load-slip relationships of the "slip" LVDTs (Figures B.2.1 to B.2.11)

4) the hysteretic lateral load-separation relationships of the "separation" LVDTs (Figures B.2.12 to B.2.30)

Appendix B.3 – the time history of the strain gages on the interface headed studs (Figures B.3.1 to B.3.22)

Appendix B.4 – the hysteretic lateral load-strain relationships of the strain gages on the top and seat angle of the PR connections (Figures B.4.1 to B.4.12)

Appendix B.1 Column Strain Gages

Appendix B.1 documents the hysteretic lateral load-strain relationships of the column strain gages. The locations of these strain gages are shown in Figure 3.4.3. Each instrumented cross section includes two strain gages on the flanges and one strain rosette at the center of the web. Correspondingly, this appendix documents the two longtudinal strains in the flanges and the shear strain at the center of the web for each instremented cross section. For example, Figures B.1.1 and B.1.2 show the longitudinal strain versus lateral load from strain gages C_NC_CF_G1 and C_NC_CF_G2, which were the two strain gages placed on the flanges at the bottom of the north column in the first story. Figure B.1.3 shows the shear strain versus lateral load from strain rosette C_NC_CW_R1 at the web center of the same cross section.

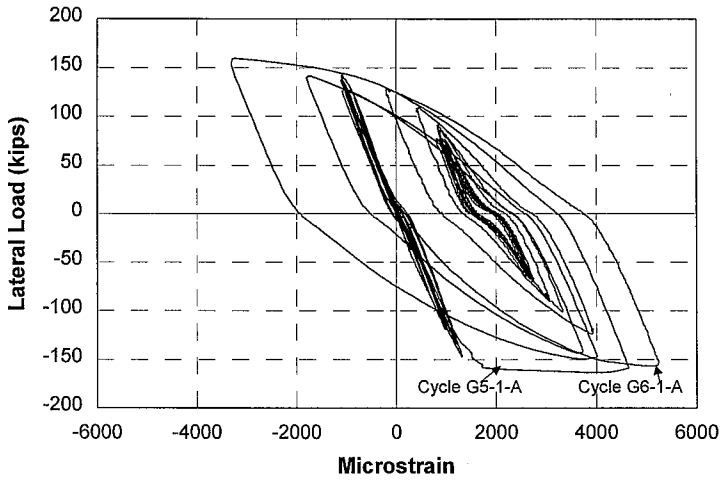

Fig. B.1.1 Longitudinal Strain from Gage C_NC_CF_G1

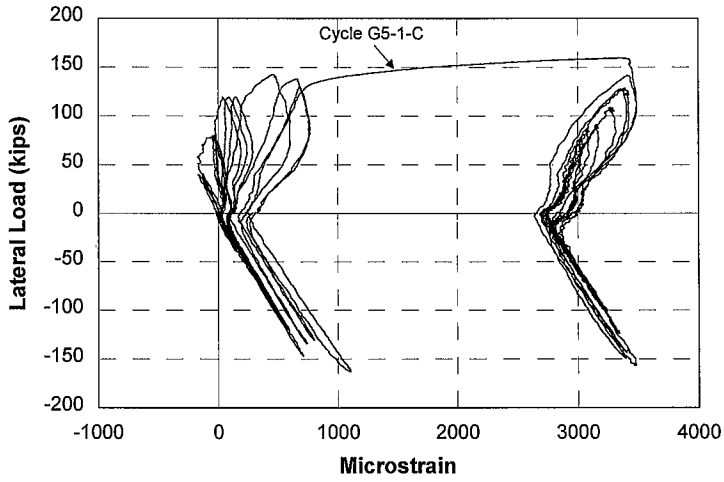

Fig. B.1.2 Longitudinal Strain from Gage C_NC_CF_G2

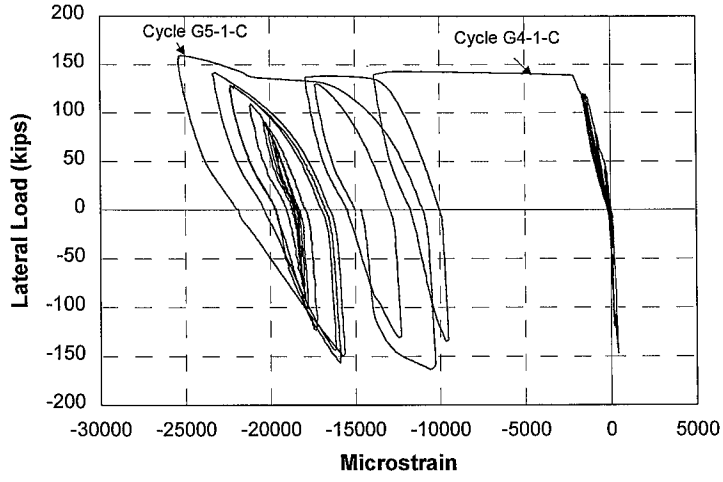

Fig. B.1.3 Shear Strain from Rosette C_NC_CW_R1

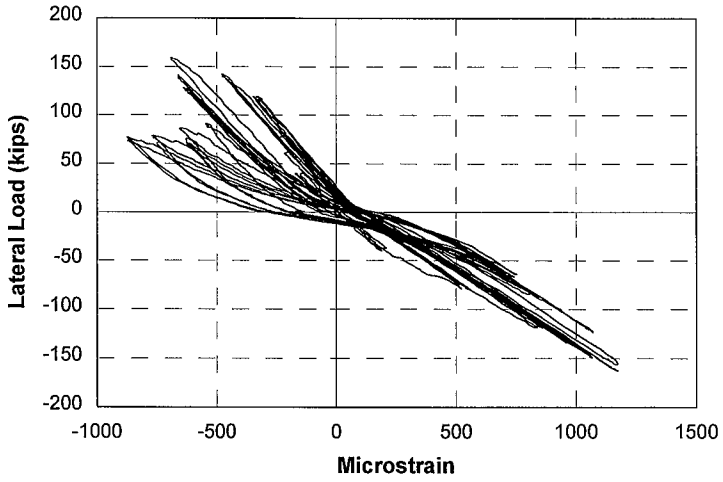

Fig. B.1.4 Longitudinal Strain from Gage C_NC_CF_G3

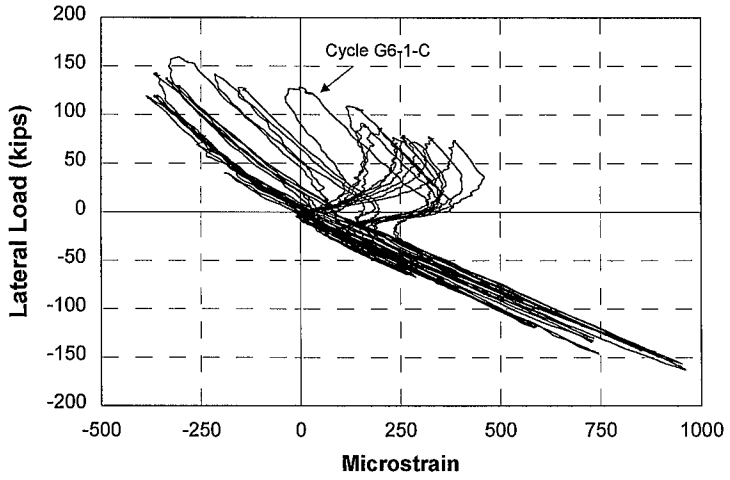

Fig. B.1.5 Longitudinal Strain from Gage C_NC_CF_G4

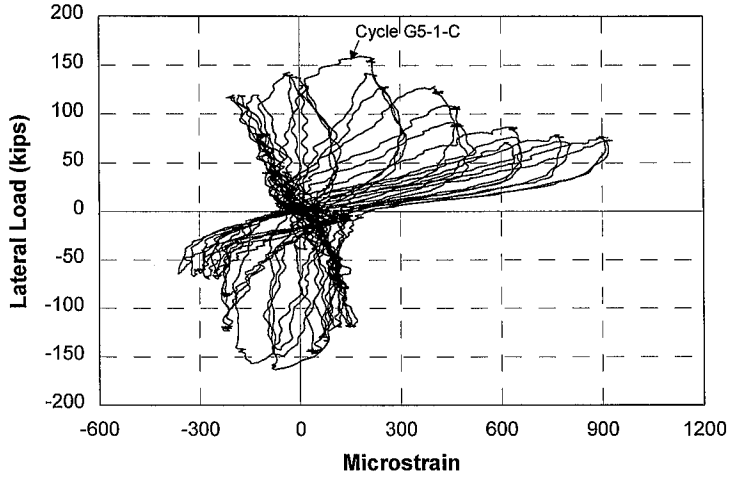

Fig. B.1.6 Shear Strain from Rosette C_NC_CW_R2

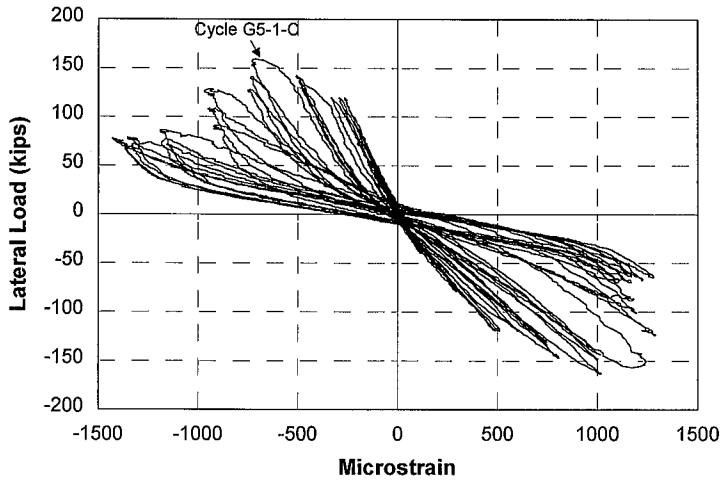

Fig. B.1.7 Longitudinal Strain from Gage C_NC_CF_G5

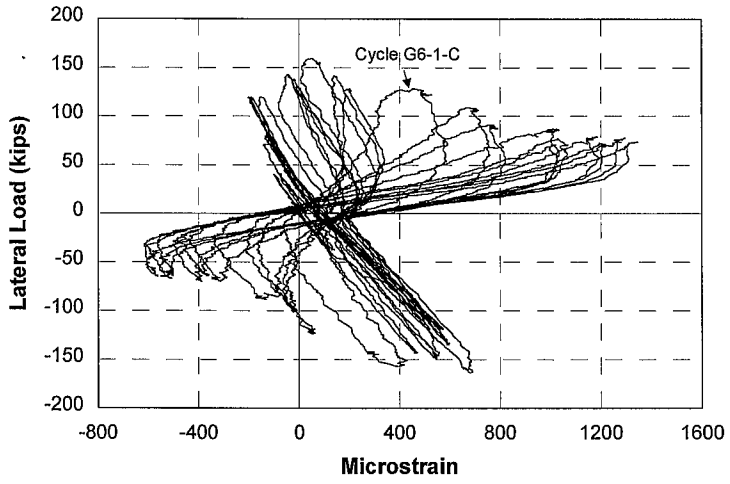

Fig. B.1.8 Longitudinal Strain from Gage C_NC_CF_G6

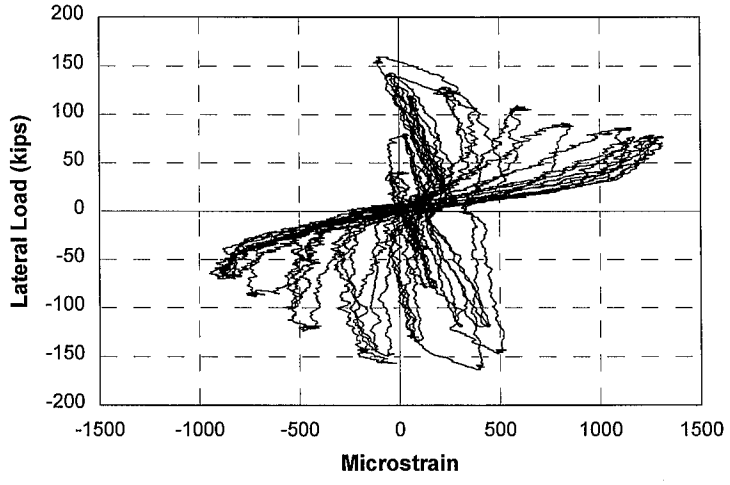

Fig. B.1.9 Strain Strain from Gage C_NC_CW_R3

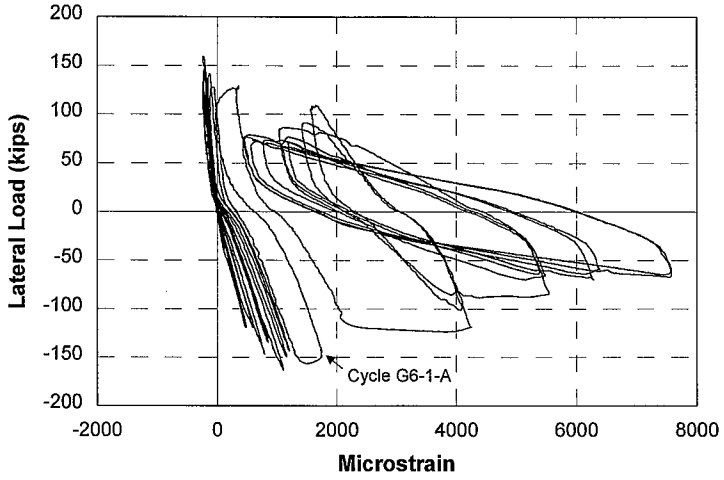

Fig. B.1.10 Longitudinal Strain from Gage C_NC_CF_G7

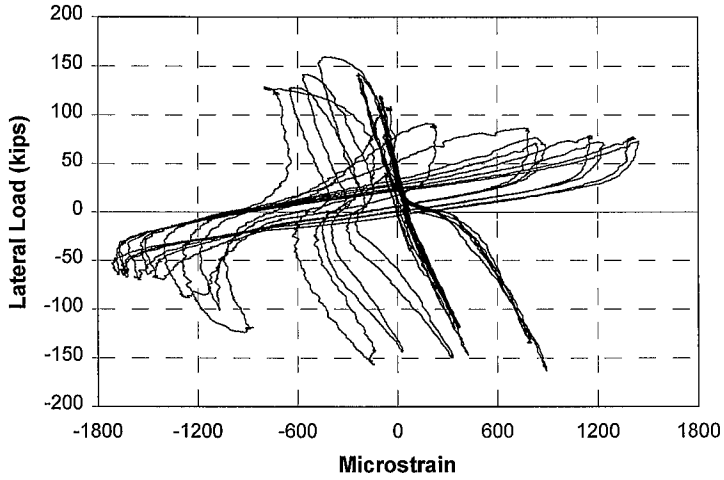

Fig. B.1.11 Longitudinal Strain from Gage C_NC_CF_G8

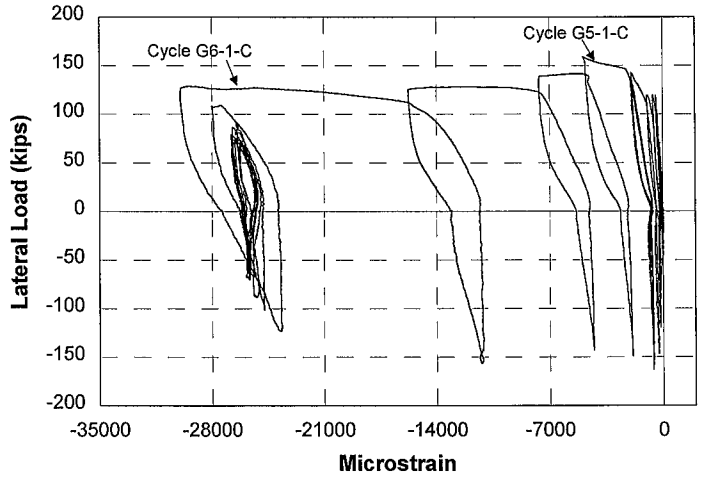

Fig. B.1.12 Shear Strain from Rosette C_NC_CW_R4

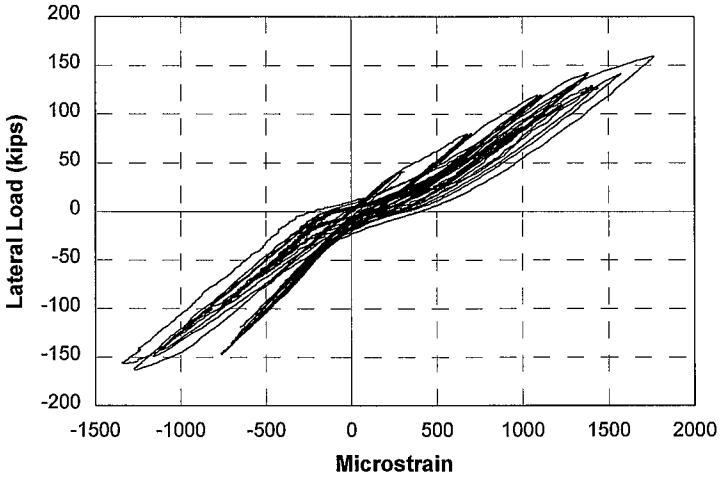

Fig. B.1.13 Longitudinal Strain from Gage C_SC_CF_G1

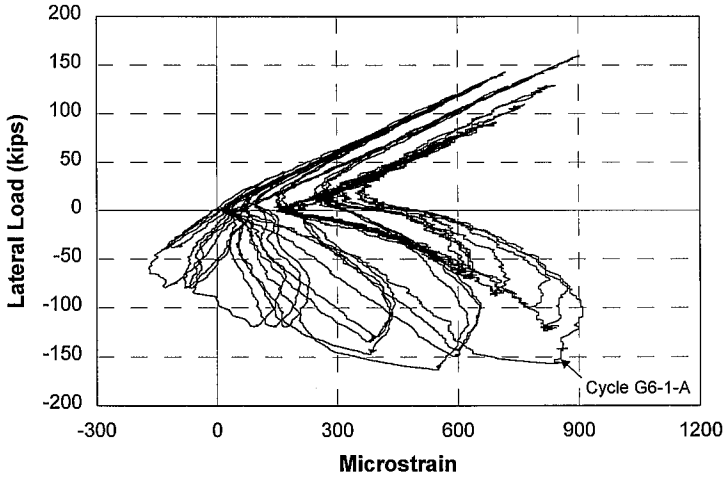

Fig. B.1.14 Longitudinal Strain from Gage C_SC_CF_G2

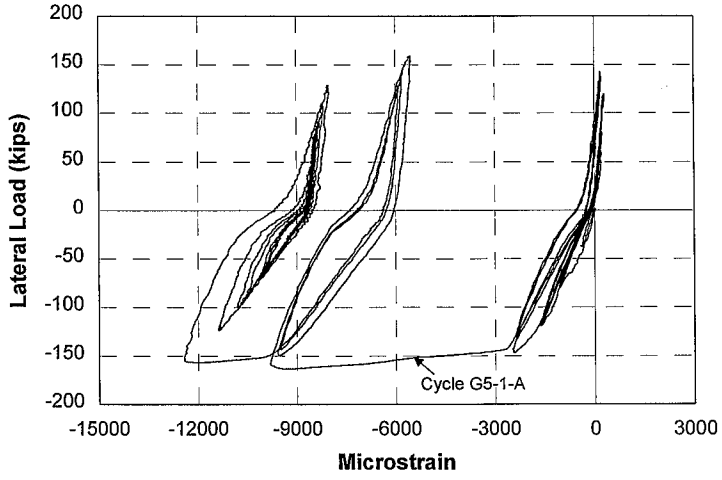

Fig. B.1.15 Shear Strain from Rosette C_SC_CW_R1

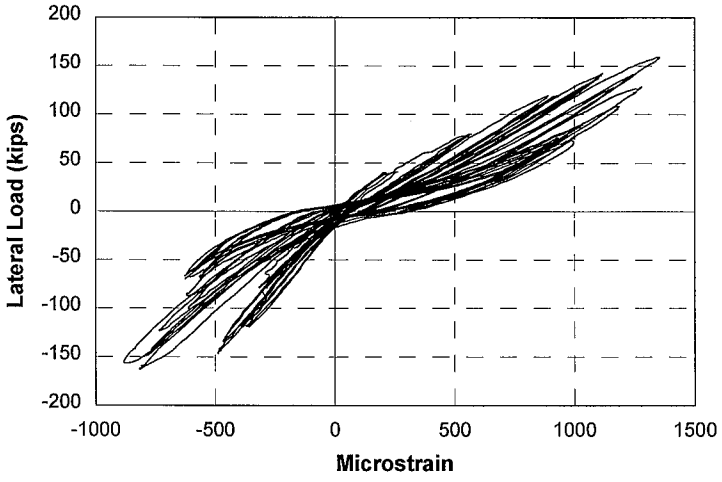

Fig. B.1.16 Longitudinal Strain from Gage C_SC_CF_G3

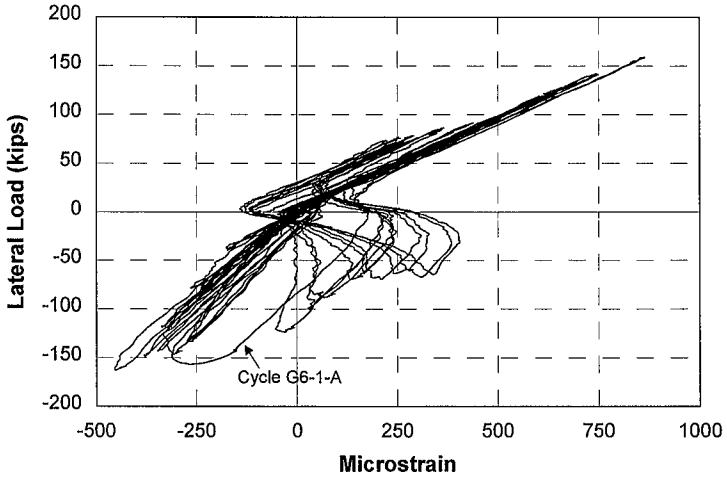

Fig. B.1.17 Longitudinal Strain from Gage C_SC_CF_G4

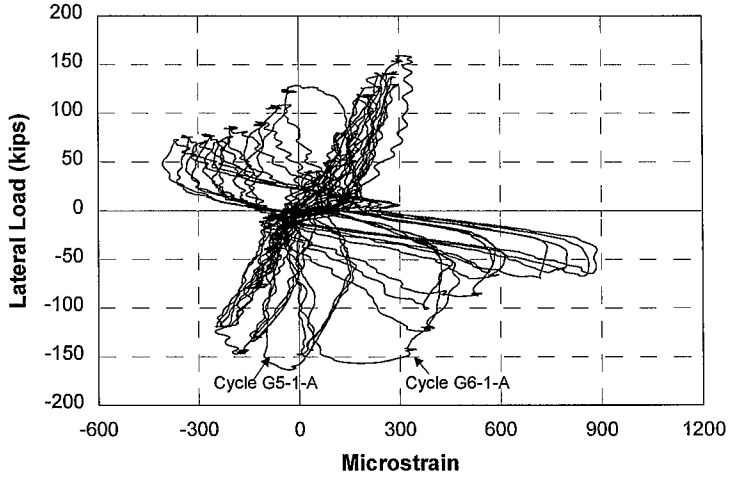

Fig. B.1.18 Shear Strain from Rosette C_SC_CW_R2

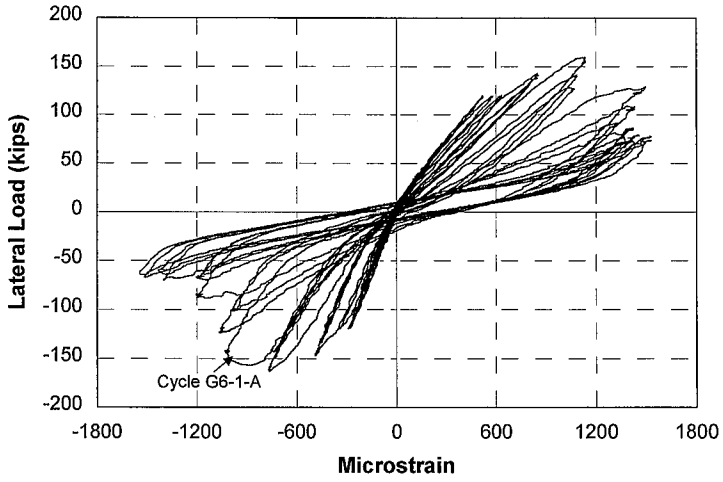

Fig. B.1.19 Longitudinal Strain from Gage C_SC_CF_G5

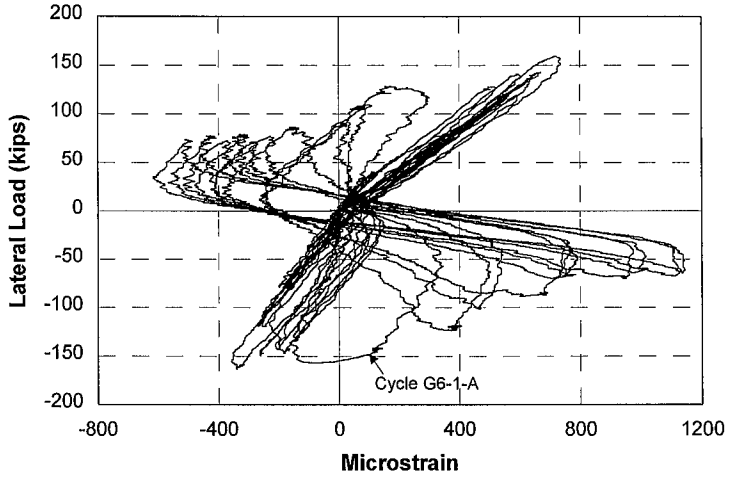

Fig. B.1.20 Longitudinal Strain from Gage C_SC_CF_G6

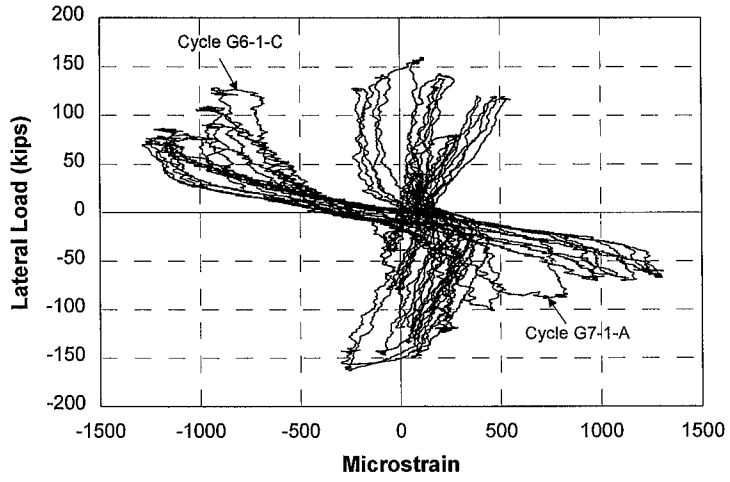

Fig. B.1.21 Shear Strain from Rosette C_SC_CW_R3

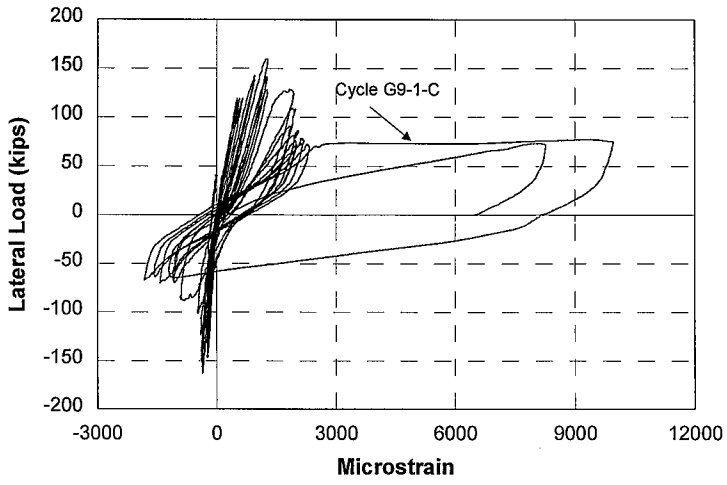

Fig. B.1.22 Longitudinal Strain from Gage C_SC_CF_G7

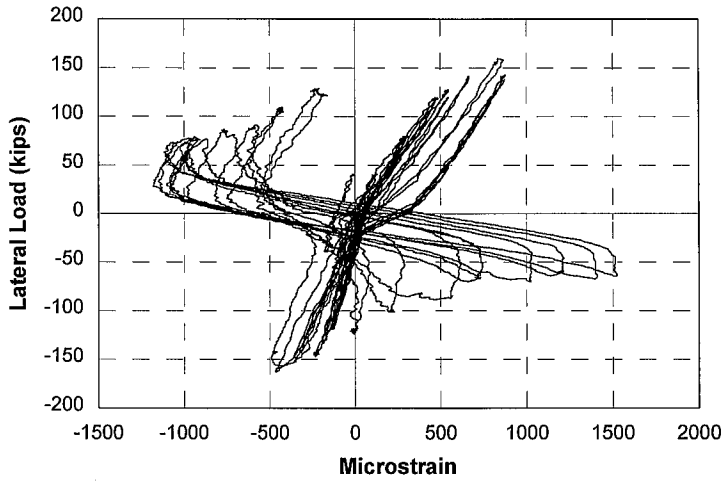

Fig. B.1.23 Longitudinal Strain from Gage C_SC_CF_G8

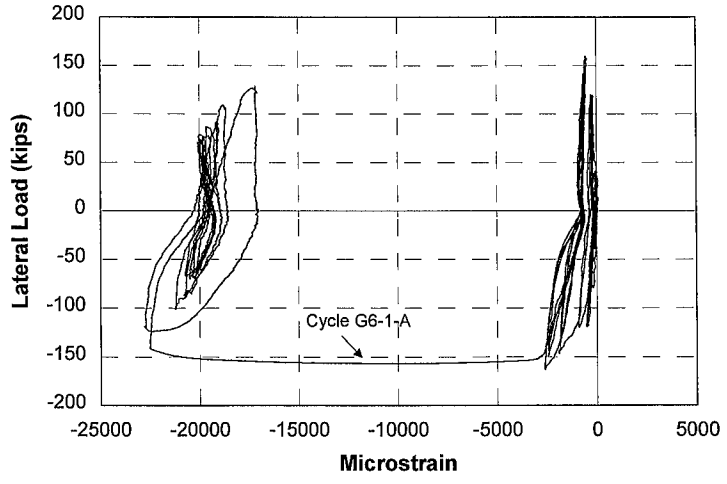

Fig. B.1.24 Shear Strain from Rosette C_SC_CW_R4

Appendix B.2 Slip and Separation LVDTs

Appendix B.2 documents both the readings of the "slip" and "separation" LVDTs along the interfaces of both stories. The locations of the slip and separation LVDTs are shown in Figure 3.4.5.

Table B.2.1 lists the reading of each slip LVDT of the first story at the peak interstory drift of each loading cycle. Table B.2.2 lists the reading of each slip LVDT of the second story at the peak interstory drift of each loading cycle. The slip values in Tables B.2.1 and B.2.2 are absolute values. Tables B.2.3 and B.2.4 list the reading of each separation LVDT of the first story at the peak interstory drift of each loading cycle. Table B.2.5 and B.2.6 list the reading of each separation LVDT of the second story at peak interstory drift of each loading cycle.

Figures B.2.1 and B.2.11 shows the hysteretic lateral load-slip relationship of each slip LVDT. The relationship between the sign of the slip and the direction of slip is related to the orientation of the slip LVDTs. For example, for LVDT LSLTI_1 at the top interface of the first story (see Figure 3.4.5), the increasing of the slip reading in the positive direction means that the middle beam was moving to the north relative to the first story infill wall; for LVDT LSLTI_2 at the top interface of the first story (see Figure 3.4.5), the increasing of the slip reading in the positive direction means that the middle beam was moving to the south relative to the first story infill wall.

Figure B.2.12 to B.2.30 shows the hysteretic lateral load-separation relationship of each separation LVDTs.

Table B.2.1 Interface Slip in the First Story of the Specimen

Loading Level	Cycle No.	Direc -tion	Peak Drift of Story 1 (%)	Bottom Interface Slip (inches)			Top Interface Slip (inches)			North Interface Slip (inches)	South Interface Slip (inches)
				L_SL_BI_1	L_SL_BI_2	Average	L_SL_TI_1	L_SL_TI_2	Average	L_SL_NI_1	L_SL_SI_1
0.05% Cycles	1	S	-0.042	0.002	0.002	0.002	0.005	0.001	0.003	0.004	0.002
		N	0.049	0.003	0.002	0.003	0.000	0.005	0.003	0.003	0.005
	2	S	-0.066	0.002	0.004	0.003	0.006	0.002	0.004	0.007	0.004
		N	0.055	0.005	0.002	0.004	0.002	0.005	0.004	0.004	0.007
	3	S	-0.073	0.003	0.004	0.004	0.006	0.004	0.005	0.007	0.004
		N	0.050	0.003	0.003	0.003	0.003	0.004	0.004	0.005	0.006
0.2% Cycles	1	S	-0.179	0.003	0.007	0.005	0.011	0.008	0.010	0.008	0.009
		N	0.166	0.009	0.003	0.006	0.006	0.012	0.009	0.011	0.009
	2	S	-0.171	0.003	0.008	0.006	0.011	0.009	0.010	0.007	0.010
		N	0.168	0.009	0.003	0.006	0.005	0.012	0.009	0.011	0.009
	3	S	-0.182	0.003	0.008	0.006	0.012	0.009	0.011	0.007	0.010
		N	0.174	0.009	0.003	0.006	0.006	0.012	0.009	0.011	0.009
0.3% Cycles	1	S	-0.297	0.004	0.013	0.009	0.021	0.010	0.016	0.009	0.015
		N	0.279	0.015	0.003	0.009	0.008	0.022	0.015	0.016	0.009
	2	S	-0.314	0.004	0.014	0.009	0.023	0.011	0.017	0.008	0.015
		N	0.296	0.018	0.003	0.011	0.009	0.025	0.017	0.016	0.009
	3	S	-0.332	0.005	0.015	0.010	0.026	0.014	0.020	0.008	0.015
		N	0.308	0.023	0.003	0.013	0.010	0.029	0.020	0.016	0.009
0.5% Cycles	1	S	-0.481	0.026	0.030	0.028	0.042	0.022	0.032	0.010	0.020
		N	0.389	0.044	0.004	0.024	0.016	0.043	0.030	0.018	0.011
	2	S	-0.465	0.032	0.031	0.032	0.042	0.024	0.033	0.010	0.020
		N	0.396	0.053	0.005	0.029	0.018	0.046	0.032	0.018	0.011
	3	S	-0.466	0.038	0.032	0.035	0.043	0.025	0.034	0.010	0.020
		N	0.384	0.053	0.005	0.029	0.018	0.045	0.032	0.018	0.011

Table B.2.1 (continued) Interface Slip in the First Story of the Specimen

Loading Level	Cycle No.	Direc -tion	Peak Drift of Story 1 (%)	Bottom Interface Slip (inches)			Top Interface Slip (inches)			North Interface Slip (inches)	South Interface Slip (inches)
				L_SL_BI_1	L_SL_BI_2	Average	L_SL_TI_1	L_SL_TI_2	Average	L_SL_NI_1	L_SL_SI_1
0.75% Cycles	1	S	-0.673	0.065	0.055	0.060	0.066	0.036	0.051	0.012	0.027
		N	0.520	0.096	0.011	0.054	0.031	0.071	0.051	0.022	0.016
	2	S	-0.666	0.061	0.057	0.059	0.069	0.041	0.055	0.012	0.027
		N	0.487	0.093	0.011	0.052	0.035	0.071	0.053	0.022	0.015
	3	S	-0.667	0.063	0.058	0.061	0.071	0.044	0.058	0.012	0.027
		N	0.459	0.089	0.010	0.050	0.036	0.071	0.054	0.022	0.014
1.0% Cycles	1	S	-0.804	0.079	0.070	0.075	0.085	0.053	0.069	0.012	0.031
		N	0.469	0.089	0.008	0.049	0.046	0.079	0.063	0.023	0.011
	2	S	-0.729	0.066	0.062	0.064	0.081	0.055	0.068	0.009	0.030
		N	0.417	0.078	0.005	0.042	0.053	0.077	0.065	0.022	0.009
	3	S	-0.653	0.054	0.056	0.055	0.078	0.055	0.067	0.007	0.028
		N	0.364	0.067	0.002	0.035	0.057	0.073	0.065	0.021	0.006
1.25% Cycles	1	S	-0.618	0.045	0.052	0.049	0.076	0.057	0.067	0.006	0.027
		N	0.353	0.063	0.000	0.032	0.064	0.076	0.070	0.021	0.004
	2	S	-0.561	0.036	0.047	0.042	0.073	0.059	0.066	0.004	0.025
		N	0.324	0.059	0.000	0.030	0.066	0.076	0.071	0.020	0.004
	3	S	-0.542	0.032	0.046	0.039	0.073	0.060	0.067	0.003	0.024
		N	0.316	0.057	0.001	0.029	0.068	0.077	0.073	0.021	0.003

Table B.2.2 Interface Slip in the Second Story of the Specimen

Loading Level	Cycle No.	Direc-tion	Peak Drift of Story 2 (%)	Bottom Interface Slip (inches)			Top Interface Slip (inches)	North Interface Slip (inches)	South Interface Slip (inches)
				L_SL_BII_1	L_SL_BII_2	Average	L_SL_TII_1	L_SL_NII_1	L_SL_SII_1
0.02& Cycle	1	S	-0.063	0.003	0.003	0.003	0.005	0.006	0.000
		N	0.082	0.003	0.003	0.003	0.005	0.001	0.000
	2	S	-0.018	0.003	0.003	0.003	0.008	0.007	0.001
		N	0.017	0.003	0.003	0.003	0.006	0.000	0.007
	3	S	-0.081	0.003	0.004	0.004	0.008	0.006	0.002
		N	0.069	0.003	0.003	0.003	0.006	0.003	0.006
0.2% Cycles	1	S	-0.186	0.005	0.009	0.007	0.014	0.011	0.004
		N	0.219	0.009	0.003	0.006	0.010	0.004	0.011
	2	S	-0.229	0.004	0.012	0.008	0.013	0.013	0.002
		N	0.206	0.011	0.002	0.007	0.009	0.002	0.012
	3	S	-0.228	0.004	0.011	0.008	0.013	0.012	0.004
		N	0.206	0.011	0.003	0.007	0.009	0.002	0.011
0.3% Cycles	1	S	-0.332	0.009	0.018	0.014	0.021	0.017	0.005
		N	0.347	0.016	0.009	0.013	0.015	0.004	0.014
	2	S	-0.342	0.020	0.024	0.022	0.022	0.018	0.005
		N	0.377	0.027	0.028	0.028	0.016	0.003	0.017
	3	S	-0.387	0.056	0.041	0.049	0.021	0.022	0.002
		N	0.423	0.041	0.056	0.049	0.017	0.004	0.021
0.5% Cycles	1	S	-0.527	0.121	0.085	0.103	0.032	0.032	0.003
		N	0.627	0.091	0.121	0.106	0.024	0.000	0.032
	2	S	-0.534	0.122	0.086	0.104	0.032	0.032	0.002
		N	0.646	0.099	0.130	0.115	0.026	0.000	0.033
	3	S	-0.523	0.122	0.088	0.105	0.032	0.032	0.000
		N	0.632	0.098	0.129	0.114	0.026	0.000	0.032

Table B.2.2 (continued) Interface Slip in the Second Story of the Specimen

Loading Level	Cycle No.	Direc-tion	Peak Drift of Story 2 (%)	Bottom Interface Slip (inches)			Top Interface Slip (inches)	North Interface Slip (inches)	South Interface Slip (inches)
				L_SL_BII_1	L_SL_BII_2	Average	L_SL_TII_1	L_SL_NII_1	L_SL_SII_1
0.75% Cycles	1	S	-0.841	0.189	0.135	0.162	0.051	0.049	0.002
		N	1.024	0.200	0.250	0.225	0.052	0.009	0.048
	2	S	-0.820	0.190	0.138	0.164	0.055	0.052	0.002
		N	1.051	0.232	0.281	0.257	0.056	0.013	0.049
	3	S	-0.826	0.194	0.144	0.169	0.059	0.053	0.003
		N	1.084	0.262	0.309	0.286	0.058	0.016	0.050
1.0% Cycles	1	S	-1.234	0.379	0.324	0.352	0.089	0.069	0.003
		N	1.585	0.495	0.537	0.516	0.084	0.015	0.058
	2	S	-1.298	0.410	0.368	0.389	0.113	0.071	0.005
		N	1.622	0.511	0.537	0.524	0.144	0.000	0.056
	3	S	-1.379	0.569	0.371	0.470	0.187	0.067	0.003
		N	1.701	0.476	0.503	0.490	0.273	0.016	0.049
1.25% Cycles	1	S	-1.938	0.468	0.454	0.461	0.404	0.077	0.007
		N	2.227	0.600	0.572	0.586	0.449	0.025	0.053
	2	S	-1.988	0.462	0.451	0.457	0.451	0.065	0.016
		N	2.281	0.643	0.572	0.608	0.480	0.022	0.072
	3	S	-2.003	0.443	0.436	0.440	0.475	0.056	0.020
		N	2.258	0.624	0.572	0.598	0.488	0.022	0.079

Table B.2.3 Interface Separation at Peak Drift in the First Story of the Specimen (Loaded in the South Direction)

Loading Level	Cycle No.	Peak Drift of Story 1 (%)	Bottom Interface Separation (inches)			Top Interface Separation (inches)			North Interface Separation (inches)	South Interface Separation (inches)
			L_SE_BI_1	L_SE_BI_2	L_SE_BI_3	L_SE_TI_1	L_SE_TI_2	L_SE_TI_3	L_SE_NI_1	L_SE_SI_2
0.05% Cycles	1	-0.042	0.004	0.000	-0.006	0.000	-0.001	-0.002	0.003	0.000
	2	-0.066	0.003	0.000	0.000	0.002	0.000	0.000	0.001	0.001
	3	-0.073	0.004	0.000	0.000	0.003	0.001	0.000	0.001	0.001
0.2% Cycles	1	-0.179	0.005	0.003	0.008	0.005	0.001	0.002	0.002	0.001
	2	-0.171	0.005	0.003	0.008	0.004	0.000	0.003	0.001	0.001
	3	-0.182	0.005	0.003	0.009	0.005	0.000	0.003	0.001	0.001
0.3% Cycles	1	-0.297	0.007	0.003	0.011	0.006	-0.001	0.004	0.002	0.001
	2	-0.314	0.007	0.003	0.010	0.005	-0.002	0.003	0.003	0.001
	3	-0.332	0.007	0.002	0.010	0.005	-0.001	0.002	0.003	0.001
0.5% Cycles	1	-0.481	0.011	0.006	0.010	0.006	0.001	0.003	0.006	0.001
	2	-0.465	0.017	0.006	0.009	0.006	0.000	0.002	0.008	0.001
	3	-0.466	0.023	0.007	0.008	0.006	0.001	0.001	0.009	0.001
0.75% Cycles	1	-0.673	0.033	0.011	0.007	0.005	0.001	0.002	0.015	0.005
	2	-0.666	0.029	0.011	0.006	0.005	0.000	0.000	0.018	0.007
	3	-0.667	0.028	0.011	0.006	0.005	0.000	0.000	0.019	0.009
1.0% Cycles	1	-0.804	0.031	0.015	0.007	0.006	0.001	0.001	0.021	0.013
	2	-0.729	0.023	0.012	0.005	0.004	0.002	0.001	0.018	0.016
	3	-0.653	0.019	0.008	0.005	0.003	0.002	0.000	0.018	0.016
1.25% Cycles	1	-0.618	0.016	0.006	0.005	0.003	0.002	0.001	0.017	0.016
	2	-0.561	0.013	0.003	0.005	0.003	0.002	0.004	0.016	0.013
	3	-0.542	0.011	0.003	0.005	0.003	0.003	0.005	0.016	0.014

Table B.2.4 Interface Separation at Peak Drift in the First Story of the Specimen (Loaded in the North Direction)

Loading Level	Cycle No.	Peak Drift of Story 1 (%)	Bottom Interface Separation (inches)			Top Interface Separation (inches)			North Interface Separation (inches)	South Interface Separation (inches)
			L_SE_BI_1	L_SE_BI_2	L_SE_BI_3	L_SE_TI_1	L_SE_TI_2	L_SE_TI_3	L_SE_NI_2	L_SE_SI_1
0.05% Cycles	1	0.049	-0.002	0.000	-0.001	-0.001	-0.001	-0.001	0.001	0.001
	2	0.055	-0.003	0.002	0.001	-0.001	0.000	0.002	0.001	0.001
	3	0.050	-0.002	0.001	0.001	0.000	0.001	0.003	0.000	0.001
0.2% Cycles	1	0.166	0.002	0.004	0.002	0.002	0.002	0.008	0.001	0.001
	2	0.168	0.002	0.003	0.002	0.003	0.001	0.007	0.000	0.002
	3	0.174	0.002	0.003	0.001	0.003	0.001	0.006	0.001	0.002
0.3% Cycles	1	0.279	0.003	0.005	0.001	0.004	-0.001	0.006	0.001	0.004
	2	0.296	0.003	0.003	0.001	0.004	0.000	0.005	0.001	0.005
	3	0.308	0.003	0.001	0.001	0.004	-0.001	0.004	0.001	0.005
0.5% Cycles	1	0.389	0.002	0.001	0.002	0.005	0.002	0.005	0.002	0.006
	2	0.396	0.004	0.001	0.002	0.005	0.002	0.004	0.003	0.006
	3	0.384	0.004	0.000	0.001	0.004	0.002	0.004	0.002	0.006
0.75% Cycles	1	0.520	0.011	0.005	0.005	0.003	0.003	0.004	0.008	0.010
	2	0.487	0.011	0.005	0.004	0.002	0.003	0.005	0.009	0.010
	3	0.459	0.011	0.004	0.003	0.001	0.003	0.004	0.011	0.011
1.0% Cycles	1	0.469	0.010	0.004	0.003	0.001	0.002	0.004	0.013	0.012
	2	0.417	0.007	0.002	0.003	0.001	0.004	0.004	0.011	0.012
	3	0.364	0.006	0.001	0.002	0.004	0.003	0.004	0.008	0.011
1.25% Cycles	1	0.353	0.006	0.001	0.001	0.008	0.004	0.004	0.009	0.011
	2	0.324	0.006	0.000	0.001	0.010	0.004	0.004	0.009	0.010
	3	0.316	0.006	0.000	0.002	0.012	0.005	0.003	0.009	0.010

Table B.2.5 Interface Separation at Peak Drift in the Second Story of the Specimen (Loaded in the South Direction)

Loading Level	Cycle No.	Peak Drift of Story 1 (%)	Bottom Interface Separation (inches)			Top Interface Separation (inches)		North Interface Separation (inches)	South Interface Separation (inches)
			L_SE_BII_1	L_SE_BII_2	L_SE_BII_3	L_SE_TII_1	L_SE_TII_2	L_SE_NII_1	L_SE_SII_2
0.05% Cycles	1	-0.063	0.002	0.000	-0.001	0.002	-0.002	-0.001	-0.001
	2	-0.018	0.002	0.001	0.000	0.001	0.000	-0.001	0.000
	3	-0.081	0.002	0.001	-0.001	0.001	0.001	-0.001	0.001
0.2% Cycles	1	-0.186	0.002	0.002	0.001	0.003	0.001	-0.001	0.001
	2	-0.229	0.001	0.001	0.000	0.002	0.000	-0.001	0.000
	3	-0.228	0.001	0.001	0.001	0.002	0.000	-0.002	0.000
0.3% Cycles	1	-0.332	0.002	0.001	0.001	0.002	0.001	-0.001	0.001
	2	-0.342	0.003	0.000	0.000	0.001	0.001	-0.002	0.000
	3	-0.387	0.016	0.005	0.001	0.001	0.001	0.006	0.000
0.5% Cycles	1	-0.527	0.033	0.014	0.004	0.004	0.001	0.022	0.000
	2	-0.534	0.033	0.017	0.008	0.002	0.002	0.027	0.000
	3	-0.523	0.034	0.019	0.013	0.002	0.002	0.030	0.001
0.75% Cycles	1	-0.841	0.046	0.025	0.030	0.005	-0.003	0.059	0.004
	2	-0.820	N. A.	0.032	0.036	0.004	-0.001	0.081	0.006
	3	-0.826		0.033	0.036	0.003	0.000	0.100	0.008
1.0% Cycles	1	-1.234		0.023	0.023	0.004	-0.002	0.252	0.011
	2	-1.298		N .A.	N. A.	0.001	0.002	N. A.	0.037
	3	-1.379				-0.005	0.010		0.060
1.25% Cycles	1	-1.938				-0.004	0.020		0.146
	2	-1.988				-0.003	0.019		N. A.
	3	-2.003				-0.001	0.019		

Table B.2.6 Interface Separation at Peak Drift in the Second Story of the Specimen (Loaded in the North Direction)

Loading Level	Cycle No.	Peak Drift of Story 1 (%)	Bottom Interface Separation (inches)			Top Interface Separation (inches)		North Interface Separation (inches)	South Interface Separation (inches)
			L_SE_BII_1	L_SE_BII_2	L_SE_BII_3	L_SE_TII_1	L_SE_TII_2	L_SE_NII_2	L_SE_SII_1
0.05% Cycles	1	0.082	0.000	0.000	0.001	0.001	-0.003	0.000	0.001
	2	0.017	0.001	0.001	0.002	0.002	-0.001	-0.001	0.001
	3	0.069	0.001	0.001	0.002	0.002	0.000	0.000	0.001
0.2% Cycles	1	0.219	0.000	0.002	0.003	0.002	-0.001	-0.001	0.000
	2	0.206	0.000	0.001	0.002	0.002	-0.001	-0.001	0.000
	3	0.206	0.000	0.001	0.002	0.002	-0.001	0.000	0.000
0.3% Cycles	1	0.347	0.000	0.002	0.001	0.002	0.000	0.000	0.001
	2	0.377	0.000	0.002	0.004	0.002	0.000	0.000	0.005
	3	0.423	0.006	0.005	0.021	0.001	0.000	0.000	0.012
0.5% Cycles	1	0.627	0.011	0.016	0.041	0.003	0.001	-0.001	0.035
	2	0.646	0.013	0.019	0.043	0.003	0.001	-0.001	0.041
	3	0.632	0.013	0.020	0.043	0.003	0.001	-0.001	0.042
0.75% Cycles	1	1.024	N. A.	0.044	0.063	0.009	0.010	0.000	0.112
	2	1.051		0.050	0.065	0.008	0.010	0.002	0.162
	3	1.084		0.054	0.061	0.007	0.010	0.004	0.206
1.0% Cycles	1	1.585		N. A.	N. A.	0.011	0.007	0.025	N. A.
	2	1.622				0.023	0.006	0.047	
	3	1.701				0.024	0.005	0.073	
1.25% Cycles	1	2.227				0.022	0.004	N. A.	
	2	2.281				0.017	0.002		
	3	2.258				0.015	0.001		

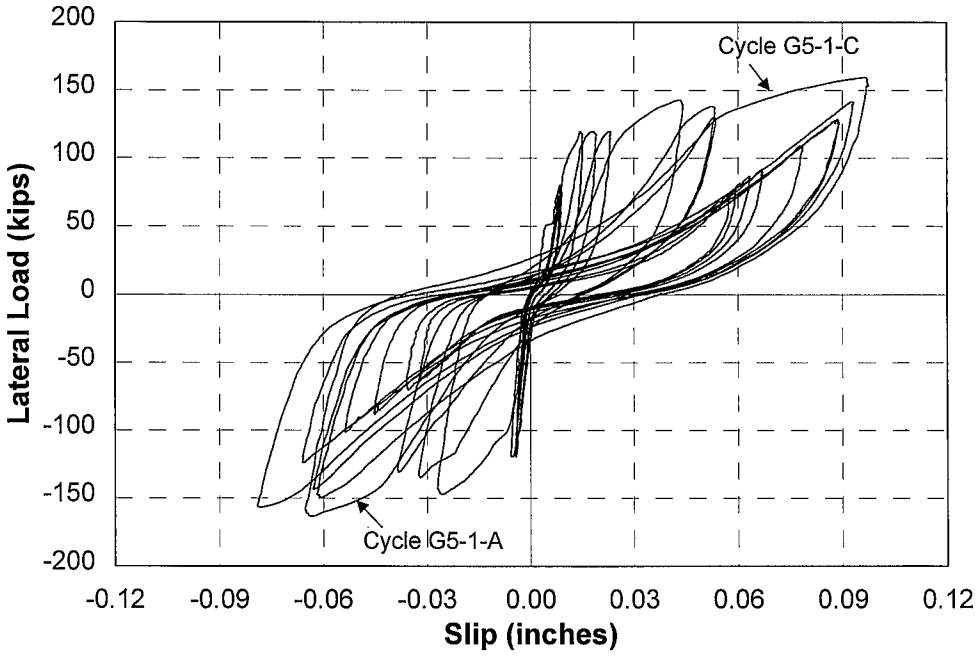

Fig. B.2.1 Slip Reading of LVDT L_SL_BI_1

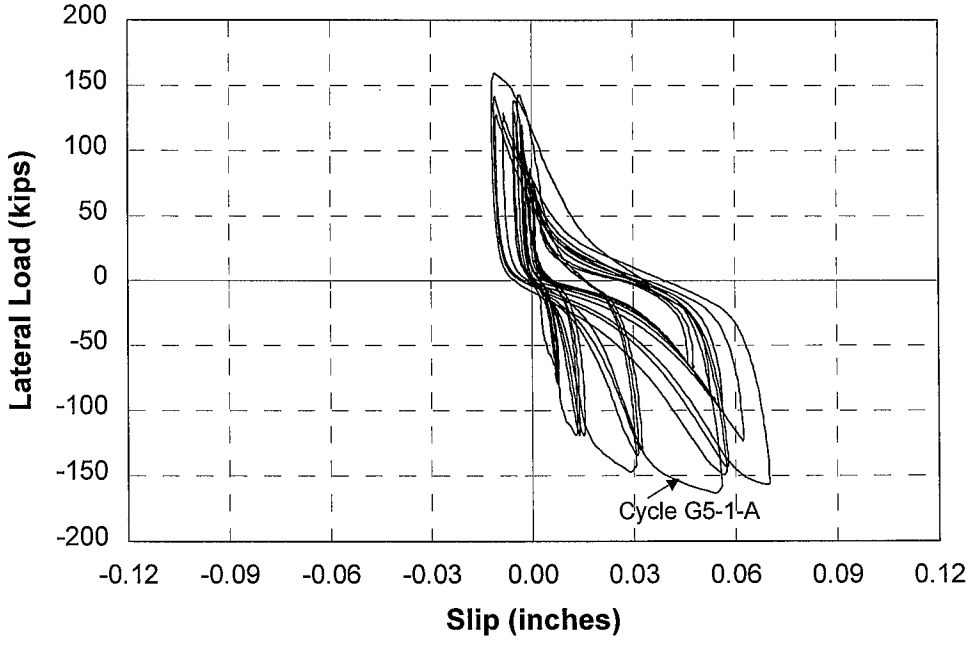

Fig. B.2.2 Slip Reading of LVDT L_SL_BI_2

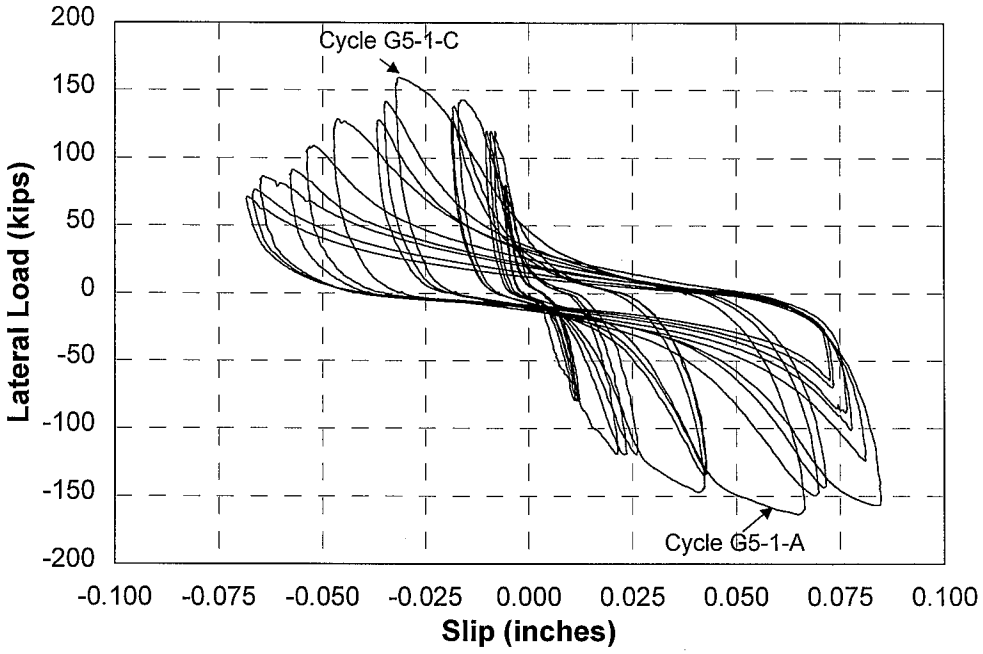

Fig. B.2.3 Slip Reading of LVDT L_SL_TI_1

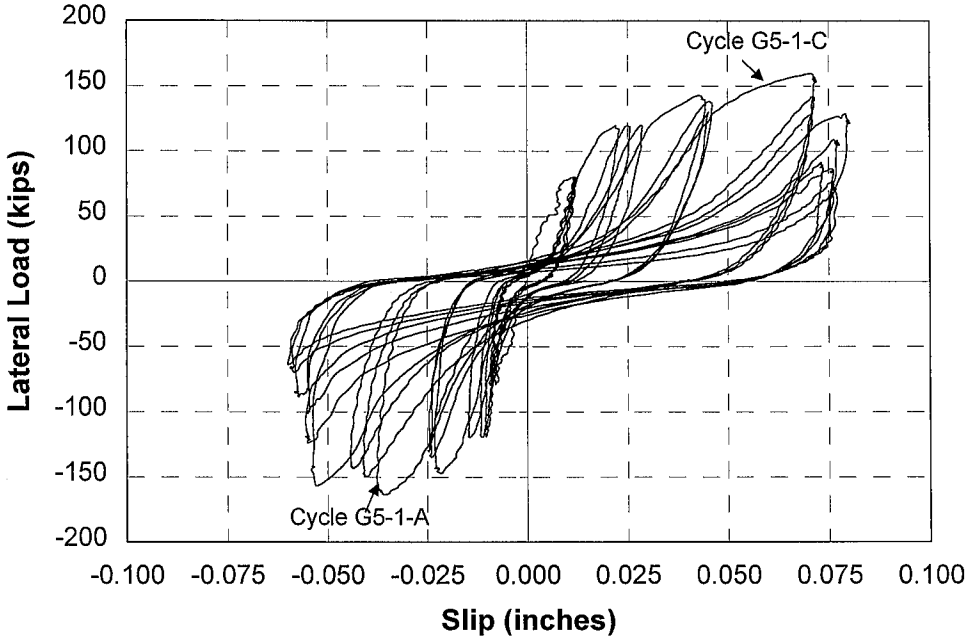

Fig.B.2.4 Slip Reading of LVDT L_SL_TI_2

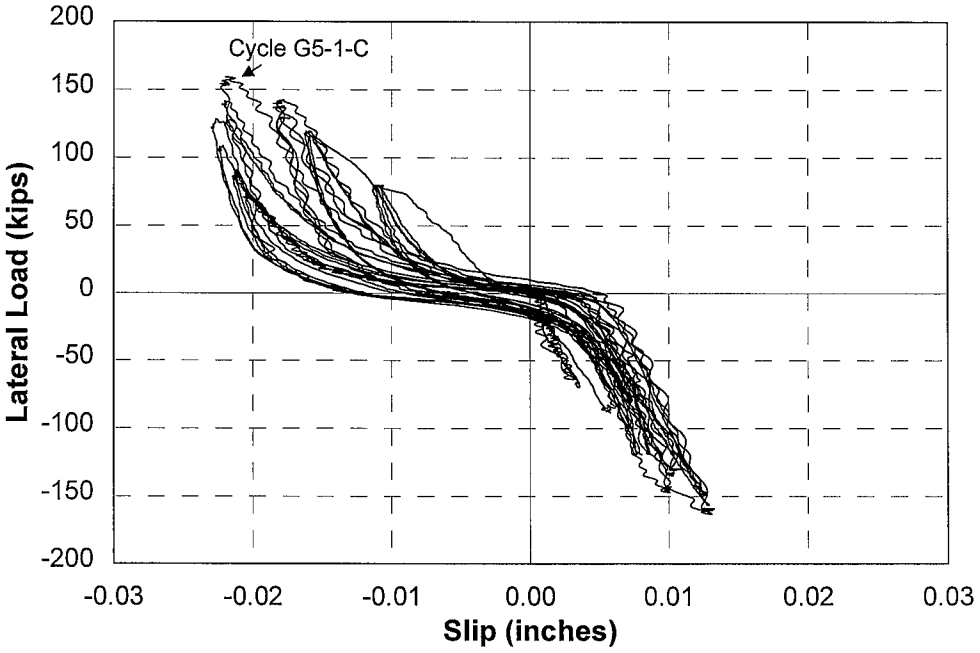

Fig. B.2.5 Slip Reading of LVDT L_SL_NI_1

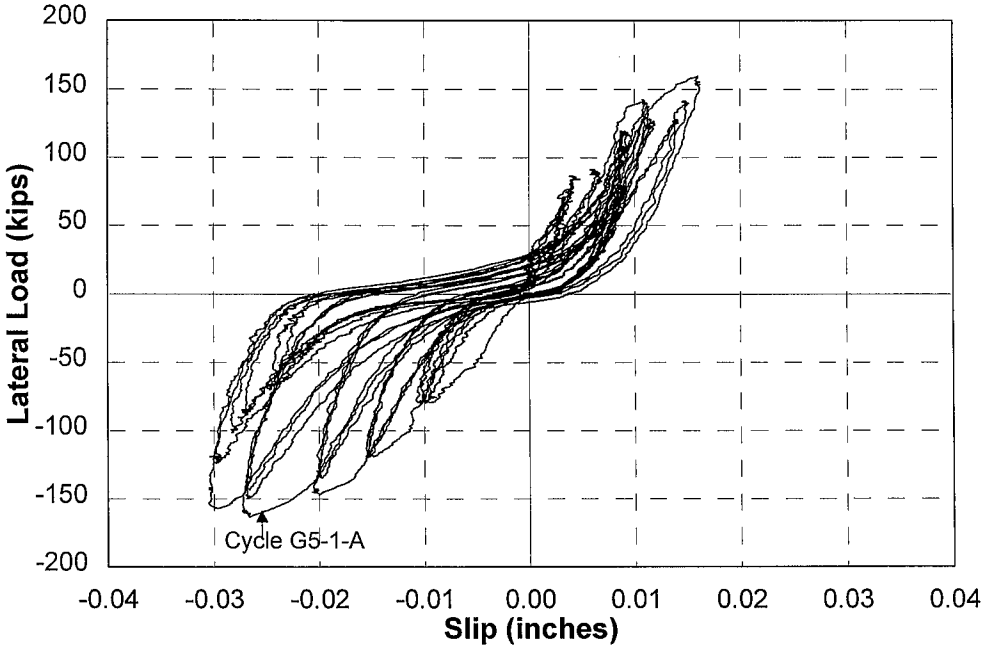

Fig. B.2.6 Slip Reading of LVDT L_SL_SI_1

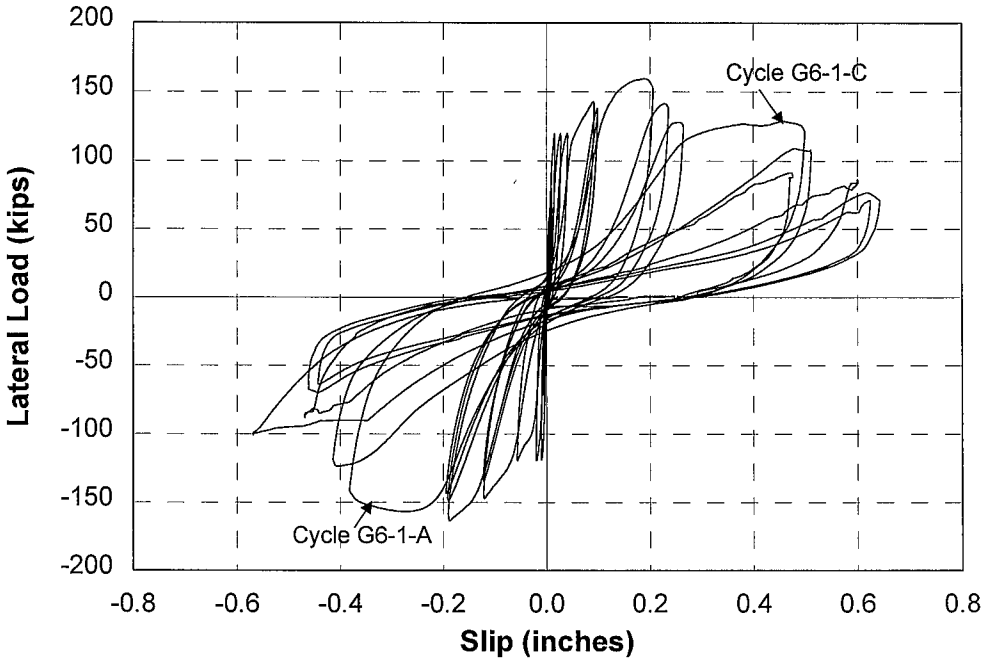

Fig. B.2.7 Slip Reading of LVDT L_SL_BII_1

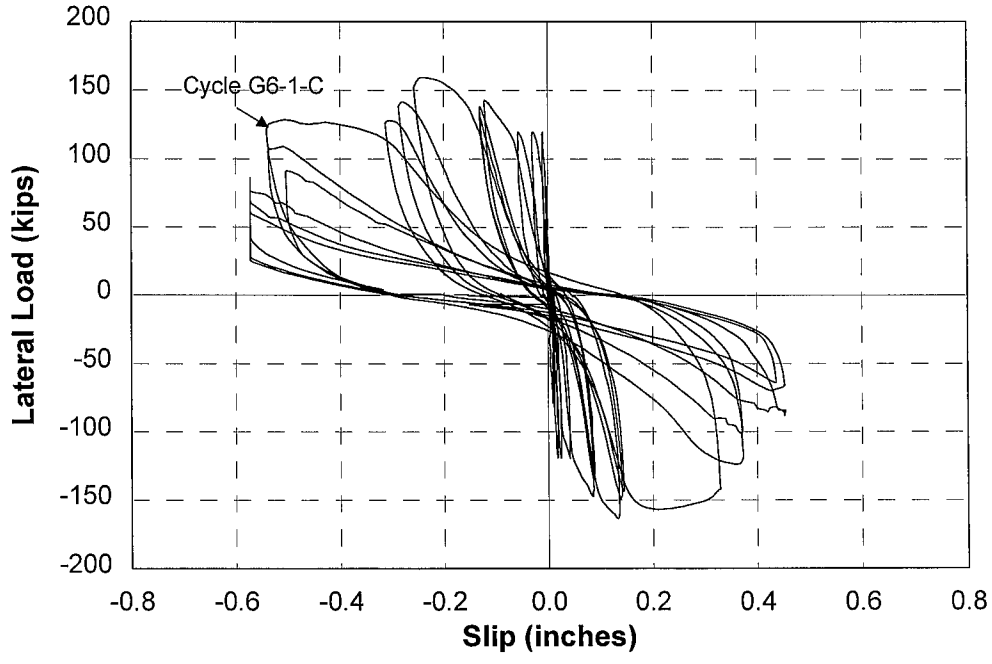

Fig. B.2.8 Slip Reading of LVDT L_SL_BII_2

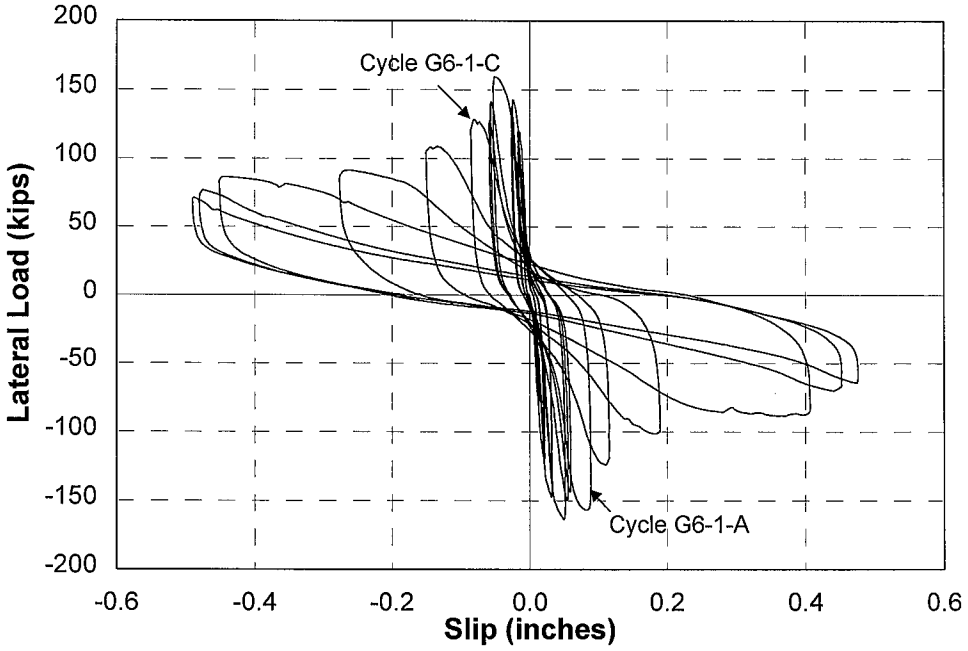

Fig. B.2.9 Slip Reading of LVDT L_SL_TII_1

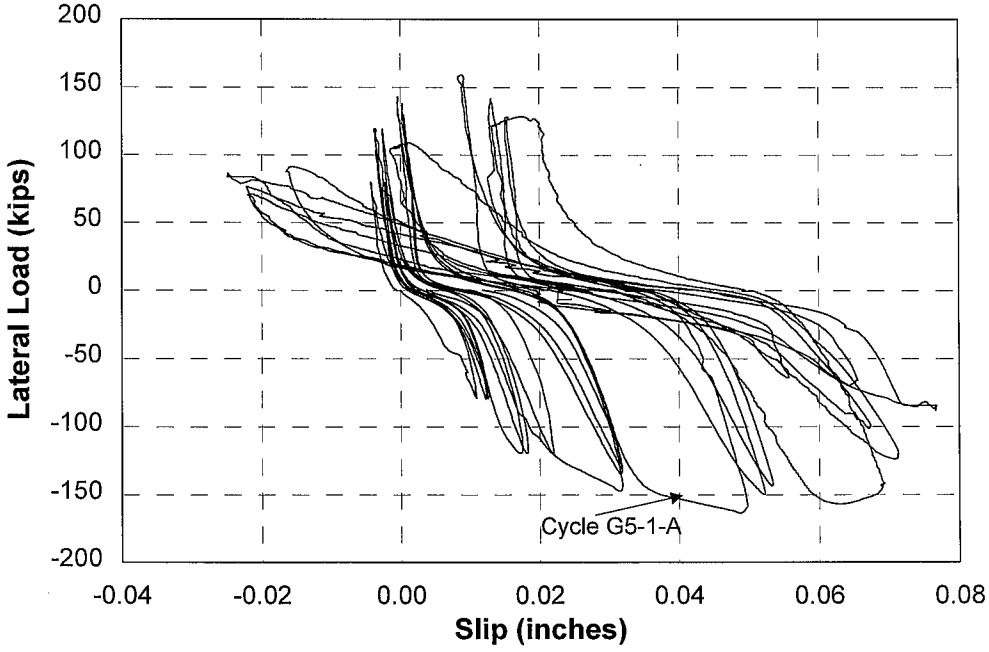

Fig. B.2.10 Slip Reading of LVDT L_SL_NII_1

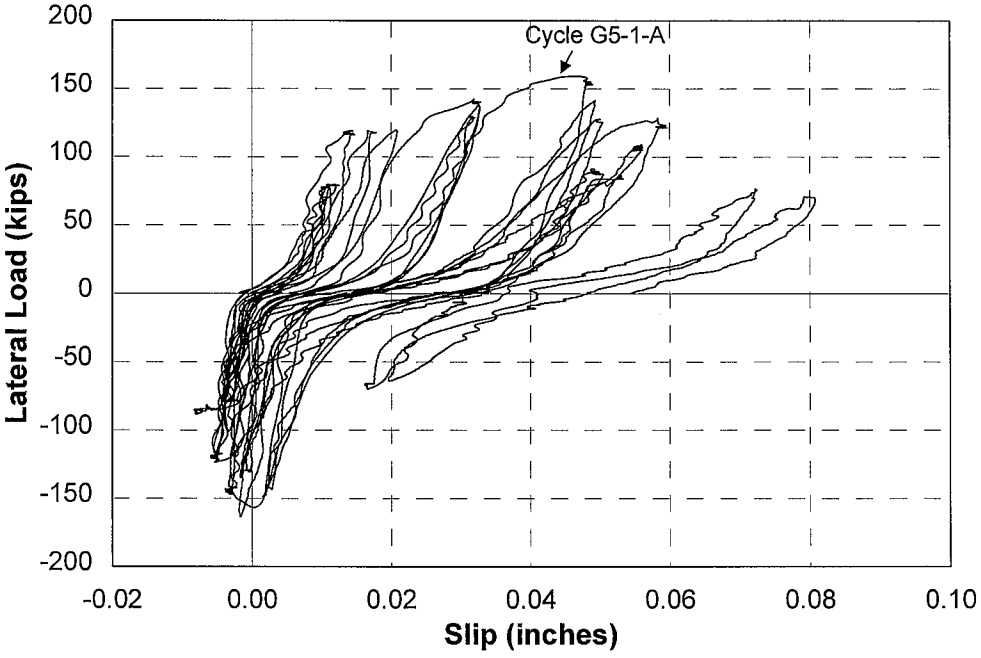

Fig. B.2.11 Slip Reading of LVDT L_SL_SII_1

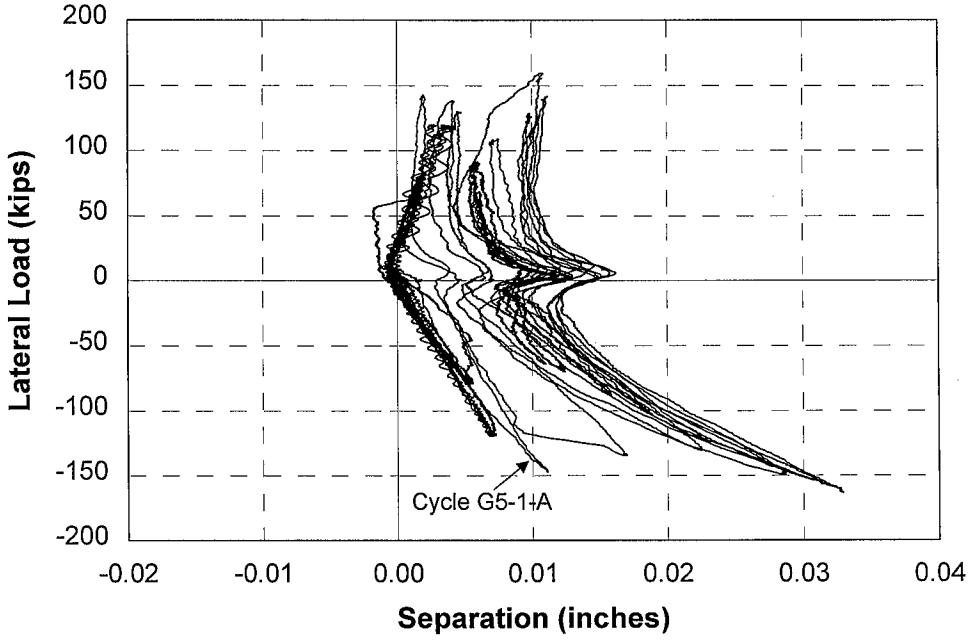

Fig. B.2.12 Separation Reading of LVDT L_SE_BI_1

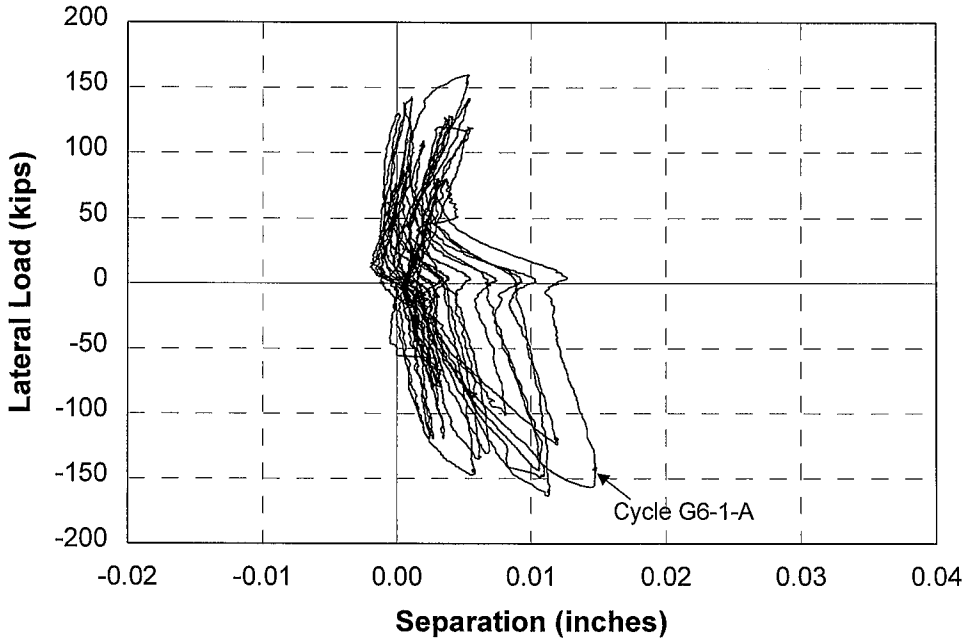

Fig. B.2.13 Separation Reading of LVDT L_SE_BI_2

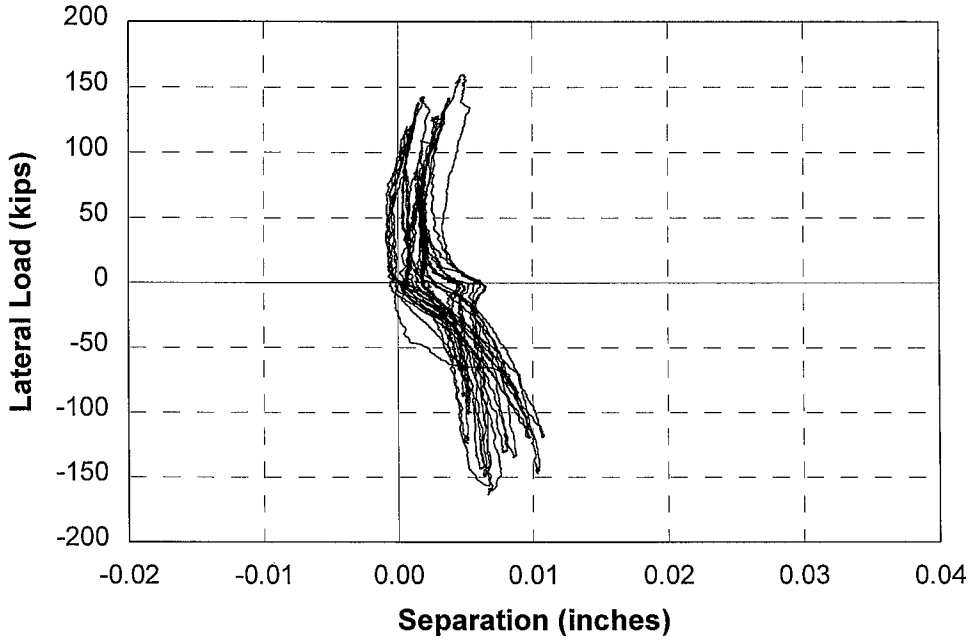

Fig. B.2.14 Separation Reading of LVDT L_SE_BI_3

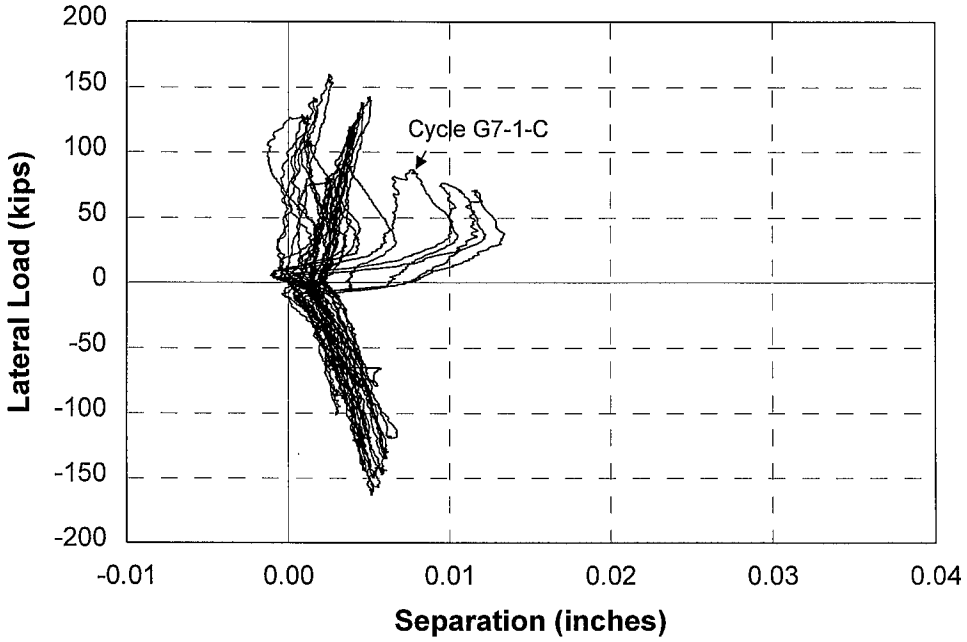

Fig. B.2.15 Separation Reading of LVDT L_SE_TI_1

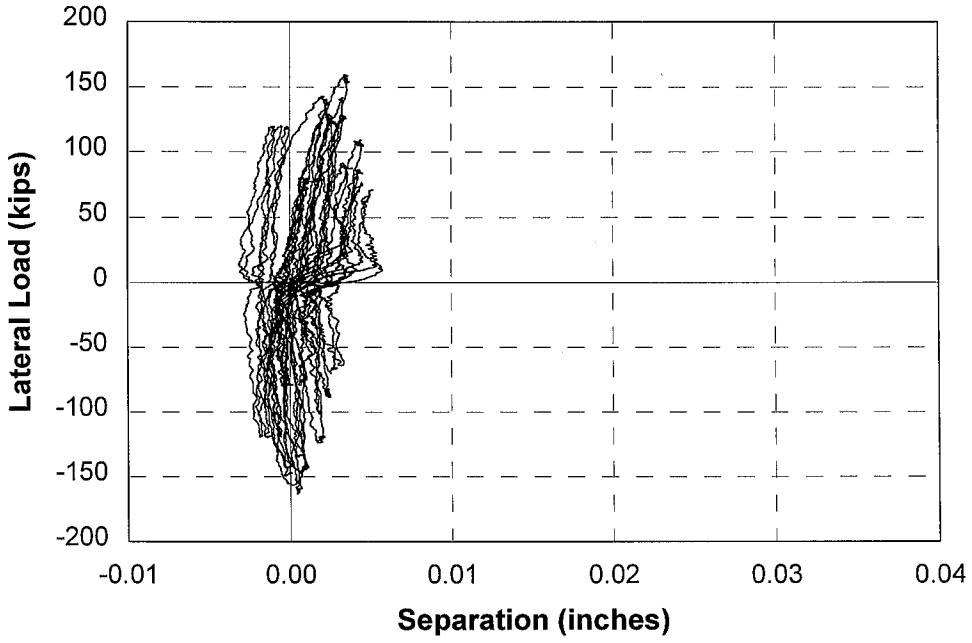

Fig. B.2.16 Separation Reading of LVDT L_SE_TI_2

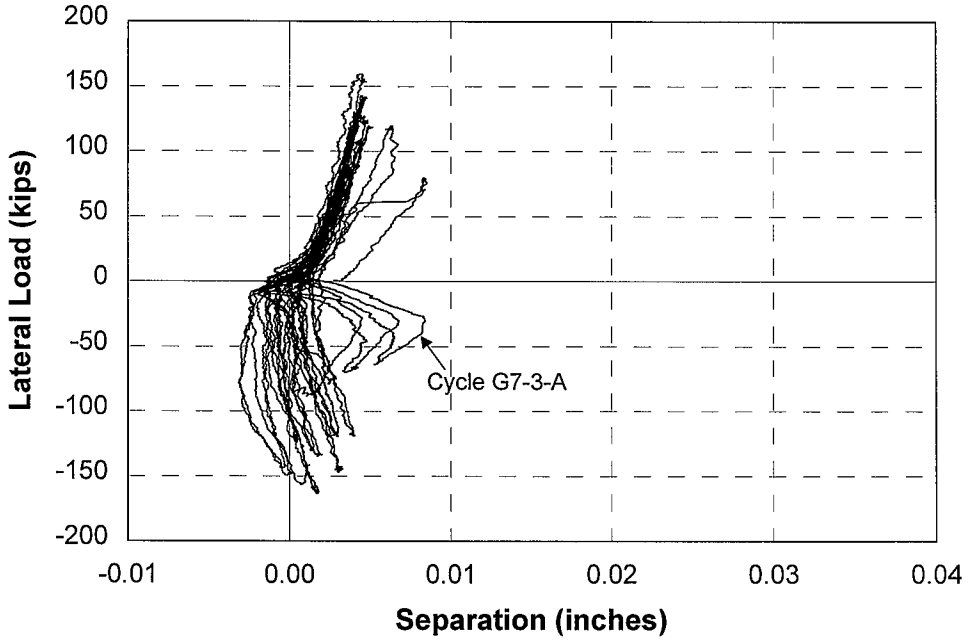

Fig. B.2.17 Separation Reading of LVDT L_SE_TI_3

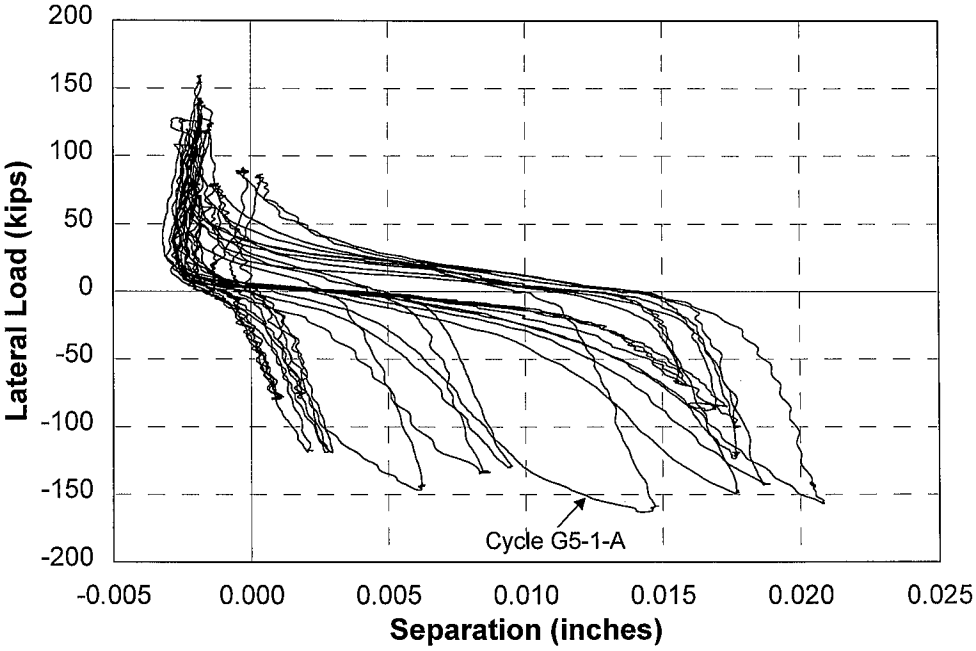

Fig. B.2.18 Separation Reading of LVDT L_SE_NI_1

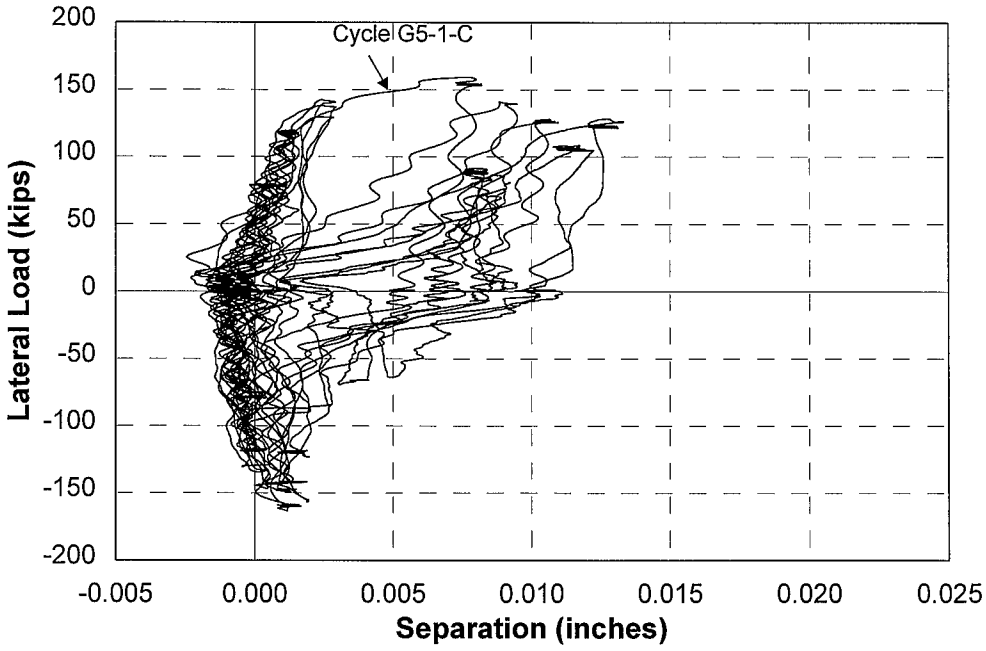

Fig. B.2.19 Separation Reading of LVDT L_SE_NI_2

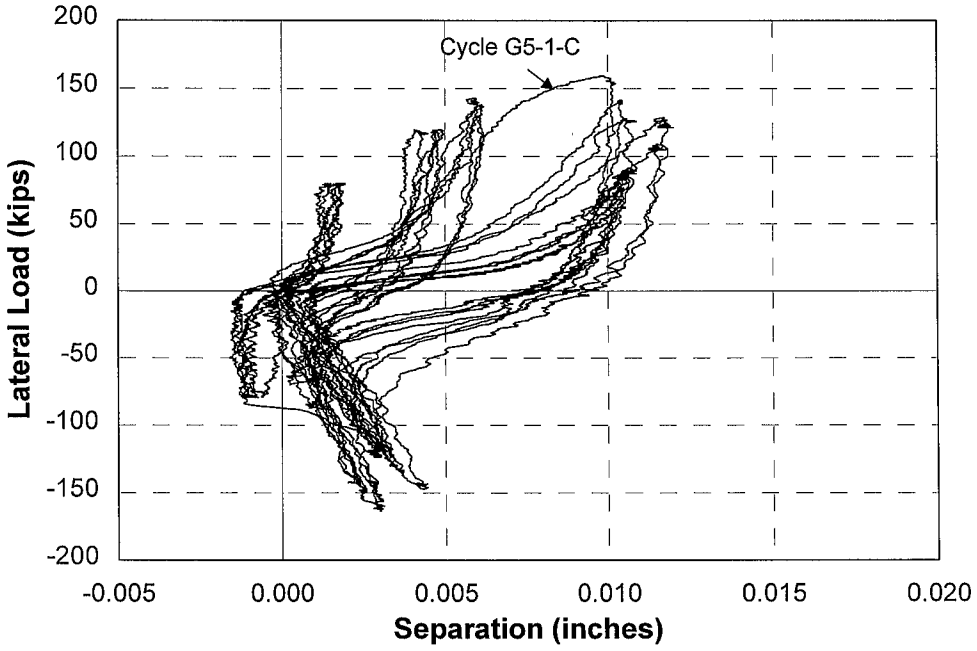

Fig. B.2.20 Separation Reading of LVDT L_SE_SI_1

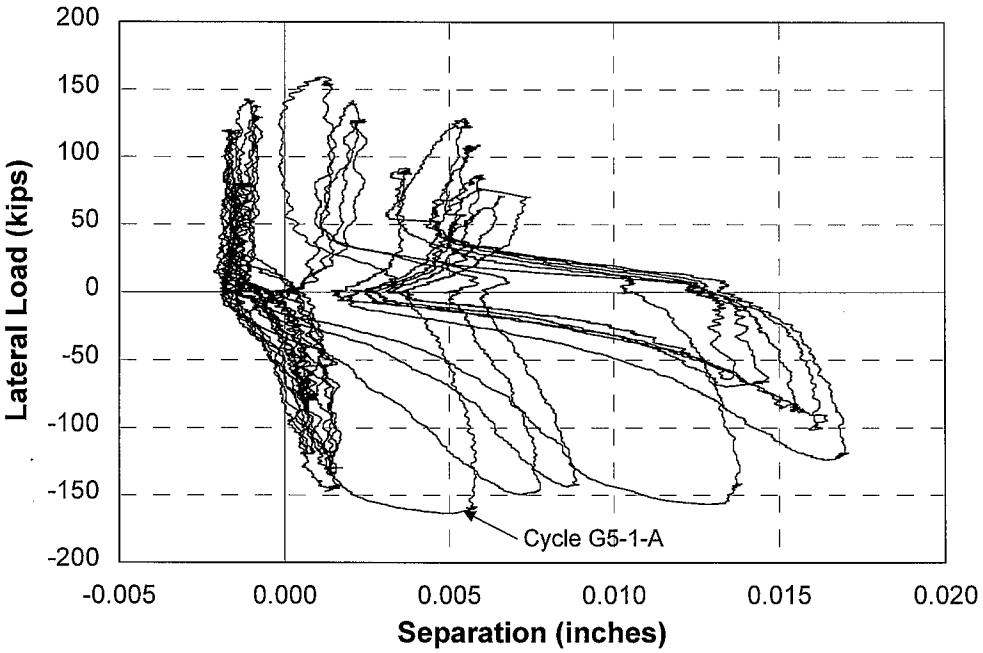

Fig. B.2.21 Separation Reading of LVDT L_SE_SI_2

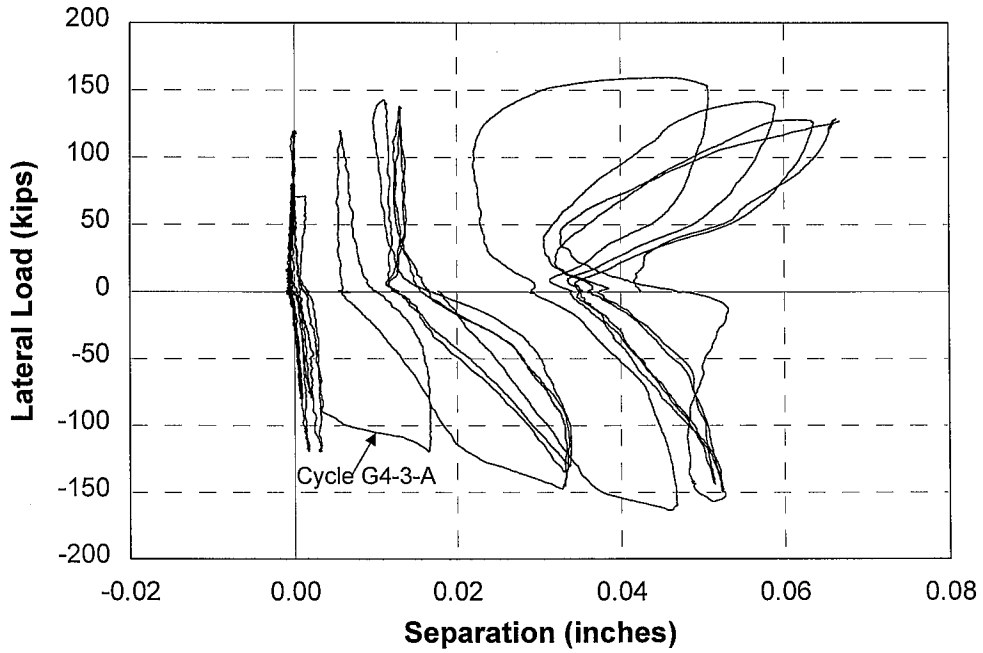

Fig. B.2.22 Separation Reading of LVDT L_SE_BII_1

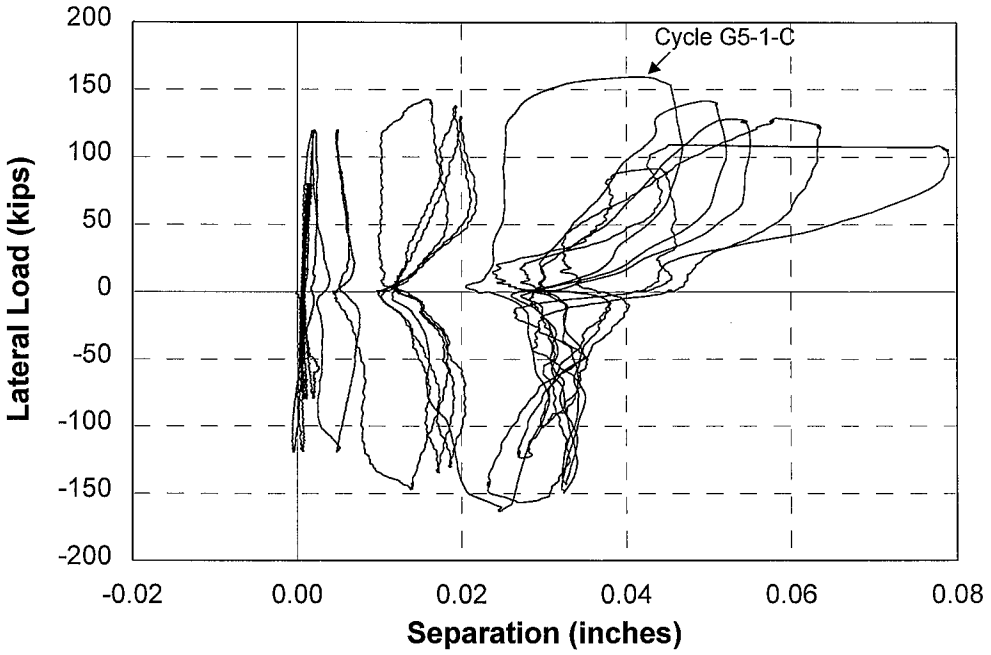

Fig. B.2.23 Separation Reading of LVDT L_SE_BII_2

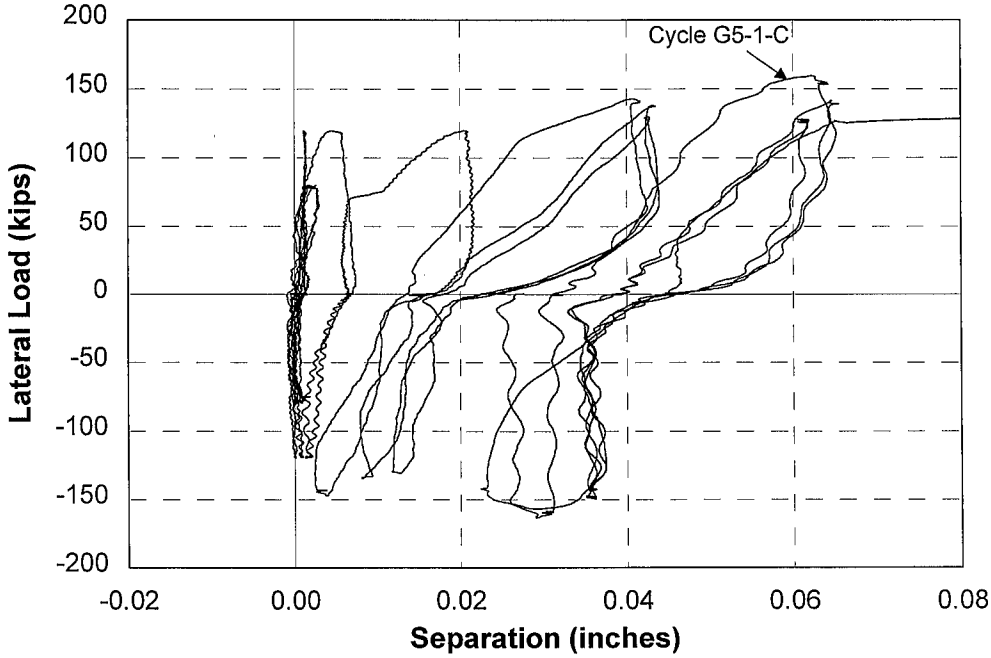

Fig. B.2.24 Separation Reading of LVDT L_SE_BII_3

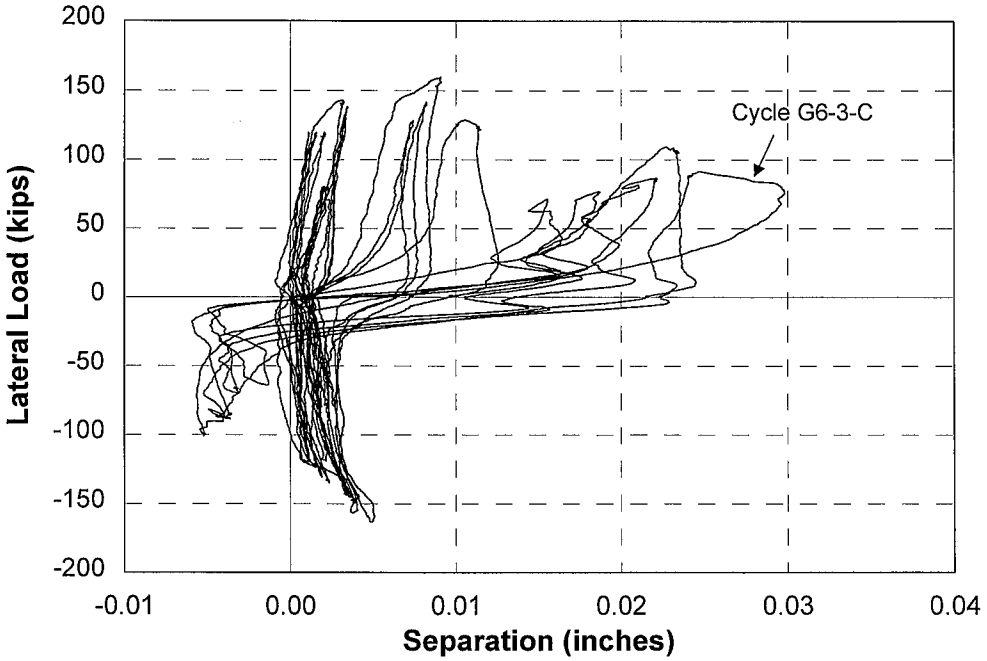

Fig. B.2.25 Separation Reading of LVDT L_SE_TII_1

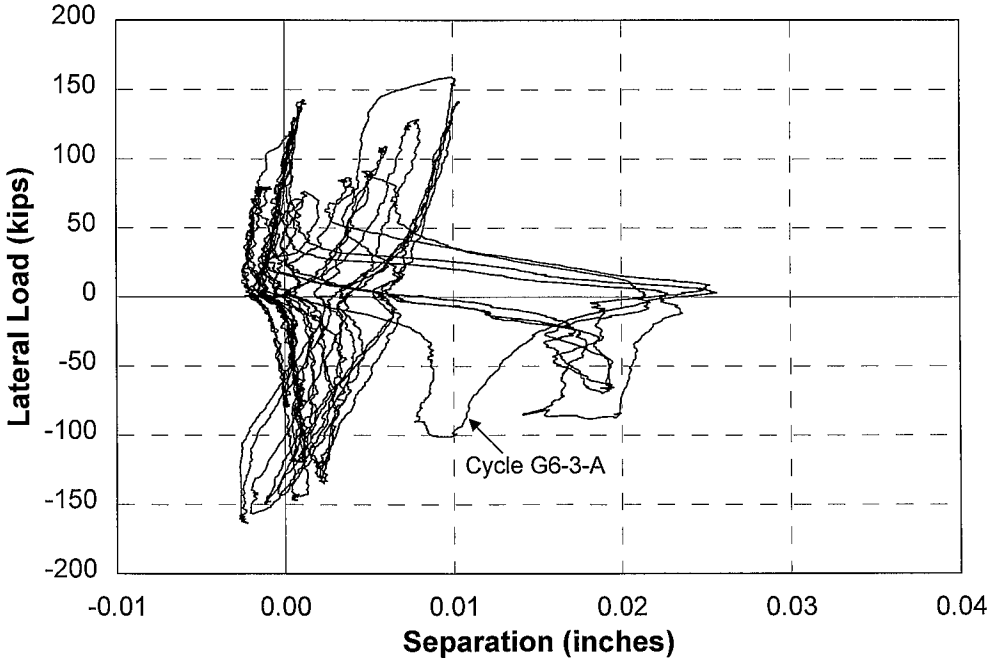

Fig. B.2.26 Separation Reading of LVDT L_SE_TII_2

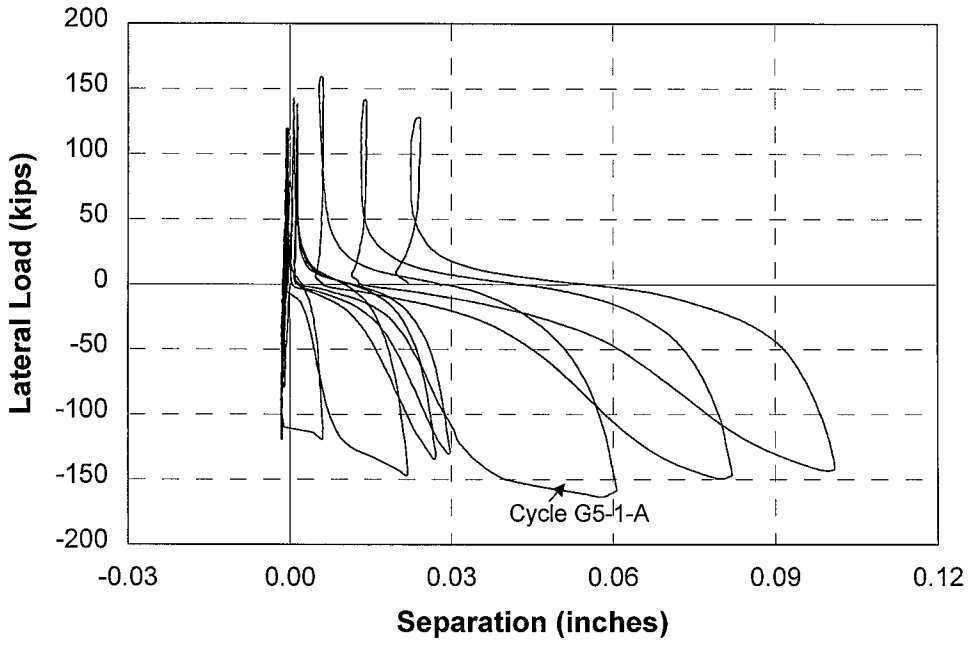

Fig. B.2.27 Separation Reading of LVDT L_SE_NII_1

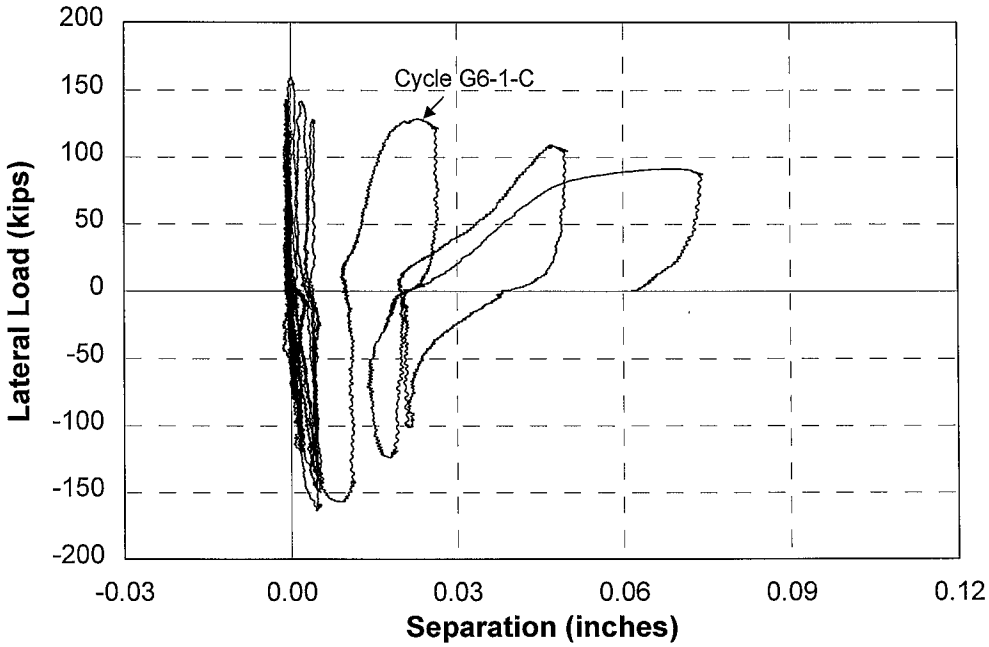

Fig. B.2.28 Separation Reading of LVDT L_SE_NII_2

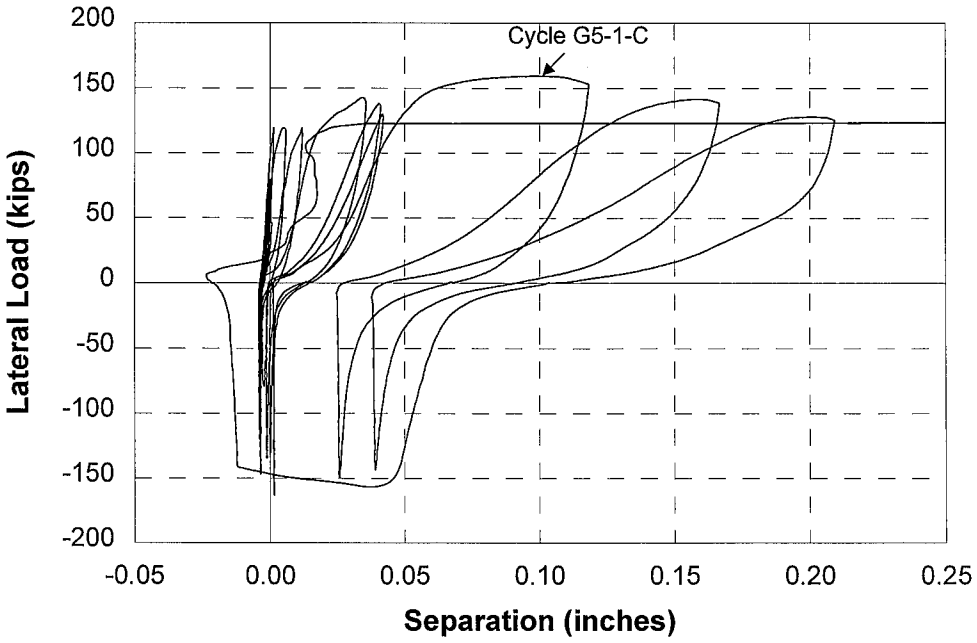

Fig. B.2.29 Separation Reading of LVDT L_SE_SII_1

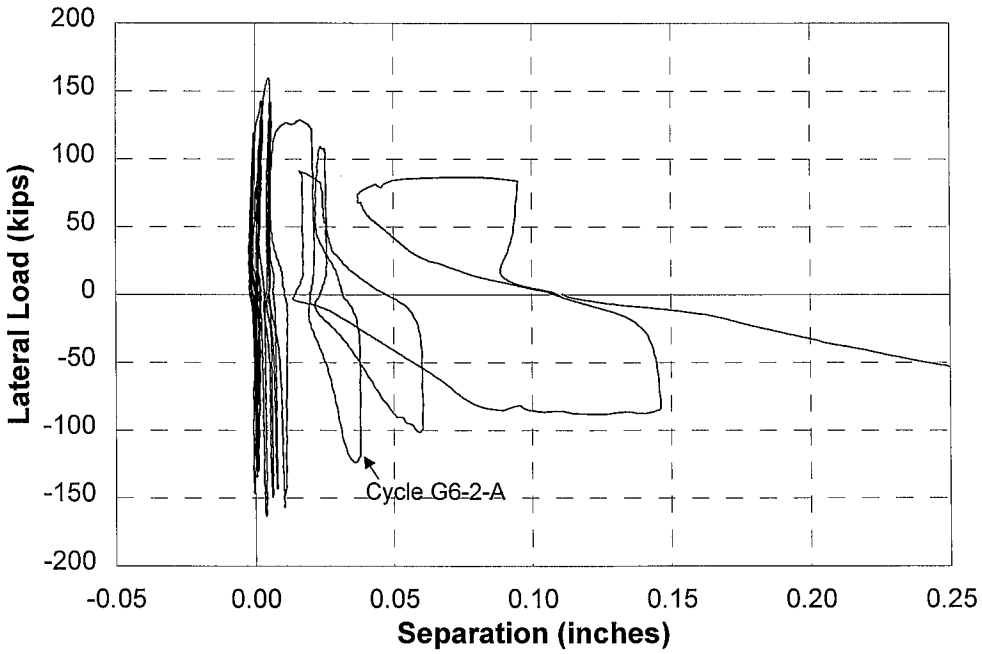

Fig. B.2.30 Seperation Reading of LVDT L_SE_SII_2

Appendix B.3 Stud Strain Gages

Appendix B.3 documents the readings of the strain gages placed at the base portion of the headed studs. The locations of these gaged headed studs are shown in Figure 3.4.4. Each stud had two strain gages placed on the opposite sides of the shaft, and the readings of these two gages are plotted versus time in the same figure.

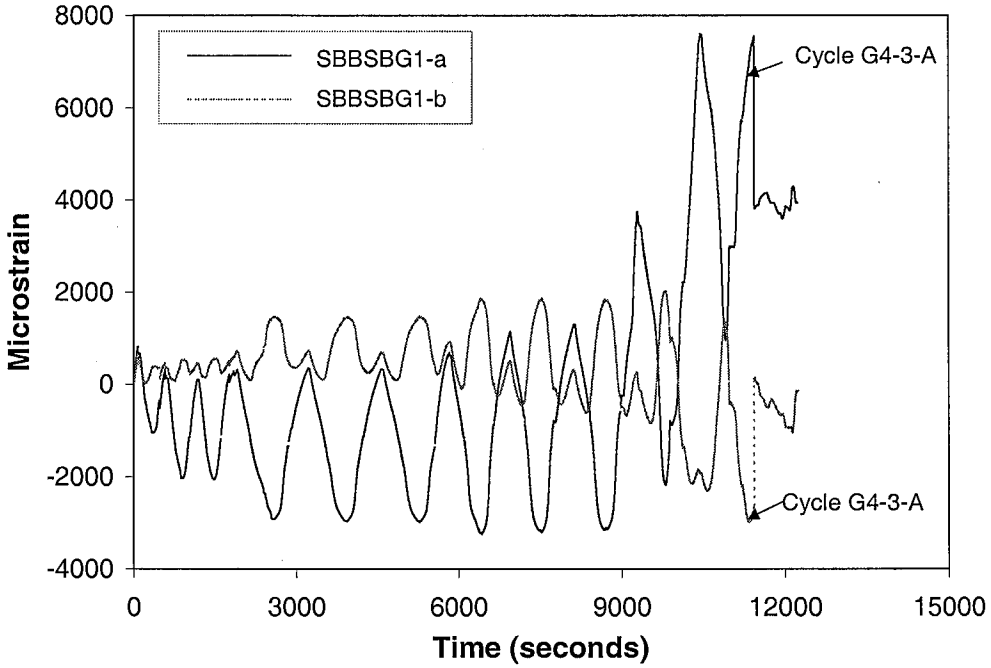

Fig. B.3.1 Strain Reading of Stud Gage SBBSBG1-a and SBBSBG1-b

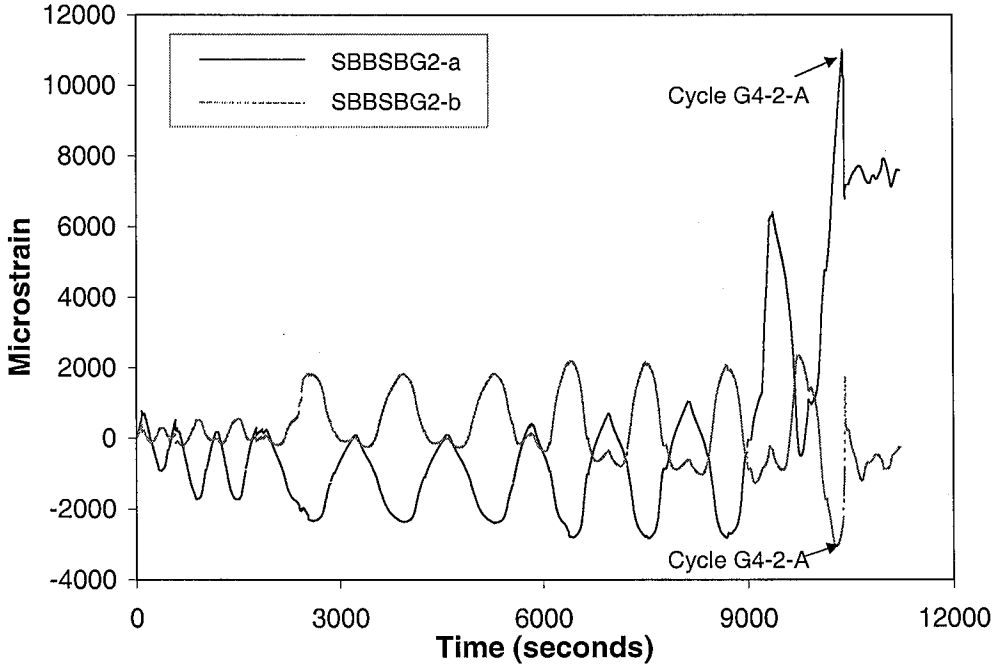

Fig. B.3.2 Strain Reading of Stud Gage SBBSBG2-a and SBBSBG2-b

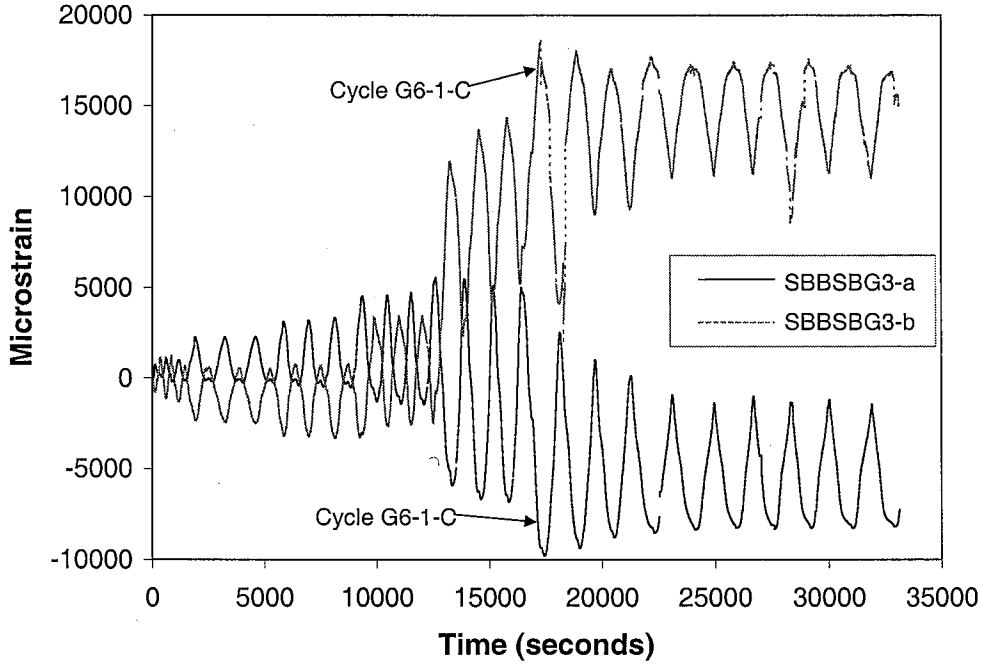

Fig. B.3.3 Strain Reading of Stud Gage SBBSBG3-a and SBBSBG3-b

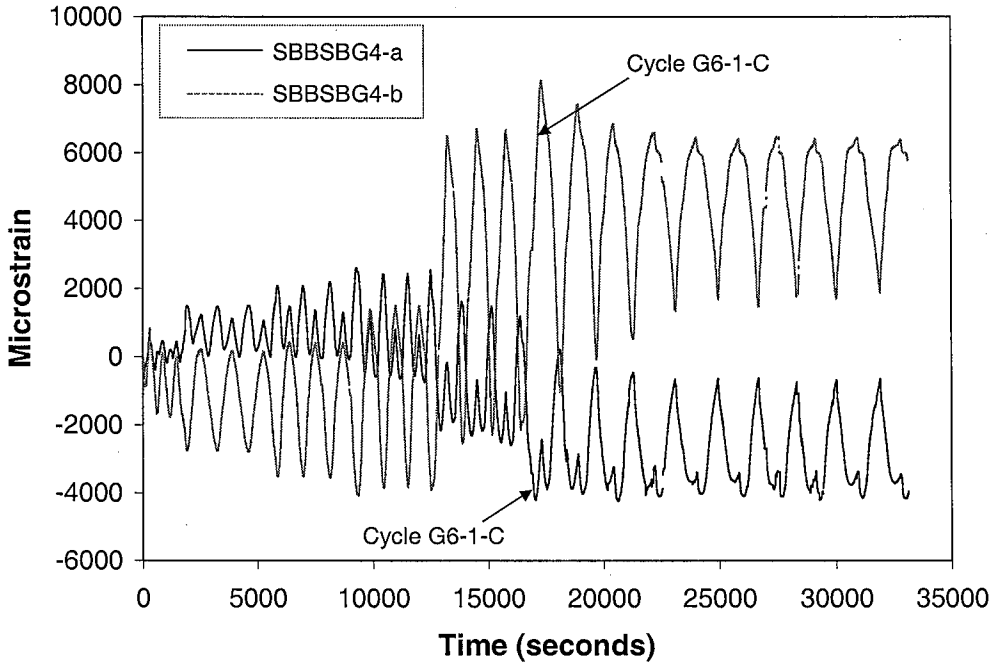

Fig. B.3.4 Strain Reading of Stud Gage SBBSBG4-a and SBBSBG4-b

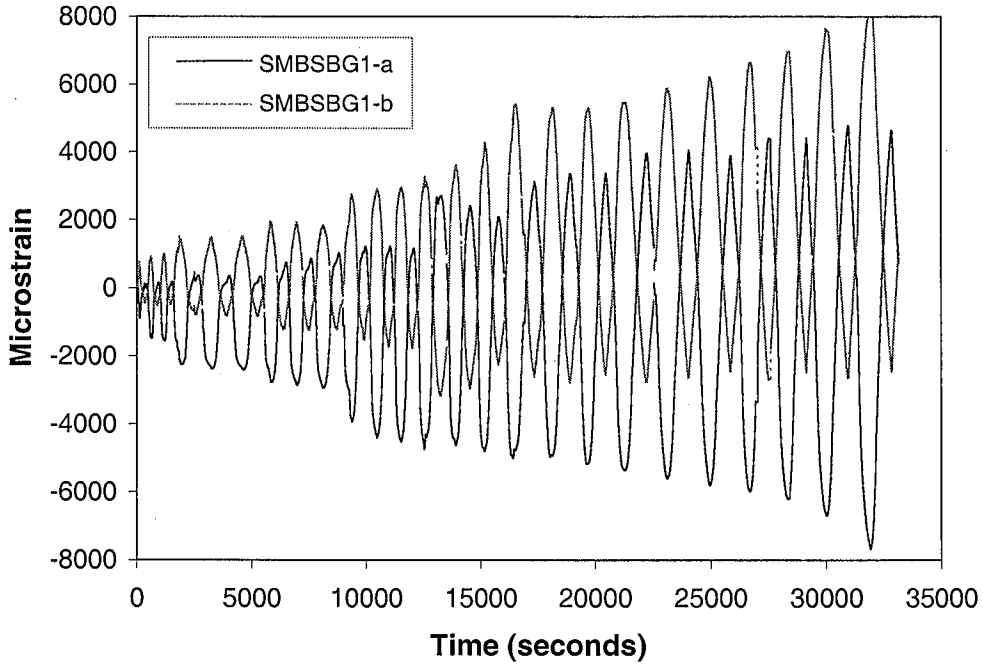

Fig. B.3.5 Strain Reading of Stud Gage SMBSBG1-a and SMBSBG1-b

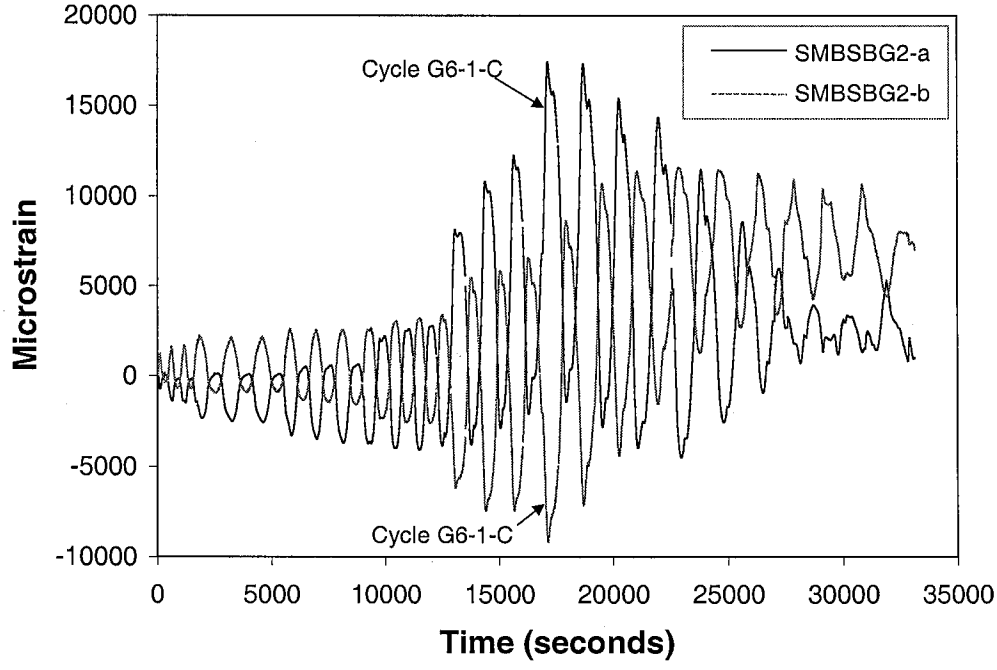

Fig. B.3.6 Strain Reading of Stud Gage SMBSBG2-a and SMBSBG2-b

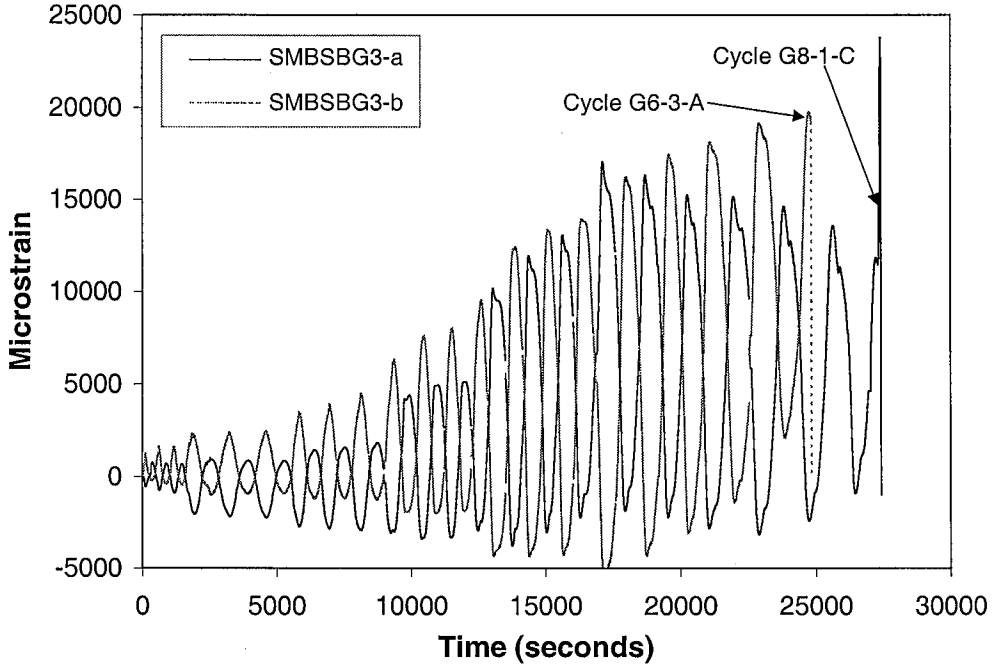

Fig. B.3.7 Strain Reading of Stud Gage SMBSBG3-a and SMBSBG3-b

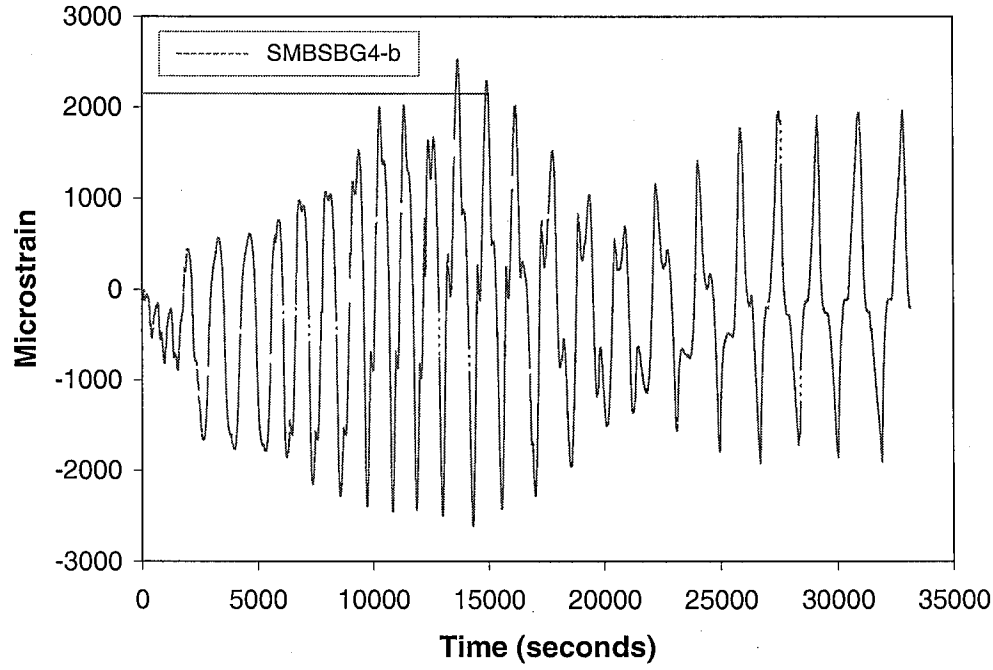

Fig. B.3.8 Strain Reading of Stud Gage SMBSBG4-a and SMBSBG4-b

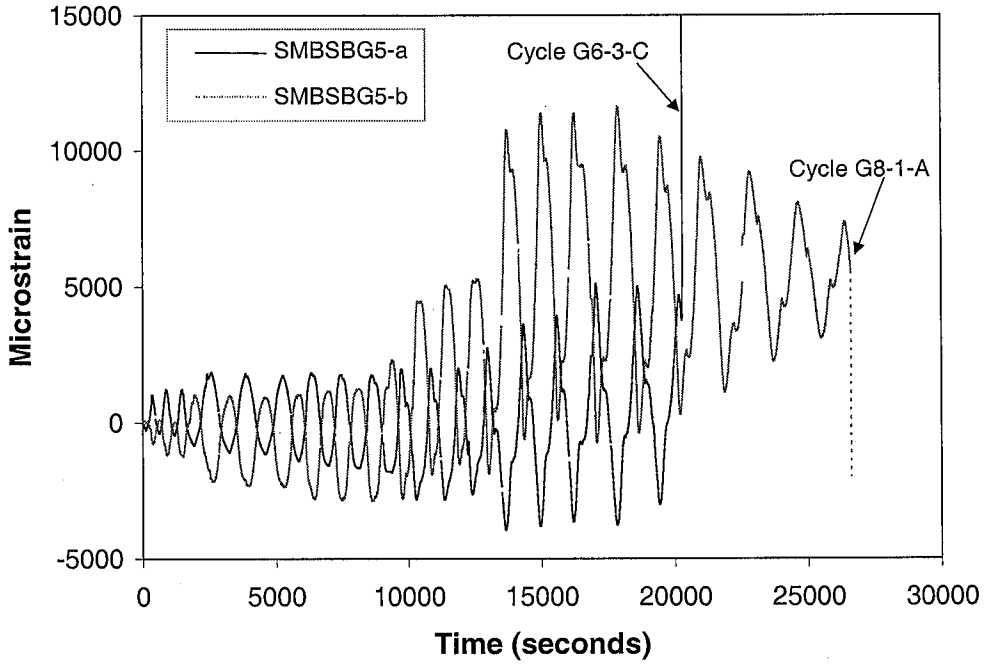

Fig. B.3.9 Strain Reading of Stud Gage SMBSBG5-a and SMBSBG5-b

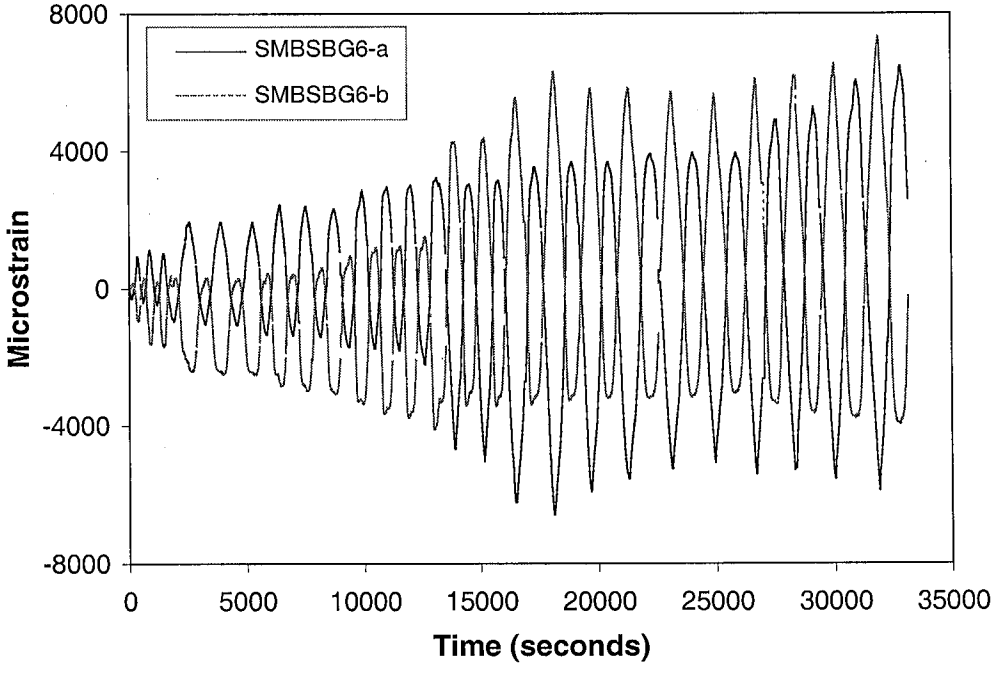

Fig. B.3.10 Strain Reading of Stud Gage SMBSBG6-a and SMBSBG6-b

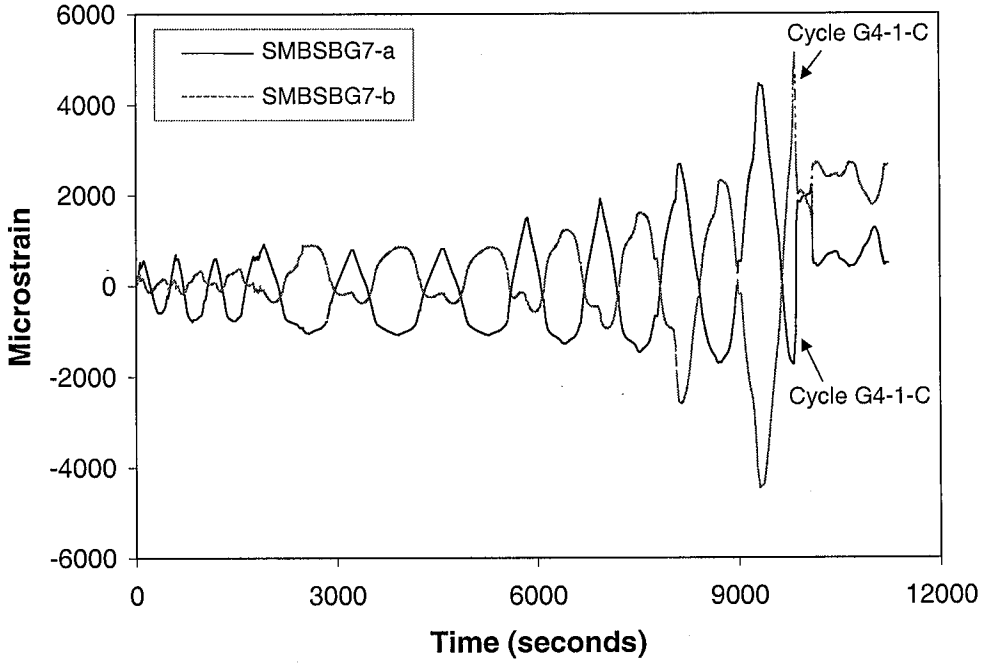

Fig. B.3.11 Strain Reading of Stud Gage SMBSBG7-a and SMBSBG7-b

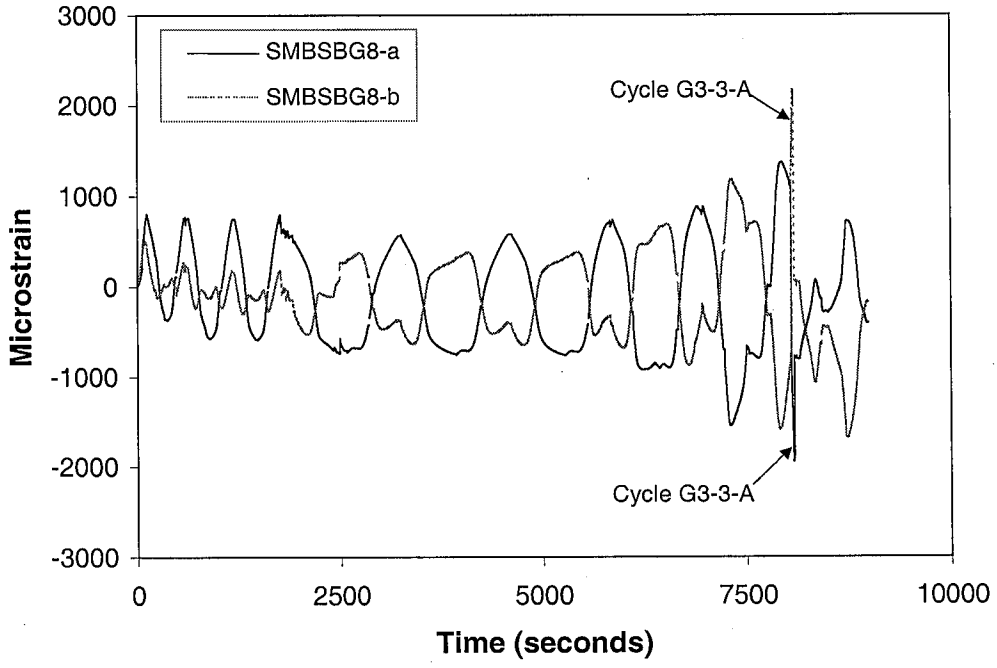

Fig. B.3.12 Strain Reading of Stud Gage SMBSBG8-a and SMBSBG8-b

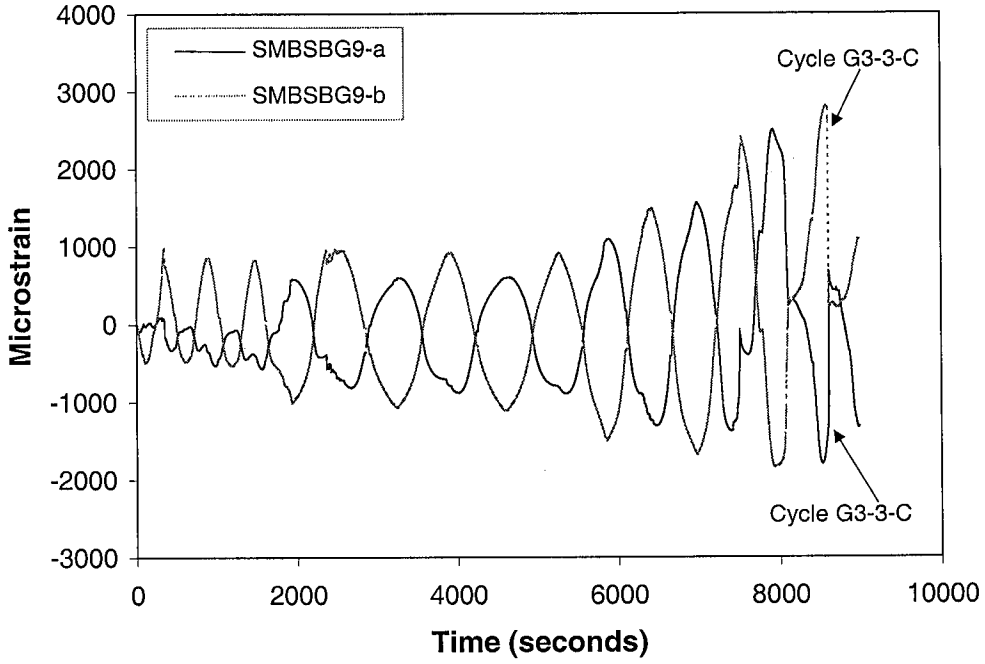

Fig. B.3.13 Strain Reading of Stud Gage SMBSBG9-a and SMBSBG9-b

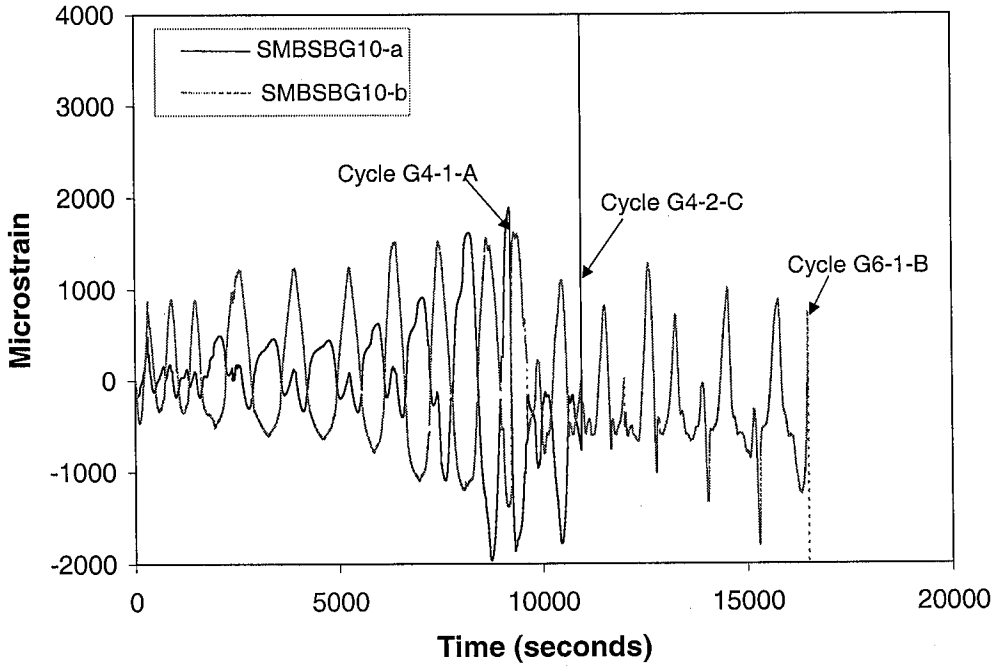

Fig. B.3.14 Strain Reading of Stud Gage SMBSBG10-a and SMBSBG10-b

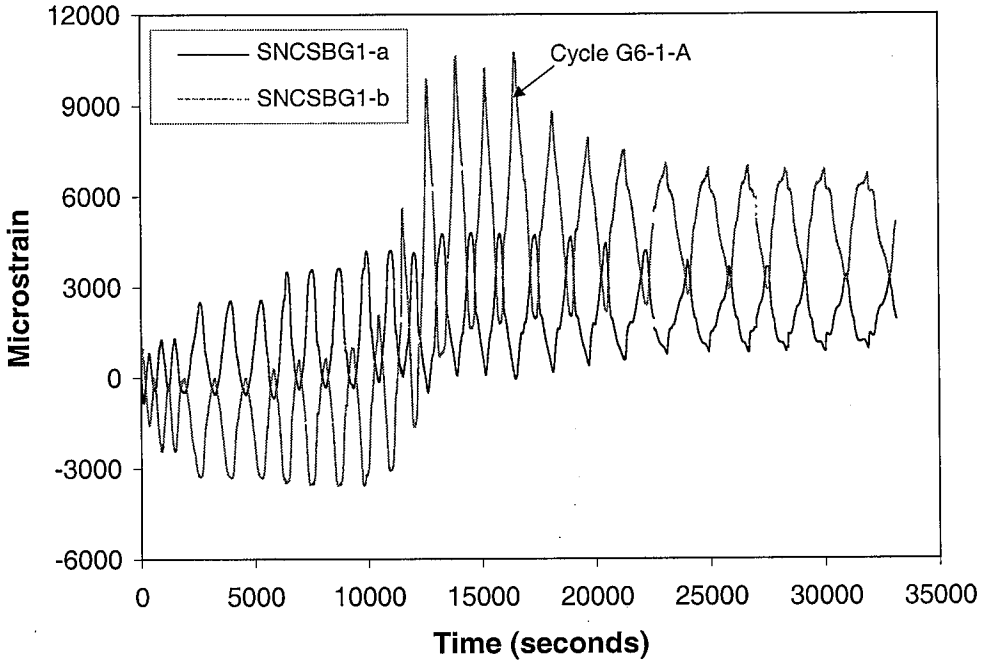

Fig. B.3.15 Strain Reading of Stud Gage SNCSBG1-a and SNCSBG1-b

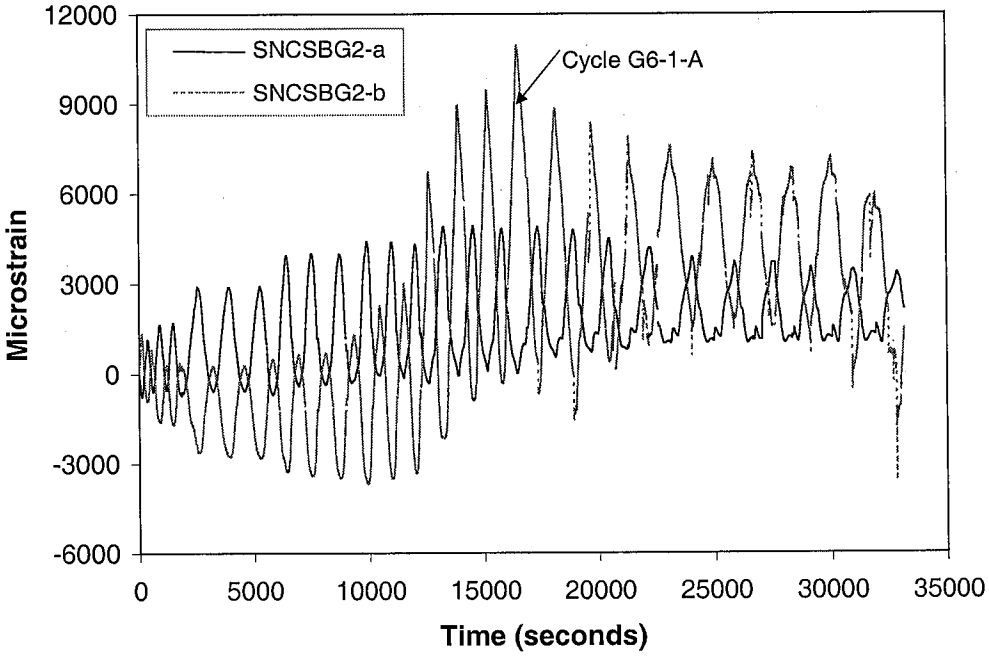

Fig. B.3.16 Strain Reading of Stud Gage SNCSBG2-a and SNCSBG2-b

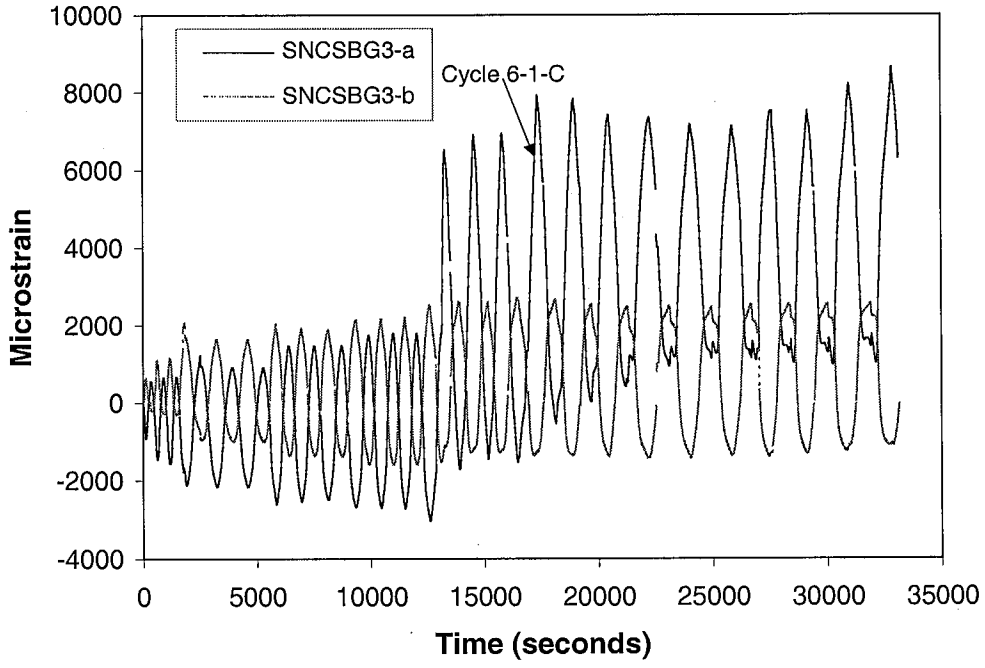

Fig. B.3.17 Strain Reading of Stud Gage SNCSBG3-a and SNCSBG3-b

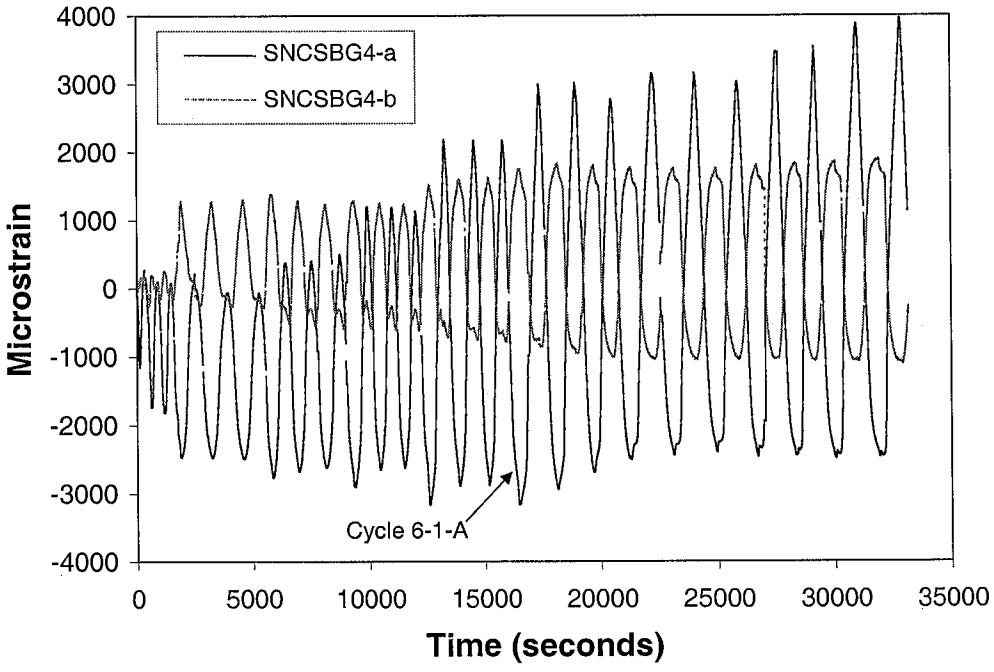

Fig. B.3.18 Strain Reading of Stud Gage SNCSBG4-a and SNCSBG4-b

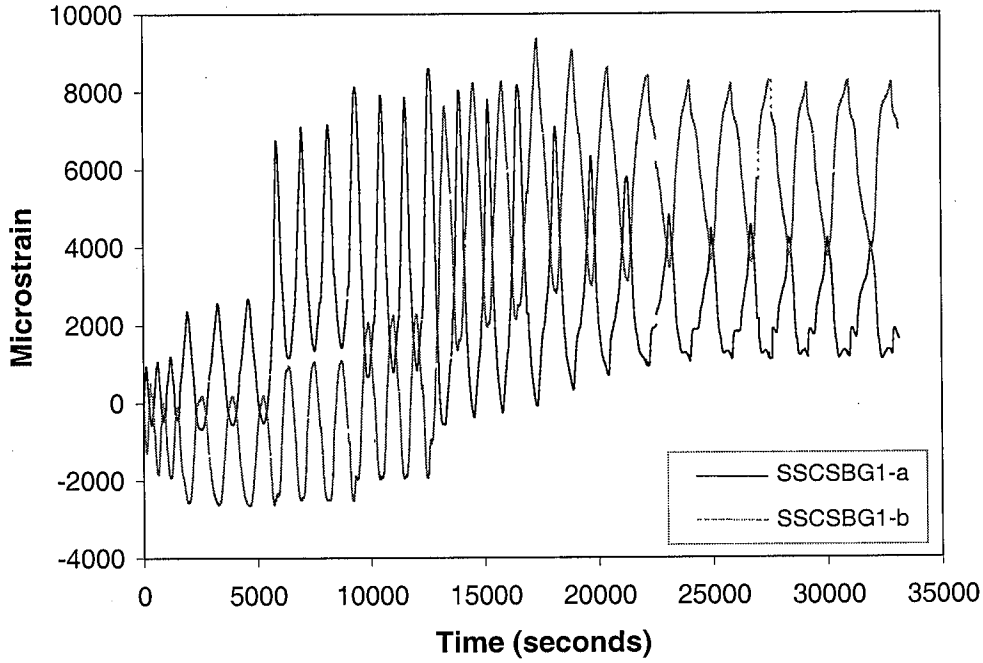

Fig. B.3.19 Strain Reading of Stud Gage SSCSBG1-a and SSCSBG1-b

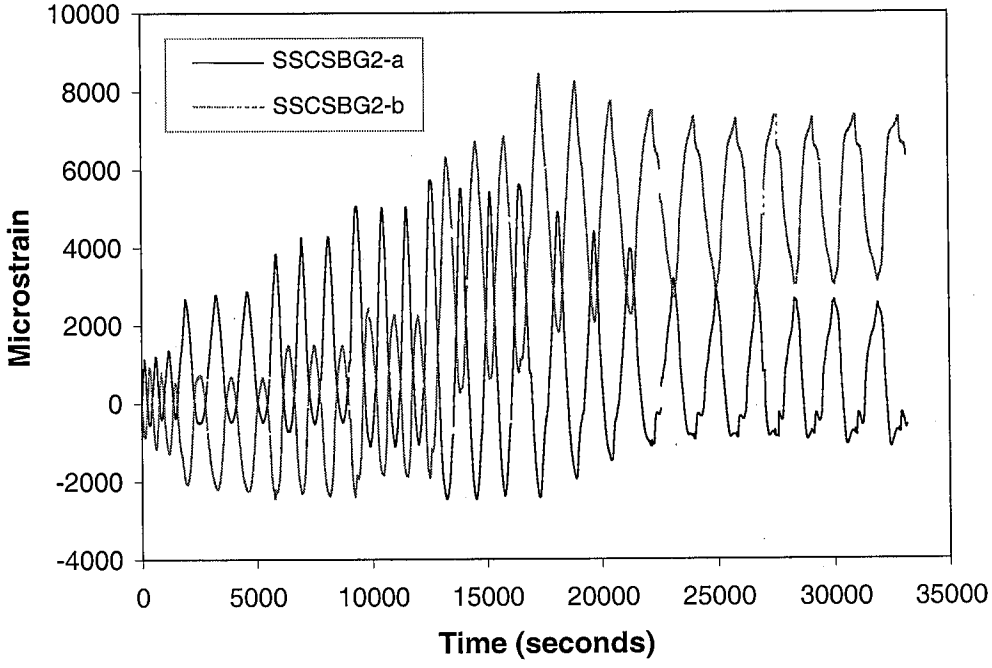

Fig. B.3.20 Strain Reading of Stud Gage SSCSBG2-a and SSCSBG2-b

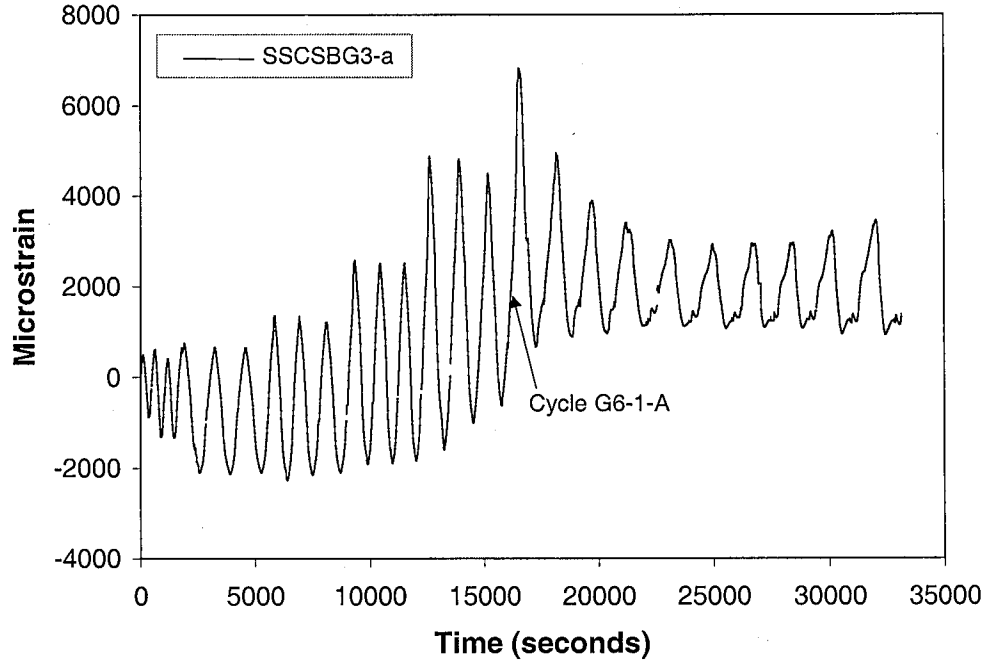

Fig. B.3.21 Strain Reading of Stud Gage SSCSBG3-a and SSCSBG3-b

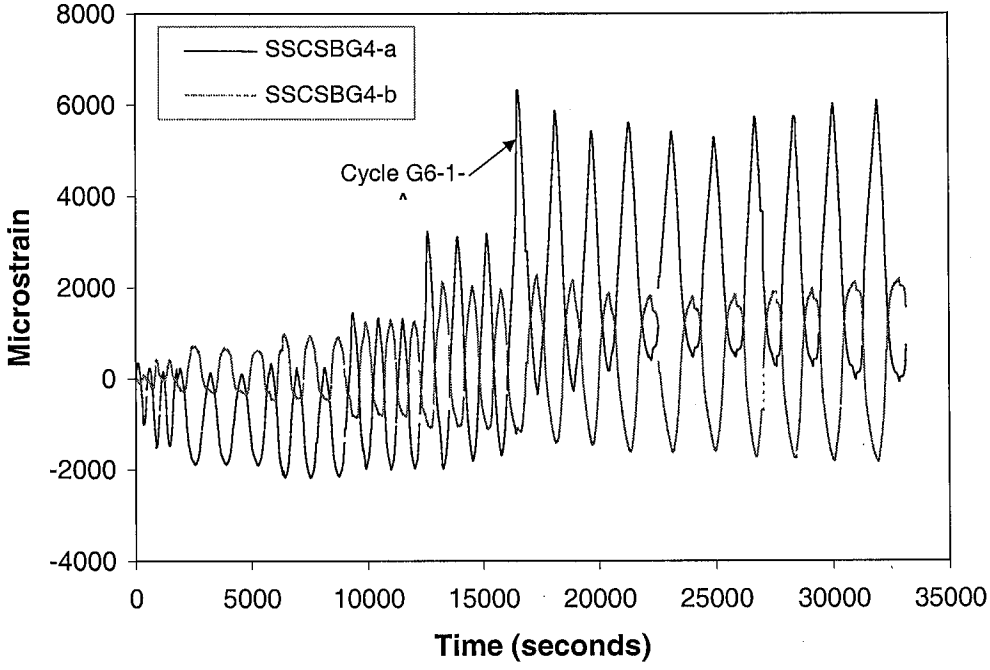

Fig. B.3.22 Strain Reading of Stud Gage SSCSBG4-a and SSCSBG4-b

Appendix B.4 Top and Seat Angle Strain Gages

Appendix B.4 documents the reading of the strain gages on the top and seat angles of the PR connections connecting the middle beam to the columns. The locations of the strain gages are shown in Figure 3.4.8. For each top or seat angle, there were two gages placed in the k-line regions of the opposite sides of the horizontal leg, and there was one gage placed in the k-line region of the vertical leg. The strain is plotted versus the lateral load history in each figure.

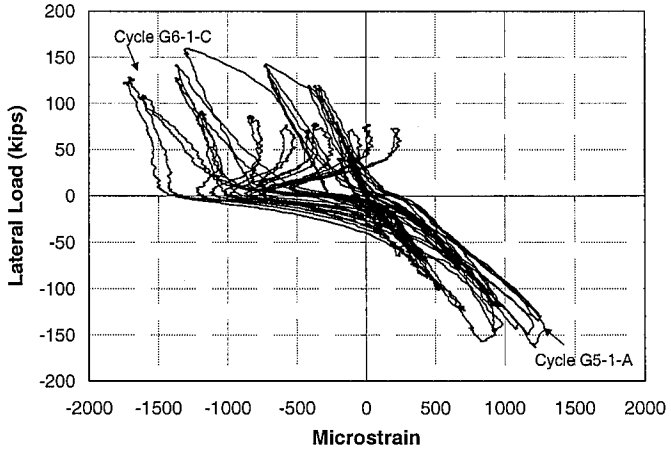

Fig. B.4.1 Reading of Strain Gage A_NJ_BA_G1

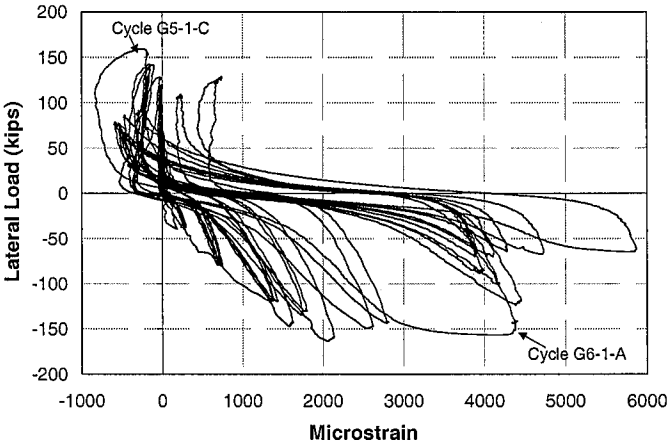

Fig. B.4.2 Reading of Strain Gage A_NJ_BA_G2

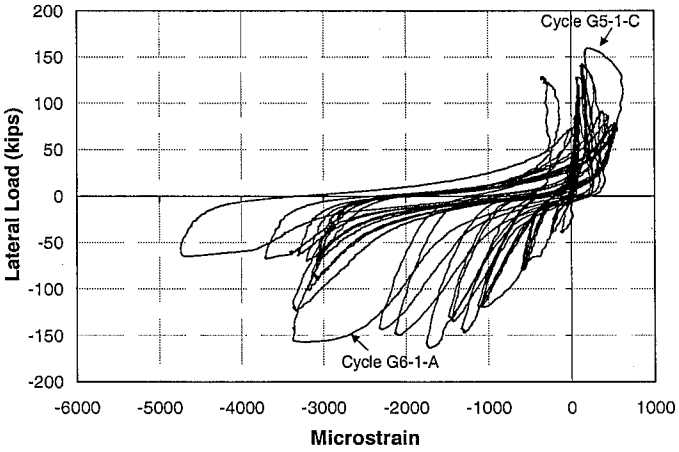

Fig.B.4.3 Reading of Strain Gage A_NJ_BA_G3

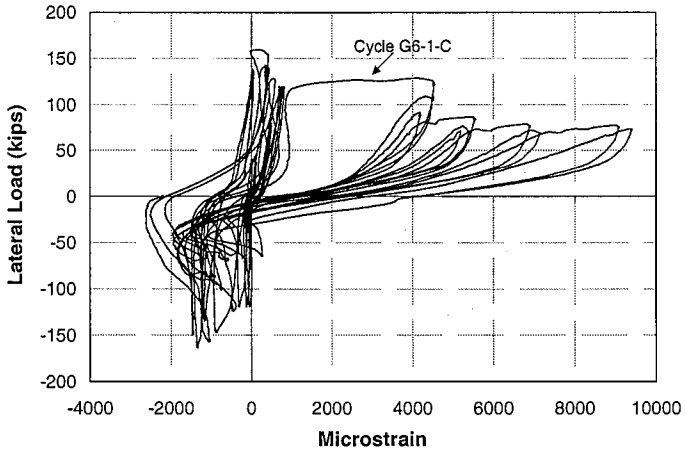

Fig. B.4.4 Reading of Strain Gage A_NJ_TA_G1

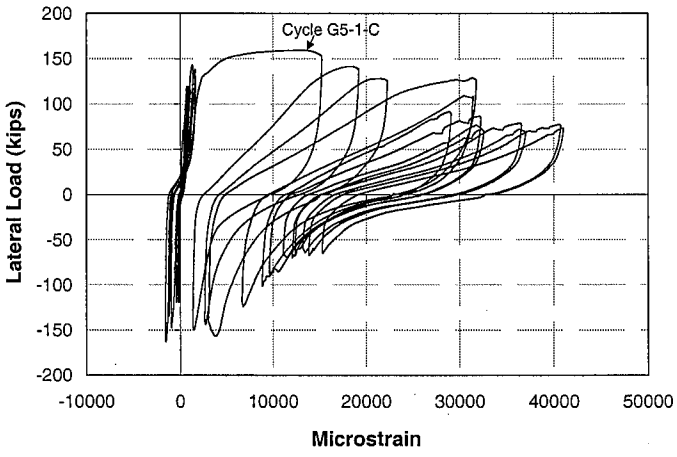

Fig. B.4.5 Reading of Strain Gage A_NJ_TA_G2

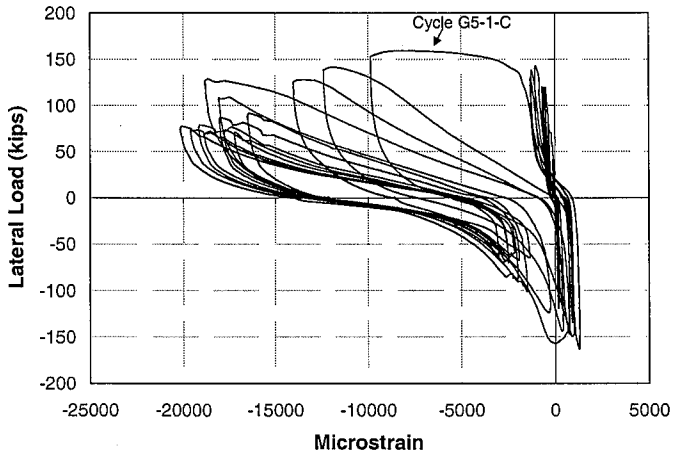

Fig. B.4.6 Reading of Strain Gage A_NJ_TA_G3

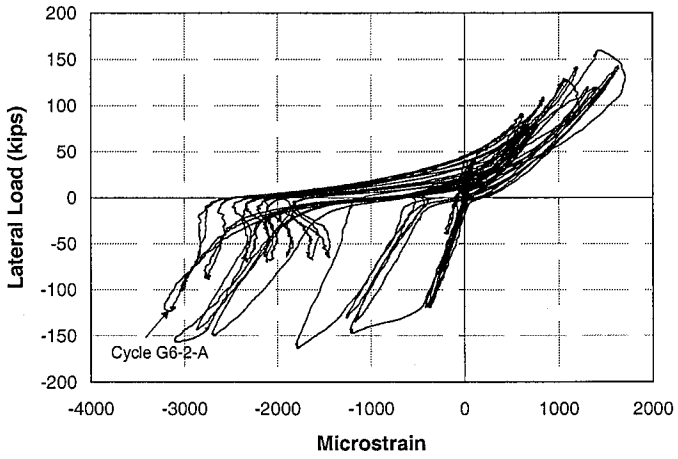

Fig. B.4.7 Reading of Strain Gage A_SJ_BA_G1

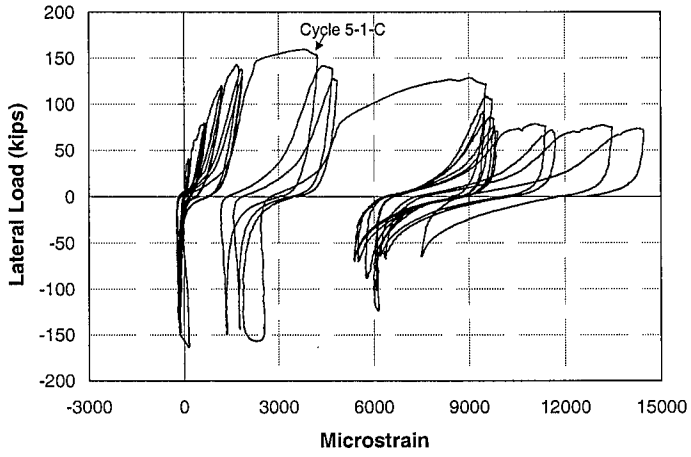

Fig. B.4.8 Reading of Strain Gage A_SJ_BA_G2

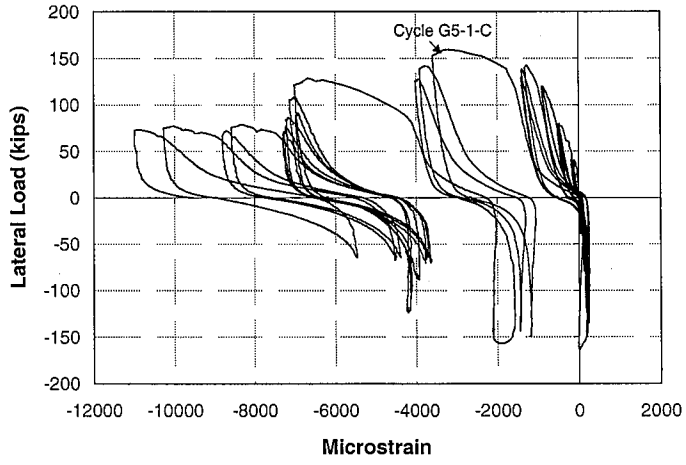

Fig. B.4.9 Reading of Strain Gage A_SJ_BA_G3

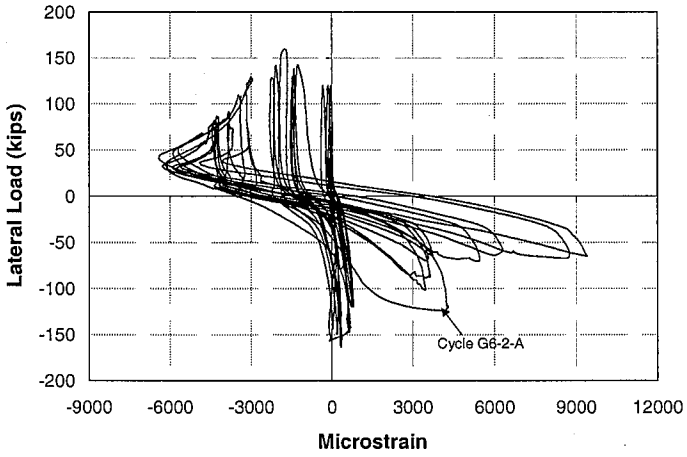

Fig. B.4.10 Reading of Strain Gage A_SJ_TA_G1

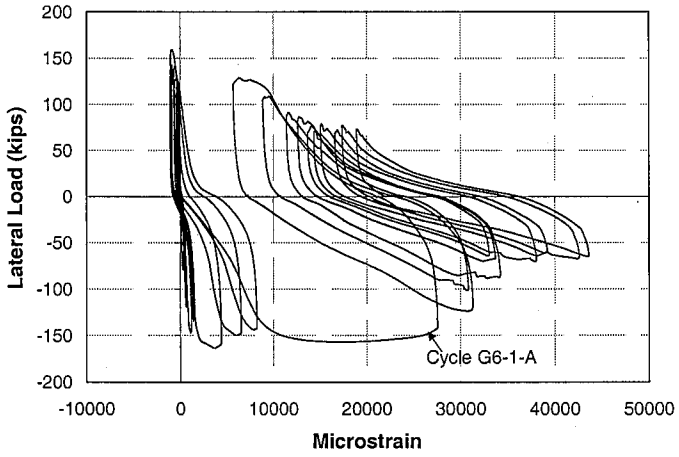

Fig. B.4.11 Reading of Strain Gage A_SJ_TA_G2

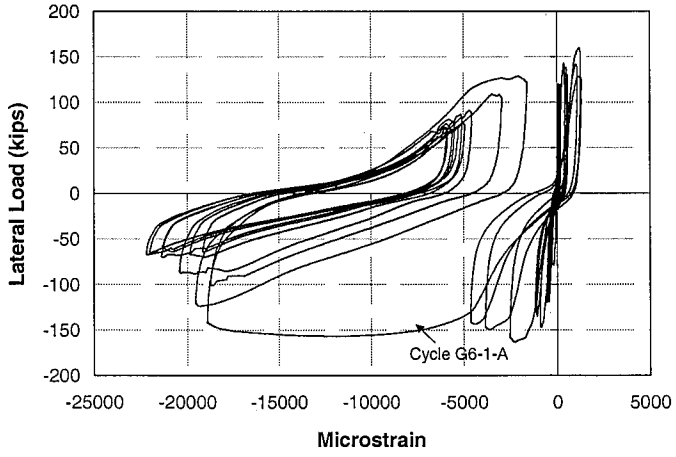

Fig. B.4.12 Reading of Strain Gage A_SJ_TA_G3

Appendix C

Calculation of the Internal Forces in the Steel Columns

As shown in Figure 3.4.3, a set of strain gages and strain rosettes were placed across four cross sections of each column: at the bottom of the first story, in the middle of the first story, at the top of the first story, and at the bottom of the second story. The longitudinal strain across each cross section was measured by one strain gage on the inside surface of each flange and the vertical leg of the strain rosette at the web center. Figure C.1 illustrates the position of these three strain gages. The strains measured by these gages are defined as ε_1, ε_2, and ε_3. The three longitudinal strain measurements were then employed to compute the curvature of the cross section utilizing linear regression, based on the assumption that the longitudinal strain distribution across the cross section was linear. According to the method of least squares, the slope, a, of the linear regression line through the three strain measurements was calculated using the measured strain magnitudes and their respective positions on the column cross-section as follows:

$$a = \frac{3\left(\sum_{i=1}^{3} x_i \varepsilon_i\right) - \left(\sum_{i=1}^{3} x_i\right)\left(\sum_{i=1}^{3} \varepsilon_i\right)}{3\left(\sum_{i=1}^{3} x_i^2\right) - \left(\sum_{i=1}^{3} x_i\right)^2} \tag{C.1}$$

The longitudinal strain at any position of the column cross-section is

$$\varepsilon_x = ax + b \tag{C.2}$$

where

$$b = \frac{\left(\sum_{i=1}^{3} x_i^2\right)\left(\sum_{i=1}^{3} \varepsilon_i\right) - \left(\sum_{i=1}^{3} x_i \varepsilon_i\right)\left(\sum_{i=1}^{3} x_i\right)}{3\left(\sum_{i=1}^{3} x_i^2\right) - \left(\sum_{i=1}^{3} x_i\right)^2} \tag{C.3}$$

As long as the cross section does not yield, the stress at any position of the column cross-section can be obtained as:

$$\sigma_x = E\varepsilon_x \tag{C.4}$$

where

E = elastic modulus of the steel material in the web or the flange

The longitudinal strain across the cross section of the steel columns is induced by the axial force and bending moment. The axial force at the centroid is the result of the integration of stress over the cross section area. The bending moment at the centroid is the result of the integration over the cross section of the axial force at any position times the distance of this position to the centroid.

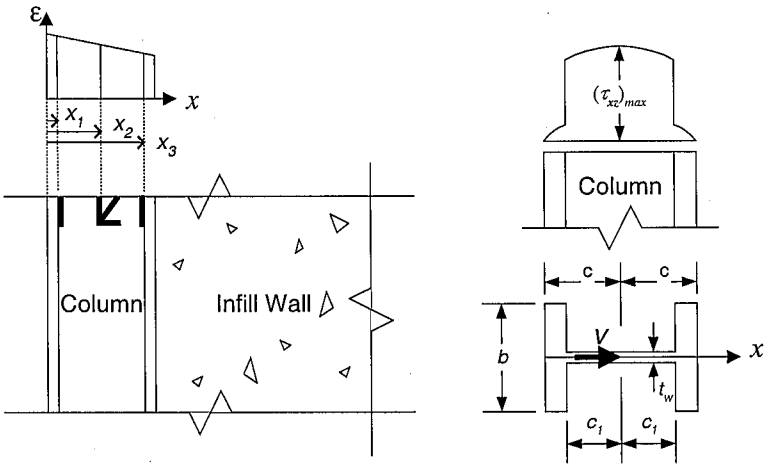

(a) Longitudinal Strain (b) Shear Stress

Fig. C.1 Stress and Strain Distribution in the Steel Column

As illustrated in Section 5.1, the measurements from the strain rosette at the web center are used to calculate the shear strain, γ_{xz}, along the cross section of the steel column. Before yielding, the elastic shear stress in the web center can then be obtained as:

$$(\tau_{xz})_{\max} = G(\gamma_{xz})_{\max} \tag{C.5}$$

where

G = shear modulus of the steel material in the web

If one considers that the steel column transmits a shear force V perpendicular to the longitudinal axis, the shear stress distribution is shown in Figure C.1. The shear stress, τ_{xz}, has its maximum magnitude in the web center and the shear force V can be calculated as:

$$V = (\tau_{xz})_{\max} \frac{2It_w}{bc^2 - bc_1^2 + t_w c_1^2} \tag{C.6}$$

where

t_w = web thickness, inches

b = flange width, inches

c_1 = half depth of the web, inches

c = half depth of the section, inches

I = moment of inertia of the entire cross section about the centroid axis y_c, in^4

For $t_f \le x \le h\text{-}t_f$, where t_f is the flange thickness, the shear stress at any position of the web can be computed as:

$$\tau_{xz} = \frac{V}{2It_w}\left[b(c^2 - c_1^2) + t_w(c_1^2 - (x-c)^2)\right] \tag{C.7}$$

The above equations are valid only when the deformation of the cross section is in the elastic range and the assumption of the linear distribution of longitudinal strain is

fulfilled. Figure 5.1.5 and Figure 5.1.6 show that, at the bottom cross-section of the north column in the first story, the assumption of a linear distribution of the longitudinal strain did not hold starting with the 0.75% drift cycles; at the bottom cross section of both columns in the second story, this assumption did not hold starting from 1.0% drift cycles. The von Mises yield criterion was used to determine the elastic limits of the cross section under the combined states of the longitudinal stress σ_x and the shear stress τ_{xz}, so that the cross section was assumed to be yielded when the stresses at any point reached

$$\sqrt{\sigma_x^2 + 3\tau_{xz}^2} = \sigma_y \tag{C.8}$$

where

σ_y = yield stress of the flange material or web material in uniaxial tension.

After yielding, the internal forces of any cross-sections are not reducible by using above equations.

References

American Concrete Institute (ACI) (1995). *Building Code Requirements for Structural Concrete (ACI 318-95) and Commentary (ACI 318R-95)*, ACI, Detroit, Michigan.

American Institute of Steel Construction (AISC) (1993). *Load and Resistance Factor Design Specification for Structural Steel Buildings*, AISC, Chicago, Illinois.

American Institute of Steel Construction (AISC) (1997). *Seismic Provisions for Structural Steel Buildings*, AISC, Chicago, Illinois.

Architectural Institute of Japan (AIJ) (1985). *Design Recommendation for Composite Construction*, AIJ, Tokyo, Japan.

American Society of Civil Engineers-Welding Research Council (ASCE-WRC) (1971). *Plastic Design in Steel*, ASCE-WRC, New York, New York.

American Society for Testing and Materials (ASTM) (1996). *Standard Test Method for Compressive Strength of Cylindrical Concrete Specimens (C39-96)*, ASTM, Philadelphia, Pennsylvania.

American Society for Testing and Materials (ASTM) (1994). *Standard Test Method for Static Modulus of Elasticity and Poisson's Ratio of Concrete in Compression (C469-94)*, ASTM, Philadelphia, Pennsylvania.

American Society for Testing and Materials (ASTM) (1996). *Standard Test Method for Splitting Tensile Strength of Cylindrical Concrete Specimens (C496-96)*, ASTM, Philadelphia, Pennsylvania.

American Society for Testing and Materials (ASTM) (1998). *Method of Making and Curing Concrete Test Specimen in the Laboratory (C192-98)*, ASTM, Philadelphia, Pennsylvania.

American Society for Testing and Materials (ASTM) (1999). *Specification for Concrete Aggregates (C33-99)*, ASTM, Philadelphia, Pennsylvania.

American Society for Testing and Materials (ASTM) (1999). *Specification for Portland Cement (C150-99)*, ASTM, Philadelphia, Pennsylvania.

American Society for Testing and Materials (ASTM) (1999). *Specification for Fly Ash and Raw or Calcined Natural Pozzolan for Use as a Mineral Admixture in Portland Cement Concrete (C618-99)*, ASTM, Philadelphia, Pennsylvania.

American Society for Testing and Materials (ASTM) (1999). *Specification for Chemical Asmixtures for Concrete (C494-99)*, ASTM, Philadelphia, Pennsylvania.

Balogh, T., Kovavshazy, G., and Frigy, A. (1991). "Pull-Out Tests on Steel Embedments in Concrete." *ACI Special Publication SP130-9*, ACI, Detroit, Michigan, pp. 221-233.

Benjamin, J. R. and Williams, H. A. (1957). "The Behavior of One-Story Reinforced Concrete Shear Walls." *Proceedings of the ASCE*, V. 83.

Bode, H. and Roik, K. (1987). "Headed Studs-Embedded in Concrete and Loaded in Tension." *ACI Special Publication SP103-4*, ACI, Detroit, Michigan, pp. 61-88.

Computer and Structures, Inc. (CSI) (1996). *Sap2000 Analysis Reference*, CSI, Berkeley, California, December.

Cook, R. A., Collins D. M., Klingner, R. E., and Polyzois. D. (1992). "Load-Deflection Behavior of Cast-in-Place and Retrofit Concrete Anchors." *ACI Structural Journal,* V. 89, No. 6, November-December, pp. 639-649.

Dawe, J. L., Schriver, A. B., and Sofocleous, C. "Masonry Infilled Steel Frames Subjected to Dynamic Load." *Canadian Journal of Civil Engineering*, V. 16, No. 6, December, pp. 877-885.

Drucker, D. C. (1956). "The Effect of Shear on the Plastic Bending of Beams." *Journal of Applied Mechanics*, ASME, December, pp. 509-514.

DeVries, R. A. (1996). "Anchorage of Headed Reinforcement in Concrete." Ph.D. Dissertation, University of Texas at Austin.

Federal Emergency Management Agency (1997). "NEHRP Guidelines for the Seismic Rehabilitation of Buildings." Report No. FEMA 273, Federal Emergency Management Agency, Washington, D.C.

Federal Emergency Management Agency (2000). "Recommended Seismic Design Criteria for New Steel Moment-Frame Buildings." Report No. FEMA 350, Federal Emergency Management Agency, Washington, D.C.

Hayashi, M. and Yoshinaga, K. (1985). "An Experimental Study of Practical Application of Composite Structures of a Frame and an Earthquake-Resistant Wall 1." *Synopses of the Conference of Architecture Institute of Japan*, AIJ, Tokyo, Japan, October, pp. 1335-1336.

Hayashi, M. and Yoshinaga, K. (1986). "An Experimental Study of Practical Application of Composite Structures of a Frame and an Earthquake-Resistant Wall 2." *Synopses of the Conference of Architecture Institute of Japan*, AIJ, Tokyo, Japan, August, pp. 1367-1368.

Hayashi, M. and Yoshinaga, K. (1987). "An Experimental Study of Practical Application of Composite Structures of a Frame and an Earthquake-Resistant Wall 3." *Synopses of the Conference of Architecture Institute of Japan*, AIJ, Tokyo, Japan, October, pp. 1317-1318.

Hayashi, M. and Yoshinaga, K. (1994). "An Experimental Study of Practical Application of Composite Structures of a Frame and an Earthquake-Resistant Wall 9." *Synopses of the Conference of Architecture Institute of Japan*, AIJ, Tokyo, Japan, September, pp. 1617-1618.

Holmes, M. (1961). "Steel Frames with Brickwork and Concrete Infilling." *Proceedings of the Institution of Civil Engineers*, V. 19, August, pp. 473-478.

Kim, Y. and Chen, W. F. (1998). "Design Tables for Top- and Seat-Angle with Double Web-Angle Connections." *Engineering Journal*, AISC, V. 35, No. 2, pp. 50-75.

Klingner, R. E. and Bertero, V. V. (1978). "Earthquake Resistance of Infilled Frames." *Journal of Structural Engineering*, ASCE, V. 104, No. 6, June, pp. 973-989.

Kwan, A. K. H. and Xia, J. Q. (1995). "Shake-Table Tests of Large-Scale Shear Wall and Infilled Frame Models." *Proceedings of the Institution of Civil Engineers: Structures and Buildings*, V. 110, No. 1, February, pp. 66-77.

Liauw, T. C. (1979). "Test on Multistory Infilled Frames Subject to Dynamic Lateral Loading." *ACI Journal*, V. 76, No. 4, April, pp. 551-564.

Liauw, T. C. and Kwan, K. H. (1983a). "Plastic Theory of Non-Integral Infilled Frames." *Proceedings of the Institution of Civil Engineers*, V. 75, September, pp. 379-96.

Liauw, T. C. and Kwan, K. H. (1983b). "Plastic Theory of Infilled Frames with Finite Interface Shear Strength." *Proceedings of the Institution of Civil Engineers*, V. 75, December, pp. 707-723.

Liauw, T. C. and Kwan, K. H. (1984). "Nonlinear Behaviour of Non-Integral Infilled Frames." *Computer and Structures*, V. 18, No. 3, pp. 551-560.

Liauw, T. C. and Kwan, K. H. (1985). "Static and Cyclic Behavior of Multistory Infilled Frames with Different Interface Conditions." *Journal of Sound and Vibration,* V. 99, No. 2, pp. 275-283.

Leon, R. T. and Shin, K. (1995). "Performance of semi-rigid frames." *Restructuring: America and Beyond Structures Congrees – Proceedings*, V. 1, ASCE, New York, New York, pp. 1020-1035.

MacGregor, J. G. (1997). *Reinforced Concrete: Mechanics and Design*, Prentice-Hall, Inc., New Jersey, New Jersey.

Makino, M., Kawano, A., Kurobane, Y., Saisho, M. and Yoshinaga, K. (1980). "An Investigation for the Design of Framed structures with Infill Walls." *Proceedings of the Seventh World Conference on Earthquake Engineering*, Istanbul, Turkey, September 8-13, 1980, V. 4, pp. 369-372.

Makino, M. (1984). "Design of Framed Steel Structures with Infilled Reinforced Concrete Walls." *Composite and Mixed Construction*, Roeder, C.W. (ed.), ASCE, New York, New York, pp. 279-287.

Mallick, D. V. and Severn, R. T. (1968). "Dynamic Characteristics of Infilled Frames." *Proceedings of the Institution of Civil Engineers*, V. 39, pp. 261-288.

Mander, J. B. and Nair, B. (1994). "Seismic Resistance of Brick-Infilled Steel Frames with and without Retrofit." *The Masonry Society Journal*, V. 12, No. 2, February, pp. 24-37.

Masubuchi K. (1980). *Analysis of Welded Structures: Residual Stresses, Distortion, and their Consequences*, Pergamon Press Inc. Elmsford, New York.

Mehrabi, A. B., Shing, P. B., Schuller, M. P., and Noland, J. L. (1996). "Experimental Evaluation of Masonry-Infilled RC Frames." *Journal of Structural Engineering*, ASCE, V. 122, No. 3, March, pp. 228-237.

Mosalam, K. M., White, R. N. and Gergely, P. (1997). "Static Response of Infilled Frames using Quasi-Static Experimentation." *Journal of Structural Engineering*, ASCE, V. 123, No. 11, November, pp. 1462-1469.

Nadjai A. and Kirby P. (1998). "Collapse of Infilled Steel Frames with Semi-Rigid Connections." *Proceedings of the Institution of Civil Engineers,* V.128, pp. 103-111.

National Earthquake Hazard Reduction Program (NEHRP) (1997). *Recommended Provisions for the Development of Seismic Regulations for New Buildings. Part I – Provisions. Part 2 – Commentary.* Building Seismic Safety Council, Federal Emergency Management Agency, Washington, D.C.

Negro, P. and Verzeletti, G. (1996). "Effect of Infills on the Global Behaviour of R/C Frames: Energy Considerations from Pseudodynamic Tests." *Earthquake Engineering and Structural Dynamics*, V. 25, No. 8, August, pp. 753-773.

Nozaka, K., Hajjar, J. F., Schultz, A. E., and Shield, C. K. (1998). "Design of an Experimental Test Facility for Steel Frames with RC Infill Walls." Structural Engineering Report No. ST-98-5, Department of Civil Engineering, University of Minnesota, Minneapolis, Minnesota, September.

Oehlers, D. J. (1989). "Splitting Induced by Shear Connectors in Composite Beams." *Journal of Structural Engineering*, ASCE, V. 115, No. 2, pp. 341-362.

Oehlers, D. J. and Bradford M. A. (1995). *Composite Steel and Concrete Structural Members: Fundamental Behavior*, Elsevier Science Ltd.

Ollgaard, J. G., Slutter, R. G. and Fisher, J. W. (1971). "Shear Strength of Stud Connectors in Lightweight and Normal-Weight Concrete." *Engineering Journal*, AISC, V. 8, No. 2, April, pp. 55-64.

Precast/Prestressed Concrete Institute (PCI) (1992). *PCI Design Handbook: Precast and Prestressed Concrete,* PCI, Chicago, Illinois.

Saari, W. K. (1998) "Behavior of Shear Connectors in Steel Frames with Reinforced Concrete Infill Walls." Masters Thesis, Department of Civil Engineering, University of Minnesota, Minneapolis, Minnesota, February.

Structural Stability Research Council (SSRC) (1998). *Guide to Stability Design Criteria for Metal Structures*, 5th Edition, T. V. Galambos (Editor), John Wiley & Sons Inc.

Sabnis G. M., Harris, H. G., White, R. N. and Mirza M. S. (1983). *Structural Modeling and Experimental Techniques*, Prentice-Hall, Inc., Englewood Cliffs, New Jersey.

SAC Joint Venture (1997). *Protocol for Fabrication, Inspection, Testing, and Documentation of Beam-Column Connection Tests and Other Experimental Specimens.* Report No. SAC/BD-97/02, SAC Joint Venture, Sacramento, California.

Saneinejad, A. and Hobbs, B. (1995). "Inelastic Design of Infilled Frames." *Journal of Structural Engineering*, ASCE, V. 121, No. 4, April, pp. 634-650.

Shahrooz, B. M., Gong B., and Arnol J. (1996). "Seismic Behavior and Design of Composite Coupling Beam." Internal Report, Department of Civil Engineering, University of Cincinnati, Cincinnati, Ohio.

Stafford Smith, B. (1966). "Behavior of Square Infilled Frames." *Proceedings of the ASCE*, V. 92, Febuary, pp. 381-403.

Stafford Smith, B. and Carter, C. (1969). "A Method of Analysis for Infilled Frames." *Proceedings of the Institution of Civil Engineers*, No. 44, September, pp. 31-48.

Taranath, B. S. (1997). *Steel, Concrete, and Composite Design of Tall Buildings*, McGraw Hill, New York, New York.

Tong, X., Schultz, A. E., and Hajjar, J. F. (1999). "Prototype Design and Plastic Analysis of Steel Frames with Composite Reinforced Concrete Infill Walls." Report No. ST-99-02, Department of Civil Engineering, University of Minnesota, Minneapolis, Minnesota, February.

Uang, C. (1991) "Establishing R (or R_w) and C_d Factors for Building Seismic Provisions." *Journal of Structural Engineering*, ASCE, V. 117, No. 1, January, pp. 19-28.

Wallace, J. W., McConnell S. W., Gupta P., and Cote P. A. (1998). "Use of Headed Reinforcement in Beam-Column Joints Subjected to Earthquake Loads." *ACI Structural Journal*, Vol. 95, No. 5, September/October, pp. 590-606.

Wood, R. H. (1978). "Plasticity, Composite Action and Collapse Design of Unreinforced Shear Wall Panels in Frames." *Proceedings of the Institution of Civil Engineers*, No. 41, September, pp. 205-222.